Jeroen Schouwenberg

General Search

for beyond the Standard Model physics

in 13 TeV *pp* collisions with the ATLAS detector

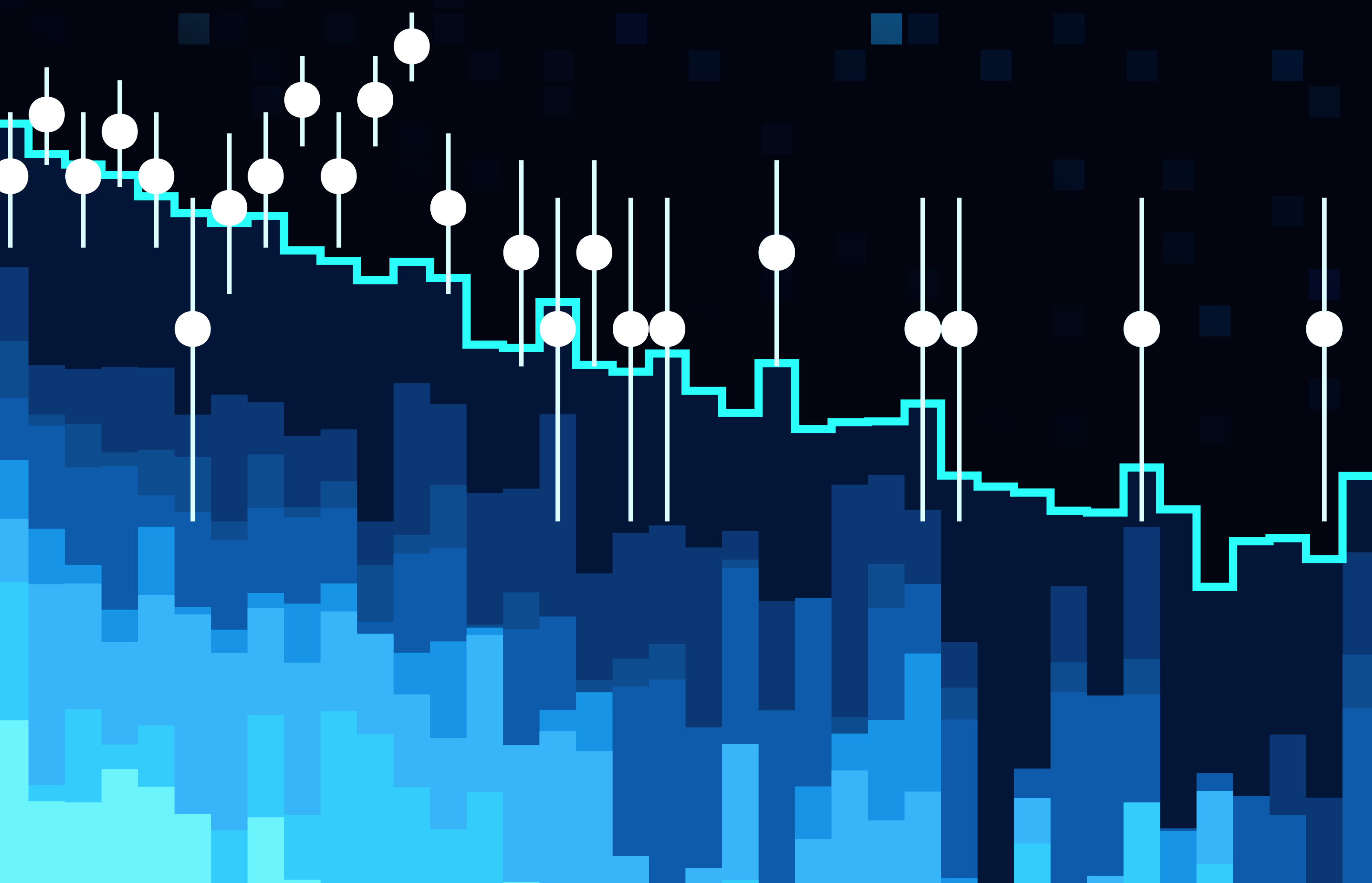

General Search

for beyond the Standard Model physics in 13 TeV pp collisions with the ATLAS detector

Proefschrift

ter verkrijging van de graad van doctor
aan de Radboud Universiteit Nijmegen
op gezag van de rector magnificus prof. dr. J.H.J.M. van Krieken,
volgens besluit van het college van decanen
in het openbaar te verdedigen op
donderdag 3 september 2020
om 15.30 uur precies

door

Jeroen Franciscus Paulus Schouwenberg

geboren op 2 augustus 1987
te Boxmeer

PROMOTOR prof. dr. N. de Groot

COPROMOTOR dr. S. Caron

MANUSCRIPTCOMMISSIE prof. dr. G.J. Lord (voorzitter)

prof. dr. Th. Hebbeker
RWTH Aachen, Duitsland

prof. dr. R. Fleischer
Vrije Universiteit Amsterdam

prof. dr. P.J. de Jong
Universiteit van Amsterdam

dr. I.B. van Vulpen
Universiteit van Amsterdam

General Search for beyond the Standard Model physics in 13 TeV *pp* collisions with the ATLAS detector
Thesis, Radboud University Nijmegen
x + 209 pages; illustrated, with bibliographic references and summary in Dutch
Printed by Ipskamp Printing

This work is part of the research programme of the Foundation for Fundamental Research on Matter (FOM), which is part of the Dutch Research Council (NWO).

Contents

Introduction

The Standard Model (SM) of particle physics is a theory that classifies the known elementary particles and formulates our current knowledge of their interactions. It has been incredibly successful at predicting a wide variety of experimental results. Several phenomena, however, lead to fundamental questions that cannot be answered within the SM, such as gravity, the observation of Dark Matter, and the matter-antimatter asymmetry of the universe among others. Many, so called, beyond the Standard Model (BSM) extensions have been proposed that address (some of) these open questions, often predicting new heavy particles and interactions that might be produced in the high centre-of-mass energy pp collisions attained by the Large Hadron Collider (LHC).

Direct searches for unknown particles and interactions are, therefore, a primary objective of the physics programme at the LHC. The ATLAS experiment at the LHC has thoroughly analysed the Run 1 pp collision dataset (recorded in 2010–2012) and the Run 2 dataset (2015–2018) but no evidence of physics beyond the Standard Model has been found in any of the searches performed so far.

In the past couple of decades, breakthrough discoveries of new particles and interactions were often the result of searches that were strongly motivated and guided by theoretical arguments, as was the case for e.g. the search for the Higgs boson, the search for the top quark, or the search for the weak neutral current. After the discovery of the Higgs boson, the last missing piece of the SM 'puzzle', the theoretical guiding power has become far weaker. A plethora of BSM extensions have been described in literature some of which introduce vast number of (sometimes barely constrained) parameters. Several strategies attempting to make sense out of these large parameter spaces have been employed, such as: excluding regions that are at tension with current (precision) measurements; excluding regions that would require some sort of fine-tuning of parameters to be viable; singling out parameter regions that are more attractive from a theoretical point of view; or by constructing simplified models that try to capture the essence of phenomenological signatures. The latter can be constructed bottom-up (from an Effective Field Theory) or top-down by integrating-out parameters of more ultraviolet-complete models.

Direct searches that have been performed to date do not (and cannot) fully cover the enormous parameter space of masses, cross sections and decay channels of possible new particles. Signals might be hidden in kinematic regimes and final states that have remained unexplored. This motivates a BSM-model-independent analysis for which the guiding principle is shifted from theoretical arguments to experimental data by searching for BSM signals in a structured, global and automated way, such that many of the final states not yet covered can be probed.

General searches without a specific BSM signal assumption have been been performed by the DØ Collaboration [1–4] at the Tevatron, by the H1 Collaboration [5, 6] at HERA, and by the CDF Collaboration [7, 8] at the Tevatron. At the LHC, (preliminary) versions of such searches have been performed by the ATLAS Collaboration at $\sqrt{s} = 7$, 8 and 13 TeV [9–11], and by the CMS Collaboration at $\sqrt{s} = 7$ and 8 TeV [12, 13].

This thesis will outline and analyse the strategy employed by the ATLAS Collaboration to search systematically for deviations of the data from the SM prediction. No BSM signal is assumed explicitly but some generic features of a potential BSM signal are assumed, such as the expectation that signal events have reconstructed objects with relatively large momentum transverse to the beam axis. The main objective of this strategy is to identify any phase-space regions with significant deviations of the data from the SM prediction in a subset of the total dataset available. The observation of one (or more) significant deviations in some phase-space region(s) initiates the performance of a dedicated analyses focussing on these 'data-derived' phase-space signal region(s). The main advantage of this procedure is that it allows a large number of final states and phase-space regions to be explored and tested with the available resources, thus minimising the possibility of missing a signal for new physics, while simultaneously maintaining a low false discovery rate by reanalysing the data-derived signal regions (DDSRs) in a dedicated analysis, allowing further optimisation of the background model, and subsequently testing it on an independent dataset.

The procedure starts by classifying events into different (mutually exclusive) categories, labelled with the multiplicity of final-state objects in an event, such as muons, electrons, jets, missing transverse momentum, etc. In each final-state category an algorithmic search is performed to locate the region with the largest deviation of the data from the SM prediction in a certain distribution. The search is performed on several different BSM-sensitive distributions. Sensitivity tests for specific signal models are performed to demonstrate the effectiveness of the approach. The method has been applied to a subset of the $\sqrt{s} = 13$ TeV proton–proton (pp) collision data collected in 2015 and corresponding to an integrated luminosity (L_{int}) of 3.2 fb^{-1}. It was first reported in Ref. [11]. This thesis contains: a more detailed analysis of the methodology; the application of the method to the aforementioned 2015 dataset including several new developments in the analysis; and the application to a larger subset of the Run 2 data, corresponding to $L_{\text{int}} = 36.2$ fb^{-1} collected in 2015 and 2016, in a preliminary version of the analysis including further developments.

Outline

Chapter 1 gives a summary of the SM and its application to collider experiments. The classification of the elementary particles and the formulation of their interactions is summarized, followed by a short discussion of the shortcomings of the SM and several extensions that have been proposed to address these shortcomings. Finally, a summary is given of how predictions for collider experiments are obtained from the SM using Monte Carlo (MC) integration.

Chapter 2 gives a brief overview of the LHC and the ATLAS experiment, summarizing the different subdetectors, trigger system and its simulation for MC simulated events.

Chapter 3 describes the reconstruction of the pp collision events which includes the identification and reconstruction of each of the physics objects considered in the analyses described in this thesis by combining the information from the different subdetectors.

Chapter 4 outlines the strategy to search for unanticipated signals for new physics. A brief introduction to the strategy is given, followed by an analysis of the strategy using simplified examples. The last part of the chapter describes the analysis strategy as it is applied to the ATLAS datasets and summarises the advantages and disadvantages of the method.

Chapter 5 describes the application of the search strategy to the 2015 ATLAS dataset. This is an updated version of the analysis previously published in Ref. [11].

Chapter 6 describes a preliminary version of the analysis using the combined 2015 & 2016 ATLAS datasets. The analysis is based on the one described in Chapter 5 but applied to a larger dataset and extending the search to classes of more inclusive event selections and additional objects.

Chapter 7 contains the conclusions and the outlook on future applications of the search method to larger datasets.

Additional information that is considered too long or too detailed for the main body is contained in the appendices at the end of the thesis and is referenced from the main body where appropriate.

Personal contributions

The work described in this thesis, especially Chapter 5, is based on Ref. [11] for which the author (of this thesis) was one of the main contributors. Contributions have been made ranging from the development of the main analysis software, the construction of the background model and the statistical procedures, to the editing of the paper and internal support note. The studies in Chapter 4, the updated version of the analysis in Chapter 5, and the preliminary analysis in Chapter 6 were performed (exclusively) by the author. All figures in these chapters and corresponding appendices are produced by the author and have not undergone ATLAS approval, hence the absence of the 'ATLAS' label in all those figures.

Several other contributions have been made to projects outside the scope of this thesis. Among others to: the commissioning of a new trigger algorithm for missing transverse momentum [14] operating at the first trigger level (L1); the investigation and truth-level analysis of many (order 100,000) 'troublesome' pMSSM models points in order to evaluate the impact of the Run 1 SUSY searches performed by ATLAS on the constraints on dark matter candidates [15]; the initial background studies of a new and ongoing analysis searching for the production of supersymmetric particles in final states with three soft leptons; sensitivity evaluations in an ongoing effort to identify effective classifiers based on unsupervised machine learning methods for model-independent searches for new physics; the development of an internal webpage for interactive browsing of the vast number of plots that can be produced with the analysis software used for the work described in this thesis; (credited) service work for the collaboration (such as trigger efficiency studies, on-call shifts and comparisons of major ATLAS software releases).

1 Beyond the Standard Model

During the second half of the 20$^{\text{th}}$ century, the work of many theoretical and experimental particle physicist (see Ref. [16–43] among others) culminated in the formulation of a quantum field theory (QFT), now known as the Standard Model of particle physics. It describes the elementary particles and their interactions that have been observed at experiments thus far within the theories of electroweak and strong interactions. The electroweak theory [16–18] unifies the weak interactions [44] and quantum electrodynamics (QED) [19–21], and predicted the existence of the, at the time, unobserved weak neutral current. The strong interaction is described by quantum chromodynamics (QCD) [22–24]. At that point, the SM also anticipated yet unobserved elementary particles: the charm [25], bottom and top [26] quark, the tau lepton and neutrino [45] and the Higgs boson [27, 28], which have subsequently been discovered at experiments [46–52]. Additionally, since then, experimental predictions provided by the SM have withstood many precision tests (see e.g. Chapter 10 of Ref. [53]) firmly establishing the SM as the most-successful theoretical model for the description of high-energy particle interactions to date. Notwithstanding its successes, it falls short of being a complete theory that incorporates gravitational interactions and still leaves many phenomena unexplained.

This chapter starts with a summary of the SM. A pedagogical introduction to the SM can by found, among others, in Ref. [54–56]. This is followed by a summary of the phenomena that are not understood within the context of the SM and which motivate the search for its extension. Finally, some aspects important to the description and simulation of hadron collider experiments are discussed.

1.1 The Standard Model of particle physics

The SM encodes our current understanding of three out of the four[1] known fundamental forces and the fundamental building blocks of matter: elementary particles. It is a renormalisable [33] QFT, i.e. a field theory in Minkowski spacetime invariant under spacetime translations and *all* Lorentz transformations (or *relativistically* invariant) in which elementary particles are quanta of a corresponding field and interactions are described by a Lagrangian density ($\mathcal{L}$). The SM has an $SU(3)_C \times SU(2)_L \times U(1)_Y$ gauge symmetry[2] that describes the dynamics and interactions of the strong force (QCD) with an $SU(3)_C$ Yang-Mills theory [34], and unifies the electromagnetic (QED) and weak forces into a single electroweak theory forming the $SU(2)_L \times U(1)_Y$ Yang-Mills component which, after spontaneous electroweak gauge symmetry breaking (EWSB) to a $U(1)_Q$ gauge symmetry via the Higgs mechanism [27–30] describes the elementary particle spectrum observed in experiments.

[1] The SM does not incorporate gravitational interactions.

[2] The subscripts C, L, Y and Q stand for colour charge, (weak) left-handed isospin, (weak) hypercharge and electric charge respectively.

1.1.1 Particle content

The particles of the SM can be classified into two main categories: particles with half-integer spin, so called *fermions* that obey the *Pauli exclusion principle* and hence follow Fermi–Dirac statistics, and particles with integer spin, so called *bosons* obeying Bose–Einstein statistics. Fermions are the *matter* particles while bosons include all the *force-carrying* particles and the Higgs boson. All elementary particles are a priori massless as 'bare mass-terms' in the Lagrangian density (or, for short, Lagrangian) would break the theory's invariance under local gauge transformations. The EWSB mechanism generates masses for all elementary particles observed to be massive in a way that maintains local gauge invariance, and predicts the existence of the Higgs boson in addition.

Fermions There are 12 *flavours* of fermions in the SM and 12 corresponding antiparticles. They can be further classified into three *generations*, ordered such that each successive generation is a more massive 'copy'[3] of the previous generation of fermions. Each generation contains two *quarks*: an up-type quark with charge[4] $+^2/_3$ and a down-type quark with charge $-^1/_3$, as well as two *leptons*: one with charge -1, and a corresponding *neutrino* without charge. The classification as one of these four types of fermions is based on the *charges* the particle carries, such as the electric charge, allowing QED interactions, and colour charges, allowing QCD interactions.

Quarks are the only fermions to carry a colour charge, of which there are three types or *colours* (and anti-colours for anti-quarks), and are thereby subject to the strong force. They *hadronize*, i.e. form colour-neutral bound states (hadrons) of two or more (anti-)quarks, and are therefore not observed as free particles. Quarks can also interact via the weak and QED interactions. The names of the up-type quark flavours are *up* (u), *charm* (c) and *top* (t), the down-type flavours are called *down* (d), *strange* (s) and *bottom* (b).

Leptons do not carry colour charge, are therefore not subject to the strong force, and can be observed as free particles. Neutrinos only have weak interactions while charged leptons can undergo weak and QED interactions. The lepton flavours are called electron (e), muon (μ) and tau (τ), and the neutrinos take the name of the corresponding leptons, e.g.: electron neutrino (ν_e).

A fermion (or a hadronic state containing a fermion) of the second or third generation produced in a high-energy environment (e.g. at a particle collider) rapidly decays to fermions of the first generation through charged weak interactions. The third generation top-quark does so even before it hadronizes. The first generation therefore describes 'everyday' matter. An exception to this are the neutrinos, which are (in the SM assumed to be) massless and therefore stable across the three generations[5].

Table 1.1 shows the arrangement of the fermions in the top half of the table where a distinction is made between *left-chiral* (subscript L) and *right-chiral* (subscript R) states. The left-chiral states form a lepton doublet (L_L) and quark doublet (Q_L) under the $SU(2)_L$ transformations.

[3]Fermions have the same quantum numbers (except for the flavour quantum numbers) across the three generations and therefore have identical interactions (except for different Yukawa couplings).

[4]Charge means electric charge, unless specified otherwise.

[5]Neutrinos are observed to oscillate between lepton flavours which implies they do have non-zero masses. However, being the lightest fermions in the SM they cannot decay to lighter states. Neutrino masses are one of the shortcomings of the SM and discussed in the next section.

Physical fermion states acquire mass through the mixing of the two chiral states enabled by (Yukawa interactions with) the non-zero vacuum expectation value of the neutral scalar (Higgs) field. Quarks form the fundamental triplet representation under $SU(3)_C$. Leptons / right-handed particles (or left-handed anti-particles) form singlets (i.e. trivial representations) of $SU(3)_C$ / $SU(2)_L$ respectively.

Table 1.1: Particle content of the SM. The $SU(2)_L$ doublets are indicated with brackets. Under the '$SU(3)_C$' column the dimension of the representation under $SU(3)_C$ is listed, column '$SU(2)_L$' lists the third component of weak isospin (T_3) and column '$U(1)_Y$' lists weak hypercharge (Y). The last column 'Q' lists the electric charge and is related to Y and T_3 as $Q = Y/2 + T_3$. Hypothetical right-chiral neutrinos (ν_R) are *sterile*, i.e. decoupled from the other SM particles and are here not considered to be part of the SM.

Type	Spin		Field	Particle content Gen. 1	Gen. 2	Gen. 3	$SU(3)_C$ Dim	$SU(2)_L$ T_3	$U(1)_Y$ Y	Q
Fermions	$^1/_2$	Leptons	L	$\begin{pmatrix}\nu_e\\ e\end{pmatrix}_L$	$\begin{pmatrix}\nu_\mu\\ \mu\end{pmatrix}_L$	$\begin{pmatrix}\nu_\tau\\ \tau\end{pmatrix}_L$	**1**	$+^1/_2$ $-^1/_2$	-1 -1	0 -1
			ℓ_R	e_R	μ_R	τ_R		0	-2	-1
		Quarks	Q	$\begin{pmatrix}u\\ d\end{pmatrix}_L$	$\begin{pmatrix}c\\ s\end{pmatrix}_L$	$\begin{pmatrix}t\\ b\end{pmatrix}_L$	**3**	$+^1/_2$ $-^1/_2$	$+^1/_3$ $+^1/_3$	$+^2/_3$ $-^1/_3$
			u_R	u_R	c_R	t_R		0	$+^4/_3$	$+^2/_3$
			d_R	d_R	s_R	b_R		0	$-^2/_3$	$-^1/_3$
Bosons	1	Mediators	G_μ	g (gluons)			**8**	0	0	0
			B_μ W^3_μ	$\xrightarrow{\text{EWSB}}$	γ & Z boson		**1**	0 0	0 0	0 0
			$W^{1,2}_\mu$	$\xrightarrow{\text{EWSB}}$	$W^\pm$			± 1	0	± 1
	0	Higgs	$\phi = \begin{pmatrix}\phi^+\\ \phi^0\end{pmatrix}$	$\xrightarrow{\text{EWSB}}$	H		**1**	$+^1/_2$ $-^1/_2$	$+1$ $+1$	$+1$ 0

Gauge bosons The gauge bosons mediate the fundamental interactions. Gauge fields arise naturally from requiring *local gauge invariance*, which means 'extending' an existing invariance under a global continuous transformation such that it also holds when applying the transformation locally, i.e. spacetime dependent. These gauge bosons either become massive as a result of spontaneous symmetry breaking: a situation where the vacuum state does not exhibit the symmetry of the Lagrangian, or remain massless when associated to an unbroken symmetry. The EWSB of the $SU(2)_L \times U(1)_Y$ gauge symmetry to $U(1)_Q$ generates masses for the $W^\pm$ and Z bosons: physical states that emerge along with the photon from a mixture of the three $W^{1,2,3}$ fields (the triplet of $SU(2)_L$) and the B field (generator of $U(1)_Y$), and separates the electromagnetic and weak forces.

The $W^{1,2,3}$ bosons couple to left-handed weak isospin (T_3), i.e. the doublets under $SU(2)_L$, while its non-abelian structure gives rise to self-interactions. The B boson couples to hypercharge.

Photons (γ) mediate QED interactions between all electrically charged particles. The massless photon corresponds to the unbroken local $U(1)_Q$ gauge symmetry of the QED interactions with electric charge, $Q = Y/2 + T_3$, being the conserved quantity. It emerges from a mixture of the neutral W^3 and B fields.

Weak interactions are mediated by the electrically charged $W^{\pm}$ bosons and the neutral Z boson. The $W^{\pm}$ bosons only couple to the *left-chiral* fermion (or the right-chiral anti-fermion) states and transform a particle into the other particle of the $SU(2)_L$ doublet. This unique property of the $W^{\pm}$ interaction is called a *flavour-changing* interaction. The weak eigenstates are mixtures of the mass eigenstates of the different generations and is encoded in the *CKM matrix* [26, 57]. This, therefore, also allow cross-generational flavour-changing interactions. The Z boson, being a mixture of the neutral W^3 and B fields like the photon, interacts with *all* SM fermions (also right(left)-chiral (anti-)fermions, although with different strength) and with the $W^{\pm}$ bosons. The weak force has a short-range effect due to masses of the bosons.

The gluons mediate the strong force and couple to the colour-charged quarks. Gluons come in eight different colour-charged forms (corresponding to the adjoint octet representation of $SU(3)_C$) which gives rise to gluon self-interactions. It also gives rise to the confinement of quarks and gluons in colour-neutral hadrons at low energies, or equivalently at long distances [58]. The physical (renormalized) coupling strengths of all three fundamental interactions are scale-dependent (known as *running coupling constants*). For the weak and electromagnetic interactions the coupling becomes weaker at lower energy scales, whereas it becomes stronger for QCD. At high energies, i.e. short distances, the QCD coupling constant becomes asymptotically weaker and the quarks and gluons are approximately free particles (known as *asymptotic freedom* [23, 24]) allowing perturbative QCD calculations.

Higgs boson The Higgs boson is a scalar particle, i.e. it has no intrinsic spin, and emerges as the massive physical state from the complex scalar field after EWSB. The mass of the Higgs boson is proportional to the vaccuum expectation value (v) and it has interactions with all other massive particles as well as self-interactions.

1.1.2 Mathematical formalism

Gauge fields The part of the Lagrangian describing the dynamics and self-interactions of the gauge fields is most compactly written in terms of the field strength tensors[6]:

$$\mathcal{L}_{\text{gauge}} = -\frac{1}{4} G^a_{\mu\nu} G^{a\mu\nu} - \frac{1}{4} W^{a'}_{\mu\nu} W^{a'\mu\nu} - \frac{1}{4} B_{\mu\nu} B^{\mu\nu} \tag{1.1}$$

with the field strength tensors defined as:

$$G^a_{\mu\nu} = \partial_\mu G^a_\nu - \partial_\nu G^a_\mu - g_s f^{abc} G^b_\mu G^c_\nu \qquad a,b,c \in \{1,\ldots,8\} \tag{1.2}$$

$$W^a_{\mu\nu} = \partial_\mu W^a_\nu - \partial_\nu W^a_\mu - g\epsilon^{abc} W^b_\mu W^c_\nu \qquad a,b,c \in \{1,2,3\} \tag{1.3}$$

$$B_{\mu\nu} = \partial_\mu B_\nu - \partial_\nu B_\mu \tag{1.4}$$

where the G (gluon), W, and B gauge fields are associated to the $SU(3)_C$, $SU(2)_L$ and $U(1)_Y$ gauge groups respectively; μ and ν are spacetime indices[7]; a, b and c run over the number of generators / gauge fields of the underlying symmetry group; f^{abc} and ϵ^{abc} are the structure constants of $SU(3)_C$ and $SU(2)_L$[8]; and g_s and g are coupling constants. The B field is abelian,

[6] All repeated indices within a term should be summed over.

[7] Lower indices are short for: $A_\mu = \eta_{\mu\nu} A^\nu$ where $\eta_{\mu\nu}$ is the Minkowski metric tensor.

[8] The structure constants (as well as the Dirac/gamma-matrices (γ^μ), Pauli matrices (σ^a), Gell-Mann matrices (λ^a), etc.) can be found in any introductory textbook (e.g. Ref. [54]), so for brevity they will not be introduced here.

so the structure constant vanishes and the field has no self-interactions, just as the physical photon field arising through EWSB and in contrast to the G and W fields.

Fermions The dynamics of the fermions and their interactions with the gauge fields is summarized by:

$$\mathcal{L}_{\text{fermions}} = \sum_{\text{fermions}} i\bar{\psi}\gamma^{\mu}D_{\mu}\psi \tag{1.5}$$

where $\psi \in \{Q,\ L,\ u_R,\ d_R,\ e_R\}$ are Dirac spinors[9], $\bar{\psi}$ is the adjoint of ψ defined as $\bar{\psi} \equiv \psi^{\dagger}\gamma^0$, γ^{μ} are the Dirac matrices, and D_{μ} is the covariant derivative encoding the interactions with the gauge fields. It contains:

$$D_{\mu} \supseteq \partial_{\mu} + \frac{1}{2}ig'B_{\mu}Y_{\mathrm{f}} \tag{1.6}$$

for each fermion field, giving the kinetic terms and interactions with the B field, where g' is the $U(1)_Y$ coupling constant and Y_{f} is the weak hypercharge of the fermion as listed in Table 1.1. For the $SU(3)_C$ triplets (quarks) it contains the interactions with the gluons:

$$D_{\mu} \supset \frac{1}{2}ig_s G^a_{\mu}\lambda^a \tag{1.7}$$

where λ^a are the Gell-Mann matrices. For $SU(2)_L$ doublets it contains the interactions with the W bosons:

$$D_{\mu} \supset \frac{1}{2}igW^a_{\mu}\sigma^a \tag{1.8}$$

where σ^a are the Pauli matrices. These interaction terms with the gauge fields, in the covariant derivative, make the Lagrangian invariant under local gauge transformations of the SM symmetry group.

Scalar field The generation of masses for the three weak bosons, requires at least three degrees of freedom. An $SU(2)$ doublet of complex scalar fields which has four degrees of freedom is therefore the minimal requirement. The part of the Lagrangian describing the complex scalar fields is given by:

$$\mathcal{L}_{\text{Higgs}} = (D^{\mu}\phi)^{\dagger}D_{\mu}\phi - V(\phi) = (D^{\mu}\phi)^{\dagger}D_{\mu}\phi - \mu^2\phi^{\dagger}\phi - \lambda(\phi^{\dagger}\phi)^2 \tag{1.9}$$

where ϕ is an $SU(2)$ doublet of two complex scalar fields as given in Table 1.1, and μ and λ are parameters defining the scalar potential $V(\phi)$. EWSB occurs for the case where $\mu^2 < 0$ (and $\lambda > 0$ in order for the potential to be bounded from below). Rather than having a minimum at $\phi = 0$ for $\mu^2 > 0$, when $\mu^2 < 0$ the potential has minima at $\phi^{\dagger}\phi = -\mu^2/(2\lambda) \equiv v^2/2$. Choosing a point from this degenerate minimum such that only the real component of the electrically neutral field is non-zero, the vaccuum expectation value for the doublet is:

$$\langle\phi\rangle_0 = \langle 0|\phi|0\rangle = \frac{1}{\sqrt{2}}\begin{pmatrix} 0 \\ v \end{pmatrix} \tag{1.10}$$

Rewriting the Lagrangian in terms of v and complex scalar field components that are zero at v, followed by a gauge transformation that eliminates the unphysical fields (unitary gauge), the

[9] A Dirac spinor ψ is a four-component spinor containing both a left- and right-chiral representation. The projection operator $P_{R/L}$ projects ψ onto the left- and right-chiral parts: $\psi_R = P_R\psi = \frac{1}{2}(1+\gamma^5)$ and $\psi_L = P_L\psi = \frac{1}{2}(1-\gamma^5)$.

field becomes:

$$\phi = \frac{1}{\sqrt{2}}\begin{pmatrix} 0 \\ v+H \end{pmatrix} \tag{1.11}$$

where H is the physical Higgs field and the remaining three degrees of freedom of the complex scalar doublet are no longer explicitly present since, in this gauge, they are associated with the longitudinal polarizations of the three massive weak bosons.

The covariant derivate in Eq. 1.9, acting on a $SU(2)_L$ doublet, consists of the terms in Eqs. 1.6 and 1.8. Expanding it using the field in Eq. 1.11 and using the following redefinitions of the gauge fields (in terms of the *weak mixing angle* θ_w):

$$\begin{aligned} W^{\pm}_{\mu} = \frac{W^1_{\mu} \mp iW^2_{\mu}}{\sqrt{2}}, \qquad Z^0_{\mu} = \frac{gW^3_{\mu} - g'B_{\mu}}{\sqrt{g^2+g'^2}} = \cos\theta_w W^3_{\mu} - \sin\theta_w B_{\mu} \\ A_{\mu} = \frac{gW^3_{\mu} + g'B_{\mu}}{\sqrt{g^2+g'^2}} = \cos\theta_w W^3_{\mu} + \sin\theta_w B_{\mu} \end{aligned} \tag{1.12}$$

reveals the (absence of) bilinear mass terms for the physical electroweak gauge bosons in the Lagrangian with the masses:

$$m_{W^{\pm}} = \frac{vg}{2}, \qquad m_Z = \frac{v\sqrt{g^2+g'^2}}{2} = \frac{m_{W^{\pm}}}{\cos\theta_w}, \qquad m_{\gamma} = 0 \tag{1.13}$$

The massless photon reflecting the unbroken $U(1)_Q$. Additionally, the terms in the expansion containing H give the kinetic term for the Higgs field and the interactions of the Higgs boson with the massive $W^{\pm}$ and Z gauge bosons.

The scalar potential, rewritten using Eq. 1.11, becomes:

$$V(H) = \left(-\frac{\lambda}{4}v^4\right) + \lambda v^2 H^2 + \lambda v H^3 + \frac{\lambda}{4}H^4 \tag{1.14}$$

where the term between brackets is a constant and therefore irrelevant and the second term, squared in H, is a mass term, hence the Higgs boson mass is defined as:

$$m_H = \sqrt{2\lambda}v \tag{1.15}$$

The last two terms are the Higgs self-interactions with coupling constant λ.

Yukawa The scalar field also provides a way to generate gauge invariant mass terms for fermions through Yukawa couplings. The Yukawa part of the Lagrangian is given by:

$$\mathcal{L}_{\text{Yukawa}} = -\bar{\mathbf{L}}\mathbf{y}_e\phi\mathbf{e}_R - \bar{\mathbf{Q}}\mathbf{y}_d\phi\mathbf{d}_R - \bar{\mathbf{Q}}\mathbf{y}_u\left(i\sigma_2\phi^*\right)\mathbf{u}_R + \text{h.c.} \tag{1.16}$$

where $\mathbf{L}$, $\mathbf{Q}$, $\mathbf{e}_R$, $\mathbf{d}_R$ and $\mathbf{u}_R$ are column vectors in generation space, e.g. $\mathbf{e}_R = (e_R,\ \mu_R,\ \tau_R)^{\text{T}}$, and $\mathbf{y}_e$, $\mathbf{y}_d$ and $\mathbf{y}_u$ are the Yukawa couplings represented in complex 3×3 matrices. After EWSB, using Eq. 1.11, this becomes:

$$\mathcal{L}_{\text{Yukawa}} = -\frac{v+H}{\sqrt{2}}\left(\bar{\mathbf{e}}_L\mathbf{y}_e\mathbf{e}_R + \bar{\mathbf{d}}_L\mathbf{y}_d\mathbf{d}_R + \bar{\mathbf{u}}_L\mathbf{y}_u\mathbf{u}_R + \text{h.c.}\right) \tag{1.17}$$

The physical states or mass eigenstates of the fermion fields are those for which the Yukawa coupling matrices are diagonal and have positive and real entries. Applying the appropriate (bi-unitary) transformations to obtain the diagonal Yukawa coupling matrices and fermionic fields in this new bases (m), the Yukawa part becomes:

$$\mathcal{L}_{\text{Yukawa}} = -\frac{v+H}{\sqrt{2}}\left(\sum_{\text{fermions}} [\bar{\psi}_L]_m y_\psi [\psi_R]_m + [\bar{\psi}_R]_m y_\psi [\psi_L]_m\right) \tag{1.18}$$

$$= -\frac{v+H}{\sqrt{2}} \sum_{\text{fermions}} \bar{\psi} y_\psi \psi \tag{1.19}$$

where the brackets with the subscript m indicate the transformed fermion fields and y_ψ are the Yukawa couplings from the diagonalized matrix.

So the Yukawa Lagrangian describes two phenomenological aspects after EWSB: interactions between the Higgs boson and the fermions, and mass terms for the physical fermion states with $m_\psi = v y_\psi/\sqrt{2}$. The left and right chiral fields are related to each other, and are mixed into the physical states $\psi \equiv \bar{\psi}_L\psi_R + \bar{\psi}_R\psi_L$, only through the Yukawa interactions.

Electroweak interactions Using the gauge field definitions given by Eq. 1.12, the interactions of the electroweak sector between the gauge fields and fermions, given by Eqs. 1.6 and 1.8, can be rewritten in terms of the physical fields arising after EWSB as:

$$\mathcal{L}_{\text{neutral}} = g\sin\theta_w J^A_\mu A^\mu + \frac{g}{\cos\theta_w} J^Z_\mu Z^{0\mu} \tag{1.20}$$

$$\mathcal{L}_{\text{charged}} = \frac{g}{\sqrt{2}}\left(J^+_\mu W^{+\mu} + J^-_\mu W^{-\mu}\right) \tag{1.21}$$

with:

$$J^A_\mu = Q_{\text{f}}\bar{\psi}\gamma_\mu\psi \tag{1.22}$$

$$J^Z_\mu = \frac{1}{4}\bar{\psi}\gamma_\mu\left[(2T_{3\text{f}} - 4Q_{\text{f}}\sin^2\theta_w) - \gamma_5(2T_{3\text{f}})\right]\psi \tag{1.23}$$

$$J^+_\mu = \frac{1}{2}\bar{\psi}_u\gamma_\mu(1-\gamma_5)\psi'_d \tag{1.24}$$

where Q_{f} and $T_{3\text{f}}$ are the electric charge and third component of weak isospin of the fermion as given in Table 1.1, and ψ_u and ψ_d are the up- and down-type fermions as they appear in the $SU(2)_L$ doublet. The $(1-\gamma_5)/2$ structure projects ψ onto the left-chiral part. Most parts of the Lagrangian are unaffected by the change in bases that were performed to diagonalize the Yukawa coupling matrices. The notable exception being the charged current interactions $J^\pm_\mu$ for which the current eigenstates remain different from the mass eigenstates after changing the fermionic bases. The current eigenstates ψ' are related to the mass eigenstates by a unitary transformation described by the *CKM matrix* (V_{CKM}) and is customarily applied to the down-type quarks[10], such that:

$$(d'\ s'\ b')^{\text{T}} = V_{\text{CKM}}\,(d\ s\ b)^{\text{T}} \tag{1.25}$$

[10] For the leptons the mass and current eigenstates coincide since the neutrinos are massless. Neutrinos with Dirac masses have a similar *PMNS* matrix [59, 60].

The largest elements in the CKM matrix are on the diagonal and the smallest elements are those furthest away of the diagonal. It is completely characterized by four real parameters[11]: three independent mixing angles between the generations and one CP violating complex phase. The latter requires at least three generations of fermions [26].

1.1.3 Parameters of the Standard Model

Table 1.2 summarizes the parameters of the SM that passed the discussion in the previous sections, with the exception of θ_{QCD} which will be discussed in Section 1.2. These parameters are determined by experiment and a review of recent values and world averages can be found in Ref. [53].

Table 1.2: The 19 parameters of the Standard Model.

Symbol	**Description**	**Param. count**	**Alternative forms**
g_s, g, g'	$SU(3)_C, SU(2)_L, U(1)_Y$ gauge couplings	3	$\tan\theta_w = g/g'$ (weak mixing angle) $e = g\sin\theta_w$ ($U(1)_Q$ coupling) $\alpha = (4\pi)^{-1}(g'g)^2 / (g'^2+g^2)$ $= (4\pi)^{-1} e^2$ (fine structure constant) $\alpha_s = (4\pi)^{-1} g_s^2$
y_f	Yukawa couplings	9	$m_f = y_f v/\sqrt{2}$ (fermion mass)
$\theta_1, \theta_2, \theta_3$	CKM mixing angles	3	
δ	CKM CP-violating phase	1	
v	Vacuum expectation value	1	
λ	Higgs self-coupling	1	$m_H = \sqrt{2\lambda}v = \sqrt{-2\mu^2}$ (Higgs mass)
θ_{QCD}	QCD vacuum angle	1	

1.1.4 Renormalization

The coupling constants listed in Table 1.2 are so-called *bare parameters* and do not correspond to the *physical* and experimentally measurable couplings. Renormalization is the reparametrization of a QFT in terms of physical or *renormalized* parameters, after *regularization* of the logarithmically ultraviolet (UV) divergent integrals in the perturbative expansions. Regularization procedures introduce an arbitrary scale (e.g. a cut-off mass) which is eliminated by allowing the couplings and masses to become dependent on an energy scale (Q) and renormalizing them to a measured value at an arbitrary reference or *renormalization scale* μ (or μ_R). The resulting Q dependent couplings $\alpha(Q^2)$ (and masses) are called *running coupling constants*. Varying Q changes the coupling $\alpha(Q^2)$ and is described by *beta-functions*:

$$Q^2 \frac{\partial\alpha(Q^2)}{\partial Q^2} \equiv \beta(\alpha) = -(\beta_0\alpha^2 + \beta_1\alpha^3 + \beta_2\alpha^4 + \ldots) \tag{1.26}$$

[11] The remaining five degrees of freedom are phase factors that can be absorbed by a redefinition of the fermion fields.

which are obtained (at each order) by requiring that perturbatively calculated observables $R(\alpha, \mu)$ are independent of the arbitrary reference scale μ, i.e.:

$$\frac{\mathrm{d}R(\alpha,\mu)}{\mathrm{d}\ln(\mu^2)} = \left(\mu^2 \frac{\partial}{\partial \mu^2} + \beta(\alpha)\frac{\partial}{\partial \alpha}\right) R(\alpha,\mu) = 0 \tag{1.27}$$

This is the *renormalization group equation* and it requires all explicit μ-dependence to be exactly cancelled by the μ-dependence of $\alpha(\mu^2)$. Only in the exact case, i.e. summing the perturbation series of R to all orders, would α indeed be independent of μ, whereas finite perturbation series will have a decreasing residual dependence with increasing number of terms.

The running of α can then, once measured at some scale μ, be used to make theoretical predictions at any other scale Q. The one-loop QED running coupling is:

$$\alpha(Q) = \frac{\alpha(\mu)}{1+\beta_0\alpha(\mu)\ln(Q^2/\mu^2)} \quad \text{with} \quad \beta_0 = -\frac{1}{3\pi} \tag{1.28}$$

while for QCD this becomes:

$$\alpha_s(Q) = \frac{\alpha_s(\mu)}{1+\beta_0\alpha_s(\mu)\ln(Q^2/\mu^2)} \quad \text{with} \quad \beta_0 = \frac{11n_c - 2n_f}{12\pi} \tag{1.29}$$

with $n_c = 3$ colour charges and $n_f = 6$ flavours in the SM.

Intuitively, for QED the running electric charge can be understood as an effective charge screened due to vacuum polarisation, becoming smaller for larger distances i.e. small momentum transfer. This is reflected by the positive beta-function in QED. For QCD the beta-function is negative as a result of the additional contributions from gluon self-interactions (anti-screening), which means that for larger distances the renormalized coupling keeps increasing until $\alpha_s(Q^2) > 1$ (at roughly 1 GeV) and perturbation theory breaks down. Observationally, this leads to the *confinement* of quarks and gluons in hadrons. Conversely, at short distances this leads to *asymptotic freedom* allowing the use of perturbation theory for the computation of e.g. hard scattering cross sections of hadronic interactions at the LHC. The running of the QED $\alpha(Q^2)$ is a small effect compared to the running of $\alpha_s(Q^2)$.

1.2 Shortcomings of the Standard Model

The SM, despite its immense successes as a description of particle interactions at the current experimentally accessible energy scales, falls short of being a *theory of everything* which is often considered to be the ultimate goal of (particle) physics. Shortcomings in this respect can stem from its inability to explain observed phenomena, observed phenomena at odds with its predictions, or from fine-tuning problems. Some of these phenomena are summarized below.

Gravity Gravitational interactions are not described in the SM. They are expected to become non-negligible, and therefore to break the predictions of the SM, in processes involving energies near the Planck scale ($\Lambda_{\text{Planck}} \approx 10^{19}$ GeV). The quanta of gravitational interactions, *gravitons*, must be massless spin-2 bosons. However, naive models obtained from a QFT treatment of gravity are not renormalizable, demanding a more complete theory. A complete and consistent theory that includes quantum gravity effects and effectively reduces to the SM at low energies does not yet exist.

Dark Matter Numerouos cosmological observations [61] show that the majority ($\approx$ 85%) of matter in the observable universe is non-luminous and non-absorbing. This matter, observed through its gravitational effects, is termed *dark matter*. Most dark matter is cold (i.e. non-relativistic), non-baryonic matter not described by SM matter. Possible candidates for non-baryonic particle dark matter must be stable (at least on cosmological time scales), interact very weakly with electromagnetic (EM) radiation, thus be electrically neutral, and have the right relic density. Popular candidates include: primordial black holes, axions (see *strong CP problem*), sterile neutrinos (see *neutrino oscillations*) and weakly interacting massive particles or *WIMPs*. The latter constitutes a new hypothetical massive particle for which it can be shown that it produces the correct relic density by assuming thermal production and subsequent *freeze-out* of thermal equilibrium in the early universe if it has a mass of the order of 100 GeV and an annihilation cross section corresponding to typical weak interactions. This makes it a prime candidate for direct detection experiments and production searches at the LHC. Currently though, direct detection experiments have been putting tight constraints on some of these hypotheses.

Dark Energy The bulk ($\approx$ 68%) of the content of the universe is an unknown form of energy, *Dark Energy*, which is believed to be a constant vacuum energy that drives the accelerated expansion of the universe. Calculated values of the zero-point energy in the SM are, however, many (120) orders of magnitude larger than the observed vacuum energy density in cosmology which is referred to as the *cosmological constant problem* [62].

Neutrino oscillations Neutrinos are assumed massless in the SM. They are, however, observed to change flavour [63] which indicates they are massive [64]. The upper limit on the sum of masses of the neutrinos is constrained to 0.170 eV [65] and so the masses are much smaller than the masses of the other fermions in the SM. The relation between the mass eigenstates and the weak eigenstates is encoded in the *PMNS matrix*, analogous to the CKM matrix for quarks. The exact ordering of neutrino masses is not known to date, neither is the mechanism behind the generation of the neutrino masses. Masses can be generated by either (or both): the Dirac mechanism, like for other SM fermions, requiring the existence of a right-chiral neutrino forming an $SU(2)_L$ singlet having only Yukawa interactions and therefore also called a *sterile neutrino*; or the Majorana mechanism, in which case the neutrinos are Majorana fermions, i.e. they are their own antiparticles, allowing possible lepton-number violating decays such as neutrinoless $\beta^-\beta^-$ decay.

Baryon asymmetry In the early hot universe, pair creation and annihilation were in thermal equilibrium, until the universe cooled down too much for pair creation to occur and the matter and anti-matter annihilated. A small excess of matter over anti-matter (of the order 10^{-10} [66]) resulted in what makes up the matter content of our current universe. While the SM of particle physics and cosmology fulfil the necessary conditions (i.e. baryon number violation, CP violation, and a deviation from thermal equilibrium) to generate a matter-antimatter asymmetry dynamically, also called *baryogenesis*, it is unlikely to explain the entirety of the asymmetry observed. Many BSM theories provide additional mechanisms or explanations for baryogenesis.

Higgs mass At some high-energy scale (Λ_{UV}) the SM, being an effective 'low-energy' field theory, is expected to become invalid, e.g. at $\Lambda_{\mathrm{UV}} = \Lambda_{\mathrm{Planck}}$ where a more complete theory which includes quantum gravity is needed. The vast difference in Λ_{UV} and the electroweak scale then becomes a problem (the *hierarchy problem*) as it introduces contributions to the Higgs mass of the order Λ_{UV} such that a fine-tuning between the quadratically divergent radiative corrections and the bare mass of one part in $\Lambda^2_{\mathrm{UV}}/v^2$ is required. This is considered *unnatural* and believed to be indicative of additional underlying symmetries.

Electric charge quantization Experimentally, electric charges appear to be quantized and existing only as integer multiples of the down-type quark electric charge. However, the SM as presented in this chapter (in particular, having three generations and only left-chiral massless neutrinos) does not account for this quantization [67, 68] and, in the view of the stringent experimental limits on the amount of charge dequantization ($< 10^{-21}\ e$ [69, 70]), poses a naturalness problem. Many proposed extensions of the SM such as extra dimensions, magnetic monopoles and grand unified theories do offer an explanation, but also introduce a lot of (yet unobserved) new physics. The minimally sufficient condition, however, to realize charge quantization can be achieved by a small modification of the minimal SM Lagrangian such that it breaks any additional (to $U(1)_Y$) global anomaly-free $U(1)$ symmetries. This can be achieved by extensions of, for instance, the lepton sector with three right-handed neutrinos with Majorana mass terms, but many other extensions work equally well.

Strong *CP* problem The QCD Lagrangian allows a CP-violating term characterized by the parameter θ_{QCD}. Experimental limits (from measurements of the neutron electric dipole moment [71]) on θ_{QCD} require it to be smaller than 10^{-10} or, in other words, to be fine-tuned. A well-known solution is the addition of a spontanuously broken $U(1)_{\mathrm{PQ}}$ global symmetry (for Peccei–Quinn theory) to the SM [72]. This would then require the existence of axions, the Nambu–Goldstone boson of the broken symmetry [73, 74].

Generations and parameters The SM does not provide a deeper insight into the structure of the fermions, i.e. it does not provide an answer to the questions of why there are three generations and why there is an approximate exponential relation between the Yukawa couplings of the successive generations. It also does not explain the origin of the CKM mixing and CP-violating angles, the gauge symmetry group, and the scalar potential. Many extensions of the SM attempt to explain some of these parameters or their relationships rather than having them as free parameters of the theory.

Muon anomalous magnetic moment The muon magnetic anomaly ($(g-2)/2$) comprises of the SM loop corrections to the muon magnetic moment. It is sensitive to loop contributions from new heavy particles with mass M. Such contributions are suppressed by a factor $(m_\mu/M)^2$ making it far more sensitive than the electron anomalous magnetic moment (which is suppressed by a factor $(m_e/M)^2$). Current experimental values are at tension (approx. 3.5 σ) with the SM prediction, but are generally considered inconclusive [53]. It is therefore debatable whether it currently is a shortcomings of the SM but is nevertheless often considered in the construction of new BSM models. Efforts are ongoing to improve the experimental results [75].

1.3 Possible extensions of the Standard Model

1.3.1 Unification of gauge couplings

So called *grand unified theories* (GUTs) are extensions of the SM in which the three gauge interactions are merged into a single force, so that they are described by a single, larger gauge group such as $SU(5)$ [76] or $SO(10)$ [77], at the GUT scale (approx. 10^{16} GeV). The scale dependence (or running) of the renormalized SM gauge couplings is such that the they nearly converge at the GUT scale (after normalizing the hypercharge as required by $SU(5)$ or $SO(10)$ gauge groups) but do not unify. When the existence of (some form of) supersymmetry (SUSY) is assumed, the running of the gauge couplings can be modified to meet exactly at the GUT scale [78]. Such theories are attractive as they explain some of the free SM parameters and, because quarks and leptons fit within a single representation, provide an explanation for charge quantization. GUTs also predict new heavy gauge bosons with interactions that violate lepton and baryon number [79], allowing proton decay. Experimental lower limits on the proton's lifetime, which are of the order of 10^{34} years [80], form an important constraint on possible GUTs.

1.3.2 Supersymmetry

SUSY [81] refers to a class of theories that posses an additional spacetime symmetry relating bosons to fermions. Every SM fermion has a bosonic superpartner and every SM boson has a fermionic superpartner, which together form a supermultiplet. The non-observation of superpartners in experiments thus far means that, if SUSY is realized, the symmetry is broken and the more massive superpartners have so far been out of experimental reach. Nevertheless, SUSY potentially addresses some of the issues listed in the previous section:

Higgs mass The additional quantum corrections to the Higgs mass coming from the superpartners in a SUSY SM cancel out the quadratically divergent radiative corrections of the SM particles exactly. SUSY thus protects against large quantum corrections resolving the fine-tuning problem and stabilizing the Higgs mass.

Unification of gauge couplings In SUSY models the running of the gauge couplings can be modified such that they unify at a GUT scale.

Dark Matter The lightest SUSY particle can be protected against decaying into SM particles by imposing R-parity conservation[12]. This is needed to make the model phenomenologically viable (e.g. to be compatible with the proton's lifetime). SUSY can thereby provide a WIMP candidate to explain the observed non-baryonic dark matter density.

[12] R-parity is a multiplicative quantum number given by $P_R \equiv (-1)^{3(B-L)+2s}$, where B, L and s are baryon number, lepton number and spin respectively. It evaluates to +1 for SM particle and to -1 for superpartners.

Gravity Promoting global SUSY to a *local* symmetry results in gauge theories known as *supergravity* which are supersymmetric theories of gravity. They contain (at least) a spin-2 *graviton* and a spin-$^3/_2$ superpartner the *gravitino* as the gauge field of local SUSY. It is currently understood to be consistent only as an effective field theory of a (class of) theories with a larger structure: *superstring theories*, which address the non-renormalizability issue of quantum gravity.

Muon anomalous magnetic moment Certain regions in SUSY parameter space can lead to a deviation in the muon anomalous magnetic moment of the observed magnitude from virtual corrections of supersymmetric particles [82, 83].

SUSY is furthermore considered interesting as it realizes the only possible external symmetry left beyond the Poincaré symmetry (Lorentz and translational invariance), combining space-time and internal symmetries, while resulting in non-trivial scattering amplitudes [84, 85].

The many new states that SUSY models predict might be detectable at the LHC. A SUSY signal can be any of the large number of possible signatures that depend on many (new) parameters.

1.3.3 Extra dimensions

Theories involving additional dimensions were introduced as early as the 1920's in an attempt to unify gravity and EM [86]. In the past two decades the interest in this class of theories has risen again after new insights from (super)string theory. The idea was first introduced by Kaluza, Klein and Mandel [87–90], assuming a $4 + n$ dimensional spacetime with n compactified (e.g. on a circle for $n = 1$) extra dimensions. Fields defined in $4 + n$ dimension are periodic in each of the n compactified dimensions, resulting in a Fourier series of *modes* which are observable as four-dimensional fields and referred to as Kaluza–Klein (KK) excitations or a KK tower. A massless fundamental (scalar) field results in a KK tower with a massless *zero mode* and all higher modes massive and increasing in mass.

Following developments in (super)string theory during the 1980's and 90's *Large Extra Dimensions* were proposed [91, 92] in order to offer a solution to the hierarchy problem of the weak and the Planck scale. In this mechanism, gravity can propagate through the $4 + n$ dimensional *bulk* of spacetime, while SM particles are localized on a four dimensional *domain wall*. Depending on the thickness of the wall, all of physics is effectively four-dimensional, except for gravity, below a corresponding energy scale (e.g. $O(10\,\text{TeV})$). The result is that the *fundamental* Planck scale (Λ_D) in the bulk can be of $O(10\,\text{TeV})$ while appearing effectively as Λ_Planck in the four-dimensional domain wall. One effect of extra dimensions would be a modification of Newtonian gravity at distances comparable to the size R of the extra dimension. For a given Λ_D of $O(10\text{ TeV})$ this results in R of $O(10^{12}\text{ cm})$ for $n = 1$ and R of $O(0.1\text{ mm})$ for $n = 2$. The existence of two or more extra dimensions is therefore possible as experimental constraints on departures from Newtonian gravity at a scale of $O(0.1\,\text{mm})$ and smaller are weak.

Many different variations on theories with extra dimensions exist such as *Warped Extra Dimensions* [93, 94], *Infinitely Large Extra Dimensions* [95] and *Universal Extra Dimensions* [96].

Collider signatures of models with extra dimensions that lower Λ_D to the TeV scale consist e.g. of the production and subsequent decay of microscopic black holes.

1.3.4 New heavy gauge bosons

SUSY and extra dimensions play a central role in GUTs motivated by superstring theories, e.g. the E_6 gauge group GUT model [97]. These models, starting from some large gauge group, break to an extended SM gauge group with (one or more) additional $U(1)'$ or $SU(2)'$ symmetries which correspond to new heavy vector bosons referred to as Z' or W' bosons that might be observed at the TeV scale [98]. Many different models can be constructed and motivated [99, 100] and are not necessarily GUT motivated. The *Sequential Standard Model* is the simplest (benchmark) model having one additional Z' boson with fermions couplings taken to be the same as those of the SM vector boson and the mass is a free parameter.

1.3.5 Phenomenology

The classes of models described above in general introduce many new parameters and the different models corresponding to each point in parameter space can differ vastly phenomenologically. To make sense out of these large parameter spaces, searches for new physics effects in favour of a class of models is often performed using simplified or constraint versions of the parameter spaces. Simplified models try to capture the essence of phenomenological signatures of a large part of a parameter space, while constraint parameter spaces exclude regions that are at tension with current (precision) measurements, would require fine-tuning of some sort to be viable, or single out regions that are more attractive from a theoretical viewpoint. Besides the classes of models listed above, many other possible models of extensions of the SM exist and many more might yet be unthought-of. It is therefore important to supplement collider searches for new physics that are based on existing models and which cannot completely cover the enormous parameter spaces of all (un)known SM extensions, with model-independent generic searches for signatures signalling departure from the SM.

1.4 Hadron collider physics

For colliders of elementary particles, such as e^+e^- colliders, the incoming elementary particle and momentum are fixed. At hadron colliders, such as the LHC, this is not the case as the incoming partons participating in the hard scattering are part of the hadrons and carry a fraction x of each hadron's momentum. These hadrons (protons) cannot be described by perturbative QCD. The QCD *factorization theorem* allows the separation or *factorization* of the short and long distance descriptions of the interaction, i.e. the perturbatively calculable hard scattering of incoming partons versus the universal non-perturbative and infrared-singular parton distributions. In this section, some of the aspects important to the description and simulation of hadron collider experiments are discussed.

1.4.1 Accelerators

The physics performance of a collider is characterized by the instantaneous luminosity (L) and the center-of-mass energy ($\sqrt{s}$) that is achieved. The expected rate of events ($\mathrm{d}N/\,\mathrm{d}t$) of a (rare) process X is given by:

$$\frac{\mathrm{d}N}{\mathrm{d}t} = L \cdot \sigma_{pp \to X}(s) \tag{1.30}$$

where $\sigma_{pp\to X}(s)$ is the total cross section for the process $pp \to X$ as a function of $\sqrt{s}$, typically increasing with $\sqrt{s}$ as the more abundant partons with a lower longitudinal momentum fraction start contributing or opening up the possibility for the production of new heavy particles. The rare processes that are of interest are many orders of magnitude smaller than the total pp cross section which is dominated by soft QCD processes.

1.4.2 Parton densities

The partons of the hadron, e.g. a proton, are assumed to move collinear with the proton while carrying a fraction of the longitudinal momentum of the proton. The number of partons of type i inside the proton, where i can be u, d, c, s, (b,) the corresponding anti-quarks, and g, carrying a fraction of the proton's momentum between x and $x + \mathrm{d}x$ is given by $f_i(x)\mathrm{d}x$ where $f_i(x)$ is the parton density function (PDF). For the valence quarks of the proton, $f_u(x)$ and $f_d(x)$ have a maximum just below $x = 1/3$ while the gluon density is negligible at $x \approx 1$ and grows rapidly for increasingly smaller x. The other sea-quark density functions also increase for smaller x but are much smaller than the gluon densities.

The PDFs cannot be computed from theory and need input from experiment, however for a proton the following sum rules apply in order to obtain the right quantum numbers:

$$\langle N_u \rangle = \int_0^1 \left(f_u(x) - f_{\bar{u}}(x)\right) \mathrm{d}x = 2 \tag{1.31}$$

$$\langle N_d \rangle = \int_0^1 \left(f_d(x) - f_{\bar{d}}(x)\right) \mathrm{d}x = 1 \tag{1.32}$$

which is saying that the excess of quarks are precisely the expected valence quarks. Contributions from sea-quarks come in the form of quark-antiquark ($q\bar{q}$) pairs from gluon splitting and do not contribute. Furthermore it holds that the sum of the momenta fractions of the partons is unity hence:

$$\langle \sum x_p \rangle = \int_0^1 x \left(\sum_q f_q(x) + \sum_{\bar{q}} f_{\bar{q}}(x) + f_g(x) \right) \mathrm{d}x = 1 \tag{1.33}$$

To remove the infrared-singularities arising in the collinear or soft radiation limits, the divergences are regularized and eliminated by introducing renormalized PDFs $f_i(x, \mu_F)$. This new arbitrary scale, reminiscent of the renormalization scale, is called the *factorization scale* (μ_F) and separates what is considered long and short-distance physics. Long-distance physics is factored in the renormalized PDFs and their evolution is described by the renormalisation group equation or *DGLAP*[13] *evolution equation* [35, 101, 102]. They are used to compute the hadronic pp cross section for the generic process $pp \to X$ at a centre-of-mass energy of $\sqrt{s}$:

$$\sigma_{pp\to X}(s) = \sum_{i,j} \int_0^1 \mathrm{d}x_1 \int_0^1 \mathrm{d}x_2\, f_i(x_1, \mu_F^2)\, f_j(x_2, \mu_F^2)\, \hat{\sigma}_{ij\to X}(\hat{s}, \mu_F^2, \mu_R^2) \tag{1.34}$$

where $\hat{\sigma}(\hat{s}, \mu_F^2, \mu_R^2)$ is the perturbatively calculated partonic cross section with incoming partons i and j at a centre-of-mass energy of $\sqrt{\hat{s}} = \sqrt{x_1 x_2 s}$.

[13] Dokshitzer–Gribov–Lipatov–Altarelli–Parisi

1.5 Monte Carlo simulations

MC simulations of high-energy hadron collision events attempt to simulate the details of the exclusive final state. Simulations of SM and BSM processes are widely used in the design of particle physics experiments and data analysis and often also to simulate the expected background contribution and compare it to the experimental data, e.g. in this work. General-purpose MC event generators such as SHERPA [103, 104], PYTHIA [105–107] and HERWIG [108–110] can be used for such comparisons in many different observables. The simulation of events consists of several aspects: the hard scattering process, parton shower, hadronization and the underlying event. While the integration of high-dimensional phase-space integrals might necessitate the use of MC integration, it has the additional advantage that the use of pseudorandom numbers can be exploited to mimic to probabilistic nature of individual quantum events, allowing them to be used as such for further detector simulation and to model any observable of choice.

Comprehensive review can be found in Chapter 41 of Ref. [53] and Ref. [111].

1.5.1 Hard scattering process

The simulation starts from the hard scattering process. Typically, the processes of interest at the LHC have large momentum transfers (Q) or high invariant-mass final-states. These processes in which the incoming partons interact to produce few outgoing SM (or BSM) particles can be computed using perturbation theory due to the asymptotic freedom of QCD. The factorization Ansatz in Eq. 1.34 is used to compute the inclusive cross section, where

$$\hat{\sigma}_{ij\to X}(\hat{s}, \mu_F^2, \mu_R^2) = \int \mathrm{d}\Phi_{ij\to X} \frac{1}{2\hat{s}} |\mathcal{M}_{ij\to X}|^2 (\Phi_{ij\to X}, \mu_F^2, \mu_R^2) \tag{1.35}$$

with $|\mathcal{M}_{ij\to X}|^2$ the (appropriately summed and averaged over helicities and colours) matrix element (ME) squared for the partonic process, i.e. the sum over contributing Feynman diagrams, and $\mathrm{d}\Phi_{ij\to X}$ the differential phase space element over the final-state particles. The Feynman rules, and hence diagrams, are derived from the SM Lagrangian. Therefore, the ME contains the dynamics of the process, while the phase-space factor contains the kinematics.

For leading order (LO) processes automated tools exist to construct and evaluate the MEs for processes with many final-state particles. MC samples computed with a LO ME describe the differential shape well but will have large higher-order corrections on the inclusive cross section, i.e. normalization. They are therefore typically rescaled to the higher-order inclusive cross section by a single factor (K-factor), which is only approximately valid. However, many generators nowadays use automated calculations of next-to-leading order (NLO) MEs. In this case the matrix element consist of the tree (Born) level terms, an infrared-finite real-emissions term, and a term containing the subtracted infrared-divergent (soft and colinear) emmissions in combination with the loop (i.e. virtual) corrections. For infrared-safe observables then, the divergences in the latter term cancel [112–114]. The virtual contribution is commonly provided by specialized *one-loop provider* software interfaced with the tree-level ME generator.

The cross section, necessarily computed at finite order, depends on the choice for μ_F and μ_R and on the choice of PDF. Typical choices for the scales are related to the hard scale (Q), e.g. $\mu_F^2 = \mu_R^2 = Q^2$, but 'educated' choices depend on the final-state. Higher order computations reduce the dependency on the arbitrary and non-physical scales and therefore reduce the uncertainty on the MC prediction, but require the regularization and subsequent renormalization of virtual divergence / cancellation of virtual against real divergences of the additional UV / IR divergences respectively.

1.5.2 Parton showers

The ME produces only the inclusive final-state X. Additional radiation from the incoming or outgoing partons (or colour-charged BSM particles) of the ME, happening at timescales corresponding to the hard scale $1/Q$ up to the $1/\Lambda$ corresponding to the confinement scale (Λ), are simulated by parton shower (PS) algorithms. They describe successive emissions from partons (or pairs of partons forming a coloured dipole) while conserving four-momentum and the inclusivity of the ME process. As such, they represent approximate higher-order corrections to the hard process, summing the dominant contributions (leading logarithms) of all orders in α_s.

The (differential) cross section for a final-state with an additionally radiated parton diverges for collinear emission and soft gluon emission. The collinear-dominant contribution factorizes into the cross section without the radiated parton and an additional factor, proportional to $\alpha_s(q^2)$. This factor corresponds therefore to the probability of an emission and can be applied as an iterative Markov chain after each parton splitting creating a *parton shower*. The divergence is regulated by introducing a cut-off scale, on e.g. the virtuality (Q_0^2), the relative transverse momentum of the emission, or the opening angle, for which the splitting is just physically *resolvable*. Starting from the hard scale Q^2, and requiring $q^2 < Q^2$ to be smaller for each successive splitting than the value it originated from, the shower develops until no resolvable splitting take place above Q_0^2, resulting in a finite number of emitted partons. In practice though, the running of $\alpha_s(q^2)$ requires the cut-off on Q_0^2 to be larger than Λ^2. It can be shown that for showers evolving and ordered by the opening angle (rather than the virtuality) of the emission (or dipole showers evolving by the transverse momentum of the emission) the soft gluon effects are also correctly taken into account [115]. This is therefore called *coherent showering*.

Initial state radiation is obtained by backward evolution: starting from the incoming hard partons the probability that it came from another parton at higher x and lower q^2 can be obtained from the evolution of the PDFs as given by the DGLAP equations. It can again be applied iteratively until reaching a cut-off scale Q_0^2.

Modern PSs furthermore consider effects arising from colour coherence and massive partons. It should be noted that the PS is an approximation derived in the soft and/or collinear limit which it describes well, but hard wide-angle emissions are not.

1.5.3 Matching and merging

A fixed-order ME takes into account *all* higher-order corrections up to a fixed order in α_s, while a PS resums (next-to-)leading-logarithmic corrections in all orders of α_s. A combination of both would provide the most accurate result. *Matching* is the correct integration of the higher-order corrections to the inclusive ME process with the PS by matching the hardest emission to exactly reproduce the ME. Another strategy is *merging*, in which all partons produced above an arbitrary scale (merging scale) are generated with a (higher-order-)ME, while partons below this scale are evolved with the PS. Care should always be taken to avoid any double counting, especially when the PS is not ordered in hardness. State-of-the-art MC generation schemes employ a combination of matching and merging.

1.5.4 Hadronization

As the evolution of the PS has reached Q_0^2 and α_s is becoming non-perturbatively large, confinement should occur. This can be simulated with the phenomenological *Lund string model* [116] in which gluonic field lines between separated quarks-antiquark pairs (or quarks-antiquark-gluon systems) form and are attracted into *QCD strings* due to the gluon self-interactions. The potential energy grows linearly with distance between colour charges causing new quarks-antiquark pairs to be formed when this is energetically favourable, separating the string iteratively. This model correctly predicts many phenomenological features such as the formation of additional hadrons in-between the original quarks along the string.

An alternative model, the *cluster model* [117], is based on the theoretical observation that as the shower evolves from Q^2 to Q_0^2 clusters of partons emerge in a colour singlet state with a mass of order Q_0, which the authors call *pre-confinement*. The process of confinement which occurs somewhere in the evolution from Q_0^2 down to the mass scale of hadrons, can then simply be described by the decaying of these colourless clusters into hadrons.

1.5.5 Underlying event

The underlying event constitutes the multiple interactions of the hadron remnants that do not participate in the hard interaction but which still produce more activity than events without any identifiable hard process. These arise from the inclusive jet cross section growing larger than the inclusive pp cross section at low transverse momentum, i.e. the production of multiple jets in a single pp collision. The underlying event is therefore not only consisting of non-perturbative physics and requires showering of relatively hard partons as well. Understanding and modelling it is complex but necessary to understand its effect on the hard interaction and detector. The activity and effects from multiple particle interactions in the underlying event depends, among others, on the impact parameters of the hadrons and the colour arrangements.

2 The LHC and the ATLAS experiment

The data studied in this thesis are gathered from a large number of high energy pp collisions. These collisions are realised by the LHC located at the European Organization for Nuclear Research (CERN). The remnants of these collisions are recorded by the ATLAS particle detector. This chapter gives a concise summary of the LHC and the ATLAS experiment.

2.1 The Large Hadron Collider

In an attempt to answer some of the open questions in particle physics discussed in Chapter 1, CERN has built the world's largest and most powerful particle accelerator to date: the LHC [118]. The LHC is located in a 27 km long circular tunnel close to Geneva and is designed to provide pp collisions with a $\sqrt{s}$ of 14 TeV at an instantaneous luminosity of $10^{34}\,\text{cm}^{-2}\,\text{s}^{-1}$ by colliding bunches of up to 10^{11} protons at a rate of 40 MHz. It is also designed to collide heavy ions (lead nuclei) at $\sqrt{s} = 5.5$ TeV per nucleon pair with a luminosity of $10^{27}\,\text{cm}^{-2}\text{s}^{-1}$, and has successfully collided protons with heavy ions as well.

In the initial data taking period from 2010 to 2012 (Run 1) the LHC produced pp collisions at a $\sqrt{s}$ of 7 and 8 TeV with a peak instantaneous luminosity of $7.7 \cdot 10^{33}\,\text{cm}^{-2}\,\text{s}^{-1}$ [119, 120]. Following the first Long Shutdown, the LHC has resumed pp collisions in 2015 at $\sqrt{s} = 13$ TeV reaching peak luminosities in excess of $2 \cdot 10^{34}\,\text{cm}^{-2}\,\text{s}^{-1}$ [121] as part of the Run 2 data taking period which will last until the end of 2018. The work described in this thesis only uses data recorded in Run 2 from pp collisions at $\sqrt{s} = 13$ TeV.

The LHC acts as a double storage ring for the two counter-circulating proton beams, as well as a particle accelerator, receiving the beams at 450 GeV through a chain of linear and circular pre-accelerators, and accelerating each proton beam to 6.5 TeV in Run 2. The beam consists of bunches with a minimal temporal spacing of 50 ns in Run 1 and 25 ns in Run 2, and are brought into collision at shallow angles (of a few hundred microradians) in four interaction points around the ring.

Each interaction point has one of the four major particle detectors of the LHC constructed around it: ALICE and LHCb are two specialised detectors to study quark–gluon plasma produced in heavy ion collisions and the decay modes of b-hadrons respectively; ATLAS [122] and CMS [123] are two general-purpose detectors optimised to detect a very wide range of possible signals and precisely measure SM physics processes [124, 125]. The LHC also accommodates three smaller experiments: TOTEM, LHCf, and MoEDAL to respectively measure the total (in)elastic pp cross section, complement cosmic ray experiments by studying collision remnants very close to the beam-pipe, and search directly for magnetic monopoles.

2.2 ATLAS experiment

The ATLAS experiment [122] is a multipurpose particle physics detector with a forward-backward symmetric cylindrical geometry and a coverage of nearly 4π steradian in solid angle. It has recorded the pp collisions delivered by the LHC which correspond to an integrated luminosity of 5.5 fb^{-1} at $\sqrt{s} = 7$ TeV [119] and 22.7 fb^{-1} at $\sqrt{s} = 8$ TeV [120] during Run 1. In Run 2 the LHC has delivered 158 fb^{-1} of pp collision data at $\sqrt{s} = 13$ TeV [121]. The data used in this thesis are the 3.9 fb^{-1} recorded in 2015, the first year of data taking in Run 2, and the 35.6 fb^{-1} of data recorded in 2016.This section contains details on the various sub-detectors, the Trigger and Data Acquisition system (TDAQ) and the detector simulation.

2.2.1 Coordinate system

The coordinate system used by the ATLAS experiment to describe a collision event is a right-handed coordinate system coinciding with the nominal interaction point; the x-axis points towards the centre of the LHC ring; the y-axis is perpendicular to the beam pointing upwards; and hence the z-axis is parallel to the beam direction. More commonly though, the cylindrical coordinate representation is used in which ρ is the distance to the z-axis, the azimuthal angle ϕ is the angle with the x-axis in the plane orthogonal to the z-axis, and the polar angle θ is the angle with the z-axis. A more convenient coordinate for which differences are invariant under boosts along the z-axis is rapidity (y) defined as $y \equiv 1/2 \cdot \ln[(E + p_z)/(E - p_z)]$ where E denotes the energy and p_z is the component of the momentum along the beam direction. For massless particles, or in the relativistic case where particle masses can be neglected, y reduces to the pseudorapidity η, defined as $\eta \equiv -\ln\tan(\theta/2)$ and depending only on the polar angle. Angular separations are measured either as $\Delta R \equiv \sqrt{(\Delta\eta)^2 + (\Delta\phi)^2}$ or, less commonly, as a function of y: $\Delta R_y \equiv \sqrt{(\Delta y)^2 + (\Delta\phi)^2}$ which is again Lorentz invariant under boosts along the z-axis. Transverse momentum (p_{T}), transverse energy (E_{T}), and missing transverse momentum ($E_{\mathrm{T}}^{\mathrm{miss}}$) are defined as the magnitudes of the projections of the corresponding three-dimensional vectors in the plane orthogonal to the z-axis. The transverse impact parameter (d_0) is defined as the distance of closest approach to a reference point, such as the z-axis, beam-line or a vertex, in the plane orthogonal to the z-axis. The longitudinal impact parameter (z_0) is defined as the z-value of the point that determines d_0.

2.2.2 Detector requirements

The requirements for the ATLAS detector, shown in Figure 2.1, have been defined using an extensive set of SM and new physics processes that might be observed at the TeV scale, with the search for the SM Higgs boson having been an important benchmark. The expected small cross-sections for possible new physics phenomena requires a high luminosity collider which in turn results in a large number of inelastic pp collisions per bunch crossing (μ), or *pile-up*, that accompany a new physics or rare SM candidate event. The overwhelmingly dominating QCD jet production cross-section over the rare SM or BSM processes, which are of interest, require the identification of specific signatures characterising these rare processes through e.g. particle-identification, the detection of missing transverse momentum ($E_{\mathrm{T}}^{\mathrm{miss}}$), secondary vertex finding or the identification of disappearing tracks. These challenges define a general set of requirements for the detector:

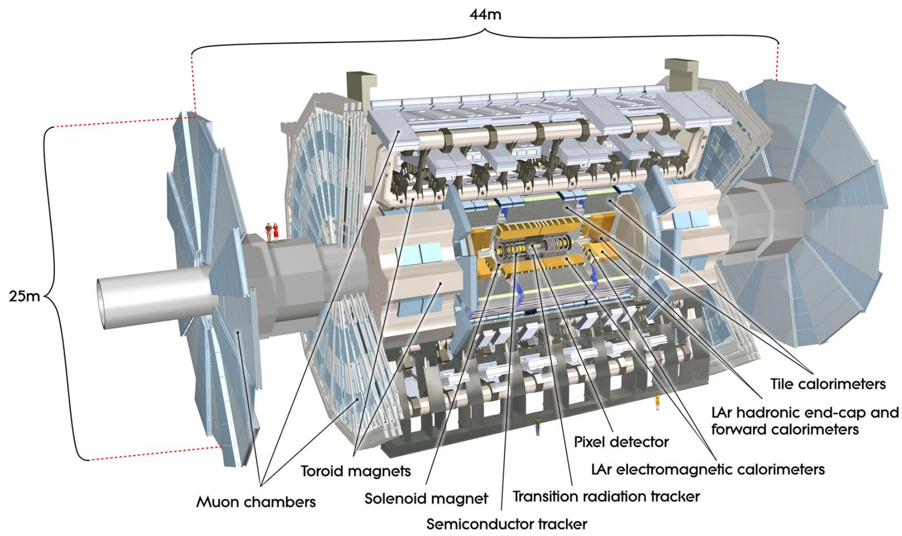

Figure 2.1: Cut-away view of the ATLAS detector revealing the different sub-detectors. The dimensions are indicated and several human-sized figures are drawn next to and on top of the detector to give a sense of the scale.

- Fast and radiation-hard electronics and detector elements with a high granularity to cope with the high particle flux.
- High detector hermeticity, i.e. an almost full coverage in both the η and ϕ coordinate range.
- Good momentum resolution, reconstruction efficiency, and the ability to reconstruct secondary vertices for b-jet, c-jet and τ-lepton tagging.
- EM calorimetry with a high energy resolution for the measurement and identification of EM objects. Almost hermetic (hadronic) calorimetry is required for jet energy measurements and precise measurements of $E_{\mathrm{T}}^{\mathrm{miss}}$.
- Good identification of muons and their charge up to high-p_{T} and a high momentum resolution over a large range of momenta.
- Maintain acceptable trigger rates while efficiently triggering low-p_{T} objects and achieving a sufficiently large background rejection.

2.2.3 Tracking

The Inner Detector (ID) is the sub-detector closest to the interaction point and is used for tracking, momentum measurements and reconstruction of primary and secondary vertices. It consists of three sub-components, as illustrated in Figure 2.2, each with a fine granularity: a high-resolution Pixel Detector closest to the beam pipe; surrounded by silicon microstrip detector layers forming the Semiconductor Tracker (SCT); and completed by the gas-filled straw-tubes of the Transition Radiation Tracker (TRT). The ID is immersed in a 2 T solenoidal field to allow charge-to-momentum ratio measurements.

The Pixel Detector consists of four barrel layers and three end-cap wheels on each side. These include a new inner barrel layer of pixels, the Insertable B-Layer (IBL) [126], which was

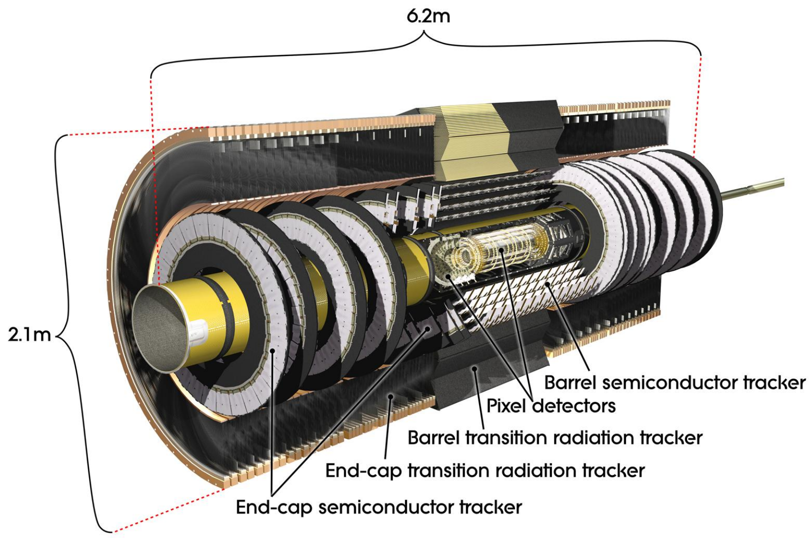

Figure 2.2: Cut-away view of the Inner Detector (ID) with labelled sub-components.

installed between Run 1 and Run 2 within the previously inner-most barrel layer of pixels, by mounting it on a new beam pipe with a smaller diameter. The pixel size is $50 \times 400\ \mu m^2$ in $\rho\phi \times z$ ($\rho\phi \times \rho$) for the barrel (end-cap) configuration, and the intrinsic accuracy in the barrel is $10 \times 115\ \mu m^2$. The IBL has a reduced pixel size of $50 \times 250\ \mu m^2$ in $\rho\phi \times z$. This, and its closer proximity to the interaction point improves tracking, vertexing, and the identification of b-jets, c-jets and τ-leptons which is necessary to maintain the Run 1 performance at the higher instantaneous luminosities of Run 2 and to mitigate the deteriorating effects of irreversible radiation damage to the existing pixel layers. The Pixel Detector with the IBL amount to approximately 86.42 million readout channels.

The SCT comprises silicon microstrip detectors, with a mean pitch of 80 μm, in four concentric barrel layers and nine end-cap wheels on each side. The strip sensors are mounted in pairs at a stereo angle of 40 mrad to measure both coordinates. The intrinsic accuracy is $17 \times 580\ \mu m^2$ in $\rho\phi \times z$ ($\rho\phi \times \rho$) in the barrel (end-caps). The SCT amounts to approximately 6.3 million read-out channels.

The TRT consists of 298,304 gas-filled straw tubes arranged in 73 straw planes in barrel configuration and 160 straw planes in end-cap configuration, amounting to 350,848 readout channels, and generating a large number of charged-particle hits at larger radii. The straws are drift tubes with a diameter of 4 mm acting as a proportional counters. They provide only $\rho\phi$ (z) coordinate information in the barrel (end-caps) with an intrinsic accuracy of 120 μm per straw. The volume between the straws is filled with polymer fibres or foils providing contrasting dielectric media that induces transition radiation directly proportional to the Lorentz factor when a relativistic charged particle traverses the material boundary. The transition radiation photons are absorbed by the gas mixture in the tubes enhancing the readout signal and thereby providing particle-identification that is used primarily to distinguish between electrons and pions.

The ID has a coverage of $|\eta| < 2.5$ and is designed to attain a momentum resolution of $\sigma_{p_T}/p_T = 0.05\% \cdot p_T \oplus 1\%$ in units of GeV. During a data-taking run, the IBL and Pixel Detector undergo significant displacements due to changing power and cooling requirements as the instantaneous luminosity changes. Track-based alignment algorithms for Run 2 apply fully

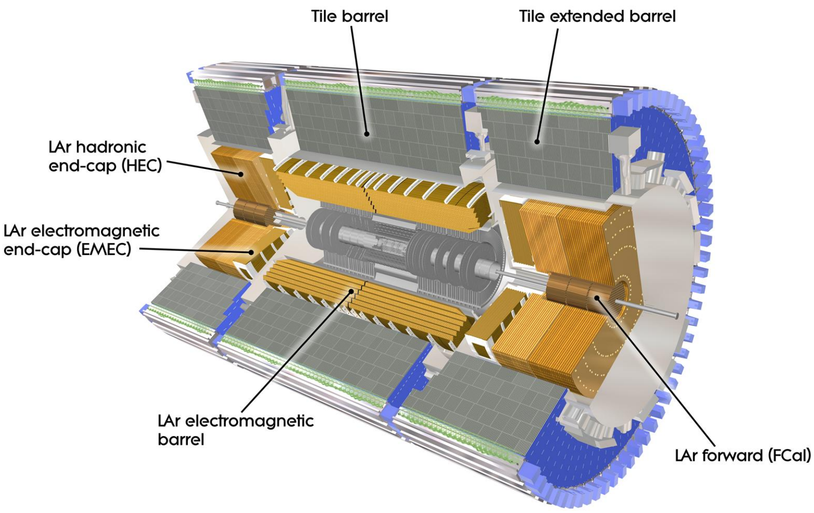

Figure 2.3: Cut-away view of the calorimeter system with labelled sub-components. The brown-coloured calorimeters are based on the liquid-argon (LAr) technology. The scintillator-tile calorimeters are shown in grey.

automated corrections for these effects at regular time intervals during a run [127]. The data from the ID are not used in the initial Level-1 trigger system (L1).

2.2.4 Calorimetry

The calorimeters are centred around the central solenoid surrounding the ID. EM calorimetry in the range $|\eta| < 3.2$ is provided by high granularity sampling calorimeters with a high energy and position resolution using liquid argon (LAr) as the active material and lead as the absorber material. The EM calorimeters are surrounded by the scintillator-tile sampling calorimeters in barrel configuration, using plastic scintillator tiles for the active layers and steel for absorption, and providing hadronic calorimetry over the range $|\eta| < 1.7$. The range of the hadronic calorimeter is extended to match that of the EM LAr calorimeter by the Hadronic End-cap Calorimeter (HEC) which uses LAr and copper plates for hadronic calorimetry. Forward LAr calorimeters (FCals) provide additional EM and hadronic calorimetry up to $|\eta| = 4.9$ using copper and tungsten as absorber material. Figure 2.3 shows the layout of the different calorimeters.

Each region of the detector has at least three calorimeter read-out layers to sample showers longitudinally. The layers of the EM calorimeter have granularities in $\Delta\eta \times \Delta\phi$ varying between 0.0031×0.1 in the central barrel region of the first layer and up to 0.1×0.1 in the second and third layer of the end-caps. The hadronic calorimeters have granularities varying between 0.1×0.1 in the first two layers of the scintillator-tile barrel and up to 0.2×0.2 in the HEC.

The EM calorimeter has a thickness between 22 and 33 radiation lengths (X_0) in the barrel and between 24 and 38 X_0 in the end-caps. The EM and hadronic calorimeters together amount to 9.7 interaction lengths (λ) in the barrel and 10 λ in the end-caps and forward regions.

The LAr EM calorimeters are designed to attain an energy resolution of $\sigma_E/E = 10\%/\sqrt{E} \oplus 0.7\%$. The design resolution for the hadronic calorimeters is $\sigma_E/E = 50\%/\sqrt{E} \oplus 3\%$, and for

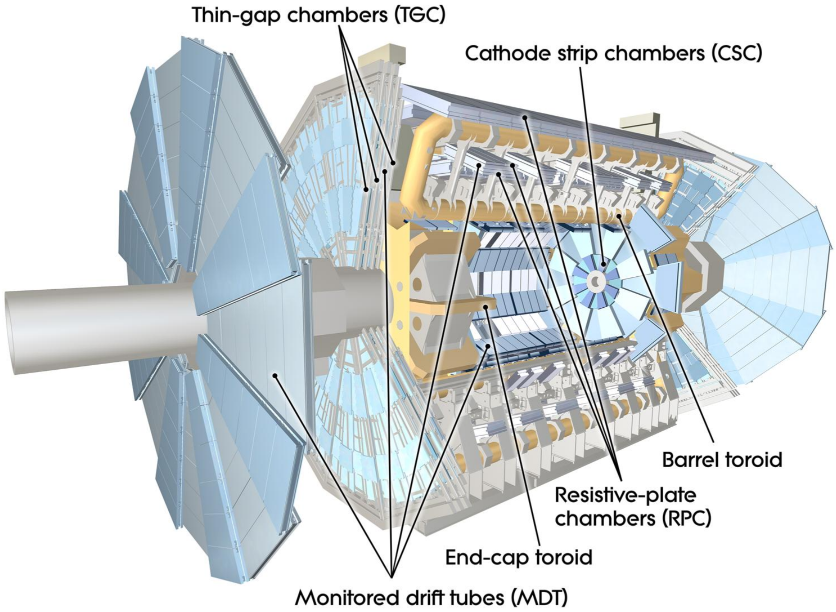

Figure 2.4: Cut-away view of the ATLAS Muon Spectrometer (MS) with labelled sub-components. The MS defines the overall size of the ATLAS detector. The toroidal air-core magnet system is shown in yellow.

the forward calorimeters $\sigma_E/E = 100\%/\sqrt{E} \oplus 10\%$ in units of GeV. The $1.37 < |\eta| < 1.52$ region contains a transition between the barrel and end-cap cryostats which causes significant energy resolution degradation and is therefore not used for photon identification or precision measurements with electrons. The EM calorimeter provides trigger data for (isolated) EM objects in the region $|\eta| < 2.5$, and the calorimeters combined provide trigger data for triggers such as for jets, $E_{\mathrm{T}}^{\mathrm{miss}}$ and scalar sum of transverse energy ($\sum E_T$) over the entire calorimeter acceptance.

2.2.5 Muon system

The outer part of the detector comprises the Muon Spectrometer (MS). A strong toroidal magnetic field, generated by a long superconducting air-core barrel magnet and two inserted air-core end-cap toroids, provides strong bending power in a large volume of air. The open structure reduces multiple scattering to a minimum. Three high-precision tracking layers provide excellent momentum resolution.

Figure 2.4 shows the layout of the MS. In the barrel region ($|\eta| < 1.05$) the precision tracking is performed by three concentric layers of chambers consisting of Monitored Drift Tubes (MDTs), while Resistive-Plate Chambers (RPCs) provide muon triggers as well as a measurement of the second coordinate. In the end-cap, three layers of MDT chambers provide the precision tracking for the region $1.05 < |\eta| < 2.0$ completed by two outer layers of MDT chambers and an inner layer of Cathode Strip Chambers (CSCs) for the region $2.0 < |\eta| < 2.7$. Thin-Gap Chambers (TGCs) provide muon triggers and second coordinate measurements in the end-cap regions.

MDT chambers consist of three to eight layers of drift tubes with a position resolution of 35 µm per chamber in the bending plane (ρ–z). CSCs consist of four layers of multiwire proportional chambers, each with one cathode plate segmented into strips orthogonal to the radially-oriented anode wires and the other anode plate segmented parallel to the anode wires to measure both coordinates. This results in a position resolution of 40 µm per chamber in the bending plane and 5 mm in the non-bending plane. The RPC stations each consist of two independent detection layers using resistive parallel plates with a small (2 mm) gap and a large electric field to induce a fast signal through a Townsend discharge upon the passage of a charged particle. A position resolution of $z \times \rho\phi = 10\,\text{mm} \times 10\,\text{mm}$ is obtained. Seven layers of TGCs complement the middle layer of MDTs in the end-cap, and two layers of TGCs complement the innermost end-cap layer. They are multiwire proportional chambers with a small (1.4 mm) gap between the wires and the cathode plates to achieve the required time resolution for triggering. The position resolution varies between 2 to 6 mm for the ρ coordinate and 3 to 7 mm for $\rho\phi$. The use of different technologies in the barrel and end-cap regions is the result of optimising for rate capabilities, radiation hardness, and granularity for the different regions.

To obtain the required momentum resolution, the relative positions of the chambers and their deformations are continuously monitored by approximately 12,000 alignment sensors and reconstructed with a precision of at least 30 µm. Approximately 1,800 Hall sensors measure the magnetic field to determine the bending power along a muon trajectory and to reconstruct the position of the toroid coils based on magnetic-field simulations.

The MS covers the range $|\eta| < 2.7$ and has a relative momentum resolution better than 3% over a wide p_{T}-range, going up to $\sigma_{p_T}/p_T = 10\%$ at $p_T = 1$ TeV. The trigger chambers provide p_{T}-based muon triggers in the range $|\eta| < 2.4$ with a low latency of 1.5 to 4 ns, which allows bunch-crossing identification.

2.2.6 Trigger and data acquisition

The Trigger and Data Acquisition system (TDAQ) [128] in Run 2 reduces the event rate from 40 MHz, at which the events are produced in *pp* runs, to about 1 kHz, at which the data of the events can be stored, in about 200 ms. The initial decision layer is the hardware-based Level-1 trigger system (L1), followed by the software-based High Level Trigger (HLT).

L1 uses custom LHC-clock-driven hardware to reduce the acceptance rate to at most 100 kHz with a latency of 2.5 µs by performing an initial selection on events using coarse-grained calorimeter signals identified by the Level-1 Calorimeter trigger (L1Calo) and muon trigger chamber hits identified by the Level-1 Muon trigger (L1Muon). The results from L1Calo and L1Muon are processed by the Central Trigger Processor (CTP) and a *L1 Accept* is generated if one or more L1 trigger objects pass a (combination of) trigger selection(s) listed in a *trigger menu*. Trigger menu items can be *pre-scaled* such that only one out of X events is accepted in order to optimise bandwidth usage by limiting or maintaining the rate as luminosity or background conditions change.

In case of a *L1 Accept*, the Region-of-Interest (RoI), i.e. the η and ϕ region containing the signal, serves as input to the HLT where more sophisticated selection algorithms and analyses of the detector data in full granularity provide the final trigger decision. RoIs are defined for (isolated) electron, photon, hadronically decaying τ-lepton and jet candidates exceeding a given E_{T} threshold, for large $E_{\mathrm{T}}^{\mathrm{miss}}$ or large $\sum E_T$ candidate events, and for muon candidates exceeding a given p_{T} threshold.

Events accepted by the HLT are transferred to local storage at the experimental site and exported to the Tier-0 facility at the CERN computing centre for offline reconstruction.

For Run 2 several upgrades have been deployed to the trigger system:

- L1Calo has an updated pre-processor applying auto-correlation filters and per-bunch dynamical pedestal correction mitigating the increasing $E_{\mathrm{T}}^{\mathrm{miss}}$ trigger rates as a function of the instantaneous luminosity.
- Fake-muon[1] trigger rates in the end-cap regions have been reduced with minimal efficiency loss by introducing new trigger logic at L1Muon requiring additional TGC coincidences.
- The muon trigger coverage has been expanded by the addition of trigger chambers in the structural feet and elevator shafts of the detector.
- A major upgrade of L1 is the Level-1 Topological trigger (L1Topo) allowing more sophisticated topological and kinematic trigger selections based on multiple L1 trigger objects, thereby achieving far greater background suppression than simple threshold selections.
- The Fast Track Trigger (FTK) commissioning is ongoing in Run 2 and will in future provide reconstructed tracks from the full Pixel and SCT detectors to the HLT algorithms for each *L1 Accept*. The HLT tracking and flavour tagging algorithms have been adapted to include the IBL and to use the tracks from the FTK when commissioned.
- The HLT is the result of merging the Run 1 *Level-2 trigger system* and *Event Filter*, and optimising the trigger algorithms, resource usage and output rate.

2.2.7 Detector simulation

ATLAS uses a simulation framework [129], integrated into the ATLAS software framework Athena [130], to transform the particle-level output (in HepMC format [131]) of MC event generators to a digitised detector output format which is identical to the output format of the real TDAQ. The propagation of particles through the detector and their interactions with detector material are modelled using GEANT4 [132] after which energy deposits in active detector regions (hits) are catalogued and stored. The detector geometry and conditions data including misalignments, distortions and temperatures, are stored in databases and contain all the information needed to emulate a single data-taking run of the real detector. The digitisation step overlays simulated hits from the hard scattering event with hits from minimum bias[2], beam and cavern background events (pile-up) before the detector signals are generated and digitised. The hardware-based L1 trigger hypotheses are also evaluated at this stage and the result is stored. The output format of the digitisation step is identical to the detector output format, allowing the HLT trigger and reconstruction algorithms to run on both.

An important feature of simulated events is the stored *truth* information which includes: the history of particle interactions between incoming and outgoing particles in the event generation process; the truth tracks and decays in the detector volume such as photon conversions;

[1] Fake objects, such as tracks, muons, electrons, $E_{\mathrm{T}}^{\mathrm{miss}}$ etc. are detector signals or noise mimicking the signal of a particular object and are reconstructed as such, but do not originate from a corresponding real object. The absence of a real (or truth) object can only be determined in simulations.

[2] Minimun-bias simulations model the total inelastic pp scattering cross section including diffractive and soft nondiffractive interactions. Dedicated Minimum Bias Trigger Scintillators [133] are used to trigger and record such events at the ATLAS detector.

information on the origin of a particle e.g. whether it originates from the hard scattering vertex or from a pile-up event.

The detailed simulation of particle interactions in the complex detector geometry performed in GEANT4 is computationally expensive. Several fast simulation tools have been developed to speed up the simulation process and to achieve the high-statistics simulated samples required for many analysis at the expense of extremely accurate modelling of detector response. Tactics to speed up the simulation include: replacing low energy particles with pre-simulated calorimeter showers stored in libraries; parametrizing the longitudinal and lateral energy profiles of calorimeter showers; simplifying the ID and MS geometries; smearing of truth objects to approximate the detector simulation plus reconstruction steps and obtain four-momenta of objects as output.

3 Event and object reconstruction

Event reconstruction is the algorithmic process of combining the relevant raw detector read-outs into abstract objects such as particle tracks, showers, and decays in order to *reconstruct* and describe the hard scattering event by identifying the interaction vertex and final state particles or their subsequent decays. The algorithms for event and objects reconstruction are implemented in the ATLAS software framework Athena [130] which is based on the GAUDI framework [134].

3.1 Tracks and vertices

3.1.1 Track reconstruction

Charged-particle trajectories, or tracks, are reconstructed from hits in the ID covering $|\eta| < 2.5$. The reconstructed tracks are important inputs for further particle identification and object reconstruction. The standard track reconstruction reconstructs tracks of charged particles with a $p_{\mathrm{T}} > 400$ MeV and uses an *inside-out* and consecutive *outside-in* track finding strategy which can be summarised in several steps [135]:

- Reconstruction starts in the Pixel (including the IBL) and SCT detectors by defining three-dimensional *space points* from *clusters*[1], representing the point where a charged particle traversed the active detector material, while *drift circles* are created from timing information of the TRT drift tubes.
- Track-finding requires three space points in unique layers of the Pixel and/or SCT detector comprising a track seed. Track seeds passing initial p_{T} and impact parameter requirements and which are compatible with a fourth space point are extended into a track candidate by incorporating space points in the remaining layers using a combinatorial Kalman filtering technique [136].
- Track candidates failing basic quality cuts are rejected and remaining tracks are scored penalising holes (i.e. the absence of clusters along a track) and the sharing of a given cluster by multiple track candidates. Special care is taken not to penalise shared clusters that are compatible with originating from multiple particles, which can happen in dense environments such as collimated high-p_{T} jets and τ-lepton decays, by using a neural network for the pixel layers [137–139]. Higher-scoring tracks are favoured in resolving ambiguities.
- The remaining track candidates are extended into the TRT and associated to the drift circles and a final refit is performed using the full ID information. Tracks that cannot be

[1] Clusters are adjacent channels in a sensor yielding a charge-over-threshold. In the SCT a single space point can be defined from the intersection point of two cluster-containing strips in the stereo-angle-mounted sensor pairs. Clusters are identified as either *single-particle*, compatible with originating from a single charged particle, or *merged*, compatible with a cluster created by multiple charged particles.

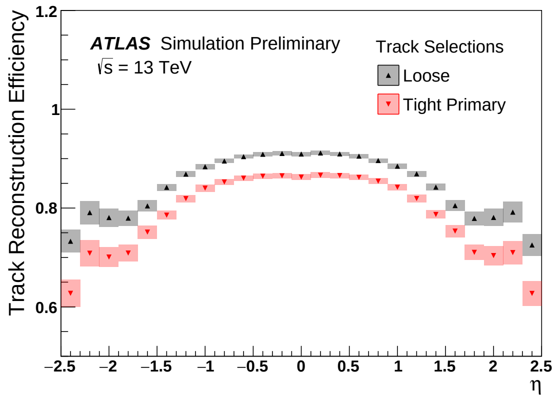

(a)

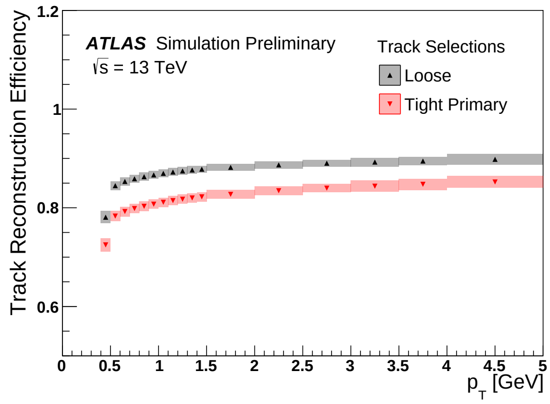

(b)

Figure 3.1: Track reconstruction efficiency, evaluated using minimum-bias simulated events, as a function of truth η (a) and p_T (b) for the *Loose* and *Tight Primary* track collections. The bands indicate the total systematic uncertainty [141].

extended (e.g. at large $|\eta|$) are kept and marked as *extension failed*. TRT-extended tracks whose score is reduced compared to the non-extended track are marked as *rejected* but retained in the final track collection.

- A second *outside-in* pass is performed using track segments in regions of the TRT seeded by the EM calorimeter that are not associated to any track candidates and are extended into to the SCT and Pixel layers. Segments that cannot be extended are kept for the reconstruction of converted photons.

A third *large-radius-tracking* pass [140] works in a similar way as the inside-out tracking using leftover space points but with much looser requirements on: the impact parameters, η-range and number of shared clusters per track. This allows tracks with large impact parameters to be reconstructed, which are missed by the standard track reconstruction as it requires track seeds to be compatible with small impact parameters. It improves track-finding efficiencies for tracks from decaying long-lived (BSM) particles at the cost of a high rate of poor quality and fake tracks. Large radius tracking is computationally expensive and therefore only performed on a subset of pre-selected events. The analysis presented in this thesis does not make use of this track collection.

The standard track reconstruction has two *working-points* [141]: *Loose* and *Tight Primary*, providing two track collections that follow a different set of quality criteria. *Loose* requires minimal cuts on p_T, η and the number of hits, holes and shared clusters in each of the subdetector components, and is optimised for track reconstruction efficiency. *Tight Primary* imposes a tighter requirement on the number of hits and holes and is optimised to reject fake tracks. Figure 3.1 shows the track reconstruction efficiency for these working-points as a function of η and p_T using a MC simulated minimum-bias sample and evaluating the ratio of truth-matched reconstructed tracks to the total number of generated tracks. The *Tight Primary* track reconstruction efficiency is overall lower due to the tighter requirements. The efficiency reduction with increasing $|\eta|$ is caused by the increasing amount of material traversed, while the small increase at $|\eta| > 2$ is due to more active layers being traversed. For tracks with $p_T > 5$ GeV the efficiency plateaus at approximately 90% and 85% for the two working points.

3.1.2 Vertex reconstruction

After the track-finding stage, the reconstructed tracks are used for identifying and reconstructing primary vertices in order to compute the kinematic properties of the hard-scattering interaction and to distinguish it from pile-up interactions.

A vertex candidate requires at least two *Tight Primary* tracks [142]. The vertex position is determined using an annealing fitting procedure that iteratively down-weights less compatibles tracks and recomputes the vertex position starting from an initial position determined by the beam spot in the transverse plane and by the tracks along the z-axis. Tracks that are incompatible by more than seven standard deviations are dissociated from the reconstructed vertex and are used in the next primary vertex finding iteration which is repeated until all tracks are associated to a vertex or no additional vertices can be found. For each event, the vertex with the highest $\sum p_{\mathrm{T}}^2$ of all associated tracks is considered the hard-scattering vertex.

Primary vertex reconstruction efficiency exceeds 99% in simulated minimum-bias interactions producing at least two charged particles. The efficiency of reconstructing and identifying the hard-scattering vertex correctly, depends on the number of inelastic pp collisions per bunch crossing (μ) and the final state of the hard scatter. Physics processes producing only a few or no charged particles, such as $h \to \gamma\gamma$ or $Z \to \mu\mu$, have a lower reconstruction plus selection efficiency, but nevertheless is still 98% for $Z \to \mu\mu$ at $\mu = 40$ within the ID acceptance. For e.g. $h \to \gamma\gamma$, alternatives for determining the hard-scattering interaction, tailored to the final state, perform better.

The primary vertex resolution in the transverse plane is between 20 to 155 µm depending on the number of tracks, and between 40 to 330 µm along the z-axis [143].

3.2 Electrons

3.2.1 Electron reconstruction

Electron[2] candidates are reconstructed in the region $|\eta| < 2.47$ from isolated energy deposits in the EM calorimeter that can be matched to a track in the ID [144].

In this region, covered by the barrel and the end-cap sections, the middle layer of the EM calorimeter contains most of the energy of EM showers and has a fine segmentation of $\Delta\eta \times \Delta\phi = 0.025 \times 0.025$. The longitudinal extension of one such segment including all layers of the EM calorimeter is called a *tower*. A sliding window of 3×5 towers in $\eta \times \phi$ is used to search for cluster seeds with $E_{\mathrm{T}} > 2.5$ GeV after which a clustering algorithm is used around the seed.

Tracks are loosely matched to EM clusters and, if the track quality is sufficient, a refit is performed taking bremsstrahlung effects into account. If multiple tracks can be matched, a dedicated algorithm chooses a primary track based on track quality and compatibility with different momenta hypotheses. If no tracks can be matched to the EM cluster the electron candidate is discarded and considered as photon candidate. In Run 2, the track matched to the electron candidate is additionally required to be compatible with the hard-scattering primary vertex of the event.

[2] Unless stated otherwise, references to specific particles implicitly include anti-particles.

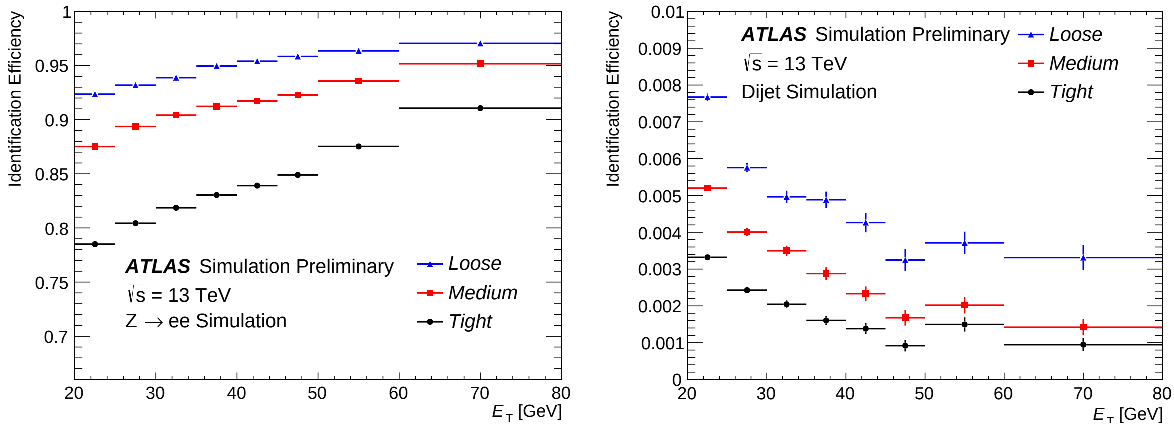

(a) (b)

Figure 3.2: Electron identification efficiency in a sample of simulated $Z \to ee$ decays (a) and the efficiency to identify hadrons as electrons (b) in a simulated dijet sample. The efficiencies are measured with respect to reconstructed electrons. The candidates are matched to true electron candidates for $Z \to ee$ events. For the dijet events, the electrons matched to true electron candidates are not included in the analysis. Note that the last bin used for the optimisation of the identification algorithms is 45-50 GeV, which is why the efficiency increases slightly more in the 50 GeV bins of both (a) and (b) than in other bins [144].

Finally, the electron cluster is re-clustered using 3×7 (5×5) towers in the barrel (end-caps) and the energy of the cluster is calibrated. The energy of the reconstructed electron is computed using the calibrated cluster energy, while the direction with respect to the z-axis is determined from the best-matching track.

3.2.2 Electron identification

To distinguish reconstructed electron candidates from e.g. jets or converted photons that can leave similar calorimeter and track signatures, an electron identification algorithm is applied exploiting information from the calorimeter shower, transition radiation in the TRT, quality of the track-cluster match, track properties, and bremsstrahlung effects.

In contrast to Run 1, when a sequential cut-based algorithm was used, a likelihood-based method is employed in Run 2 evaluating most of the input variables simultaneously in a multivariate analysis. Three identification working points are provided with an increasing fake-electron rejection: *Loose*, *Medium* and *Tight*. Figure 3.2 shows the identification efficiency of the three working points for both real electrons in a MC simulated sample of $Z \to ee$ events, and for fake-electrons (hadrons) in a MC sample of dijet events. The efficiency at $E_T = 25$ GeV ranges between 78% to 90% for candidates from real electrons, and between 0.3% to 0.8% for electron candidates originating from hadrons, depending on the working point used. Cuts on the likelihood-based discriminant corresponding to these working points are loosened as pile-up increases to maintain the efficiencies.

3.2.3 Electron isolation

Further discrimination between prompt electrons and non-prompt electrons originating from e.g. converted photons produced in hadronic decays, heavy flavour hadron decays and misidentified hadron jets, can be obtained by requiring the electron candidate to be isolated in the calorimeter and tracker.

Calorimetric-isolation working points use $E_{\mathrm{T}}^{\mathrm{cone0.2}}$ as a discriminating variable: the EM-calibrated transverse energy deposit in a cone of $\Delta R \leq 0.2$ around the electron candidate, after subtracting the energy of the electron cluster and the leakage outside the cluster.

Track-isolation working points use the variable $p_{\mathrm{T}}^{\mathrm{varcone0.2}}$: the $\sum p_{\mathrm{T}}$ of all tracks with $p_{\mathrm{T}} > 1$ GeV within $\Delta R \leq \min(0.2,\ 10\,\mathrm{GeV}/E_{\mathrm{T}})$ of the electron candidate's matched track, while additionally originating from the hard-scattering vertex and satisfying track quality criteria. The matched track and identified bremsstrahlung tracks are not included.

Two types of isolation working points are provided: either based on fixed cuts on $p_{\mathrm{T}}^{\mathrm{varcone0.2}}/E_{\mathrm{T}}$ and $E_{\mathrm{T}}^{\mathrm{cone0.2}}/E_{\mathrm{T}}$, or E_{T}-dependent cuts targeting E_{T}-dependent isolation efficiencies.

3.2.4 Electron trigger

Electron candidates are identified at L1 using a sliding window of 4×4 *trigger towers* corresponding to $\Delta\eta \times \Delta\phi = 0.4 \times 0.4$. The inner trigger towers are used to measure the energy of the electron candidate, while the surrounding trigger towers are used for isolation measurements. The trigger decision is based on E_{T} thresholds and can be refined by applying vetoes based on isolation and energy deposits in the hadronic calorimeter behind the EM cluster.

Initial fast clustering and tracking algorithms applied to the RoI at the HLT provide additional background rejection before making a final trigger decision by employing precise reconstruction algorithms similar to the offline electron reconstruction.

The lowest-threshold unprescaled single-electron trigger for the 2015 data-taking (`e24_lhmedium_L1EM20VH`) requires the electron candidate to have $E_{\mathrm{T}} > 24$ GeV and pass the *Medium* likelihood-based identification requirements. It is seeded by the `L1_EM20VH` L1 trigger which requires an EM cluster with $E_{\mathrm{T}} > 20$ GeV after η-dependent corrections for the amount of passive material in front of the calorimeter (`V`), and applying a veto on energy deposits in the hadronic calorimeter if $E_{\mathrm{T}} < 50$ GeV (`H`) . To recover efficiency at high E_{T}, a logical 'or' is taken with `e120_lhloose` and `e60_lhmedium`. The lowest-threshold unprescaled dielectron trigger is `2e12_lhloose_L12EM10VH`, using the same naming logic but requiring (at least) two electrons to pass the respective requirements at the L1 and HLT.

3.2.5 Efficiency

The total efficiency ($\epsilon_{\mathrm{total}}$) to find and select an electron with the ATLAS detector is the product of the efficiencies of the different components:

$$\epsilon_{\mathrm{total}} = \epsilon_{\mathrm{trigger}} \times \epsilon_{\mathrm{reconstruction}} \times \epsilon_{\mathrm{identification}} \times \epsilon_{\mathrm{isolation}} \tag{3.1}$$

Each of the different components is measured in both data and MC simulation using a tag-and-probe method in which $Z \to ee$ and $J/\psi \to ee$ events are selected by the dielectron mass of an electron candidate passing strict selection criteria (the 'tag') and a loosely identified electron candidate that is used to measure the efficiency (the 'probe'). The ratio between data and MC efficiencies is used as a correction factor for MC simulations. Data-to-MC correction factors are derived as a function of E_{T} and η. Figure 3.3 shows the reconstruction times identification

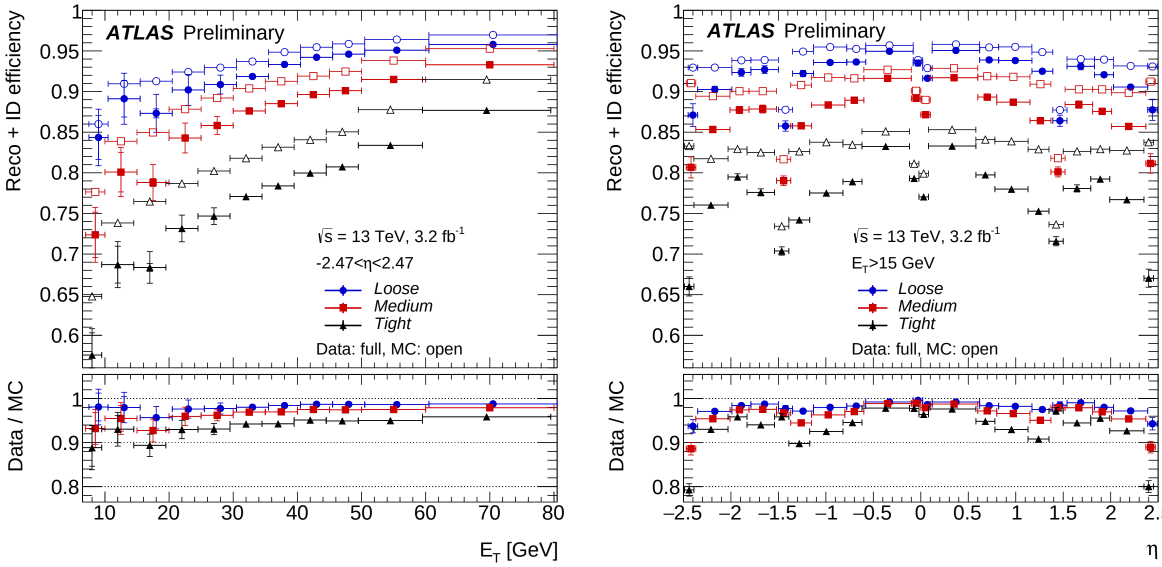

(a) (b)

Figure 3.3: Combined electron reconstruction and identification efficiencies in $Z \to ee$ events as a function of E_{T}, integrated over the full η range (a), and as a function of η, integrated over the full E_{T} range (b). The data efficiencies are obtained from the data-to-MC efficiency ratios measured using J/ψ and Z tag-and-probe, multiplied by the MC prediction for electrons from $Z \to ee$ decays. Two sets of uncertainties are shown: the inner error bars show the statistical uncertainty, the outer error bars show the combined statistical and systematic uncertainty [144].

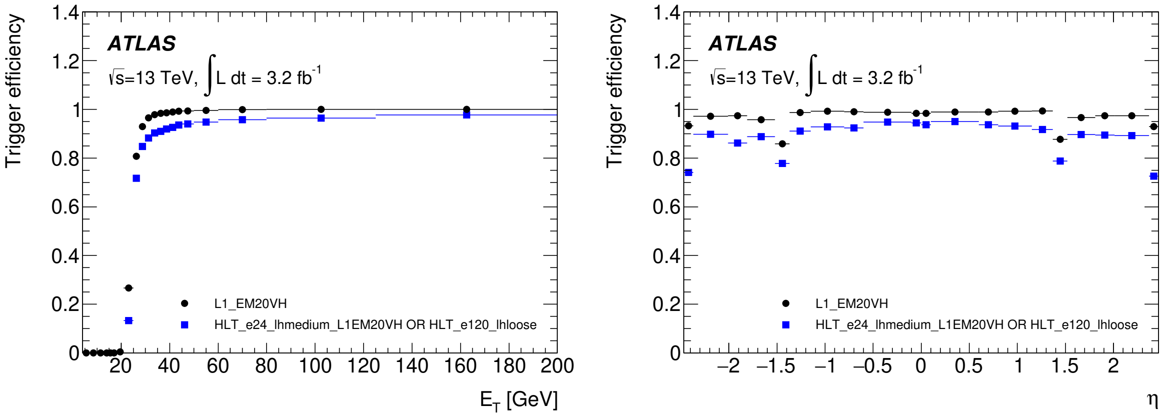

(a) (b)

Figure 3.4: Efficiency of the unprescaled L1 and HLT single-electron trigger with the lowest E_{T}-threshold as a function of E_{T} (a) and η (b) of the probe electron [128].

efficiency for the three working points and Figure 3.4 shows the trigger efficiency for the nominal single-electron trigger.

3.3 Muons

3.3.1 Muon reconstruction

Muon reconstruction in the MS starts with the generation of track segments from hit patterns in each of the muon chambers [145]. Tracks are then reconstructed with an algorithm that is seeded from segments in the middle layer and fits to hits from segments in different layers, followed by iterations using segments in the inner and outer layer as seeds. Track segments are selected based on the number of hits and fit quality and are matched using their relative position and angles. Two matching segments are required in order to form a muon-track candidate, with the exception of tracks in the transition region between barrel and end-cap where a single high-quality segment can be used.

An overlap removal algorithm is applied to assign segments that are shared between multiple track candidates to a single track. Two track candidates, each having segments in all three layers but sharing the segments in the inner two layers, are both kept to maintain a high efficiency for close-by muons as long as the track candidates have no shared hits in the outer layer.

The individual hits associated with the segments of a track candidate are fitted using a global-χ^2 fit and the track candidate is selected based on fit quality criteria. Hits giving large contributions to the χ^2 are removed while additional hits compatible with the track are recovered and added to the fit.

Information from the ID and calorimeter is also used in the reconstruction, leading to four types of reconstructed muons:

Combined muons: the MS track can be matched to an ID track using an outside-in, or complementary inside-out pattern recognition, after which a global refit is performed using the individual hits. MS hits can be added or removed to improve the fit quality.

Segment-tagged muons: an extrapolated ID track matches at least one segment in the MS. These are used to reconstruct low-p_T muons or muons in regions with limited MS acceptance.

Calorimeter-tagged muons: an ID track matches with an energy deposit in the calorimeter compatible with a minimum-ionising particle. This type is optimised for the region $|\eta| < 0.1$ where services for the calorimeters cause the MS acceptance to be low, and for the p_T range of 15 to 100 GeV. Among the different reconstructed muons types, this type has the lowest purity.

Extrapolated muons: the muon four-vector is determined from an extrapolated MS track that is loosely compatible with originating from the interaction point and corrects for the estimated energy loss in the calorimeters. A three-segment track is required in the forward region while a two-segment requirement applies elsewhere. This type is used for tracks outside the ID acceptance, i.e. $2.5 < |\eta| < 2.7$.

Overlaps between the different muon types are removed giving preference to *combined muons*, follow by *segment-tagged muons*, then *extrapolated muons*.

3.3.2 Muon identification

Prompt muons are differentiated from e.g. non-prompt muons from pion or kaon decays by imposing quality criteria on:

- the number of hits and holes in the ID and MS tracks;
- the q/p significance, which is the absolute value of the difference in charge to momentum ratio as measured by the ID versus the MS divided by the sum in quadrature of the corresponding uncertainties;
- the absolute value of the difference between the transverse momenta of a track as measured in the ID versus the MS divided by the transverse momentum of the combined track (ρ');
- and the normalised χ^2 of the combined track fit.

Four identification working points are provided: *Loose*, *Medium*, *Tight* and *High-p_T*. The former three are inclusive, meaning that the looser working points include at least all the muons from a tighter working point.

Medium is the default working point and minimises the systematic uncertainties associated with muon reconstruction and calibration. It uses *combined muons* complemented by *extrapolated muons* in the region outside the ID acceptance. The *Loose* working point maximises the reconstruction efficiency for good-quality muon tracks. *Combined* and *extrapolated muons* are used complemented by *segment-tagged* and *calorimeter-tagged muons* in the region $|\eta| < 0.1$. *Tight* muons offer maximum purity at the expense of some efficiency, and *High-p_T* muons are selected to maximise momentum resolution for tracks with $p_{\mathrm{T}} > 100$ GeV.

For the default *Medium* working point, the identification efficiency of prompt muons with $20 < p_{\mathrm{T}} < 100$ GeV is 96.1%, while for non-prompt muons, originating from in-flight decays of charged hadrons, the efficiency is 0.17% as determined in a MC simulated sample of $t\bar{t}$ events. Applying isolation criteria further reduces the misidentification rate by more than an order of magnitude.

3.3.3 Muon isolation

Similar to the electron isolation working points, muon isolation working points are based on calorimetric and track isolation with discriminating variables $E_{\mathrm{T}}^{\mathrm{cone0.2}}$ and $p_{\mathrm{T}}^{\mathrm{varcone0.3}}$ respectively. Isolation working points are either based on: fixed cuts on $p_{\mathrm{T}}^{\mathrm{varcone0.3}}/p_{\mathrm{T}}$ and $E_{\mathrm{T}}^{\mathrm{cone0.2}}/p_{\mathrm{T}}$; cuts targeting given p_{T}-dependent isolation efficiencies; or cuts targeting flat efficiencies in η and p_{T}.

3.3.4 Muon trigger

Muon candidates in the region $|\eta| < 2.4$ are identified and triggered at L1 using a minimal number of spatial and temporal coincident hits in the RPCs or TGCs, depending on the estimated p_{T} and η of the muon candidate [128]. The deviation of the hit pattern from a straight line is used to estimate the p_{T}.

At the HLT an initial fast reconstruction stage uses the trigger chambers and precision hits of the MDTs and CSCs in the RoIs to build tracks and assign a p_{T} via look-up tables. The tracks

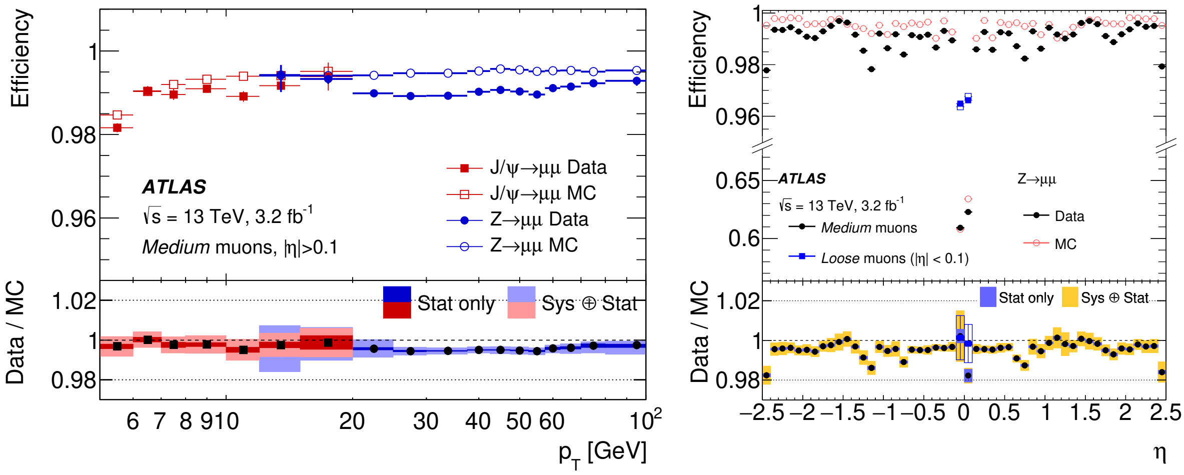

(a) (b)

Figure 3.5: Muon reconstruction efficiency as a function of p_{T} in the region $0.1 < |\eta| < 2.5$ measured in $Z \to \mu\mu$ and $J/\psi \to \mu\mu$ events (a), and as a function of η measured in $Z \to \mu\mu$ events for muons with $p_{\mathrm{T}} > 10$ GeV (b), both shown for the *Medium* muon selection. In addition, plot (b) also shows the efficiency of the *Loose* selection (squares) in the region $|\eta| < 0.1$ where the *Loose* and *Medium* selections differ significantly. The error bars on the efficiencies indicate the statistical uncertainty. Panels at the bottom show the ratio of the measured to predicted efficiencies, with statistical and systematic uncertainties [145].

are extrapolated and matched to ID tracks to form combined muon candidates. If candidates pass selection cuts to reduce fake muons, a precision stage follows, closely resembling the offline reconstruction using only the RoI. A full MS and ID scan is performed for multi-muon triggers when one muon candidate has been found recovering inefficiencies of the L1 trigger.

The lowest-threshold unprescaled single-muon trigger for the 2015 data-taking (`mu20_iloose_L1MU15`) requires the muon candidate to have $p_{\mathrm{T}} > 20$ GeV and a loose isolation, i.e. the $\sum p_{\mathrm{T}}$ of the tracks in a cone $\Delta R < 0.2$ around the muon candidate is less than 12% of the muon p_{T}. It is seeded by the `L1_MU15` L1 trigger. To recover efficiency at high-p_{T}, a logical 'or' is taken with `mu50`. The lowest-threshold unprescaled dimuon triggers are `2mu10` seeded by `L1_2MU10`, and `mu18_mu8noL1` seeded by `L1_MU15`, the latter requiring only one muon candidate at L1 to improve the efficiency.

3.3.5 Efficiency

The muon reconstruction, identification and isolation efficiency in the region $|\eta| < 2.5$ are measured using a tag-and-probe method in samples of $Z \to \mu\mu$ and $J/\psi \to \mu\mu$ events and the ratio between the measured efficiencies in data and MC simulations is used as a correction factor for MC simulations. In the region $2.5 < |\eta| < 2.7$, outside the ID acceptance, the correction factors for *Loose* and *Medium* muons are determined by taking the ratio of the observed number of muons to the observed number of muons in $2.2 < |\eta| < 2.5$ for both MC simulation and data. The ratio of the two ratios determines the correction factors. Figure 3.5 shows the reconstruction times identification efficiency for *Loose* and *Medium* muons measured in data and MC simulation as a function of η. Figure 3.6 shows the efficiency of the lowest-threshold unprescaled L1 and HLT single-muon trigger.

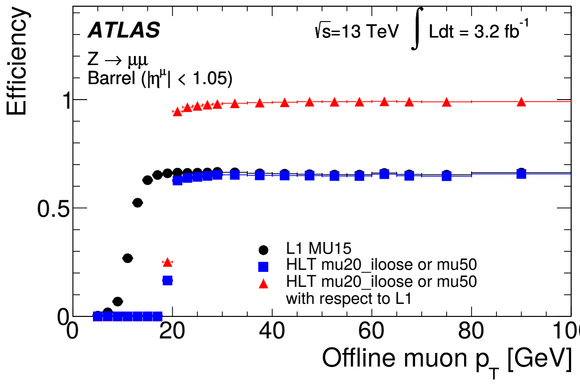

(a)

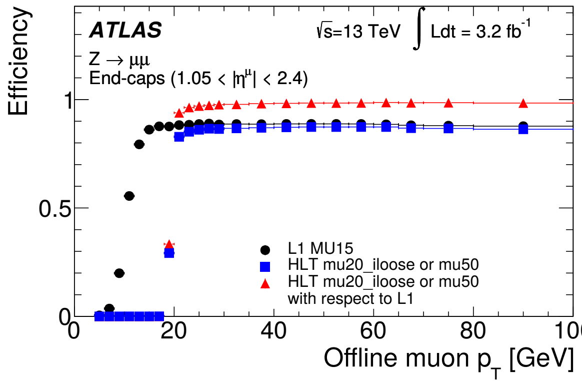

(b)

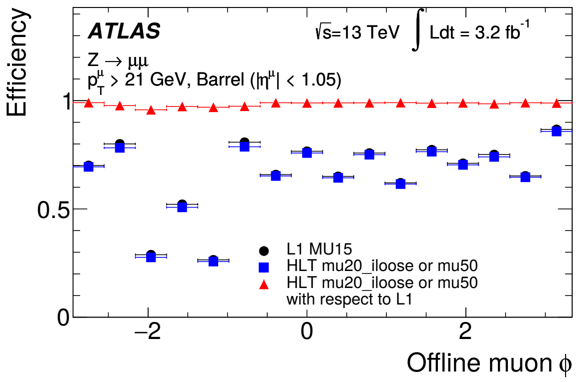

(c)

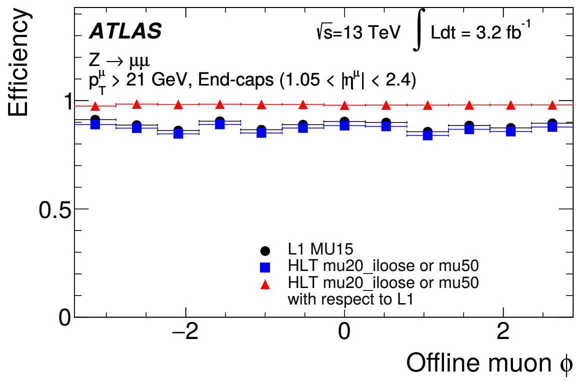

(d)

Figure 3.6: Efficiency of the unprescaled L1 and HLT single-muon trigger with the lowest p_T-threshold as a function of the probe muon's p_T, separately for the barrel (a) and the end-cap regions (b), and as a function of the probe muon's azimuthal angle ϕ in the barrel (c) and the end-cap regions (d). The bins with reduced barrel efficiencies correspond to the eight sectors containing toroid coils and the two structural feet [128].

3.4 Photons

3.4.1 Photon reconstruction

Photons are reconstructed following the same procedure as for electrons . When no ID track can be associated to a reconstructed EM cluster it is considered a prompt uncovered photon candidate [146]. If the clusters can be matched to two oppositely-charged tracks, producing transition radiation in the TRT compatible with electrons, and whose apex lies within the detector volume and points to the hard-scattering vertex, the signal is considered a converted photon candidate. As the latter procedure becomes inefficient for high-p_T converted photons, also clusters matched to a single track with no hits in the innermost pixel layer can be considered as converted photons.

3.4.2 Photon identification

Prompt photons are discriminated from background photons originating from hadron decays using quantities related to the shape and properties of the EM shower, and by requiring the cluster to be isolated. Photons can be identified in the region $|\eta| < 1.37$ and $1.52 < |\eta| < 2.37$.

Elsewhere, the EM calorimeter depth is insufficient or the segmentation too coarse to allow proper discrimination. Two identification working points are available: *Loose* and *Tight*. Both use a set of discriminating variables describing the fraction of energy deposited in the hadronic calorimeter and the shower shape in the EM calorimeter. The *Tight* working point applies tighter requirements on the discriminating variables and additionally uses discriminating variables for the shower shape based on the first sampling layer of the EM calorimeter which has a very fine segmentation in η ($\Delta\eta = 0.0031$).

The purity (i.e. fraction of prompt, real photons) of an inclusive photon sample collected with single-photon triggers and passing *Loose* identification requirements goes from 30% at $E_{\mathrm{T}} = 25$ GeV (55% at $E_{\mathrm{T}} = 50$ GeV) to 85% at high E_{T} for uncoverted photons [147]. After imposing the *Tight* criteria, the purity increases to 55% at $E_{\mathrm{T}} = 25$ GeV (75% at $E_{\mathrm{T}} = 50$ GeV) to 95% at high E_{T}. For converted photons the purity is lower and ranging between 20% to 60% before, and 40% to 80% after imposing *Tight* requirements. The average rates at which electrons are misreconstructed as photons (with $E_{\mathrm{T}} > 25$ GeV) are measured in data, using (misreconstructed) $Z \to ee$ candidate events, to be 1.5% and 3% for unconverted and converted photons respectively.

3.4.3 Photon isolation

Isolation requirements further help to distinguish between prompt photons and photons originating from hadron decays as the latter is usually surrounded with hadronic activity. Similar to the electron isolation working points, photon isolation working points are based on calorimetric and track isolation with discriminating variables $E_{\mathrm{T}}^{\mathrm{cone0.4}}$ and $p_{\mathrm{T}}^{\mathrm{cone0.2}}$ (a fixed-size cone of $\Delta R = 0.2$) respectively. Isolation working points are based on: a fixed cut on $p_{\mathrm{T}}^{\mathrm{cone0.2}}/p_{\mathrm{T}}$ and a p_{T}-dependent cut on $E_{\mathrm{T}}^{\mathrm{cone0.4}}$; or on a p_{T}-dependent cut on $E_{\mathrm{T}}^{\mathrm{cone0.4}}$ only.

3.4.4 Photon trigger

The online photon reconstruction and identification steps are identical to those of the electron trigger, with the exception of any track requirements, up to the HLT precision stage where the shower shape of the photon candidate is analysed in a similar way as in the offline photon reconstruction and identification algorithms [128].

The nominal single-photon trigger in 2015 was `g120_loose` requiring $E_{\mathrm{T}} > 120$ GeV and passing the *Loose* identification criteria. It is seeded by the L1 `L1_EM22VHI` trigger, similar to the `L1_EM20VH` trigger seeding the single-electron trigger, but additionally requiring the EM cluster to be isolated (`I`). The hadronic veto and isolation requirement are applied only for clusters with $E_{\mathrm{T}} < 50$ GeV. The main diphoton triggers were `g35_loose_g25_loose` and `2g20_tight`, the latter with *Tight* identification requirements. Both are seeded by the `L1_2EM15VH` trigger.

3.4.5 Efficiency

The identification efficiency is measured using three different data-driven methods covering complementary E_{T}-ranges. Radiative photons from a sample of $Z \to ll\gamma$ events cover the low-E_{T} range. Probe electrons obtained from a tag-and-probe method in a $Z \to ee$ sample cover EM

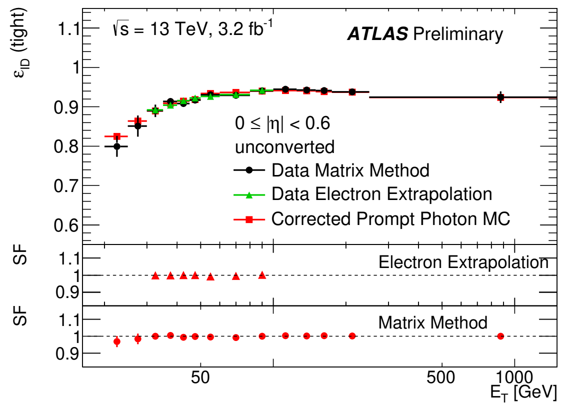

(a)

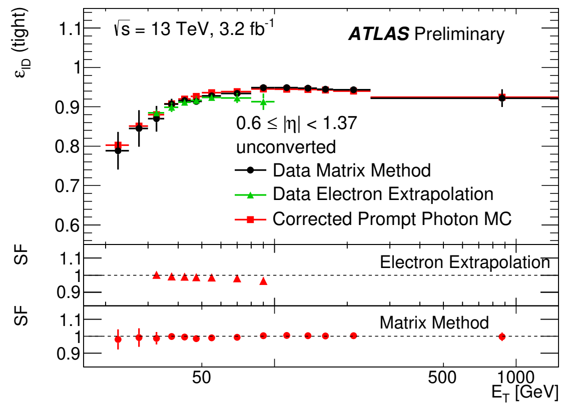

(b)

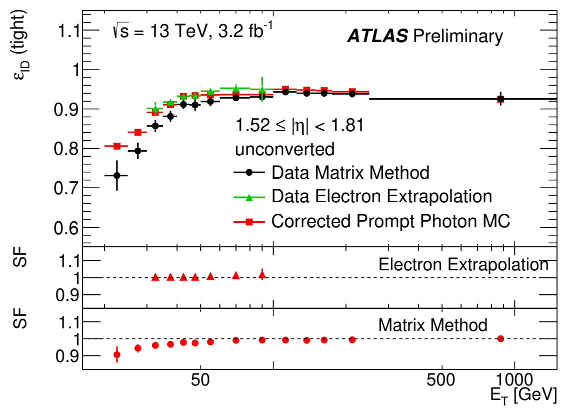

(c)

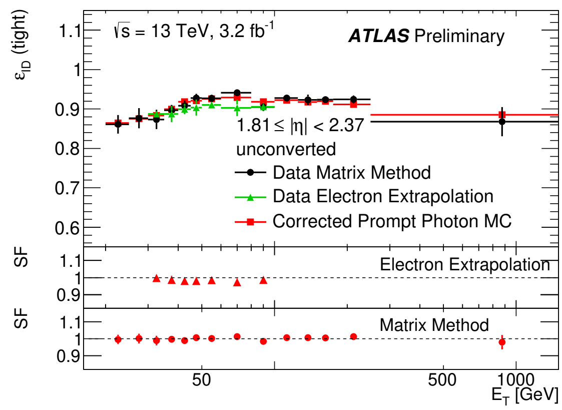

(d)

Figure 3.7: Comparison of the electron extrapolation and matrix method data-driven efficiency measurements of unconverted photons to the respectively prompt-photon MC predictions as function of E_T in the region $20 < E_T < 1500$ GeV, in the four η intervals. The bottom panels show the scale factors (SF) derived from the ratio of the efficiency between data-driven method and simulation. The uncertainty bars represent the sum in quadrature of the statistical and systematic uncertainties [146].

showers in the intermediate E_T-range. The differences in shower-shape between electrons and (un)converted photons are studied in simulations and corrected for. A matrix method using the isolation to determine the sample purity is used to measure the identification efficiency in the high E_T-range. The photon identification efficiency increases from approximately 50-60% for (un)converted photons at $E_T = 10$ GeV to 90% for unconverted and 97% for converted photons at $E_T = 100$ GeV. Differences in the efficiencies derived from data and simulation are used to derive scale factors to correct the MC simulations. Figures 3.7 and 3.8 show the *Tight* identification efficiency in the 2015 dataset, as a function of E_T, as measured by two of the three methods in different regions of η, for unconverted and converted photons respectively. The scale factors obtained using the three different methods are in agreement and combined into a single scale factor for each η-region and E_T-bin.

The photon trigger efficiency is computed relative to a lower E_T-threshold trigger. Figure 3.9 shows the efficiency of the main single-photon trigger and the legs of the main diphoton trigger as a function of E_T and η measured in data and MC simulation.

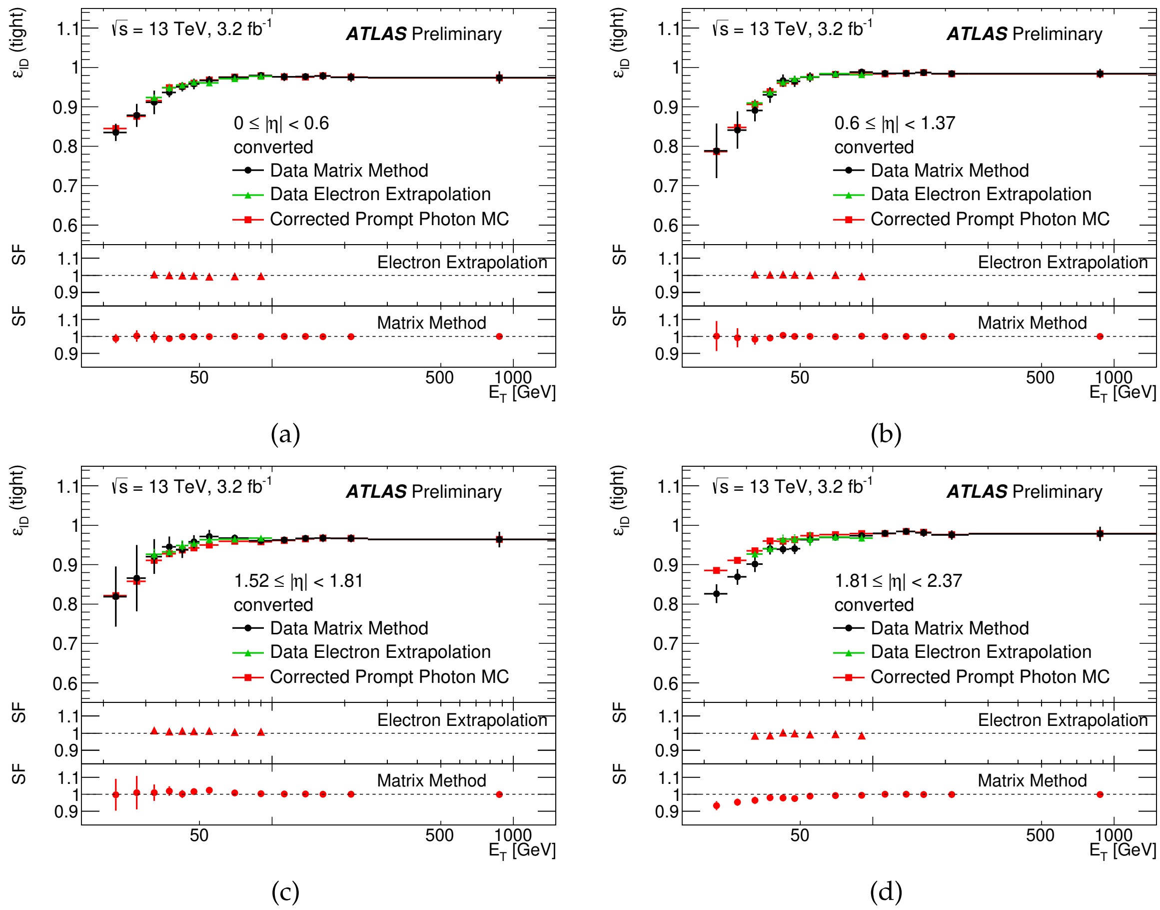

Figure 3.8: Comparison of the electron extrapolation and matrix method data-driven efficiency measurements of converted photons to the respectively prompt-photon MC predictions as function of E_T in the region $20 < E_T < 1500$ GeV, in the four η intervals. The bottom panels show the scale factors (SF) derived from the ratio of the efficiency between data-driven method and simulation. The uncertainty bars represent the sum in quadrature of the statistical and systematic uncertainties [146].

3.5 Jets

3.5.1 Jet reconstruction

Colour-charged particles such as quarks and gluons do not exist as isolated particles below the deconfinement temperature and, upon production, hadronise into collimated *jets* of many colour-neutral particles. These jets are visible as energy deposits in the calorimeters and are reconstructed from positive energy *topo-clusters* [148]: topologically connected calorimeter cells that have been clustered with an algorithm based on the cell signal significance, i.e. the ratio of the cell signal to the average expected electronic and pile-up noise. Both the cell energy and expected cell noise are measured on the EM energy scale and are not corrected for the reduced response to the hadronic part of the shower arising from the non-compensating nature of the calorimeters. The four-momenta of the topo-clusters, derived with respect to the origin of the experiment's coordinate system and treated as massless pseudo-particles, are recombined using the anti-k_t jet algorithm [149] implemented in the FastJet package [150] with distance parameter R to form jets.

The jets used in the analysis described in this work are formed from topo-clusters at the EM

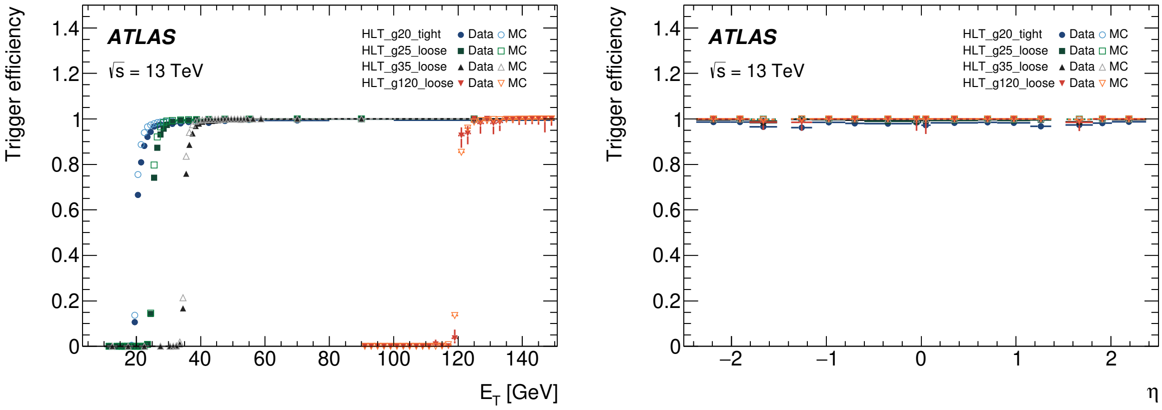

(a) (b)

Figure 3.9: Efficiency of the HLT photon triggers `g20_tight`, `g25_loose`, `g35_loose`, and `g120_loose` relative to a looser HLT photon trigger as a function of E_{T} (a) and η (b) of the offline reconstructed photon candidates satisfying the tight identification and isolation requirements. The transition region between the barrel and end-cap calorimeter ($1.37 < |\eta| < 1.52$) is excluded [128].

scale using distance parameter $R = 0.4$ for the jet algorithm. After jet formation the four-momentum is calibrated such that the jet originates from the hard-scattering vertex and the jet energy scale matches the energy scale of *truth jets*. Truth jets are reconstructed at particle-level from MC simulation by applying the same jet algorithm to the four momenta of all stable final-state particles with the exception of muons, neutrinos and particles originating from pile-up. The full jet energy scale (JES) calibration [151, 152] involves several steps:

- Pile-up corrections [153] based on the area of the jet in the η–ϕ plane, followed by residual corrections based on μ, sensitive to pile-up effects in previous bunch crossings (out-of-time pile-up), and the number of reconstructed primary vertices (N_{PV}), sensitive to in-time pile-up effects. Figure 3.10 shows the performance of the pile-up corrections.
- An MC-based calibration of the reconstructed jet four-momenta, calibrating the absolute JES to the particle-level energy scale and correcting biases in the η reconstruction due to transitions in granularity and detector technology in different regions. Figure 3.11 shows the jet response and the biases in the jet η reconstruction as a function of the detector η for different jet energies.
- A global sequential calibration uses observables from the calorimeter, tracker and muon spectrometer to obtain information on the particle composition and shower shape of the jet and aims to remove any JES dependence on the parton flavour (i.e. a quark or a gluon) initiating the jet.
- A final *in situ* calibration accounts for differences between the JES in data and MC simulation through η-intercalibration of forward jets to central jets in dijet events; or by comparing the jet p_{T} with well-measured recoiling reference objects, such as leptonically decaying Z bosons, photons, or well-calibrated lower-p_{T} jets. Figure 3.12 shows the relative jet response measured using η-intercalibration of dijet events and the combined *in situ* correction.

There are various other ways in which jets can be defined and reconstructed. Examples include jets reconstructed with a larger or variable distance parameter; jets reconstructed using tracks or a combination of tracks and topoclusters; and jets reconstructed from topoclusters with

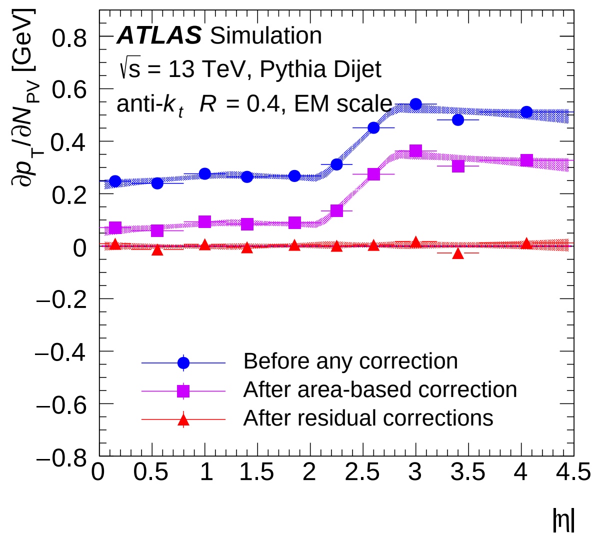

Figure 3.10: Dependence of EM-scale anti-k_t jet p_T on in-time pile-up (N_{PV}) as a function of $|\eta|$ for $p_T^{true} = 25$ GeV. The dependence is shown in bins of $|\eta|$ before pile-up corrections (blue circle), after the area-based correction (violet square), and after the residual correction (red triangle). The shaded bands represent the 68% confidence intervals of the linear fits in 4 regions of $|\eta|$ [151].

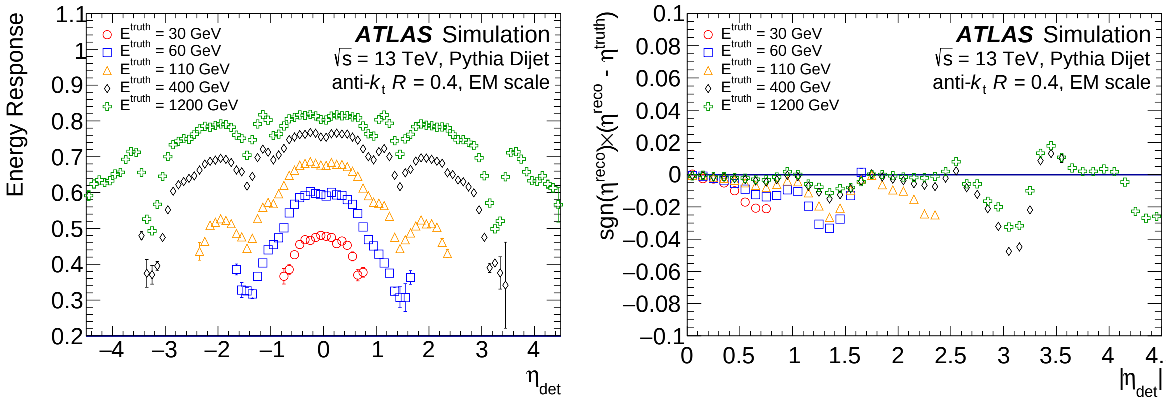

(a) (b)

Figure 3.11: (a) The average energy response as a function of η_{det} for jets of a truth energy of 30, 60, 110, 400, and 1200 GeV. The energy response is shown after origin and pile-up corrections are applied. (b) The signed difference between the truth jet η_{truth} and the reconstructed jet η_{reco} due to biases in the jet reconstruction. This bias is addressed with an η correction applied as a function of $|\eta_{det}|$ [151].

a *local hadronic cell weighting* which aims to correct for the non-compensating calorimeter response, the signal loss at the edges of the clusters due to the pile-up noise, and signal loss in inactive material without using a jet definition. Since these types of jets are not used in the analysis described in this work, these methods are not discussed here in further detail.

3.5.2 *b*-tagging

The identification of jets containing *b*-hadrons (*b*-tagging) is performed with a multivariate discriminant making use of the input variables provided by three distinct *b*-tagging algorithms based on [154, 155]:

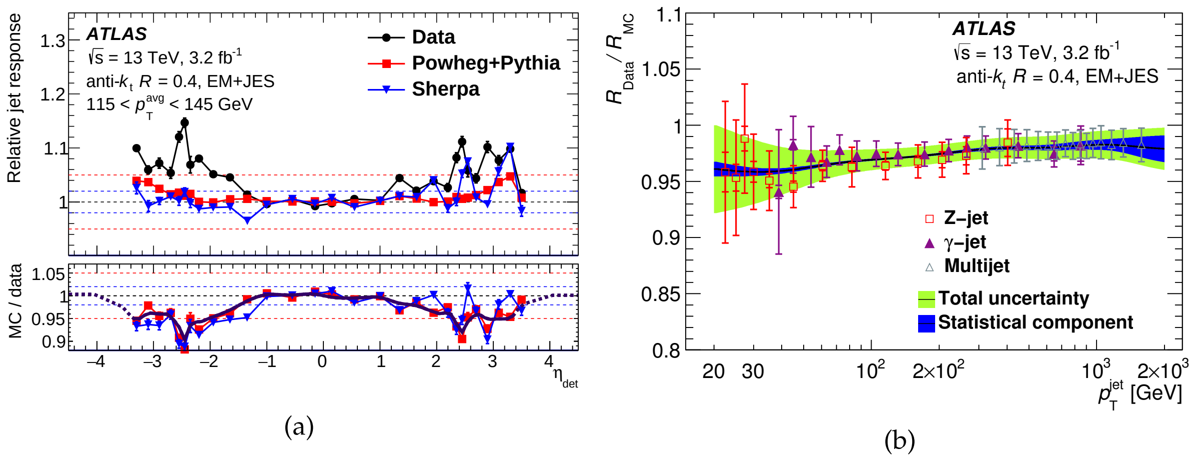

Figure 3.12: (a) Relative response of EM+JES jets as a function of η_{det} at high p_{T}. The bottom panel shows the MC-to-data ratios for two different MC generators, and the overlayed curve reflects the smoothed *in situ* correction, appearing solid in the regions in which it is derived and dotted in the regions to which it is extrapolated (using lower $p_{\text{T}}^{\text{avg}}$ jets). (b) Ratio of the EM+JES jet response in data to that in the nominal MC event generator as a function of jet p_{T} for Z-jet, γ-jet, and multijet *in situ* calibrations. The final derived correction (black line) and its statistical (dark blue) and total (light green) uncertainty bands are also shown [151].

- The transverse and longitudinal impact parameters of ID tracks that can be associated with the jet based on the ΔR.
- The explicit reconstruction of a displaced secondary vertex within the jet using at least two tracks while discarding tracks compatible with the decays of long-lived particles, photon conversion or hadronic interactions with detector material.
- The reconstruction of the full decay chain including the primary, b-hadron and c-hadron vertex using a Kalman filter and requiring a minimum of only one track per vertex.

In total 22 variables are provided by the algorithms and, in combination with the jet p_{T} and η, form the input for a boosted decision tree (BDT) algorithm to discriminate jets containing b-hadrons (b-jets) from light jets (u, d, and s-quark-initiated and gluon-initiated jets) and jets containing c-hadrons (c-jets). The MV2c20 and MV2c00 algorithms correspond to BDTs trained on $t\bar{t}$ events with a background containing 20% and 0% c-jets respectively and cut on the BDT output. Figure 3.13 shows the b-jet tagging efficiency versus the light and c-jet rejection. A better c-jet rejection is achieved with MV2c20 at the cost of a decreased light jet rejection at high-rejection working points.

Working points are defined as a given cut on the output of the BDT corresponding to an average efficiency obtained for b-jets in simulated $t\bar{t}$ events. A working point defined for the MV2c20 algorithm corresponding to a 77% b-tagging efficiency achieves rejection factors for light jets, c-jets and hadronically decaying τ-leptons of approximately 140, 4.5 and 10 respectively. Jets within $|\eta| < 2.5$ satisfying the b-tagging requirement are identified as b-jet candidates. To compensate for differences between data and MC simulation in the b-tagging efficiencies and mistag rates, correction factors are derived and applied to the simulated samples.

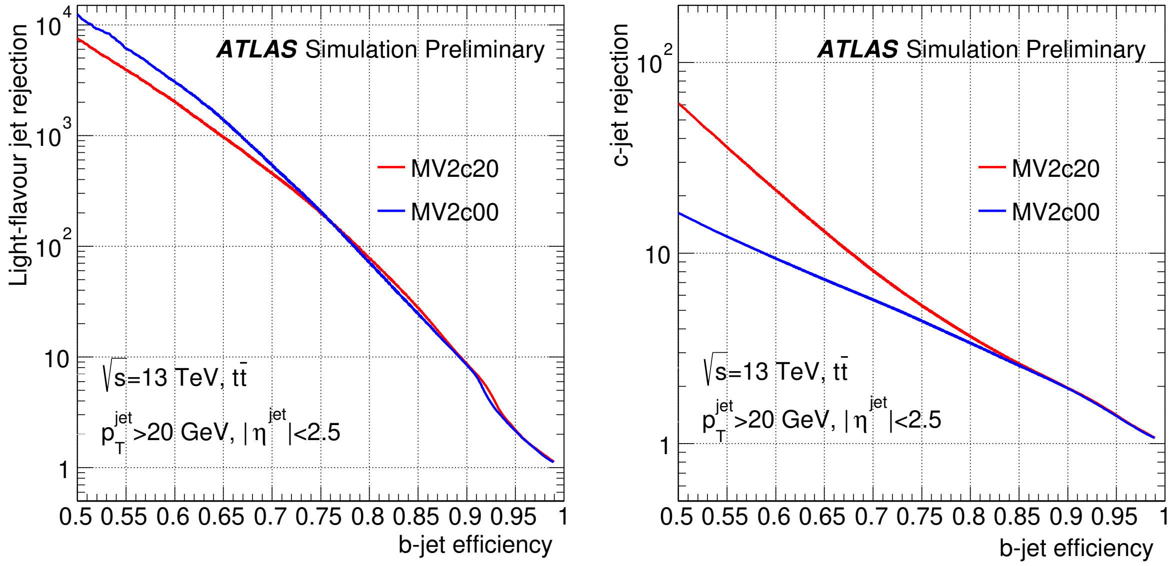

(a) (b)

Figure 3.13: The light-flavour (a) and c-jet (b) rejection versus b-jet efficiency for the MV2C20 (red) and MV2C00 (blue) b-tagging algorithms in $t\bar{t}$ events [155].

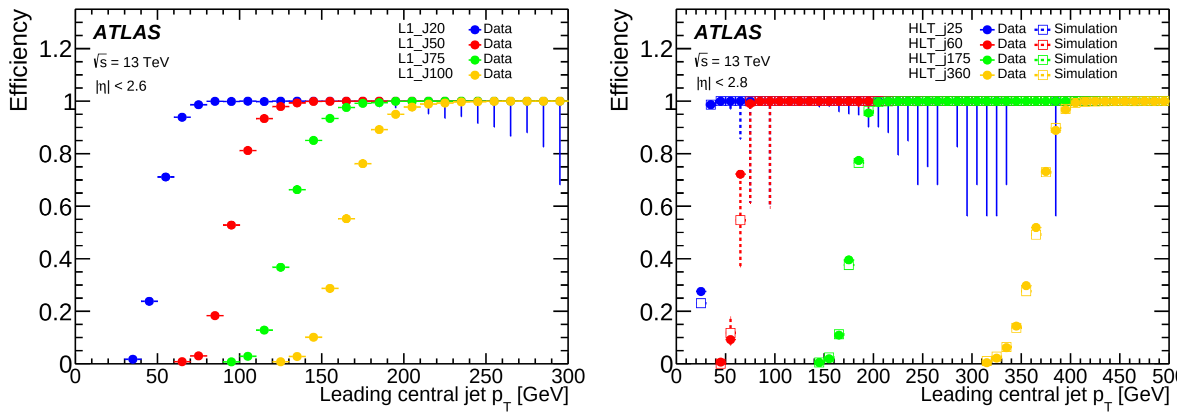

(a) (b)

Figure 3.14: Efficiency of the single-jet triggers as a function of the offline jet p_T for (a) L1 and (b) HLT in the central region [128].

3.5.3 Jet trigger

Jet RoIs are identified at L1 as the energy sum in 4×4 ($\Delta\eta \times \Delta\phi = 0.4 \times 0.4$) or 8×8 ($\Delta\eta \times \Delta\phi = 0.8 \times 0.8$) trigger tower windows with a 2×2 trigger tower core as a local maximum and exceeding a predefined E_T threshold [128]. At the HLT, jet reconstruction is similar to offline jet reconstruction and, based on the algorithm, either uses the cells from the full calorimeter or the restricted L1 RoI to construct topoclusters.

The lowest-threshold unprescaled single-jet trigger for the 2015 data-taking (`j360`) requires the jet to have $E_T > 360$ GeV and is seeded by the `L1_J100` L1 trigger requiring an $E_T >$ 100 GeV. The lowest-threshold unprescaled multijet triggers are `3j175`, `4j85`, `5j60` and `6j45` requiring a certain number of jets to have an E_T exceeding the threshold, while the H_T trigger `ht850_L1J100` requires the $\sum E_T$ of all jets to exceed the threshold of 850 GeV and at least one

L1 jet to have $E_{\mathrm{T}} > 100$ GeV. Figure 3.14 shows the the efficiency of the single jet triggers in the central region as a function of the offline reconstructed jet p_{T}.

3.6 Missing transverse momentum

Missing transverse momentum ($E_{\mathrm{T}}^{\mathrm{miss}}$) is an experimental observable used to detect transverse momentum carried away by undetected particles, such as neutrinos, produced in the hard-scattering event. It uses reconstructed objects and therefore all subcomponents of the detector.

3.6.1 $E_{\mathrm{T}}^{\mathrm{miss}}$ reconstruction

The $E_{\mathrm{T}}^{\mathrm{miss}}$ is reconstructed from the fully reconstructed and calibrated particles and jets associated with the hard-scattering vertex (*hard signals*), and from residual *soft signals* consisting of the track collection associated with hard-scattering vertex but not associated to any reconstructed hard-scattering objects [156]. The *hard objects* are reconstructed and selected at the analysis level to allow for a consistent calibration scheme for particles, jets and $E_{\mathrm{T}}^{\mathrm{miss}}$.

Since particle and jet hypotheses can be applied to the same detector signals, ambiguities must be resolved to avoid double counting the same signals as different objects. This is achieved by computing $E_{\mathrm{T}}^{\mathrm{miss}}$ in a hierarchical manner considering electrons first, followed by photons, such that a photon is rejected when it shares the same detector signal with an electron, and finally jets are considered if they do not share any signals with higher priority particles.[3] Muons typically do not share detector signals with other particles or jets. An exception however are non-isolated muons and muons with a large energy loss in the calorimeter for which more refined overlap removal procedures are applied.

Once ambiguities are resolved, $E_{\mathrm{T}}^{\mathrm{miss}}$ is defined as the magnitude of the negative vectorial sum of the transverse momenta of all selected and reconstructed particles and jets (*hard term*) and the transverse momenta of the soft signals (*soft term*). There is little pile-up dependence in $E_{\mathrm{T}}^{\mathrm{miss}}$ since the hard term includes only fully reconstructed and calibrated particles, where the calibrations include pile-up corrections. Furthermore, *jet vertex tagging* (JVT) [153] is used to select jets that are likely to originate from the hard-scattering vertex and reject pile-up jets, while the soft term uses only tracks associated to the hard-scattering vertex.

While a lower-priority particle sharing signals with a higher-priority particle is always rejected, jets can have a partial overlap with electrons or photons. In this case, the jet p_{T} is corrected to avoid double counting energy depositions in the calorimeter. If the overlapping energy fraction is larger 50% the jet is discarded and any unassociated tracks can enter the $E_{\mathrm{T}}^{\mathrm{miss}}$ computation through the soft term. In case of a muon overlapping with a jet, the origin of the jet needs to be determined: if the JVT classifies it as a pile-up jet or if the jet satisfies selection criteria that classify it as originating from significant energy losses of the muon in the calorimeter, the jet is rejected in the $E_{\mathrm{T}}^{\mathrm{miss}}$ computation; while jets satisfying criteria that classify it as originating from final state radiation off the muon are retained and enter the $E_{\mathrm{T}}^{\mathrm{miss}}$ computation at the EM energy scale.

[3]Hadronically decaying taus can be used to further refine the $E_{\mathrm{T}}^{\mathrm{miss}}$ computation. Taus are however not reconstructed in the analysis described in this work and are therefore treated as jets.

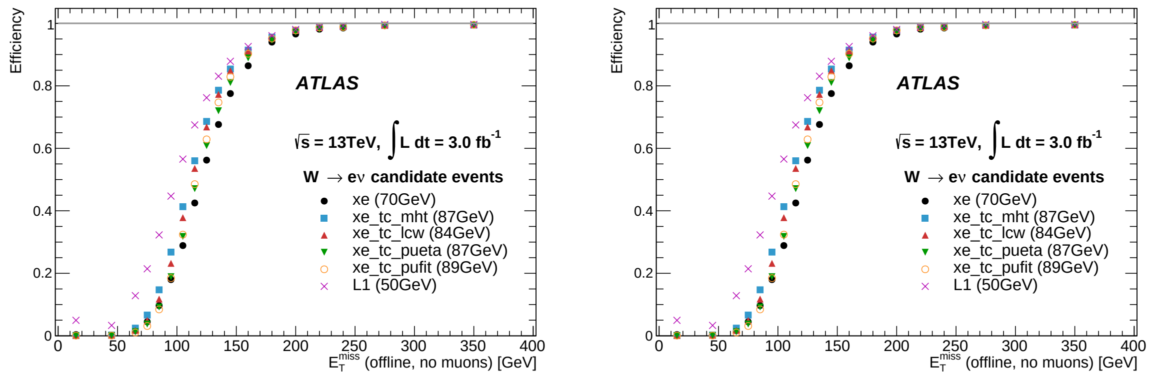

(a) (b)

Figure 3.15: $E_{\mathrm{T}}^{\mathrm{miss}}$ trigger efficiency curves with respect to the offline reconstructed $E_{\mathrm{T}}^{\mathrm{miss}}$ without muon corrections for all events passing the (a) $W \to e\nu$ or (b) $W \to \mu\nu$ selections. The different efficiencies were measured for L1, and for the combination of L1 with each of the HLT $E_{\mathrm{T}}^{\mathrm{miss}}$ algorithms. The thresholds for the different algorithms correspond to an approximately equal trigger rate [128].

3.6.2 $E_{\mathrm{T}}^{\mathrm{miss}}$ trigger

At L1, $E_{\mathrm{T}}^{\mathrm{miss}}$ is computed by the vectorial summing of all 2×2 trigger tower inputs ($\Delta\eta \times \Delta\phi = 0.2 \times 0.2$) using a dynamic bunch-by-bunch pedestal subtraction to compensate for the higher trigger rate that would otherwise occur at the beginning of the bunch train as a result of the LAr pulse shape [128]. At the HLT different calorimeter-based algorithms are available for the $E_{\mathrm{T}}^{\mathrm{miss}}$ computation using either the calorimeter cells, HLT jets or topo-clusters and dedicated pile-up suppression algorithms.

The lowest-threshold unprescaled $E_{\mathrm{T}}^{\mathrm{miss}}$ trigger for the 2015 data-taking and used in the analysis described in this work is `HLT_xe70` and uses the cell algorithm: LAr and Tile calorimeter cells with an energy, calibrated at the EM scale, exceeding twice the cell's electronic and pile-up noise level are used to compute the measured transverse momentum in the massless limit for each cell. The negative vectorial sum of the p_{T} of all cells is required to exceed 70 GeV. All unprescaled HLT $E_{\mathrm{T}}^{\mathrm{miss}}$ triggers are seeded by `L1_XE50` requiring $E_{\mathrm{T}}^{\mathrm{miss}} > 50$ GeV at the EM scale. Figure 3.15 shows the efficiency of the `L1_XE50` and the `HLT_xe70` trigger, along with the alternative HLT algorithms at equal-rate thresholds, as a function of an offline reconstructed $E_{\mathrm{T}}^{\mathrm{miss}}$, computed without considering muons.

4 A BSM-model-independent search strategy

This chapter outlines a strategy to look for unanticipated signals for new physics. In the first section, a brief introduction to the strategy is given, followed by an analysis of the strategy using toy examples involving simple hypotheses. The third section describes the analysis strategy as it is applied to the ATLAS datasets and summarises the advantages and disadvantages.

4.1 Search strategy

In order to search for unanticipated new physics signals, the data are partitioned into many *data classes*, commonly represented as bins of a histogram, each constituting a *counting experiment* for which a *background-only hypothesis test* is performed, i.e. it is assumed that the unanticipated signal can be revealed as a statistically significant deviation of the experimental data counts from the SM expectation in one or multiple combined data classes. A class can be any set of selection rules on objects or observables, e.g. the final state of an event or a specific range in one or multiple observables. There is a lot of freedom in how one can partition the data and the analysis' sensitivity to a particular signal depends on the choice of partitioning. 'BSM-model-independent' should therefore not be understood as 'sensitive to any kind of BSM signal' but as 'free of specific BSM signal assumptions'. An example of a possible partitioning choice is primarily by final state and secondarily in ranges (bins) of some observable(s) sensitive to the existence of new decay channels, new resonances, or new interference effects. This particular partitioning strategy is used in the analyses detailed in Chapters 5 and 6.

Increasing the number of data classes by e.g. specifying the final state in more detail; increasing the number of observables; or reducing bin sizes, can improve the sensitivity to small localized signals in (a corner of) phase space. However, the increase in the number of counting experiments, and thereby the number of tests performed, also increases the chance of erroneous statistical inferences, known as the look-elsewhere effect (LEE). It can be mitigated by inferring from more extreme values of the test statistic for each individual test. Manifestly, there is a trade-off: a larger number of tests covers phase space with a higher granularity and can uncover otherwise hidden signals, yet, signals need to be larger to produce a more extreme-valued test statistic. Care must be taken to balance the number of data classes and to choose observables in which a signal could be observed based on (biased) physics intuition.

A less fundamentally limiting factor for the sensitivity to a signal model is the uncertainty on the number of expected counts in a counting experiment. A substantial part of the work involved in typical model-motivated searches is concerned with estimating and reducing the effects of systematic uncertainties by using auxiliary measurements in control regions[1].

[1] A control region is a signal-free region under a given BSM hypothesis that can be used to constrain the nuisance parameters that affect the SM expectation value and thus reduce systematic uncertainties in the signal region(s).

However, here, the lack of *a priori* well-defined regions where a signal is expected and isolated, and hence which regions can be assumed to be signal-free, makes it impossible to define generic control regions that globally constrain nuisance parameters without introducing some model-dependence.

The solution proposed in this strategy is to use the counting experiments to decide if a data class potentially contains a BSM signal, and if so, mark it as a DDSR. A *dedicated analysis* and statistical model should then be constructed around a single or few DDSRs using appropriate BSM models as hypotheses. This then, in principle, allows the definition of control regions and further optimisation of the background model. In the dedicated re-analysis of the DDSRs the discrepancy between the experimental data counts and expected SM counts either remains, or, it is identified as an artefact from an incorrect modelling of the SM. In addition to a more robust background model and treatment of the systematic uncertainties, the expectation is that a dedicated analysis can enhance the sensitivity to the alternative hypothesis considerably through the use of control regions or other data-driven methods.

If the discrepancy remains, the DDSRs can be redefined and optimised to maximise the observed discrepancy or to maximise the sensitivity to an appropriate BSM model, after which the dedicated analysis is used to determine the signal strength or set exclusions limits using a (new) independent dataset. The sample size (or integrated luminosity L_{int}) of the independent dataset required for evidence or discovery of a signal can be determined from the BSM model being used as (alternative) hypothesis. As a rule-of-thumb, it is assumed that the required sample size is equal to or larger than the sample size used to determine the DDSRs.

In this strategy of sequential hypothesis testing, the initial test can be considered the decision rule for performing a dedicated analysis. A higher significance level of the initial test reduces the risk of missing a true signal at the cost of performing dedicated analyses of DDSRs more frequently.

In the following section it will be demonstrated that, under the assumption that the concentration of the analysis efforts on a DDSR lead to reduced systematic uncertainties, the DDSR approach can achieve a larger sensitivity to an unanticipated signal for new physics than the non-sequential-hypothesis-testing method in which all data (used for deriving the DDSR and the dedicated analysis on a new dataset) are combined in a single test. *Concentration of the analysis efforts* should be understood as developing data-driven techniques to estimate the background such as control regions or functional fits, and/or improving the (theoretical) predictions of relevant SM processes by e.g. generating more MC simulated events or by including higher-order corrections to the (differential) cross section.

4.2 Meta-analysis of toy examples

In the following, a comparison will be made between the so-called *DDSR method* and *global method*:

- The DDSR method performs sequential tests on two equally-sized (same L_{int}) statistically independent datasets. The tests performed on the first dataset decide if a data class contains a significant deviation in which case a dedicated analysis is performed using the second dataset.

- The *global* method combines the two datasets and performs a non-sequential set of tests. It follows exactly the same procedure as the initial step in the DDSR method but uses the combined dataset and does not report a DDSR as a result.

4.2.1 Definitions

For convenience, some terminology needed in the following is already introduced here.

The hypothesis being tested is called the *null hypothesis* and denoted H_0. In this work, the null hypothesis is always the background-only or SM-only hypothesis and an alternative hypothesis, denoted H_1, specifies the parameters of a BSM model. The H_1 is called *simple* if all parameters are specified or *composite* if a parameter can take on a range of values. Although the DDSR method itself does not involve any H_1, in the following toys examples, simple alternative hypotheses are used in order to make a comparison of the sensitivity of the two aforementioned methods.

The a priori selected significance level (α) of a test, also the *size* of a test, is the probability of falsely rejecting H_0:

$$\alpha \equiv \Pr\left(\text{test rejects } H_0 \mid H_0\right) \tag{4.1}$$

Such an error is called a *false positive* or *type I error*.

The p-value under H_0, denoted p_0, is defined as the probability of obtaining a value for the test statistic (t) being used (if the experiment were to be repeated) that is at least as extreme as the one observed (t_{obs}) assuming H_0 is true:

$$p_0 \equiv \Pr\left(t \text{ is more extreme than } t_{\text{obs}} \mid H_0\right) \tag{4.2}$$

In order to determine the value of p_0 the probability distribution of t under H_0 needs to be known either analytically or numerically. If then, $p_0 \leq \alpha$ the test is said to 'reject' H_0. The p_0-value thus corresponds to the smallest possible choice of α for which the test would have rejected H_0. It is a random variable with a uniform probability density function (pdf) between 0 and 1[2]: $p_0 \sim \mathcal{U}(0,1)$.

Often the result of a test is expressed in terms of a z_0-score rather than a p_0-value. The z_0-score is the signed value of a standard-normal-distributed test statistic under H_0 corresponding to the same p_0-value for a one-sided test. It is thus a random variable with a standard-normal pdf: $z_0 \sim \phi \equiv \mathcal{N}(\mu = 0, \sigma^2 = 1)$, where $\mathcal{N}(\mu, \sigma^2)$ is a general normal pdf with mean μ and variance σ^2. The relation between the z_0-score and the p_0-value are given by:

$$z_0 = z(p_0) \equiv \Phi^{-1}(1 - p_0) \tag{4.3}$$

$$p_0 = Q(z_0) \equiv \int_{z_0}^{\infty} \mathrm{d}x\, \phi(x) = 1 - \Phi(z_0) \tag{4.4}$$

where Φ is the cumulative distribution function (cdf) of the standard-normal distribution ϕ, Φ^{-1} is the inverse of the standard-normal cdf or *quantile function* and x is the random variable of ϕ. The function Q is also called the complementary cumulative distribution function (ccdf)

[2]A uniform distribution for p_0 is only expected for continuously distributed test statistics which, for the toy examples, is assumed for simplicity. Counting experiments, however, are obviously discrete in nature.

of ϕ. In high-energy physics (HEP) it is customary to claim a discovery when H_0 is rejected by a (one-sided) test with a level of significance of '5σ', i.e. $\alpha = Q(5)$ or $p_0 \leq 2.87 \cdot 10^{-7}$.

4.2.2 Look-elsewhere effect

When performing multiple statistical tests, increasing the number of tests also increases the LEE, i.e. the chance of erroneous statistical inferences. While for a single test the probability for a false positive is equal to α (Eq. 4.1), multiple tests of size α will have a probability of producing *at least* one false positive which is larger than α:

$$\bar{\alpha} \equiv \Pr\left(\text{at least one test rejects } H_0 \mid H_0\right) \geq \alpha \tag{4.5}$$

This probability of making at least one type I error in the family of tests is called the family-wise type I error rate ($\bar{\alpha}$) and, in analogy to α, can be called the *global significance level* of the family of tests.

For example, when n *independent* tests are performed the probability to reject a true null hypothesis in at least one test, i.e. to make one or more false positive inferences (n_{FP}), becomes:

$$\begin{aligned}\bar{\alpha} &= \Pr\left(n_{\text{FP}} \geq 1\right) = 1 - \Pr\left(n_{\text{FP}} = 0\right) \\ &= 1 - \prod_{i=1}^{n} \Pr\left(p_0^i > \alpha \mid H_0\right) = 1 - \left(\Pr\left(p_0 > \alpha \mid H_0\right)\right)^n = 1 - \left(1 - \Pr\left(p_0 \leq \alpha \mid H_0\right)\right)^n \\ &= 1 - (1-\alpha)^n \end{aligned} \tag{4.6}$$

When assuming a typical significance level of $\alpha = 0.05$, making at least one type I error is expected in the majority of the cases when $n > 14$.

By rearranging Eq. 4.6 it is clear that $\bar{\alpha}$ can be selected by choosing α according to:

$$\alpha = 1 - (1 - \bar{\alpha})^{1/n} \tag{4.7}$$

Expanding the right-hand side at $\bar{\alpha} = 0$ shows that $\alpha \approx \bar{\alpha}/n + O(\bar{\alpha}^2)$ is a good approximation for small values of $\bar{\alpha}$. Eq. 4.7 is known as the *Šidák correction* and its first order approximation is known as the *Bonferonni correction*.

Rather than correcting α, an equivalent alternative is to compare a corrected p_0-value ($\bar{p}_0$), which in analogy can be called a *global p_0-value*, directly to a predefined $\bar{\alpha}$:

$$\bar{p}_0 = 1 - (1 - p_0)^n \tag{4.8}$$

Eqs. 4.6–4.8 are valid only for *independent* tests. If the tests are *not* independent and e.g. Eq. 4.7 is used to determine α then $\Pr\left(n_{\text{FP}} \geq 1\right) \leq \bar{\alpha}$ and the method provides an upper bound on $\bar{\alpha}$. In this case, if the relation between α and $\bar{\alpha}$ (or equivalently between p_0 and $\bar{p}_0$) is not known analytically, it can often be determined numerically using simulated toy experiments.

4.2.3 Case I: Independent tests without systematic uncertainties

This case studies the sensitivity of the DDSR method in comparison to the *global* method. While using the combined dataset, as in the *global* method, statistically provides the most powerful test, it provides no opportunity to concentrate analysis resources on a reduced number of regions in a dedicated analysis, which can be advantageous in the presence of systematic uncertainties as will be demonstrated in *Case II* in the next section.

The probability for a method to report a *false positive* (reject H_0 when H_0 is true) in n signal-free independent tests is compared against the probability for the method to report a *true positive* (reject H_0 when H_0 is false) when a real signal is present in a single test. These are represented along two axes to form a ROC (receiver operating characteristic) curve where each point on the curve corresponds to a value of α. The *true positive rate* is sometimes also called *sensitivity*, *probability of a detection*, *statistical power*, or *signal efficiency* (ϵ_{sig}), while the *false positive rate* is also called the family-wise type I error rate ($\bar{\alpha}$), or *background efficiency* (ϵ_{bkg}):

$$\epsilon_{\text{sig}}(\alpha|n,\mu_{\text{sig}}) = \Pr\left(\text{test rejects } H_0 \mid H_1 \text{ is true}\right) \tag{4.9}$$
$$\epsilon_{\text{bkg}}(\alpha|n) = \Pr\left(\text{at least one test rejects } H_0 \mid H_0 \text{ is true}\right) = \bar{\alpha} \tag{4.10}$$

The ϵ_{sig} cannot be determined for the generic condition that H_0 is false. In the following an alternative hypothesis H_1 specifies a signal strength (μ_{sig}) and ϵ_{sig} is determined with respect to H_1. The signal strength is defined as the average z_0-score under H_1 such that $z_0 \sim \phi = \mathcal{N}(0,1)$ under H_0, while $z_0 \sim \mathcal{N}(\mu_{\text{sig}},1)$ under H_1[3]. The the global significance level of the (entire) procedure is by definition equal to ϵ_{bkg}.

Global method

The *global* method performs n tests on the combined data sample. For each of the n independent signal-free tests $z \sim \phi$, or equivalently $p_0 \sim \mathcal{U}(0,1)$. Under H_1 a signal of strength μ_{sig} is injected in a single test in each of the two equally-sized data samples. The signal strength in the combined (primed) dataset is therefore[4]: $\mu'_{\text{sig}} = \sqrt{2}\mu_{\text{sig}}$ such that $z_0 \sim \mathcal{N}(\sqrt{2}\mu_{\text{sig}},1)$.

The ϵ_{bkg} and ϵ_{sig} for the *global* method are thus given by:

$$\begin{aligned}\epsilon_{\text{bkg}}(\alpha \mid n) &= \Pr\left(\text{at least one test rejects } H_0 \mid H_0\right) = \bar{\alpha} \\ &= 1-[1-\alpha]^n \end{aligned} \tag{4.11}$$

$$\begin{aligned}\epsilon_{\text{sig}}(\alpha \mid \sqrt{2}\mu_{\text{sig}}) &= \Pr\left(\text{test rejects } H_0 \mid H_1\right) \\ &= \Pr\left(p_0 \le \alpha \mid H_1\right) = \Pr\left(z(p_0) \ge z(\alpha) \mid H_1\right) \\ &= \int_{z(\alpha)}^{\infty} \mathrm{d}x\, \mathcal{N}(x \mid \sqrt{2}\mu_{\text{sig}},1) = \int_{z(\alpha)-\sqrt{2}\mu_{\text{sig}}}^{\infty} \mathrm{d}x\, \phi(x) \\ &= Q\left(z\left(\alpha\right) - \sqrt{2}\mu_{\text{sig}}\right)\end{aligned} \tag{4.12}$$

When expressed in terms of $\bar{\alpha}$ instead of α, the dependence on the number of tests (n) moves

[3]The signal strength is related to the expected signal event counts (s) and background event counts (b) as $\mu_{\text{sig}} = s/\sqrt{b}$ in the large b limit.

[4]In the large b limit the relation to expected counts is again: $\mu'_{\text{sig}} = s'/\sqrt{b'} = 2s/\sqrt{2b} = \sqrt{2}\,s/\sqrt{b} = \sqrt{2}\mu_{\text{sig}}$.

from ϵ_{bkg} to ϵ_{sig}:

$$\epsilon_{\text{bkg}}(\bar{\alpha}) = \bar{\alpha} \tag{4.13}$$

$$\begin{aligned}\epsilon_{\text{sig}}(\bar{\alpha} \mid n, \sqrt{2}\mu_{\text{sig}}) &= Q\left(z\left(1-(1-\bar{\alpha})^{1/n}\right) - \sqrt{2}\mu_{\text{sig}}\right)\\ &\approx Q\left(z\left(\bar{\alpha}/n\right) - \sqrt{2}\mu_{\text{sig}}\right) \qquad \text{for } \bar{\alpha} \ll 1\end{aligned} \tag{4.14}$$

Data-derived signal region method

In the DDSR method, n tests are performed on one of the two equally-sized data samples. If one or more tests with size α_1 reject H_0, the data selection of the corresponding test is marked as a DDSR and tested using the second data sample with a test of size α_2. If also this test rejects H_0 it is said that the *test sequence* rejects H_0. To compare this method with the *global* method, the ϵ_{bkg} and ϵ_{sig} of the consecutive test sequence is determined such that the efficiencies of both methods are compared based on the same *total* data sample size used for inference.

Choosing α_2 for the parametrization of ϵ_{bkg}, it can be derived as follows:

$$\begin{aligned}\epsilon_{\text{bkg}}(\alpha_2 \mid \alpha_1, n) &= \Pr\left(\text{at least one } \textit{test sequence} \text{ rejects } H_0 \mid H_0\right)\\ &= 1 - \Pr\left(\text{none of the } n \text{ test sequences reject } H_0 \mid H_0\right)\\ &= 1 - \prod_{i=0}^{n} \Pr\left(\text{test sequence } i \text{ does not reject } H_0 \mid H_0\right)\\ &= 1 - \left[\Pr\left(\text{test sequence does not reject } H_0 \mid H_0\right)\right]^n\\ &= 1 - \left[1 - \Pr\left(\text{test sequence rejects } H_0 \mid H_0\right)\right]^n\\ &= 1 - \left[1 - \Pr\left(\text{DDSR defined} \mid H_0\right) \cdot \Pr\left(\text{test of DDSR rejects } H_0 \mid H_0\right)\right]^n\\ &= 1 - \left[1 - \Pr\left(p_{0_1} \leq \alpha_1 \mid H_0\right) \cdot \Pr\left(p_{0_2} \leq \alpha_2 \mid H_0\right)\right]^n\\ &= 1 - \left[1 - \alpha_1\alpha_2\right]^n\end{aligned} \tag{4.15}$$

where p_{0_1} and p_{0_2} are the p_0-values obtained from testing the first and second data sample respectively. The ϵ_{bkg} can, more conveniently, be expressed in terms of the family-wise type I error rate of the initial family of tests ($\bar{\alpha}_1$) which is equal to the probability of at least one false positive DDSR to be defined. Using Eq. 4.7:

$$\epsilon_{\text{bkg}}(\alpha_2 \mid \bar{\alpha}_1, n) = 1 - \left[1 - \left(1 - (1-\bar{\alpha}_1)^{1/n}\right)\alpha_2\right]^n \tag{4.16}$$

$$\approx \bar{\alpha}_1\alpha_2 \qquad \text{for } \bar{\alpha}_1 \ll 1 \text{ and } \alpha_2 \ll 1 \tag{4.17}$$

The global significance level of the test sequence ($\bar{\alpha}$) is (by definition) equal to ϵ_{bkg} and thus well approximated by $\bar{\alpha}_1\alpha_2$ for small values of $\bar{\alpha}_1$ and α_2 which are of interest.

The ϵ_{sig} of the test sequence is given by:

$$\begin{aligned}\epsilon_{\text{sig}}(\alpha_2 \mid \alpha_1, \mu_{\text{sig}}) &= \Pr\left(\text{test sequence rejects } H_0 \mid H_1\right)\\ &= \Pr\left(p_{0_1} \leq \alpha_1 \mid H_1\right) \cdot \Pr\left(p_{0_2} \leq \alpha_2 \mid H_1\right)\\ &= Q\left(z\left(\alpha_1\right) - \mu_{\text{sig}}\right) \cdot Q\left(z\left(\alpha_2\right) - \mu_{\text{sig}}\right)\end{aligned} \tag{4.18}$$

Or in terms of $\bar{\alpha}_1$:

$$\begin{aligned} \epsilon_{\text{sig}}(\alpha_2 \mid \bar{\alpha}_1, n, \mu_{\text{sig}}) &= Q\left(z\left(1-(1-\bar{\alpha}_1)^{1/n}\right)-\mu_{\text{sig}}\right)\cdot Q\left(z\left(\alpha_2\right)-\mu_{\text{sig}}\right) \\ &\approx Q\left(z\left(\bar{\alpha}_1/n\right)-\mu_{\text{sig}}\right)\cdot Q\left(z\left(\alpha_2\right)-\mu_{\text{sig}}\right) \qquad \text{for } \bar{\alpha}_1 \ll 1 \end{aligned} \tag{4.19}$$

Figure 4.1 shows the ROC curves of the *global* method (p_0) and the DDSR method (p_{0_2}) for $n = 10^5$ and $\bar{\alpha}_1 = 0.05$. As expected in this case, the DDSR method is always less powerful than the *global* method.

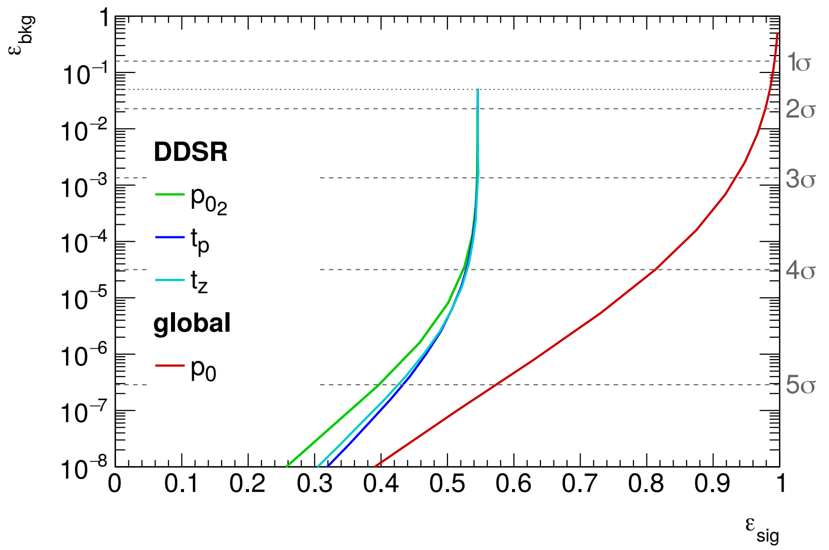

Figure 4.1: ROC curves for the three different DDSR test statistics and the *global* method. The signal efficiencies for the t_p and t_z test statistics are estimated numerically using an MC method. The statistical uncertainties on the estimates are negligible. The ϵ_{bkg} corresponds one-to-one to $\bar{\alpha}$, the global significance level. The dashed lines show the global significance levels as $z(\bar{\alpha})\sigma$. The number of tests is fixed at $n = 10^5$ and $\bar{\alpha}_1 = 0.05$. A dotted line is drawn at $\epsilon_{\text{bkg}} = \bar{\alpha}_1$ which is the maximum background efficiency by construction for the DDSR methods.

Thus far, the initial test is only used as a decision rule for performing another test using the second sample. That means that the global p_0-value of a test sequence only depends on whether $p_{0_1} \leq \alpha_1$ and on p_{0_2}. However, a p_{0_1}-value (much) smaller than α_1 can be regarded as additional evidence against H_0 and so a more powerful test sequence can be constructed by including the information of the p_{0_1}-value in the test statistic. Here, two possible test statistics, t_p and t_z, are constructed. The first one by multiplying the p_0-values and the second one by adding the z_0-scores:

$$t_p \equiv \bar{p}_{0_1} \cdot p_{0_2} \tag{4.20}$$

$$t_z \equiv \bar{z}_1 + z_2 \tag{4.21}$$

where $\bar{p}_{0_1}$ is the global p_0-value of the initial test (Eq. 4.8) and $\bar{z}_1$ is the global z-score of the initial test, defined as $\bar{z}_1 \equiv z\left(\bar{p}_{0_1}\right)$. These test statistics obtained by adding z-scores or multiplying p_0-values do not follow a standard normal distribution or uniform distribution respectively and should not be interpreted as a z_0-score or p_0-value. Their cdfs and hence the ϵ_{bkg} can be determined analytically as derived in Appendix A. For the t_p test statistic ϵ_{bkg} is

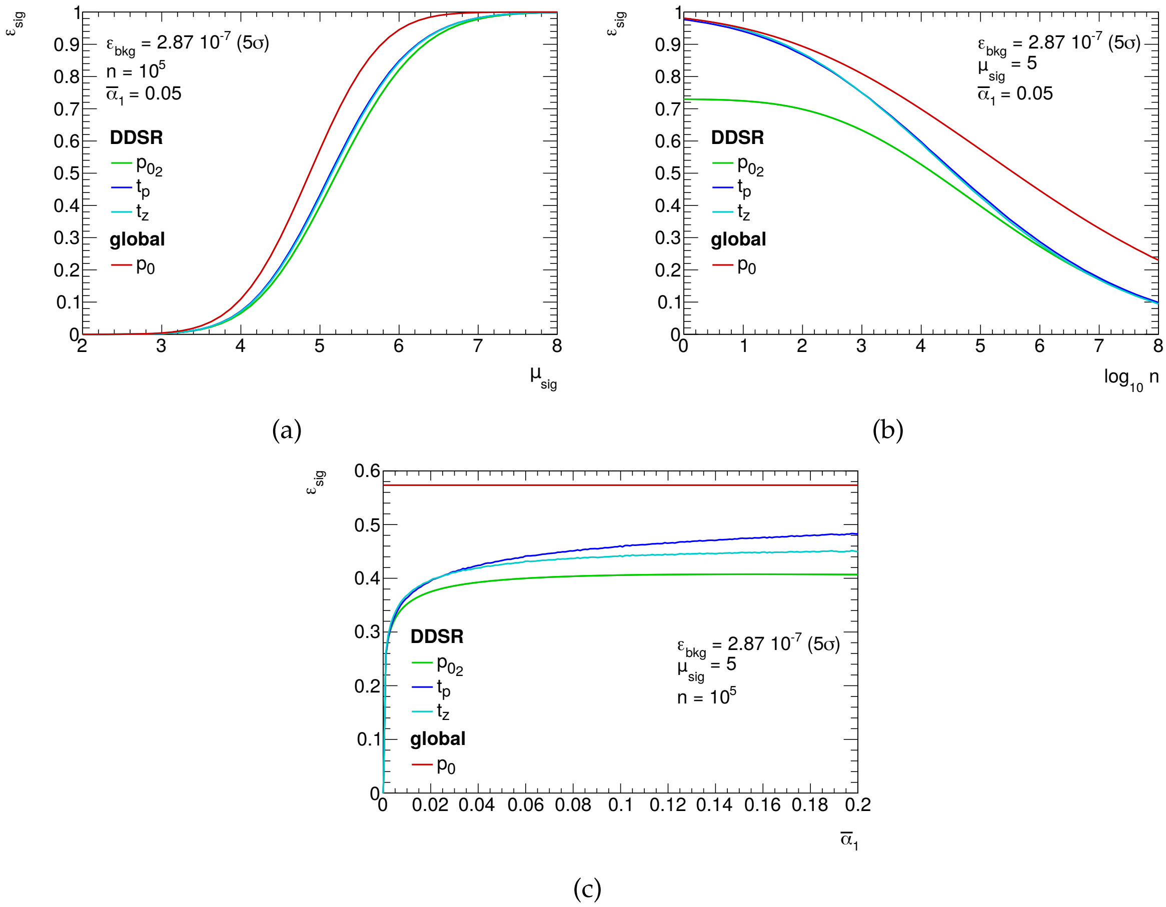

Figure 4.2: Signal efficiencies at a fixed background efficiency of $2.87 \cdot 10^{-7}$ (corresponding to 5σ) for the different test statistics as a function of the signal strength μ_{sig} (a), the number of tests n (b) and $\bar{\alpha}_1$ (c). In each case, the two remaining parameters are fixed at $\mu_{\text{sig}} = 5$, $n = 10^5$ and $\bar{\alpha}_1 = 0.05$. The signal efficiencies for the t_p and t_z test statistics are estimated numerically using an MC method. The statistical uncertainties on these estimates are negligible.

given by:

$$\epsilon_{\text{bkg}}(c_p \mid \bar{\alpha}_1) = \begin{cases} c_p \left(1 + \ln \bar{\alpha}_1 - \ln c_p\right) & \text{if } c_p \leq \bar{\alpha}_1 \\ \bar{\alpha}_1 & \text{if } c_p > \bar{\alpha}_1 \end{cases} \tag{4.22}$$

where c_p is called the *critical value* for t_p and $t_p \leq c_p$ is the *critical region* for t_p. H_0 is rejected if t_p is in the critical region.

For t_z the ϵ_{bkg} is given by:

$$\epsilon_{\text{bkg}}(c_z \mid \bar{\alpha}_1) = \int_{c_z}^{\infty} \mathrm{d}t_z\, \mathcal{N}(t_z \mid 0, 2) \cdot Q\left(\frac{2 \cdot z(\bar{\alpha}_1) - t_z}{\sqrt{2}}\right) \tag{4.23}$$

where the critical region is $t_z \geq c_z$. Both are valid for small values of $\bar{\alpha}_1$ such that the probability of finding multiple DDSRs can be neglected.

Determining ϵ_{sig} for the test statistics t_p and t_z analytically is less straight-forward as it involves determining their cdfs under H_1 (and is left as an exercise for the reader), so ϵ_{sig} is estimated numerically using toy experiments for particular values of $\bar{\alpha}_1$ and n.

The ROC curves of the three different DDSR test statistics are compared to the ROC curve of the *global* method in Figure 4.1 for $\bar{\alpha}_1 = 0.05$ and $n = 10^5$. The t_p and the t_z test statistic are indeed observed to be more powerful as they achieve a higher ϵ_{sig} for a given ϵ_{bkg} compared to the p_{0_2} test statistic.

Figure 4.2 shows the signal efficiency as a function of μ_{sig}, $\log_{10}(n)$ and $\bar{\alpha}_1$. The two alternative test statistics, t_p and t_z, improve the signal efficiency especially for a relatively small number of tests and approach the *global* method as seen in Figure 4.2(b), while for a relatively large number of tests the gain in ϵ_{sig} becomes negligible. Figure 4.2(c) shows that increasing $\bar{\alpha}_1$ beyond approximately 0.05 has no large impact on ϵ_{sig}, i.e. less stringent requirements on the definition of a DDSR do not improve the sensitivity (much) but do increase the *costs* in terms of analysis resources required linearly with $\bar{\alpha}_1$.

As mentioned before, the *global* method is the most powerful test but does not provide an opportunity to concentrate the analysis efforts on a few DDSRs which can help to constrain systematic uncertainties as discussed in the next case.

Signal efficiency and partitioning choice

When the LEE was introduced at the beginning of Section 4.1, it was mentioned that there is a trade-off between number of tests performed and sensitivity. A larger number of data selections might find signals that otherwise remain 'buried' in the background of a more inclusive data selection, but the additional tests performed increase the LEE and require larger deviations for statistical significance. This will be illustrated here using another toy example.

Figure 4.2(b) shows ϵ_{sig} as function of the number of tests (bins) n where for each value of n there is exactly one bin with a signal of $\mu_{\text{sig}} = 5$. Here, the ϵ_{sig} is considered when a signal is isolated under a certain binning (i.e. a given partitioning of the data into data selections) and the binning is then changed to become either more or less exclusive. A more exclusive binning will increase the number of bins and hence tests, and at the same time dilute the signal over multiple bins. A less exclusive binning is obtained by merging bins, resulting in fewer bins but a larger background count for the same number of signal counts.

Consider $\mu_{\text{sig}} = 5$ in a single bin under a given binning with $N = 2^m$ bins. The number of bins n are reduced from $n = N$ to $n = N/2$, $n = N/4$, etc. by merging two, four, etc. bins. For simplicity it is assumed that each bin has the same background expectation. Let m and k be non-negative integers and $n = N/2^k = 2^{m-k}$ with $k \leq m$ such that k determines the number of bins being merged. Since bins are only being merged for $k \leq m$, there is still only one bin containing all the signal. The ϵ_{sig} at a given $\bar{\alpha}$ (using the result in Eq. 4.14) becomes:

$$\begin{aligned}
\epsilon_{\text{sig}}(k \mid \bar{\alpha}, m, \mu_{\text{sig}}) &= Q\left(z\left(1 - (1-\bar{\alpha})^{1/n}\right) - \mu_{\text{sig}}/(\sqrt{2})^k\right) \\
&= Q\left(z\left(1 - (1-\bar{\alpha})^{2^{k-m}}\right) - 2^{-k/2}\mu_{\text{sig}}\right) \\
&\approx Q\left(z\left(\bar{\alpha} \cdot 2^{k-m}\right) - 2^{-k/2}\mu_{\text{sig}}\right) \qquad \text{for } \bar{\alpha} \ll 1
\end{aligned} \tag{4.24}$$

If a finer binning is chosen, the signal becomes diluted over multiple bins but at the same time there are multiple bins with a signal present. For simplicity it is again assumed that the bin containing an isolated signal under the binning with N bins is being partitioned such that each resulting bin has the same signal and background expectation. Let m and k be non-negative integers again and $n = N \cdot 2^k = 2^{m+k}$ such that k now determines the number of partitions of the signal bin. The ϵ_{sig} then becomes:

$$
\begin{aligned}
\epsilon_{\text{sig}}(k \mid \bar{\alpha}, m, \mu_{\text{sig}}) &= \Pr\left(\text{at least 1 out of } 2^k \text{ tests rejects } H_0 \mid H_1\right) \\
&= 1 - \Pr\left(\text{none of the } 2^k \text{ tests reject } H_0 \mid H_1\right) \\
&= 1 - \left[1 - \Pr\left(\text{test rejects } H_0 \mid H_1\right)\right]^{2^k} \\
&= 1 - \left[1 - \Pr\left(p_0 \leq 1 - (1-\bar{\alpha})^{1/2^{m+k}} \mid H_1\right)\right]^{2^k} \\
&= 1 - \left[1 - Q\left(z\left(1 - (1-\bar{\alpha})^{1/2^{m+k}}\right) - \mu_{\text{sig}}/(\sqrt{2})^k\right)\right]^{2^k} \\
&\approx 1 - \left[1 - Q\left(z\left(\bar{\alpha}/2^{m+k}\right) - 2^{-k/2}\mu_{\text{sig}}\right)\right]^{2^k} \qquad \text{for } \bar{\alpha} \ll 1 \qquad (4.25)
\end{aligned}
$$

Figure 4.3 shows ϵ_{sig} as a function of $\log_2 n$ when a signal is perfectly isolated in a single bin under a binning consisting of $N = 2^{17}$ bins. In Figure 4.3(a) the ϵ_{bkg} is fixed at $\bar{\alpha} = 0.05$ and the signal strength is varied between $\mu_{\text{sig}} = 5$ and $\mu_{\text{sig}} = 30$. It clearly illustrates the importance of analysing the data in different representations (i.e. a different partitioning/binning). A partitioning that is either too exclusive or too inclusive can lead to even large localised signals going unnoticed.

In Figure 4.3(b) $\bar{\alpha}$ and hence the ϵ_{bkg} is varied over a wide range while the signal strength is constant at $\mu_{\text{sig}} = 6$ for the isolated signal. It illustrates that the choice for a larger $\bar{\alpha}$ has a rather limited effect on the sensitivity to a given signal. Only by analysing the data in the correct binning can the signal be detected.

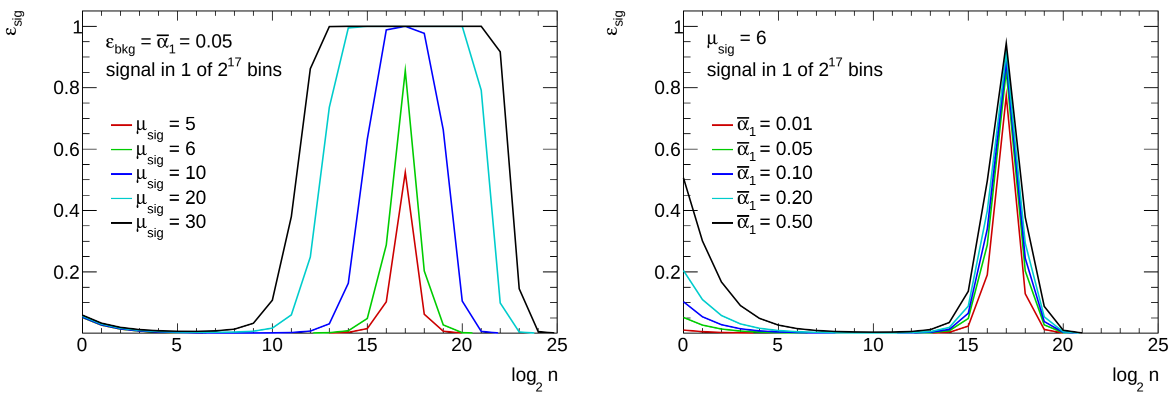

(a) (b)

Figure 4.3: Signal efficiency as a function of the number of bins (in $\log_2 n$) when a signal is perfectly isolated in a single bin under a binning consisting of $N = 2^{17}$ bins. Bins are then merged or partitioned further to create n bins increasing the background or diluting the signal. In (a) the background efficiency $\epsilon_{\text{bkg}} = \bar{\alpha}$ is fixed at 0.05 while μ_{sig} is varied, while in (b) $\bar{\alpha}$ is varied and $\mu_{\text{sig}} = 6$ for the isolated signal bin.

4.2.4 Case II: Independent tests with systematic uncertainties

As discussed in Section 4.2, the large number of tests, as well as the absence of assumptions on which regions are signal-free, make it impossible to implement background estimates using data-driven techniques. As a result, the initial tests performed in the DDSR method rely heavily on MC estimates of the SM processes. The main advantage of the DDSR method over the *global* method is that it provides an opportunity to define control and validation regions for a data-driven background estimate in the DDSR, or to improve the accuracy of the simulated MC samples after a DDSR is found. Such improvements can generally be expected to lead to a reduction of the systematic uncertainties, thereby improving the sensitivity. In this section it is shown that a DDSR method can potentially achieve a higher sensitivity to a given signal than the *global* method when the role of systematic uncertainties are taken into account.

The ϵ_{bkg} and ϵ_{sig} are determined using MC simulated toy experiments. To properly model correlated systematic effects, toy counting experiments can no longer be defined by simply drawing z_0-scores or p_0-values at random. Instead, a toy experiment is constructed by taking $n = 10^5$ counting experiments (bins) with an identical estimated background expectation of 100 event counts ($C_{\mathrm{SM}} = 100$) subject to two sources of systematic uncertainties, each 10% of the estimated background expectation ($\sigma_1 = \sigma_2 = 0.1 \cdot C_{\mathrm{SM}}$). The number of observed counts (C_{obs}) for each of the n bins is drawn at random as follows:

$$\theta_1 \sim \phi \tag{4.26}$$
$$\theta_2 \sim \phi \tag{4.27}$$
$$(C_{\mathrm{obs}})_1^i \sim \mathrm{Pois}(C_{\mathrm{SM}} + \theta_1\sigma_1 + \theta_2\sigma_2)) \quad \forall\, i \in \{1, \dots, n\} \tag{4.28}$$
$$(C_{\mathrm{obs}})_2^i \sim \mathrm{Pois}(C_{\mathrm{SM}} + \theta_1\sigma_1 + \theta_2\sigma_2)) \quad \forall\, i \in \{1, \dots, n\} \tag{4.29}$$

where ϕ is the standard normal pdf, σ_1 and σ_2 are the sizes of the systematic uncertainties, θ_1 and θ_2 are the randomized nuisance parameters of the corresponding systematic, $\mathrm{Pois}(\mu)$ is the Poisson probability mass function (pmf) with mean μ, and $(C_{\mathrm{obs}})_1^i$ and $(C_{\mathrm{obs}})_2^i$ are the observed counts in bin i for the equally-sized samples 1 and 2 respectively. The values for θ_1 and θ_2 are drawn only once for the set of n bins and both datasets and are therefore identical (correlated) among the two samples and bins.

In this simplified case all bins have the same estimated expectation value and uncertainty. However, in a generic case the expectation values and their uncertainties will differ per bin. The following test statistic (p) is a Poisson cdf convolved with a normal pdf to take the effects of non-negligible systematic uncertainties and statistical uncertainties into account:

$$\mathrm{p} = \int_0^\infty \mathrm{d}x\, \mathcal{N}(x \mid C_{\mathrm{SM}},\, \sigma_{\mathrm{SM}}^2) \cdot \sum_{c=C_{\mathrm{obs}}}^{\infty} \mathrm{Pois}(c \mid x) \tag{4.30}$$

where $\sigma_{\mathrm{SM}}^2 = \sigma_1^2 + \sigma_2^2$ is the total systematic uncertainty. For negligible systematic uncertainties $\mathcal{N}(x \mid C_{\mathrm{SM}},\, \sigma_{\mathrm{SM}}^2)$ approaches a Dirac delta function $\delta(x - C_{\mathrm{SM}})$ and p reduces to the p_0-value for a counting experiment with a known (true) background expectation ($C_{\mathrm{SM}}^{\mathrm{true}}$), given by the Poisson cdf: $p_0 = \sum_{c=C_{\mathrm{obs}}}^{\infty} \mathrm{Pois}(c \mid x = C_{\mathrm{SM}}^{\mathrm{true}})$. The test statistic p is thus the average (local) p_0-value for a counting experiment with a known background expectation x, weighted by $\mathcal{N}\left(x \mid C_{\mathrm{SM}},\, \sigma_{\mathrm{SM}}^2\right)$, where the latter is the posterior pdf of the likelihood function $L(x) = \mathcal{N}\left(C_{\mathrm{SM}} \mid x,\, \sigma_{\mathrm{SM}}^2\right)$ assuming a uniform prior probability for x. In the remainder p will be referred to as p_0 as it used as an estimate of the local p_0-value. Although this estimation of

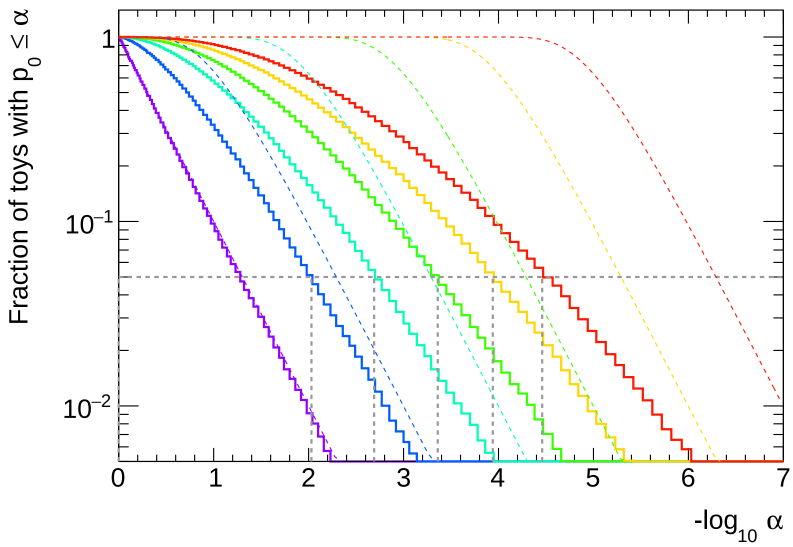

Figure 4.4: Fraction of toys having $p_0 \leq \alpha$ as a function of $-\log_{10}(\alpha)$. The solid curves are obtained using simulated toy experiments with $n = 1$, 10, 10^2, 10^3, 10^4, and 10^5, and systematic uncertainties correlated among all n bins. The dashed curves show the expected fractions in case of n independent tests. A horizontal dashed line is drawn at a fraction of 0.05 with vertical drop lines at the corresponding α values.

the p_0-value is Bayesian, it is only used as a test statistic for which the cdf is modelled (later on) in a frequentist manner using toy experiments. The routine used to numerically estimate a p_0-value for given C_{obs}, C_{SM} and σ_{SM} is denoted: $\mathrm{p}\left(C_{\mathrm{obs}}, C_{\mathrm{SM}}, \sigma_{\mathrm{SM}}\right)$

Since the tests are no longer independent due to the correlated systematic effects, the relation between $\bar{\alpha}$ and α is no longer given by Eq. 4.6 but needs to be determined using many toy experiments. Each toy experiment consists of n tests and follows Eqs. 4.26–4.29 randomizing the nuisance parameters for each new toy experiment. The fraction of toy experiments having at least one test with $p_0 \leq \alpha$ under H_0 gives a frequentist estimation of $\bar{\alpha}$ for each value of α. This numerical relation will be denoted $P_{\mathrm{exp}}(\alpha) = \bar{\alpha}$, and its inverse $\alpha = P_{\mathrm{exp}}^{-1}(\bar{\alpha})$.

$P_{\mathrm{exp}}(\alpha)$ values are plotted as solid lines in Figure 4.4 as a function of $-\log_{10}(\alpha)$ for $n = 1$, 10, 10^2, 10^3, 10^4, and 10^5. A horizontal dashed line is drawn at a fraction of 0.05 with vertical dashed lines at the corresponding $P_{\mathrm{exp}}^{-1}(0.05)$ values. Defining a DDSR if $p_0 \leq \alpha_1 \equiv P_{\mathrm{exp}}^{-1}(0.05)$ will then limit the probability of a false positive DDSR ($\bar{\alpha}_1$) to 0.05. E.g. for $n = 10^5$ (red curve) the $\alpha_1 = P_{\mathrm{exp}}^{-1}(0.05) = 10^{-4.46} = 3.47 \cdot 10^{-5}$. For reference, the dashed curves show the expected relation for independent tests obtained from Eq. 4.6.

The benchmark hypothesis H_1 injects a signal such that $p_0 \leq Q(5) = 2.87 \cdot 10^{-7}$, i.e. corresponding to a local 5σ excess:

$$\mathrm{p}\left(C_{\mathrm{SM}} + C_{\mathrm{sig}}, C_{\mathrm{SM}}, \sigma_{\mathrm{SM}}\right) \leq 2.87 \cdot 10^{-7} \tag{4.31}$$

where C_{sig} is the expected signal event count under H_1. Using the same values for C_{SM} and σ_{SM} as for the background-only bins, this is true if $C_{\mathrm{sig}} \geq 96$. For each toy the counts in the signal bin are therefore obtained from:

$$(C_{\text{obs}})_1^{\text{sig}} \sim \text{Pois}\left(C_{\text{SM}} + \theta_1\sigma_1 + \theta_2\sigma_2 + C_{\text{sig}}\right)$$
$$(C_{\text{obs}})_2^{\text{sig}} \sim \text{Pois}\left(C_{\text{SM}} + \theta_1\sigma_1 + \theta_2\sigma_2 + C_{\text{sig}}\right) \tag{4.32}$$

using the same expectation values and systematic shifts as for the background-only cases and $C_{\text{sig}} = 96$.

The test statistic for the *global* method using the combined dataset is computed as:

$$p_0 = \mathtt{p}\left((C_{\text{obs}})_1 + (C_{\text{obs}})_2,\ 2C_{\text{SM}},\ 2\sigma_{\text{SM}}\right) \tag{4.33}$$

where the linear addition of σ_{SM} is due to the fully correlated systematics between the datasets.

For the DDSR method the p_0-values from the initial tests on the first sample are computed as:

$$p_{0_1} = \mathtt{p}\left((C_{\text{obs}})_1,\ C_{\text{SM}},\ \sigma_{\text{SM}}\right) \tag{4.34}$$

A DDSR is defined if a bin has a $p_{0_1} \leq 3.47 \cdot 10^{-5}$ and it is tested using the second sample. To illustrate the potential of a DDSR method it is assumed that the concentration of the analysis resources and efforts leads to the ability to constrain one of the two systematic shifts (e.g. $\theta_1\sigma_1$) with the use of, for instance, an auxiliary measurement. The p_0-value using the second sample is therefore computed as:

$$p_{0_2} = \mathtt{p}\left((C_{\text{obs}})_2,\ C_{\text{SM}} + \theta_1\sigma_1,\ \sigma_2 \cdot \frac{C_{\text{SM}} + \theta_1\sigma_1}{C_{\text{SM}}}\right) \tag{4.35}$$

where the expectation value is corrected with the systematic shift $\theta_1\sigma_1$ (measured in an auxiliary measurement) and the total systematic uncertainty is reduced by the elimination of σ_1. Since σ_2 is defined relative to the expectation value it is also corrected for the systematic shift.

Figure 4.5 shows ϵ_{bkg} versus ϵ_{sig} for the *global* method (red) and for the DDSR method when one of the systematic uncertainties is constrained and p_{0_2} is computed using Eq. 4.35 (green). For reference, the blue curve shows the ROC curve when no systematics are constrained and p_{0_2} is computed in a similar way as p_{0_1}. It demonstrates that the DDSR method has the potential to improve the sensitivity over the *global* method if systematic uncertainties can be (partially) constrained. Since this is one of the main objectives in any analysis effort, such an assumption is not unrealistic.

4.3 Analysis steps

This section will briefly describe the analysis steps and implementation of the search strategy for application to the data collected by the ATLAS experiment.

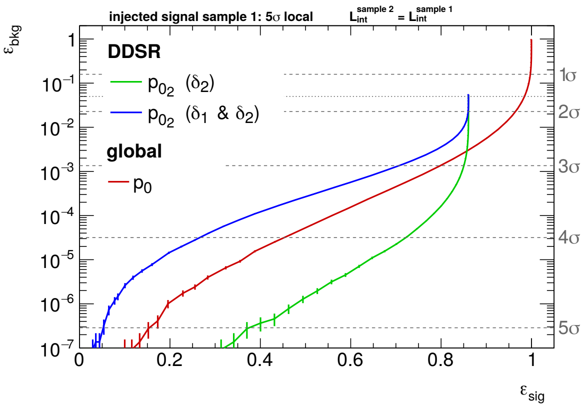

(a)

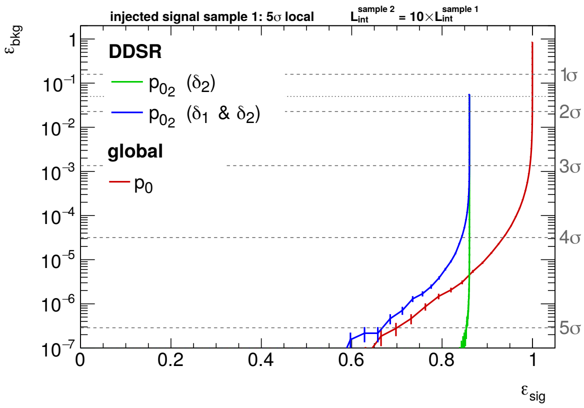

(b)

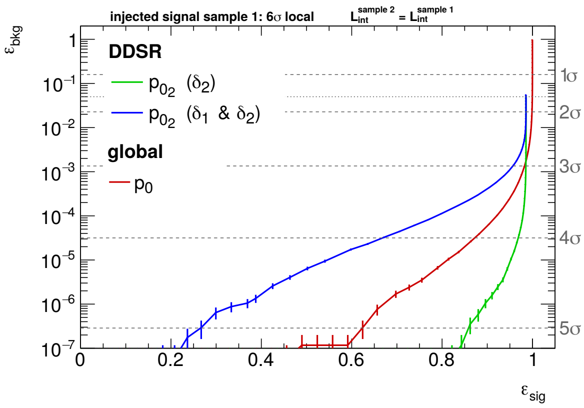

(c)

Figure 4.5: ROC curves for three different scenarios comparing the DDSR method (green and blue) with the *global* method (red) after introducing two sources of systematic uncertainty. Constraining one systematic uncertainty after a DDSR has been defined results in the green curve, while the blue curve is obtained when the systematic uncertainties remain unchanged. In scenario (a) and (b) a local 5σ-signal (per $L_{\text{int}}^{\text{sample 1}}$) is introduced, however in scenario (b) sample 2 is ten times the size of sample 1. In scenario (c) the sample sizes are equal but a 6σ-signal is injected. The signal and background efficiencies are estimated using MC simulated toys and the statistical uncertainty is indicated with error bars. The dashed lines show the corresponding global significances. The $\bar{\alpha}_1$ is set to 0.05 and the number of bins n is set to 10^5. A dotted line is drawn at $\epsilon_{\text{bkg}} = 0.05$.

4.3.1 Data selection and Monte Carlo simulation

The recorded data are reconstructed via the ATLAS software chain. Events are selected by applying event-quality criteria and object-based reconstruction-level/trigger criteria. Objects that can be considered in the selection (and classification later on) are those typically used to characterize hadron collisions such as electrons, muons, τ-leptons, photons, jets, b-tagged jets and missing transverse momentum. More complex objects, such as resonances reconstructed by a specific decay (e.g. Z or Higgs bosons decaying into two or four isolated leptons respectively, or decaying hadronically and giving rise to large-radius jets with substructure) and displaced vertices, can also be considered.

MC simulations are used to estimate the expected event counts from SM processes. To allow the investigation of signal regions with a low number of expected event counts it is important that the equivalent integrated luminosity of the MC samples significantly exceeds that of the data, and that all relevant background processes are included, in particular rare processes which might dominate certain multi-object event classes.

4.3.2 Validation

To verify the modelling of the SM background processes, several validation distributions are defined using inclusive selections for which observable signals for new physics are excluded or are expected to be small. Any discrepancies between experimental data and MC simulated expectations revealed in the validation distributions, that can be identified as known or understood MC modelling issues, are addressed either by correcting the background modelling whenever possible, or else by excluding the event class from the analysis.

Systematic uncertainties in the background estimate arise from experimental effects, and from the finite theoretical accuracy of the predicted (differential) cross-section and acceptance of the MC simulation. Their effect is evaluated for all contributing background processes and benchmark signals.

4.3.3 Classification

All selected data and MC events are classified according to the type and multiplicity of reconstructed objects defined in the analysis. After classification, all event classes having $C_{\text{SM}} > 0.1$ or $C_{\text{obs}} > 0$ are considered for analysis.

A search algorithm is applied to the subset of events classes having $C_{\text{SM}} > 0.1$. This condition ensures a finite and fixed number of event classes determined by the background model as is required for the interpretation using pseudo-experiments (toys).

For the remaining event classes, those having at least one observed event but $C_{\text{SM}} \leq 0.1$, the observed number of events is monitored and the observation of four or more events qualifies the event class as a DDSR candidate. This avoids the possibility of missing a signal in an (almost) background-free region.

4.3.4 Sensitive observables and search algorithm

Distributions of observables in the form of histograms are investigated using a search algorithm (*scanned*) for all event classes with $C_{\text{SM}} > 0.1$. Several observables are included that have a high sensitivity to a wide range of known BSM signals. Examples of such observables are:

- the effective mass (m_{eff}), defined as the scalar sum of the transverse momenta of all objects plus the magnitude of the missing transverse momentum ($E_{\text{T}}^{\text{miss}}$);
- the total invariant mass (m_{inv}), defined as the invariant mass of all visible objects;
- H_{T}, defined as the scalar sum of the transverse momenta of all visible objects;
- $E_{\text{T}}^{\text{miss}}$, etc.

Since $\bar{\alpha}_1$ is limited per observable, care must be taken not to include too many observables, as this will introduce a second LEE, i.e. it will increase the probability of finding at least one DDSR among the different observables scanned in the absence of a signal. However, the results of the scan algorithm are statistically correlated among the different observables as they use the same dataset, so the increase in this probability is far less than a naive estimation assuming independent results per observable would suggest.

A search algorithm is used to scan the distributions of each event class and quantify the deviations of the data from the SM expectation. The algorithm used in this work systematically performs tests for all of the individual bins and all possible combinations of contiguous bins in a histogram, also referred to as *regions*[5]. A routine similar to the one used in Section 4.2.4 is used to estimate the local p_0-value. If only excesses are considered the one-sided p_0 is estimated using Eq. 4.30. If deficits are considered as well, the two-sided p_0 is estimated as[6]:

$$p_0 = 2 \cdot \min\Big[\Pr\left(c \leq C_{\text{obs}}\right),\, \Pr\left(c \geq C_{\text{obs}}\right)\Big] \tag{4.36}$$

$$\Pr\left(c \leq C_{\text{obs}}\right) = \int_0^{\infty} \mathrm{d}x\, \mathcal{N}(x \mid C_{\text{SM}},\, \sigma_{\text{SM}}^2) \cdot \sum_{c=0}^{C_{\text{obs}}} \text{Pois}(c \mid x) + \int_{-\infty}^{0} \mathrm{d}x\, \mathcal{N}(x \mid C_{\text{SM}},\, \sigma_{\text{SM}}^2) \tag{4.37}$$

$$\Pr\left(c \geq C_{\text{obs}}\right) = \int_0^{\infty} \mathrm{d}x\, \mathcal{N}(x \mid C_{\text{SM}},\, \sigma_{\text{SM}}^2) \cdot \sum_{c=C_{\text{obs}}}^{\infty} \text{Pois}(c \mid x) \tag{4.38}$$

The region with the largest deviation identified by the search algorithm is defined as the selection giving the smallest p_0-value. The smallest p_0 among all regions in a histogram is defined as p_{class}, which therefore corresponds to the local p_0-value of the largest deviation in that event class. The result of scanning the distributions of all event classes is therefore a list of regions, one per event class containing the largest deviation in that class, and their local p_0-value defined as p_{class}. The p_{class}-value is the test statistic used for determining if a regions qualifies as a DDSR. To this end, the cumulative distribution of p_{class}-values under H_0 needs to be determined using pseudo-experiments as explained in the next section.

[5] A histogram of n bins has 1 region of n contiguous bins, 2 regions of $n-1$ contiguous bins, etc. down to n regions of single bins. Therefore, it has $\sum_{i=1}^{n} i = n(n+1)/2$ regions.

[6] The second term in Eq. (4.37) gives the probability of observing no events given a negative expectation from downward variations of the systematic uncertainties. It can be derived as follows:

$$\int_{-\infty}^{0} \mathrm{d}x\, \mathcal{N}(x \mid C_{\text{SM}},\, \sigma_{\text{SM}}^2) \cdot \sum_{c=0}^{C_{\text{obs}}} \lim_{\mu \to 0} \left(\frac{\mathrm{e}^{-\mu}\mu^c}{c!}\right) = \int_{-\infty}^{0} \mathrm{d}x\, \mathcal{N}(x \mid C_{\text{SM}},\, \sigma_{\text{SM}}^2) \cdot \sum_{c=0}^{C_{\text{obs}}} \delta_{c0} = \int_{-\infty}^{0} \mathrm{d}x\, \mathcal{N}(x \mid C_{\text{SM}},\, \sigma_{\text{SM}}^2)$$

where μ is the mean of the Poisson pmf and $\delta_{c0} = \{1 \text{ if } c = 0,\ 0 \text{ if } c \neq 0\}$ is the Kronecker delta. In Eq. (4.38) this term vanishes for $C_{\text{obs}} > 0$.

4.3.5 Generation of pseudo-experiments

The probability that for a given observable one or more deviations of a certain size occur, somewhere in the event classes considered, is modelled by pseudo-experiments (toys). Each pseudo-experiment consists of exactly the same event classes as those considered when applying the search algorithm to data, i.e. having $C_{\text{SM}} > 0.1$. However, the data counts are replaced by pseudo-data counts. These pseudo-data distributions are generated by drawing pseudo-random data counts for each bin taking into account both statistical and systematic uncertainties.

Correlations in the uncertainties of the SM expectation between different regions and event classes affect the chance of observing one or more deviations of a given size. The effect of correlations between regions of the same distribution and between distributions of different event classes are therefore taken into account when generating pseudo-data by randomizing the nuisance parameters for each systematic per pseudo-experiment, such that for each pseudo-experiment:

$$\theta_k \leftarrow \phi \quad \forall\, k \in \{1, \ldots, N_{\text{NP}}\} \tag{4.39}$$

$$C^i_{\text{PD}} \leftarrow \text{Pois}(C^i_{\text{SM}} + \sum_{k=1}^{N_{\text{NP}}} \theta_k \sigma^i_k) \quad \forall\, i \in \{1, \ldots, n\} \tag{4.40}$$

where θ_k is the value of the k^{th} nuisance parameter, N_{NP} is the total number of nuisance parameters in the background model, C^i_{PD} are the pseudo-data counts in bin i, σ^i_k is the size of the k^{th} systematic uncertainty in bin i, and n is the total number of bins in *all* histograms of a given observable. Correlations between distributions of different observables arise from both correlated nuisance parameters and statistical correlations in different representations of the same data. These are not taken into account and the results obtained for different observables are therefore not combined in the interpretation.

The search algorithm is applied to each of the pseudo-data distributions, resulting in a single p_{class}-value for each event class. The p_{class} distributions of a large number of pseudo-experiments and their statistical properties can be compared with the p_{class} distribution obtained from experimental data to interpret the p_{class} test statistic in a frequentist manner. The cumulative distribution, i.e. the fraction of toys having $p_{\text{class}} \leq p_{\text{min}}$ as a function of $-\log_{10}(p_{\text{min}})$[7], is similar to Figure 4.4 and is used to determine the DDSR threshold such that $\bar{\alpha}_1$ is limited per observable scanned. In addition to determining the probability that one p_{class}-value is below a given threshold value, the probability that two or three p_{class}-values in a scan are below a given threshold is also determined.

To illustrate this, Figure 4.6 shows these three cumulative distributions of p_{class}-values from pseudo-experiments. The background model and total number of event classes on which the generation of pseudo-experiments for this scan of the m_{eff} distributions is based, are taken from the analysis in Chapter 5. The blue, red and green curves in Figure 4.6 show the fractions of pseudo-experiments with at least one, two, and three p_{class}-value smaller than p_{min} respectively. For example, about 30% of the pseudo-experiments have at least one p_{class}-value smaller than $p_{\text{min}} = 10^{-4}$. The estimated probability ($P_{\text{exp},i}$) of obtaining one or more p_{class}-values ($i = 1$) smaller than 10^{-4} from experimental data in the absence of a signal is therefore

[7] Here p_{min} is the critical value for p_{class}, or DDSR threshold, and the critical region is $p_{\text{class}} \leq p_{\text{min}}$. Since p_{class} is the *minimum* p_0 of an event class, it is not itself a p_0. Hence the different nomenclature of p_{min} instead of α_1.

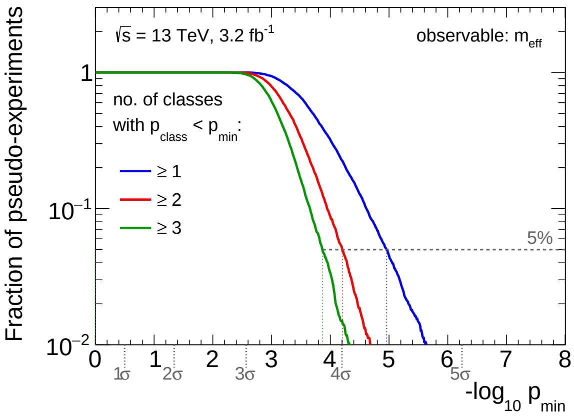

Figure 4.6: The fractions of pseudo-experiments ($P_{\mathrm{exp},i}(p_{\mathrm{min}})$) in the m_{eff} scan, which have at least one, two or three p_{class}-values smaller than a given threshold (p_{min}). Pseudo-datasets are generated from the SM expectation. Dotted lines are drawn at $P_{\mathrm{exp},i} = 5\%$ and at the corresponding $-\log_{10}(p_{\mathrm{min}})$-values.

about 30%, i.e. $P_{\mathrm{exp},1}(10^{-4}) = 0.30$. Similarly, it follows that e.g. 3% of the pseudo-experiments have at least three p_{class}-values smaller than 10^{-4}. Consequently, the probability of obtaining a third smallest p_{class}-value smaller than 10^{-4} from data in the absence of a signal is about 3%, or $P_{\mathrm{exp},3}(10^{-4}) = 0.03$.

In Figure 4.6 a horizontal dotted line is drawn at a fraction of pseudo-experiments of 5% and vertical dotted lines are drawn at the three corresponding p_{min}-thresholds. The observation of one, two or three p_{class}-values from data below the corresponding p_{min}-threshold, i.e. an observation with a $P_{\mathrm{exp},i} < 0.05$, promotes the regions to a DDSR.

4.3.6 Evaluation of the sensitivity

The sensitivity of the procedure for the general case that H_0 is false, i.e. an unspecified signal is present in the data, cannot be determined. However, as in Section 4.2, the sensitivity can be evaluated with respect to an H_1 that completely specifies the signal. Two different methods are distinguished, one uses a modified background model through the removal of SM processes, the other adds the signal contributions expected under H_1 to the pseudo-data sample.

The first method removes a rare SM process (i.e. having a low cross-section or a low reconstruction efficiency) from the background model. The search algorithm is applied to *signal* pseudo-experiments testing pseudo-data generated from the unmodified SM expectation (H_1), against the modified/incomplete background expectation (H_0). The search algorithm is thus expected to find excesses relative to the modified background prediction.

The second method uses pseudo-experiments to test the sensitivity of the analysis to benchmark signal models of new physics. The prediction of a BSM process is added to the SM prediction (H_1) and this modified expectation is used to generate the pseudo-data for the *signal* pseudo-experiments. The search algorithm, using the nominal SM background model (H_0), is again applied to the pseudo-experiments and the distribution of p_{class}-values is derived and studied.

To provide a figure of merit for the sensitivity of the analysis, the fraction of *signal* pseudo-experiments with $P_{\mathrm{exp},i} < 5\%$ for $i = 1, 2, 3$ is computed.

4.3.7 Results

Finding one or more deviations in the data with $P_{\text{exp},i} < 5\%$ defines a DDSR candidate and initiates the construction of a dedicated analysis that uses the DDSR candidate as its signal region.

If, on the other hand, no significant deviations are found (i.e. $P_{\text{exp},i} > 5\%$ for $i = 1, 2, 3$), the outcome of this analysis technique includes information such as: the number of events and expectation per event class, a comparison of the experimental data to the simulated SM expectation in the distributions of the observables considered, the scan results (i.e. the location and the local p_0-value of the largest deviation per event class) and the comparison with the expectation from pseudo-experiments.

4.3.8 Initiating a dedicated (re-)analysis of a DDSR candidate

Dedicated re-analysis of DDSR candidate using the original dataset If one or more DDSR candidates are found, the deviations are evaluated using methods similar to those of a conventional analysis. In particular, the background prediction is determined using background-enriched control selections to control and validate the background modelling whenever possible, or using other data-driven methods. Such procedures further constrain the background expectation and uncertainty, and reduce the dependence on simulation. If the re-analysis of the DDSR candidate results in an insignificant deviation, it can be inferred that the deviation seen before was due to imperfect MC modelling of the backgrounds.

Dedicated analysis of DDSR using an independent dataset If a deviation persists in the dedicated re-analysis using the original dataset, the data selection in which the deviation is observed defines a DDSR that is tested using an independent (new) dataset with a similar or larger integrated luminosity. At this point, an appropriate model of new physics that predicts a signal in the DDSR can be used to further optimise the analysis and interpret the DDSR test result. Other effects from assumptions, such as Gaussian uncertainties on the background expectations, can also be studied. Because the signal region is known, the corresponding experimental data selection can be excluded ('blinded') from the analysis until the very end to minimize any possible bias in the analysis. Since only one or a few optimized hypothesis tests are performed on the independent dataset, the result of the dedicated analysis of the DDSR is no longer subject to a large LEE as discussed in Section 4.2.

If a DDSR is found with the full High-Luminosity LHC (HL-LHC) dataset, the data-taking period of the HL-LHC may need to be extended, or the deviation may have to be followed up at a future collider.

4.4 Advantages and disadvantages

The proposed strategy has several advantages and disadvantages which are outlined below.

Advantages

- It can find unexpected signals for new physics due to the large number of event classes and phase-space regions probed, which may otherwise remain uninvestigated.
- A relatively small deviation in two or three independent regions, each of which is not large enough to qualify that region as a DDSR candidate by itself ($P_{\text{exp},1} > 5\%$), can qualify as a combination ($P_{\text{exp},2/3} < 5\%$).
- The approach is broad, and the scanned distributions can be used to probe the overall description of the experimental data by the event generators for many SM processes.
- The DDSRs approach optimizes the resources needed to perform the search and can lead to a more powerful procedure overall than the statistically favoured *global* method.
- The probability of a deviation occurring in *any* of the many different event classes under study can be determined with pseudo-experiments, resulting in a truly global interpretation of the probability of finding a deviation in a studied observable within an experiment such as ATLAS.

Disadvantages

- The outcome depends on the MC-based description of physics processes and simulations of the detector response. Event classes in which the majority of the events contain misreconstructed objects are typically poorly modelled by MC simulation and might need to be excluded from the analysis. Even though the description of the data by the MC simulation is validated, there is a possibility of false positives due to an imperfect MC modelling of a corner of phase space. The strategy aims to minimize this by reducing the dependence on pure MC predictions in a dedicated re-analysis which is performed for each DDSR candidate found.
- As this analysis is not optimized for a specific (class of) BSM signal(s), a dedicated analysis optimized for a given BSM signal achieves a larger sensitivity to that signal. The enormous parameter space of possible signals, however, makes an optimized search for each of them impossible.
- The large number of data selections introduce a large LEE, which reduces the significance of a real signal. Small signals might be missed if they do not produce a deviation large enough to qualify the region as DDSR candidate.
- Despite being broad, the procedure might miss a certain signal because it does not show a localized excess in one of the studied distributions. This can depend on the choices made for event partitioning, observables and scan algorithm, where different choices can bring sensitivity to different signals.
- It can be technically challenging to achieve the broad scope permitted by this approach as it requires the simulation of MC samples for many different SM processes over a wide range of phase-space, and because this approach does not align with the Run 2 analysis model adopted by the ATLAS experiment in which analysis data is provided in derived formats (i.e. formats in which reconstructed physics objects or events are removed) in order to work within the constraints posed by limitations on computing resources.

5 Application to the 2015 dataset

This chapter describes the application of the search strategy, outlined in the previous chapter, to the 2015 ATLAS dataset. The analysis presented in this chapter is an upgraded version of an early analysis of the 2015 dataset that was used as an example in Ref. [11] which describes the method and search strategy. Several improvements have been made to the analysis described in this chapter in preparation of the application to the combined 2015 & 2016 dataset which is detailed in Chapter 6. The changes and their effects are detailed in Appendix B.

5.1 Data selection

5.1.1 Dataset

The data used in this chapter were collected by the ATLAS detector during 2015 in pp collisions at the LHC with a centre-of-mass energy of 13 TeV and a 25 ns bunch crossing interval. After applying quality criteria for the beam, data and detector, the available dataset corresponds to an integrated luminosity of 3.2 fb^{-1}.

In this dataset, each event includes an average of approximately 14 inelastic pp collisions in the same bunch crossing (pile-up).

All candidate events are required to have a reconstructed vertex [143], with at least two associated tracks with $p_{\mathrm{T}} > 400$ MeV. The vertex with the highest sum of squared transverse momenta of the tracks is considered to be the primary vertex.

5.1.2 Definition of objects

Reconstructed physics objects considered in the analysis are:

- prompt and isolated electrons (e),
- prompt and isolated muons (μ)
- prompt and isolated photons (γ),
- b-jets (b),
- light (non-b-tagged) jets (j),
- and large missing transverse momentum ($E_{\mathrm{T}}^{\mathrm{miss}}$).

Table 5.1 lists the reconstructed physics objects along with their p_{T} and pseudorapidity requirements. Since jets and electrons misidentified as hadronically decaying τ-leptons are difficult to model with the MC-based approach being used in this analysis, the identification of hadronically decaying τ-leptons is not considered; they are mostly reconstructed as light jets.

Table 5.1: Physics objects used for classifying events, with their corresponding label, minimum p_T requirement, and pseudorapidity requirement.

Object	Label	p_T (min) [GeV]	Pseudorapidity
Isolated electron	e	25	$\|\eta\| < 1.37$ or $1.52 < \|\eta\| < 2.47$
Isolated muon	μ	25	$\|\eta\| < 2.70$
Isolated photon	γ	50	$\|\eta\| < 1.37$ or $1.52 < \|\eta\| < 2.37$
b-tagged jet	b	60	$\|\eta\| < 2.50$
Light (non-b-tagged) jet	j	60	$\|\eta\| < 2.80$
Missing transverse momentum	E_T^{miss}	200	

Leptons *Baseline electron* candidates are required to have $|\eta| < 2.47$, a $p_T > 10$ GeV, and to pass the *Loose* likelihood-based identification requirement (see Section 3.2). Candidates within the transition region between the barrel and endcap electromagnetic calorimeters, $1.37 < |\eta| < 1.52$, are removed.

Baseline muon candidates are reconstructed in the region $|\eta| < 2.7$, are required to have a $p_T > 10$ GeV and to pass the *Medium* identification requirement (see Section 3.3).

The track associated with a candidate electron or muon must have a longitudinal impact parameter (z_0) relative to the reconstructed primary vertex, satisfying $|z_0 \cdot \sin\theta| < 0.5$ mm.

Since particle and jet hypothesis can be applied to the same detector signals, overlap must be resolved to avoid double counting the same signals as different objects. All baseline leptons (electrons and muons) are used in the following object overlap removal procedure: If an electron and a muon share the same ID track, the electron is removed. Any jet within a distance $\Delta R_y = 0.2$ of an electron candidate is discarded, unless the jet has a value of the b-tagging MV2C20 discriminant [154, 155] larger than that corresponding to approximately 85% b-tagging efficiency, in which case the electron is discarded since it probably originated from a semileptonic b-hadron decay. Any remaining electron within $\Delta R_y = 0.4$ of a jet is discarded. Muons within $\Delta R_y = 0.4$ of a (b-)jet are also removed. However, if the jet has fewer than three associated tracks, the muon is kept and the jet is discarded instead to avoid inefficiencies for high-energy muons undergoing significant energy loss in the calorimeter.

After the overlap removal, tighter requirements are imposed on the lepton candidates, which are then referred to as *signal electrons* or *signal muons*. These objects are used in the analysis for event selection and classification, and in the computation of observables. Signal electrons must satisfy a *Tight* likelihood-based identification requirement. Signal muons (electrons) are selected if the matched tracks have a transverse impact parameter significance relative to the reconstructed primary vertex of $|d_0|/\sigma(d_0) < 5$ (3). Both signal electrons and muons are required to have $p_T > 25$ GeV. Isolation requirements targeting E_T-dependent efficiencies are applied to both the signal electrons and muons. The efficiency of these criteria increases with the lepton transverse momentum, reaching 95% at 25 GeV and 99% at 60 GeV, as determined in a control sample of Z decays into leptons selected with a tag-and-probe technique [144, 145]. Corrections are applied to the MC samples to match the lepton's trigger, reconstruction and isolation efficiencies in data.

Photons *Baseline photon* candidates are required to satisfy the *Tight* identification criteria (see Section 3.4). Furthermore, baseline photons are required to have $p_T > 25$ GeV and $|\eta| < 2.37$, excluding the barrel–endcap calorimeter transition in the range $1.37 < |\eta| < 1.52$.

Signal photons must additionally have a $p_{\mathrm{T}} > 50$ GeV and satisfy isolation criteria based on both track and calorimeter information. After correcting for contributions from pile-up, these criteria are $E_{\mathrm{T}}^{\mathrm{cone0.4}} < 2.45\ \mathrm{GeV} + 0.022 \cdot p_{\mathrm{T}}(\gamma)$ and $p_{\mathrm{T}}^{\mathrm{cone0.2}} / p_{\mathrm{T}}(\gamma) < 0.05$, where $p_{\mathrm{T}}(\gamma)$ is the transverse momentum of the photon candidate.

Overlap between baseline photons and other objects is resolved using the following procedure: If a baseline photon is found within $\Delta R_y = 0.4$ of a jet, the jet is discarded. Baseline photons within a cone of size $\Delta R_y = 0.4$ around a baseline electron or muon candidate are discarded.

Jets *Baseline jet* candidates are reconstructed as described in Section 3.5 using the anti-k_t algorithm [149] with a radius parameter of $R = 0.4$. Quality criteria are imposed to identify jets arising from non-collision sources or detector noise and any event containing such a jet is removed [157]. Baseline jet candidates are required to have $p_{\mathrm{T}} > 20$ GeV and $|\eta| < 2.8$.

Signal jets are required to have $p_{\mathrm{T}} > 60$ GeV and any event in which the signal jet with the highest p_{T} fails tighter quality criteria against non-collision backgrounds is removed.

***b*-tagged jets** The identification of jets containing b-hadrons (b-tagging) is performed with the MV2C20 multivariate discriminant, using a working point corresponding to a 77% average efficiency obtained for b-jets in simulated $t\bar{t}$ events. Baseline jets with $|\eta| < 2.5$ which satisfy this b-tagging requirement are identified as b-jet candidates.

Signal b-jets, like signal jets, are required to have $p_{\mathrm{T}} > 60$ GeV and meet tighter quality criteria against non-collision backgrounds.

Missing transverse momentum The missing transverse momentum vector (with magnitude $E_{\mathrm{T}}^{\mathrm{miss}}$) is computed for each event using all aforementioned selected and calibrated baseline physics objects as detailed in Section 3.6.1.

5.1.3 Definition of event classes

Events are divided into mutually exclusive classes that are labelled with the number and type of reconstructed objects listed in Table 5.1. Events with $E_{\mathrm{T}}^{\mathrm{miss}} > 200$ GeV enter separate event classes with a label bearing the prefix '$E_{\mathrm{T}}^{\mathrm{miss}}$'. Ergo, event classes without the $E_{\mathrm{T}}^{\mathrm{miss}}$-prefix contain only events with $E_{\mathrm{T}}^{\mathrm{miss}} < 200$ GeV. The classification includes all final-state configurations and object multiplicities, e.g. an event with seven reconstructed muons (and no other objects) enters a *seven muon* event class (7μ). Similarly an event with $E_{\mathrm{T}}^{\mathrm{miss}} > 200$ GeV, two muons, one photon and four jets enters the corresponding event class denoted $E_{\mathrm{T}}^{\mathrm{miss}}\ 2\mu\ 1\gamma\ 4j$.

5.1.4 Triggers and event selection

Triggers All events contributing to a particular event class are required to be selected by a trigger from a corresponding class of triggers by imposing a hierarchy in the event selection. This avoids ambiguities in the application of trigger efficiency corrections to MC simulations and avoids variations in the acceptance within an event class. The flow diagram in Figure 5.1 gives a graphical representation of the trigger and offline event selection, based on the class of the event. Since the thresholds of the single-photon and single-jet triggers are higher than the p_{T} requirements in the photon and jet object selection, an additional reconstruction-level p_{T} cut is imposed to avoid trigger inefficiencies. For the other triggers, the p_{T} requirements in the object definitions exceed the trigger thresholds by a sufficient margin to avoid additional trigger inefficiencies.

Events with $E_{\mathrm{T}}^{\mathrm{miss}} > 200$ GeV can, in addition to the selection procedure following below for events with $E_{\mathrm{T}}^{\mathrm{miss}} < 200$ GeV, be selected by the $E_{\mathrm{T}}^{\mathrm{miss}}$ trigger. If the event contains a signal electron (muon) it is required to pass the single-electron (single-muon) trigger. However, events with an additional signal electron or muon can also be selected by the dielectron, dimuon or electron-muon trigger, to reduce possible inefficiencies in the single-electron and single-muon triggers. If the event has one or more leptons (electrons or muons) but fails all lepton triggers and the $E_{\mathrm{T}}^{\mathrm{miss}}$ trigger, it is discarded and not considered for further analysis. Remaining events with a signal photon with $p_{\mathrm{T}} > 140$ GeV or two signal photons are required to pass the single-photon or diphoton trigger respectively, otherwise, they are discarded. Finally, any remaining events with no leptons or photons but containing a signal jet with $p_{\mathrm{T}} > 500$ GeV is required to pass the single-jet trigger.

Derivation Ideally, the acceptance of this analysis would only be limited by the trigger bandwidth and therefore be entirely summarized by Figure 5.1. However, the ATLAS Run 2 analysis model is based on *derivations*[1] that do not support such a large event acceptance. The acceptance is therefore limited by the derivation selection cuts. The events that are subject to additional cuts are marked in Figure 5.1 as 'Accepted*'. For event classes with $1\mu + X$, $1e + X$ and $1\mu 1e + X$, where X can be photons or jets, an additional reconstruction-level cut is applied requiring at least one of the following conditions:

- a scalar sum of p_{T} of all signal (b-)jets (H_{T}(jets)) exceeding 150 GeV
- a lepton (e/μ) with $p_{\mathrm{T}} > 100$ GeV

Event classes with $E_{\mathrm{T}}^{\mathrm{miss}} > 200$ GeV have no additional reconstruction-level cuts, but a small fraction of events might be rejected by derivation cuts. The full selection requirements per event class are discussed in Appendix C.

Quality cuts To suppress sources of fake $E_{\mathrm{T}}^{\mathrm{miss}}$, additional requirements are imposed on events classified in $E_{\mathrm{T}}^{\mathrm{miss}}$ plus photons and/or jets categories. The ratio of $E_{\mathrm{T}}^{\mathrm{miss}}$ to m_{eff} is required to be greater than 0.2, and the minimum azimuthal separation between the $E_{\mathrm{T}}^{\mathrm{miss}}$ direction and the three leading reconstructed signal jets (if present) has to be greater than 0.4, otherwise, the event is rejected. For events having two same-flavour leptons, the dilepton mass is required to be larger than 40 GeV to remove contamination from low mass resonances that are not included in the background model. Table 5.2 summarizes these additional selection requirements and lists the relevant event classes.

[1] A derivation is a subset of the total dataset, collected by the ATLAS detector for physics analysis, in order to reduce disk space requirements. Typically, the size is reduced by applying selection cuts that remove events outside of the acceptance of the targeted analyses as well as removing certain object reconstruction information not required by those analyses.

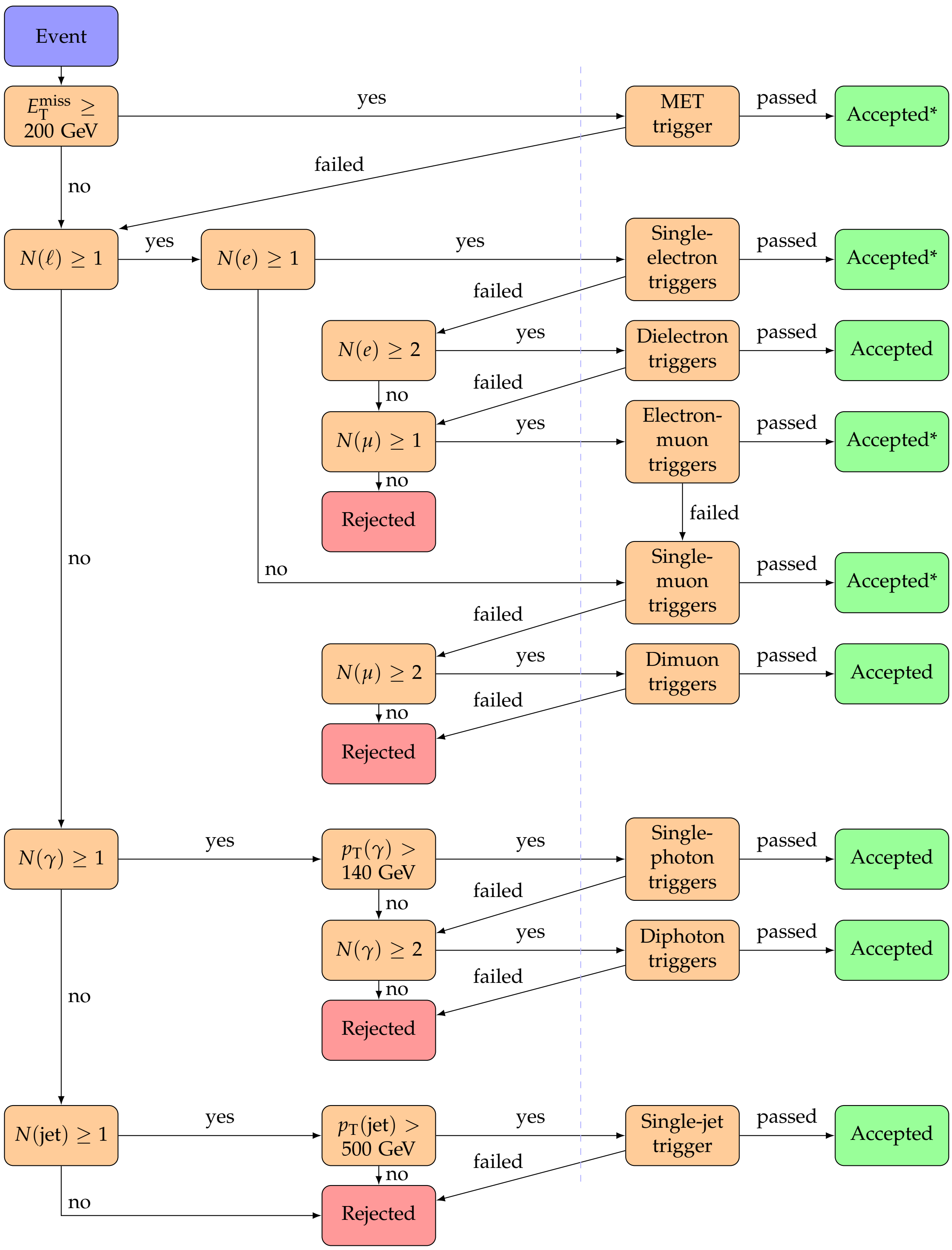

Figure 5.1: Flow diagram of the trigger and offline event selection strategy. The offline requirements are shown on the left of the dashed line and the trigger requirements are shown on the right of the dashed line. N is the object multiplicity of the object between brackets, ℓ stands for e or μ, and 'jet' for b or j as defined in Table 5.1. Events accepted by a box marked with an asterisk (*) can be subject to additional cuts which are discussed in detail in Appendix C.

Table 5.2: Additional selection requirements imposed on events passing the previous selection requirements. All relevant event classes are listed using $(X\gamma)$, (Xb) and (Xj) to denote zero or more photons, b-jets and jets respectively.

Events with	Requirements	Relevant event classes	
$E_{\mathrm{T}}^{\mathrm{miss}} \geq 200$ GeV and no leptons	$E_{\mathrm{T}}^{\mathrm{miss}} / m_{\mathrm{eff}} \geq 0.2$ and $\Delta\phi\left(E_{\mathrm{T}}^{\mathrm{miss}},\, \mathrm{jet}_{1,2,3}\right) \geq 0.4$	$E_{\mathrm{T}}^{\mathrm{miss}}\, (X\gamma)\, (Xb)\, (Xj)$	
2 electrons or 2 muons	$m_{\mathrm{inv}}(ll) \geq 40$ GeV	$E_{\mathrm{T}}^{\mathrm{miss}}\, 2e\, (X\gamma)\, (Xb)\, (Xj)$ $E_{\mathrm{T}}^{\mathrm{miss}}\, 2\mu\, (X\gamma)\, (Xb)\, (Xj)$	$2e\, (X\gamma)\, (Xb)\, (Xj)$ $2\mu\, (X\gamma)\, (Xb)\, (Xj)$

5.2 Monte Carlo simulation

5.2.1 Monte Carlo samples for Standard Model processes

MC simulated event samples [129] are used to describe SM background processes and to model possible signals. The ATLAS detector is simulated by a software system based on GEANT4 [132] or by a faster simulation method based on a parametrization of the calorimeter response and GEANT4 for the other detector systems. The impact of detector conditions on the simulation is typically corrected for as part of the calibrations and scale factors applied to the reconstructed objects.

To account for additional pp interactions from the same or nearby bunch crossings, a set of minimum-bias interactions generated using PYTHIA 8.186 [106], the MSTW2008LO [158] PDF set and the A2 [159] set of tuned parameters (tune) was superimposed onto the hard-scattering events to reproduce the observed distribution of the average number of interactions per bunch crossing.

In all MC samples, except those produced by SHERPA [103], the EVTGEN 1.2.0 [160] program was used to model the properties of the bottom and charm hadron decays. The SM MC programs are listed in Table 5.3.

Table 5.3: A summary of the MC samples used in the analysis to model SM background processes. For each sample the corresponding generator, matrix element (ME) accuracy, parton shower (PS), cross-section normalization accuracy, parton density function (PDF) set and tune are indicated. Samples with 'data' in the 'cross-section normalization' column are scaled to data as described in Section 5.3.3. Z refers to γ^* / Z.

Physics process	Generator	ME accuracy	Parton shower	Cross-section normalization	PDF set	Tune
$W\,(\rightarrow \ell\nu)$ + jets	Sherpa 2.1.1	0,1,2j@NLO + 3,4j@LO	Sherpa 2.1.1	NNLO	NLO CT10	Sherpa
$Z\,(\rightarrow \ell^+\ell^-)$ + jets	Sherpa 2.1.1	0,1,2j@NLO + 3,4j@LO	Sherpa 2.1.1	NNLO	NLO CT10	Sherpa
$Z\,(\rightarrow \nu\bar{\nu})$ + jets	Sherpa 2.1.1	0,1,2j@NLO + 3,4j@LO	Sherpa 2.1.1	NNLO	NLO CT10	Sherpa
$Z\,/\,W\,(\rightarrow q\bar{q})$ + jets	Sherpa 2.1.1	1,2,3,4j@LO	Sherpa 2.1.1	NNLO	NLO CT10	Sherpa
$Z\,/\,W + \gamma$	Sherpa 2.1.1	0,1,2,3j@LO	Sherpa 2.1.1	NLO	NLO CT10	Sherpa
$Z\,/\,W + \gamma\gamma$	Sherpa 2.1.1	0,1,2,3j@LO	Sherpa 2.1.1	NLO	NLO CT10	Sherpa
γ + jets	Sherpa 2.1.1	0,1,2,3,4j@LO	Sherpa 2.1.1	data	NLO CT10	Sherpa
$\gamma\gamma$ + jets	Sherpa 2.1.1	0,1,2j@LO	Sherpa 2.1.1	data	NLO CT10	Sherpa
$\gamma\gamma\gamma$ + jets	MG5_aMC@NLO 2.3.3	0,1j@LO	Pythia 8.212	LO	NNPDF2.3LO	A14
$t\bar{t}$	Powheg-Box v2	NLO	Pythia 6.428	NNLO+NNLL	NLO CT10	Perugia 2012
$t\bar{t} + W$	MG5_aMC@NLO 2.2.2	0,1,2j@LO	Pythia 8.186	NLO	NNPDF2.3LO	A14
$t\bar{t} + Z$	MG5_aMC@NLO 2.2.2	0,1j@LO	Pythia 8.186	NLO	NNPDF2.3LO	A14
$t\bar{t} + WW$	MG5_aMC@NLO 2.2.2	LO	Pythia 8.186	NLO	NNPDF2.3LO	A14
$t\bar{t} + \gamma$	MG5_aMC@NLO 2.2.2	LO	Pythia 8.186	LO	NNPDF2.3LO	A14
$t\bar{t} + b\bar{b}$	Sherpa 2.2.0	NLO	Sherpa 2.2.0	NLO	NLO CT10f4	Sherpa
Single-top (t-channel)	Powheg-Box v1	NLO	Pythia 6.428	app. NNLO	NLO CT10f4	Perugia 2012
Single-top (s- and Wt-channel)	Powheg-Box v2	NLO	Pythia 6.428	app. NNLO	NLO CT10	Perugia 2012
tZ	MG5_aMC@NLO 2.2.2	LO	Pythia 8.186	LO	NNPDF2.3LO	A14
3-top	MG5_aMC@NLO 2.2.2	LO	Pythia 8.186	LO	NNPDF2.3LO	A14
4-top	MG5_aMC@NLO 2.2.2	LO	Pythia 8.186	NLO	NNPDF2.3LO	A14
WW	Sherpa 2.1.1	0j@NLO + 1,2,3j@LO	Sherpa 2.1.1	NLO	NLO CT10	Sherpa
WZ	Sherpa 2.1.1	0j@NLO + 1,2,3j@LO	Sherpa 2.1.1	NLO	NLO CT10	Sherpa
ZZ	Sherpa 2.1.1	0,1j@NLO + 2,3j@LO	Sherpa 2.1.1	NLO	NLO CT10	Sherpa
Multijet	Pythia 8.186	LO	Pythia 8.186	data	NNPDF2.3LO	A14
Higgs (ggF/VBF)	Powheg-Box v2	NLO	Pythia 8.186	NNLO(+NNLL)	NLO CT10	AZNLO
Higgs ($t\bar{t}H$)	MG5_aMC@NLO 2.2.2	NLO	Herwig++	NLO	NLO CT10	UE-EE-5
Higgs (W/ZH)	Pythia 8.186	LO	Pythia 8.186	NNLO	NNPDF2.3LO	A14
Tribosons	Sherpa 2.1.1	0,1,2j@LO	Sherpa 2.1.1	NLO	NLO CT10	Sherpa

Multijet samples Samples of multijet production were simulated with a $2 \to 2$ ME at LO using the PYTHIA 8.186 [106] generator. The A14 [161] set of PS and multiple parton interactions parameters (tune) was used together with the `NNPDF2.3LO` [162] PDF set. Alternative multijet samples with a $2 \to 2$ ME at LO were generated with Herwig++ 2.7.1 [108] with the UE-EE-5 [163] underlying-event tune and the `CTEQ6L1` [164] PDF set, and with SHERPA 2.1.1 [103] with an ME for $2 \to 2$ and $2 \to 3$ partons at LO merged using the ME+PS@LO prescription. All SHERPA samples use the `CT10` [165] PDF set and the SHERPA PS [166] with a dedicated shower tuning developed by the SHERPA authors.

$W/Z +$ jets samples Events containing leptonic decays of a W or Z bosons with associated jets ($W/Z +$ jets) were simulated using the SHERPA 2.1.1 generator [167]. MEs were calculated using the Comix [168] and Open-Loops [169] generators. They include up to two partons at NLO and four partons at LO, merged using the ME+PS@NLO [170] prescription. Samples with W and Z decaying hadronically are also generated with SHERPA 2.1.1 including up to four partons at LO. The $W/Z +$ jets events were normalized to their inclusive next-to-next-to-leading order (NNLO) cross-sections [171, 172]. Simulated samples of massive vector bosons produced in association with one or two real photons were also generated with SHERPA 2.1.1 with a ME calculated at LO for up to three partons. They are scaled to their NLO cross-sections computed with `MCFM` [173, 174].

$\gamma +$ jets samples Samples of prompt photon production in association with jets ($\gamma +$ jets) were generated using SHERPA 2.1.1. For these samples up to four real parton emissions are included at LO. Events containing two prompt photons ($\gamma\gamma +$ jets) were also generated with SHERPA 2.1.1. MEs were calculated with up to two partons at LO. The gluon-induced box process is also included. These samples were scaled to data following the procedure described in Section 5.3.3. Samples of the production of three prompt photons ($\gamma\gamma\gamma +$ jets) were generated at LO with MADGRAPH5_aMC@NLO 2.3.3 [175] interfaced to PYTHIA 8.212 [107], with up to one extra parton included in the ME, and using the A14 tune together with the `NNPDF2.3LO` PDF set.

Single top and $t\bar{t}$ samples Top-quark pair production events, and single top quarks in the Wt- and s-channels, were simulated using the POWHEG-BOX v2 [176] generator with the `CT10` PDF set, as detailed in Ref. [177]. The top quark mass was set to 172.5 GeV. The h_{damp} parameter, which regulates the transverse momentum of the first extra emission beyond the Born configuration and thus controls the p_{T} of the $t\bar{t}$ system, was set to the mass of the top quark. Electroweak t-channel single-top-quark events were generated using the POWHEG-BOX v1 generator. This generator uses the four-flavour scheme for the NLO ME calculations together with the `CT10f4` fixed four-flavour PDF set. For all top-quark processes, top-quark spin correlations are preserved (for the single-top t-channel, top quarks were decayed using MadSpin [178]). An alternative sample of $t\bar{t}$ was generated with the SHERPA 2.1.1 generator, including up to one additional parton at NLO and up to four additional partons at LO accuracy, interfaced to the PS using the ME+PS@NLO prescription. The PS, fragmentation, and the underlying event of the POWHEG-BOX samples were simulated using PYTHIA 6.428 [105] with the `CTEQ6L1` PDF set and the corresponding Perugia 2012 [179] tune. The $t\bar{t}$ and single-top-quark events were normalized to the NNLO cross-section including the resummation of soft gluon emission at next-to-next-to-leading logarithmic (NNLL) accuracy [180–182] using

Top++ 2.0 [183]. Both the default and the alternative $t\bar{t}$ samples were corrected to reproduce the NNLO prediction [184, 185] of the top quark p_{T} and the p_{T} of the $t\bar{t}$ system. The contribution from $t\bar{t} + b\bar{b}$ production was simulated with SHERPA 2.1.1 at NLO [186]; the calculation was performed in the four-flavour scheme and with the CT10f4 PDF set.

Diboson and triboson samples Diboson samples were generated with the SHERPA 2.1.1 generator, and are described in Ref. [187]. The MEs contain the WW, WZ and ZZ processes and all other diagrams with four or six electroweak vertices (such as same-electric-charge W boson production in association with two jets, $W^{\pm}W^{\pm}jj$). Fully leptonic triboson processes (WWW, WWZ, WZZ and ZZZ) with on-shell bosons and up to six charged leptons were also simulated using SHERPA 2.1.1. The ME for the ZZ processes were calculated at NLO for up to one additional parton; final states with two and three additional partons were calculated at LO. The WZ and WW processes were calculated at NLO with up to three extra partons at LO using the ME+PS@NLO prescription. The WW final states were generated without bottom quarks in the hard-scattering process, to avoid contributions from top-quark-mediated processes. The triboson processes were calculated with the same configuration and with up to two extra partons at LO. The generator cross-sections were used for the normalization of these processes.

$t\bar{t} + \gamma/W/Z/WW$, tZ and multitop samples Samples of top quark production in association with vector bosons [188] (W, Z, γ and WW, including the non-resonant $\gamma^{*}/\,Z$ contributions) were generated at LO with MADGRAPH5_aMC@NLO 2.2.2 interfaced to PYTHIA 8.186, with up to two ($t\bar{t}W$), one ($t\bar{t}Z$) or no ($t\bar{t}WW$, $t\bar{t}\gamma$) extra partons included in the ME. The A14 tune was used together with the NNPDF2.3LO PDF set. The $t\bar{t}\gamma$ sample uses a fixed QCD renormalization and factorization scale of $2m_t$, and the top decay was performed in MADGRAPH5_aMC@NLO to account for hard photon radiation from the top decay products. The same generator was also used to simulate the tZ, 3-top and 4-top quarks processes. The $t\bar{t}W$, $t\bar{t}Z$, $t\bar{t}WW$ and 4-top samples were normalized to their NLO cross-sections [175] while the LO cross-section from the generator was used for tZ and 3-top quarks.

Higgs samples The Higgs boson mass was set to 125 GeV and all SM Higgs boson decay modes were considered. The production of the SM Higgs boson in the gluon–gluon fusion (ggF) and vector-boson fusion (VBF) channels was modelled using the POWHEG-BOX v2 generator with the CT10 PDF set. It was interfaced to PYTHIA 8.186 with the CTEQ6L1 PDF set and the AZNLO [189] tune. Production of a Higgs boson in association with a pair of top quarks was simulated using MADGRAPH5_aMC@NLO 2.2.2 interfaced to Herwig++ 2.7.1 [109] for showering and hadronization. The UE-EE-5 underlying-event tune was used together with the CT10 (ME) and CTEQ6L1 (PS) PDF sets. Simulated samples of SM Higgs boson production in association with a W or Z boson were produced with PYTHIA 8.186, using the A14 tune and the NNPDF2.3LO PDF set. Events were normalized to their most accurate cross-sections calculations (typically NNLO) [190].

Overlap removal To avoid double counting, events with a hard photon from final-state radiation were removed from the multijet, $t\bar{t}$ and $W/Z+$jets samples.

5.2.2 Monte Carlo signal samples

Z' samples In addition to the SM background processes, two possible signals are considered as benchmarks. The first benchmark model considered is the production of a new heavy neutral gauge boson of spin 1 (Z'), as predicted by many extensions of the SM. Here, the specific case of the sequential extension of the SM gauge group (SSM) [97, 99] is considered, for which the couplings are the same as for the SM Z boson. This process was generated at LO using PYTHIA 8.212 with the `NNPDF2.3LO` PDF set and the A14 tune, as a Drell–Yan process, for four different resonant masses, covering the range from 2 TeV to 3.5 TeV, in steps of 0.5 TeV. The considered decays of Z' bosons are inclusive, covering the full range of lepton and quark pairs. Interference effects with SM Drell–Yan production are not included, and the Z' boson is required to decay into fermions only.

Gluino samples The second signal considered is the supersymmetric [191–196] production of gluino pairs through strong interactions. The gluinos are assumed to decay promptly into a pair of top quarks and an almost massless neutralino via an off-shell top squark $\tilde{g} \rightarrow t\bar{t}\tilde{\chi}_1^0$. Samples for this process were generated at LO with up to two additional partons using MADGRAPH5_aMC@NLO 2.2.2 with the `CTEQ6L1` PDF set, interfaced to PYTHIA 8.186 with the A14 tune. The matching with the PS was done using the CKKW-L [197] prescription, with a matching scale set to one quarter of the pair-produced resonance mass. The signal cross-sections were calculated at NLO in the strong coupling constant, adding the resummation of soft gluon emission at next-to-leading logarithmic (NLL) accuracy [198–200].

5.2.3 Systematic uncertainties

Experimental uncertainties The dominant experimental systematic uncertainties in the SM expectation for the different event classes typically are the jet energy scale (JES) and jet energy resolution (JER) [151] and the scale and resolution of the $E_{\mathrm{T}}^{\mathrm{miss}}$ soft-term. The uncertainty related to the modelling of $E_{\mathrm{T}}^{\mathrm{miss}}$ in the simulation is estimated by propagating the uncertainties in the energy and momentum scale of each of the objects entering the calculation, with an additional uncertainty in the resolution and scale of the soft-term [156]. The uncertainties in correcting the b-jet identification efficiency in MC simulations are determined in data samples enriched in top quark decays, and in simulated events [154]. Leptonic decays of J/ψ mesons and Z bosons in data and simulation are exploited to estimate the uncertainties in lepton reconstruction, identification, momentum/energy scale and resolution, and isolation criteria [144, 145, 201]. Photon reconstruction and identification efficiencies are evaluated from samples of $Z \rightarrow ee$ and $Z + \gamma$ events [146, 201]. The luminosity measurement was calibrated during dedicated beam-separation scans, as described in Ref. [202]. The uncertainty of this measurement is found to be 2.1%.

In total, 35 sources of experimental uncertainties are identified pertaining to one or more physics objects considered. For each source, the one-standard-deviation (1σ) confidence interval (CI) is propagated to a 1σ CI around the nominal SM expectation. The total experimental uncertainty of the SM expectation is obtained from the sum in quadrature of these 35 1σ CIs and the uncertainty of the luminosity measurement.

Theoretical modelling uncertainties Two different sources of uncertainty in the theoretical modelling of the SM production processes are considered. A first uncertainty is assigned to account for our knowledge of the cross-sections for the inclusive processes. A second uncertainty is used to cover the modelling of the shape of the differential cross-sections. In order to derive the modelling uncertainties, either variations of the QCD factorization, renormalization, resummation and merging scales are used or comparisons of the nominal MC samples with alternative ones are used. For some SM processes additional modelling uncertainties are included. The total uncertainty is taken as the sum in quadrature of the two components and the statistical uncertainty of the MC prediction.

The inclusive W and Z cross-sections are known at NNLO, with an uncertainty of about 5% [171, 172]. Modelling uncertainties for $W +$ jets and $Z +$ jets are determined by varying the renormalization, factorization and resummation scales in the ME by factors 0.5 and 2, together with a change of the merging scale from 20 GeV to 15 GeV or 30 GeV.

For top quark pair or single-top production, processes known to NNLO+NNLL [183] or approximate NNLO [180–182], respectively, the cross-section uncertainty is 7%. The modelling uncertainty for $t\bar{t}$ is determined by comparing the nominal POWHEG+PYTHIA NLO+PS sample with an alternative sample generated with SHERPA which includes up to two partons at NLO and four at LO accuracy in the ME. The contributions from $t\bar{t} + b\bar{b}$ production generated with SHERPA are added to the inclusive top quark pair sample with a 100% normalisation uncertainty. The single-top quark uncertainty is estimated by varying the renormalization and factorization scales, and by changing the h_{damp} parameter and the shower tune of the POWHEG+PYTHIA sample. An uncertainty in the interference between the Wt and $t\bar{t}$ production is estimated by comparing the nominal Wt sample, in which all doubly resonant NLO Wt diagrams are removed, to a sample where the cross-section contribution from Feynman diagrams containing two top quarks is subtracted [203].

Diboson cross-sections (WW, WZ and ZZ) are calculated at NLO, and a 6% uncertainty, evaluated with the MCFM program [173, 174], is applied to their cross-sections. Their modelling uncertainty is evaluated analogously to $W/Z +$ jets by varying the scales used to perform the calculation. For $W + \gamma$ and $Z + \gamma$ samples, which are computed at LO, a 20% uncertainty in the cross-section is assumed, with a further 20% modelling uncertainty assigned in accordance with the measurement in Ref. [204].

The cross-sections for top-quark pair production in association with one or two vector bosons are calculated at NLO and an uncertainty of 15% is used [175]. Their modelling uncertainty is evaluated from variations of the renormalization and factorization scales, together with a change in the merging scale. For $t\bar{t} + \gamma$, an additional 12% uncertainty in the normalization is assumed, while a uniform 30% uncertainty is assigned to the modelling [188].

Multijet, $\gamma +$ jets and $\gamma\gamma +$ jets processes are scaled to data following the procedure described in Section 5.3.3. Therefore, no uncertainty is applied to their normalization. For multijet the maximum bin-by-bin difference between the PYTHIA 8 nominal sample and alternative samples generated with SHERPA and Herwig++ is considered as a shape uncertainty. In addition, the standard deviation of the 100 replica sets of the NNPDF2.3LO PDF is used. The modelling uncertainty for $\gamma +$ jets is estimated from scale variations with the same methodology as for the $W/Z +$ jets samples. The shape uncertainty in the $\gamma\gamma +$ jets modelling is instead taken to be 30% from parton-level comparisons of samples with varied scales.

A conservative uncertainty of 20% [190] is assumed for Higgs production in the ggF, VBF and VH channels. A further uncertainty of 20% is assigned as a shape uncertainty.

For the subdominant triboson (including $W/Z + \gamma\gamma$), ttH, 3-top, 4-top and tZ production processes a 50% uncertainty is assigned to the event yields, similarly to Ref. [205]. Uncertainties associated to PDFs are found to be small in all channels compared to the modelling uncertainties of the MC simulations.

5.3 Validation and correction of the background model

5.3.1 Validation selections and distributions

The evaluated SM processes, together with their standard selection cuts and the studied validation distributions, are detailed in Table 5.4. For each selection the p_{T}, η, and ϕ distributions of the objects used in the selection and of additional jets, as well as the $E_{\mathrm{T}}^{\mathrm{miss}}$ and $\phi(E_{\mathrm{T}}^{\mathrm{miss}})$ are included as validation distributions by default, the additional validation distributions per selection are listed in the table. These validation distributions rely on inclusive selections to probe the general agreement between data and simulation and are evaluated in restricted ranges where large new-physics contributions have been excluded by previous direct searches. Some selections rely on the transverse mass ($m_{\mathrm{T}}(\ell, E_{\mathrm{T}}^{\mathrm{miss}})$) which is defined as $[2 \cdot p_{\mathrm{T}}(\ell) \cdot E_{\mathrm{T}}^{\mathrm{miss}} \cdot (1 - \cos \Delta\phi(\ell, E_{\mathrm{T}}^{\mathrm{miss}}))]^{1/2}$. The $H_{\mathrm{T}}(\text{jets})$, $m_{\mathrm{T}}(\ell, E_{\mathrm{T}}^{\mathrm{miss}})$, $p_{\mathrm{T}}(\ell\ell)$, $E_{\mathrm{T}}^{\mathrm{miss}}$ and m_{inv} validation distributions are evaluated in restricted ranges where large new-physics contributions have been excluded by previous direct searches.

The validation distributions are primarily used to identify possible issues in the analysis, but can also uncover problems in the background modelling. Based on the nature of the MC modelling problem, it can be decided to either correct the background modelling or to discard certain event classes from the analysis.

5.3.2 Discarded event classes

In event classes with one electron and several (non-b-tagged) jets the SM expectation values are dominated by events in which a jet is misreconstructed as an electron (fake electron). This kind of object misidentification is poorly modelled in MC simulation, mainly due to MC statistics, i.e. the small number of simulated multijet events in which a jet fakes an electron in comparison to the number of events from the experiment. After an unsuccessful attempt at using a data-driven method to estimate the number of events in which a jet fakes an electron, the affected classes have been discarded from the analysis. The excluded classes are: $1e1j$, $1e2j$, $1e3j$, $1e4j$, $1e1b$, $1e1b1j$, $1e1b2j$, $1e1b3j$.

Event classes containing a single object ($1j$, $1b$, $1e$, 1μ, 1γ, $E_{\mathrm{T}}^{\mathrm{miss}}$), as well as those containing only $E_{\mathrm{T}}^{\mathrm{miss}}$ and a lepton ($E_{\mathrm{T}}^{\mathrm{miss}}1e$, $E_{\mathrm{T}}^{\mathrm{miss}}1\mu$) are also discarded from the analysis due to difficulties in modelling final states with one high-energy object recoiling against multiple soft (non-reconstructed) ones.

5.3.3 Corrections to the MC background

The MC samples for multijet, $\gamma + \text{jets}$ and $\gamma\gamma + \text{jets}$ production, while giving a good description of kinematic variables, predict an inclusive cross-section at LO and jet multiplicity distribution that disagrees with the experiment. Higher-order cross-section k-factors are not

Table 5.4: A summary of the SM processes and their inclusive selections used to validate the background modelling. For the distance variables ΔR and $\Delta\phi$, the two instances of the objects with the minimum distance between them are used. Same-flavour opposite-charge sign lepton pairs are referred to as SFOS pairs.

Physics process	Event selection	Additional validation distributions
$W(\rightarrow \ell\nu) + \text{jets}$	1 lepton, $E_{\mathrm{T}}^{\mathrm{miss}} > 25$ GeV and $m_{\mathrm{T}}(\ell, E_{\mathrm{T}}^{\mathrm{miss}}) > 50$ GeV	$N(\text{jets})$ $N(b\text{-jets})$ $m_{\mathrm{T}}(\ell, E_{\mathrm{T}}^{\mathrm{miss}})$ $H_{\mathrm{T}}(\text{jets})$ $\Delta R(\ell, \text{jet})$ $\Delta\phi(\ell, E_{\mathrm{T}}^{\mathrm{miss}})$ $\Delta\phi(\text{jet}, E_{\mathrm{T}}^{\mathrm{miss}})$
	& $N(\text{jets}) \geq 3$	$H_{\mathrm{T}}(\text{jets})$
	& $N(b\text{-jets}) \geq 1$	$m_{\mathrm{T}}(\ell, E_{\mathrm{T}}^{\mathrm{miss}})$
	& $N(b\text{-jets}) \geq 2$	$m_{\mathrm{T}}(\ell, E_{\mathrm{T}}^{\mathrm{miss}})$
$Z(\rightarrow \ell\ell) + \text{jets}$	1 SFOS pair $66 < m_{\mathrm{inv}}(\ell\ell) < 116$ GeV	$N(\text{jets})$ $N(b\text{-jets})$ $m_{\mathrm{inv}}(\ell\ell)$ $p_{\mathrm{T}}(\ell\ell)$ $H_{\mathrm{T}}(\text{jets})$ $\Delta R(\ell, \ell)$ $\Delta R(\ell, \text{jet})$
	& $N(\text{jets}) \geq 2$	$H_{\mathrm{T}}(\text{jets})$
	& $N(b\text{-jets}) \geq 1$	$m_{\mathrm{inv}}(\ell\ell)$ $p_{\mathrm{T}}(\ell\ell)$
	& $N(b\text{-jets}) \geq 2$	$m_{\mathrm{inv}}(\ell\ell)$ $p_{\mathrm{T}}(\ell\ell)$
$W + \gamma(\gamma)$	same selection as $W(\rightarrow \ell\nu) + \text{jets}$ and 1(2) additional photon(s)	same distributions as $W(\rightarrow \ell\nu) + \text{jets}$ and $\Delta R(\ell, \gamma)$
$Z + \gamma(\gamma)$	same selection as $Z(\rightarrow \ell\ell)$ + jets and 1(2) additional photon(s)	same distributions as $Z(\rightarrow \ell\ell) + \text{jets}$ and $\Delta R(\ell, \gamma)$
$\gamma(\gamma) + \text{jets}$	1(2) photon(s), no leptons and at least 1(0) jet(s)	$N(\text{jets})$ $N(b\text{-jets})$ $m_{\mathrm{inv}}(\gamma\gamma)$ $p_{\mathrm{T}}(\gamma\gamma)$ $H_{\mathrm{T}}(\text{jets})$ $\Delta R(\gamma, \gamma)$ $\Delta R(\gamma, \text{jet})$
$t\bar{t}$ (semi-leptonic)	1 lepton, at least 2 b-jets and at least 2 light jets	$N(\text{jets})$ $N(b\text{-jets})$ $m_{\mathrm{inv}}(jj)$ $m_{\mathrm{T}}(\ell, E_{\mathrm{T}}^{\mathrm{miss}})$ $\Delta R(\text{jet}, \text{jet})$ $\Delta R(\ell, \text{jet})$ $\Delta\phi(\ell, E_{\mathrm{T}}^{\mathrm{miss}})$ $\Delta\phi(\text{jet}, E_{\mathrm{T}}^{\mathrm{miss}})$
$t\bar{t}$ (leptonic)	1 electron and 1 muon of opposite charge and at least 2 b-jets	$N(\text{jets})$ $N(b\text{-jets})$ $\Delta R(b\text{-jet}, b\text{-jet})$ $m_{\mathrm{T}}(\ell, E_{\mathrm{T}}^{\mathrm{miss}})$ $\Delta R(\ell, \ell)$ $\Delta R(\ell, b\text{-jet})$ $\Delta\phi(\ell, E_{\mathrm{T}}^{\mathrm{miss}})$ $\Delta\phi(b\text{-jet}, E_{\mathrm{T}}^{\mathrm{miss}})$
Diboson		
WW	1 electron and 1 muon of opposite charge and no jets	$m_{\mathrm{T}}(\ell, E_{\mathrm{T}}^{\mathrm{miss}})$ $\Delta R(\ell, \ell)$ $\Delta\phi(\ell, E_{\mathrm{T}}^{\mathrm{miss}})$
WZ	1 SFOS pair $(\ell\ell)$ and 1 lepton of different flavour (ℓ') $66 < m_{\mathrm{inv}}(\ell\ell) < 116$ GeV	$m_{\mathrm{inv}}(\ell\ell)$ (SFOS pair) $p_{\mathrm{T}}(\ell\ell)$ (SFOS pair) $m_{\mathrm{T}}(\ell', E_{\mathrm{T}}^{\mathrm{miss}})$ $\Delta R(\ell, \ell)$ $\Delta\phi(\ell', E_{\mathrm{T}}^{\mathrm{miss}})$
ZZ	2 SFOS pairs $66 < m_{\mathrm{inv}}(\ell\ell) < 116$ GeV (both SFOS pairs)	$m_{\mathrm{inv}}(\ell\ell)$ (SFOS pairs) $p_{\mathrm{T}}(\ell\ell)$ (SFOS pairs) $\Delta R(\ell, \ell)$
Multijet	at least 2 jets no leptons or photons	$N(\text{jets})$ $N(b\text{-jets})$ $\Delta R(\text{jet}, \text{jet})$ $E_{\mathrm{T}}^{\mathrm{miss}}/m_{\mathrm{eff}}$ $\Delta\phi(\text{jet}, E_{\mathrm{T}}^{\mathrm{miss}})$

available (at the time of the analysis) and the total number of expected events is therefore scaled to the observed number of events for each event class using normalisation factors.

For each event class containing only the j and b signal objects, the expectation from multijet MC samples is scaled such that the total expectation value, possibly including contributions from other MC samples, matches the observed number of events, using normalisation factors typically between 0.6 and 1.1 (10^{th} and 90^{th} percentile). If a channel contains four or less data events, no modifications are made. Multijet contributions can enter other event classes through misreconstructed jets, but are subleading in the expectation value in all but some of the discarded event classes mentioned above and typically have a large statistical MC uncertainty associated with them. In all other event classes, the nominal generator prediction and uncertainties are maintained.

For each event class containing exactly one photon, no leptons or $E_{\mathrm{T}}^{\mathrm{miss}}$, and any number of jets (i.e. $1\gamma(Xb)(Xj)$ where X is zero or more) a similar rescaling procedure is applied to the $\gamma +$jets samples, using normalisation factors typically between 1.1 and 1.8 (10^{th} and 90^{th} percentile). Whereas all systematic variations are scaled to data for multijet samples, for the $\gamma +$jets samples the systematic variations associated to the theoretical modelling uncertainties are scaled with the normalisation factor derived from scaling the nominal prediction to data, as this results in a smaller systematic shape uncertainty overall.

Similarly, for each event class containing exactly two photons, no leptons or $E_{\mathrm{T}}^{\mathrm{miss}}$, and any number of jets (i.e. $2\gamma(Xb)(Xj)$ where X is zero or more) the same rescaling procedure that was applied for multijet is applied to the $\gamma\gamma +$jets samples, with normalisation factors between 1.5 and 2.0 (25^{th} and 75^{th} percentile). Tables with the normalisation factors applied per event class can be found in Appendix D.

The SHERPA 2.1.1 MC generator has a known deficiency in the modelling of $E_{\mathrm{T}}^{\mathrm{miss}}$ due to a too large forward jet activity. This results in a visible mismodelling of the $E_{\mathrm{T}}^{\mathrm{miss}}$ distribution in event classes with two photons or two leptons which also affects the m_{eff} distribution. Extensive studies have been performed by applying a reweighting procedure as a function of $E_{\mathrm{T}}^{\mathrm{miss}}$ and of the number of signal jets to quantify the impact on the results of the analysis. Since the final result is not affected by the mismodelling, the analysis documented in this thesis uses a background model in which no additional corrections are applied to address this modelling issue.

Validation regions with more than two b-jets, which strongly depend on the modelling of the heavy-flavour component of the inclusive $t\bar{t}$ sample, show an SM expectation that is systematically below the observed number of events. To obtain a conservative estimate for the SM expectation, the contribution from $t\bar{t} + b\bar{b}$ production has been estimated separately and added to the inclusive $t\bar{t}$ cross-section with a 100% normalisation uncertainty assigned to its contribution as described in Section 5.2.3.

5.4 Classification results

Table 5.5 summarizes the number of event classes after classification and removal of the 16 discarded event classes listed in Section 5.3.2. In total 750 event classes are found to have at least one observed event or an SM expectation greater than 0.1 events. The number of observed events and the predictions from MC simulations for these classes are shown in Appendix E.

Events from experiment are observed in 564 out of 750 event classes. These include events with up to four leptons (muons and/or electrons), three photons, twelve jets and eight b-jets[2].

There are 20 event classes, listed in Table 5.6, with an SM expectation of less than 0.1 events. These classes are not considered for the search algorithm and the statistical analysis. However, the observation of four or more events in event classes with $C_{\mathrm{SM}} < 0.1$ can result in a p_0-value that is smaller than the threshold for which $P_{\mathrm{exp}} = 5\%$ and should therefore be considered for a DDSR. No more than two data events are observed in any of the event classes having $C_{\mathrm{SM}} < 0.1$. The remaining 730 classes are retained for further analysis. Appendix F shows how the number of event classes and their expectation values change under different signal hypothesis.

Table 5.5: Number of event classes after classification of all accepted events.

Event classes with	Amount
$C_{\mathrm{SM}} > 0.1$ and $C_{\mathrm{obs}} \geq 1$	544
$C_{\mathrm{SM}} > 0.1$ and $C_{\mathrm{obs}} = 0$	186
$C_{\mathrm{SM}} > 0.1$	730
$C_{\mathrm{SM}} < 0.1$ and $C_{\mathrm{obs}} \geq 1$	20
$C_{\mathrm{SM}} > 0.1$ or $C_{\mathrm{obs}} \geq 1$	750

5.5 Search algorithm

In order to quantify the level of agreement between experiment and the SM expectation, and to identify regions possibly deviating from it, an algorithm for multiple hypothesis testing, derived from the one used in Ref. [5], is used. It locates a single region of largest deviation per event class in a binned distribution of an observable.

5.5.1 Search observables

For each event class, the effective mass (m_{eff}), the invariant mass (m_{inv}) and the H_{T} distributions are considered in the form of histograms. The H_{T} is the scalar sum of the p_{T} of all (visible) signal objects in the event and the effective mass is H_{T} plus $E_{\mathrm{T}}^{\mathrm{miss}}$. The invariant mass is computed from all visible objects in the event, with no attempt to use the $E_{\mathrm{T}}^{\mathrm{miss}}$ information. For all event classes having $E_{\mathrm{T}}^{\mathrm{miss}} > 200$ GeV the $E_{\mathrm{T}}^{\mathrm{miss}}$ distribution is also considered. All these variables have been widely used in searches for new physics, and are sensitive to a large range of possible signals, manifesting either as bumps, deficits or wide excesses.

[2] This analysis has been performed using early Run 2 event reconstruction algorithms. Reprocessings of the data (and simulation) with updated reconstruction algorithms, in particular, those relating to primary vertex and b-jet identification and association, show no events with eight reconstructed b-jets as seen in Chapter 6.

Table 5.6: Event classes with at least one observed event from experiment and an SM expectation smaller than 0.1. The upper limit (UL) at a 95% confidence level (CL) on the expected number of events, as obtained from the MC background, is given.

Event class	Observed events	Expected events (95% CL UL)
$2b\ 10j$	1	$8.5 \cdot 10^{-1}$
$6b\ 2j$	1	$3.5 \cdot 10^{-1}$
$8b\ 1j$	1	$5.2 \cdot 10^{-4}$
$1\gamma\ 10j$	2	$1.5 \cdot 10^{-1}$
$2e\ 1\gamma\ 3b$	1	$6.6 \cdot 10^{-3}$
$4e\ 1b$	1	$2.3 \cdot 10^{-1}$
$1\mu\ 1e\ 1b\ 7j$	1	$2.9 \cdot 10^{-1}$
$1\mu\ 1e\ 4b\ 5j$	1	$1.3 \cdot 10^{-2}$
$1\mu\ 1e\ 1\gamma\ 1b\ 4j$	1	$1.0 \cdot 10^{-1}$
$1\mu\ 2e\ 2b\ 5j$	1	$2.5 \cdot 10^{-2}$
$2\mu\ 1b\ 7j$	1	$1.5 \cdot 10^{-1}$
$2\mu\ 2\gamma\ 2j$	1	$1.2 \cdot 10^{-1}$
$2\mu\ 1e\ 1\gamma\ 1j$	1	$2.5 \cdot 10^{-1}$
$3\mu\ 1e\ 2b$	1	$3.9 \cdot 10^{-2}$
$E_{\mathrm{T}}^{\mathrm{miss}}\ 2b\ 8j$	1	$1.2 \cdot 10^{-1}$
$E_{\mathrm{T}}^{\mathrm{miss}}\ 2\gamma\ 1b\ 2j$	1	$1.5 \cdot 10^{-1}$
$E_{\mathrm{T}}^{\mathrm{miss}}\ 1e\ 1b\ 9j$	1	$3.1 \cdot 10^{-1}$
$E_{\mathrm{T}}^{\mathrm{miss}}\ 2e\ 1\gamma\ 1b\ 2j$	1	$1.5 \cdot 10^{-1}$
$E_{\mathrm{T}}^{\mathrm{miss}}\ 1\mu\ 1e\ 4b$	1	$1.6 \cdot 10^{-1}$
$E_{\mathrm{T}}^{\mathrm{miss}}\ 2\mu\ 1\gamma\ 2j$	1	$1.8 \cdot 10^{-1}$

5.5.2 Binning

For the H_{T}, m_{eff} and m_{inv} histogram, the bin widths $h(x)$ as a function of the abscissa x are determined using:

$$h(x) = \sqrt{\sum_{i}^{N_{\mathrm{objects}}} k_i^2 \sigma_i^2(x/2)}$$

where N_{objects} is the number of visible objects in the event class; $\sigma_i(x/2)$ is the expected detector resolution in the central region, as given in Table 5.7, for the p_{T} of object i evaluated at $p_{\mathrm{T}} = x/2$ to roughly approximate the largest p_{T}-scale in the event; and k_i is the number of standard deviations used to compute the width of the bin. An exception to this is the missing transverse momentum resolution ($\sigma_{E_{\mathrm{T}}^{\mathrm{miss}}}$), which is a function of $\sum E_{\mathrm{T}}$, where $\sum E_{\mathrm{T}}$ is approximated by the effective mass minus the $E_{\mathrm{T}}^{\mathrm{miss}}$ object requirement: $\sigma_{E_{\mathrm{T}}^{\mathrm{miss}}}\left(\sum E_{\mathrm{T}} = x - 200\ \mathrm{GeV}\right)$. The $E_{\mathrm{T}}^{\mathrm{miss}}$ object is only considered in the binning of the effective mass histograms, so for event classes with $E_{\mathrm{T}}^{\mathrm{miss}} > 200$ GeV the m_{eff} bin widths $h'(x)$ are computed using:

$$h'(x) = \sqrt{k^2_{E_{\mathrm{T}}^{\mathrm{miss}}}\ \sigma_{E_{\mathrm{T}}^{\mathrm{miss}}}{}^2(x - 200\ \mathrm{GeV}) + h^2(x - 200\ \mathrm{GeV})}$$

Note that for the few event classes where $N_{\mathrm{objects}} = 1$, e.g. the $E_{\mathrm{T}}^{\mathrm{miss}}\ 1j$ event class, the detector resolution in $h(x)$ is evaluated at $\sigma_i(x)$ instead of $\sigma_i(x/2)$.

For histograms of the event's missing transverse momentum the bin width $h''(x)$ is used given by:

$$h''(x) = k_{E_{\mathrm{T}}^{\mathrm{miss}}} \, \sigma_{E_{\mathrm{T}}^{\mathrm{miss}}} \left(\max \left[\sum p_{\mathrm{T}}^{\mathrm{min}}, N_{\mathrm{objects}} \cdot x \right] \right)$$

where $\sum p_{\mathrm{T}}^{\mathrm{min}}$ is the sum of the minimum p_{T} requirements of all visible objects in the event class. The number of visible objects times the missing transverse momentum ($N_{\mathrm{objects}} \cdot x$) is used as a rough estimation of the $\sum E_{\mathrm{T}}$-scale and used to compute the bin width if it is larger than the $\sum p_{\mathrm{T}}^{\mathrm{min}}$ of the event class.

Table 5.7 lists the resolution parametrisation, derived from Ref. [122], used for each object. A $\pm 1\sigma$ interval is used for the bin width ($k = 2$) for all objects except for photons and electrons, for which a $\pm 3\sigma$ interval is used ($k = 6$) to avoid having too finely binned histograms with (too) few MC events. This procedure results in variable bin widths with values ranging from 20 GeV to about 2000 GeV.

For a given event class, the m_{eff}, m_{inv} and H_{T} scans start at an abscissa equal to two times the sum of the minimum p_{T} requirement of each contributing object, taking into account p_{T} requirements in object definitions, trigger thresholds and other selection criteria, e.g. $2 \cdot (25 + 25) = 100$ GeV for the 2μ class and $2 \cdot (500 + 60 + 60) = 1240$ GeV for the $3j$ class. This avoids sensitivity to spurious deviations that can arise from insufficiently well-modelled threshold regions (e.g. due to recoils against the underlying event or non-reconstructed jets). For event classes having $E_{\mathrm{T}}^{\mathrm{miss}} > 200$ GeV the $\sum p_{\mathrm{T}}^{\mathrm{min}}$ includes 200 GeV for the $E_{\mathrm{T}}^{\mathrm{miss}}$ object in the m_{eff} scan. The $E_{\mathrm{T}}^{\mathrm{miss}}$ scan starts at a fixed value of 200 GeV.

Table 5.7: Detector resolution parametrisation of the different signal objects at, or close to $\eta = 0$, used to compute the bin width. The $\oplus$ sign means taking the quadrature-sum.

Object	Resolution
electron/photon	$\sigma_{e,\gamma}/E = 9\%/\sqrt{E} \oplus 350\ \mathrm{MeV}/E \oplus 0.7\%$
jet	$\sigma_{\mathrm{jet}}/E = 70\%/\sqrt{E} \oplus 1.8\ \mathrm{GeV}/E \oplus 3.3\%$
muon	$\sigma_{\mu}^{\mathrm{MS}}/p_{\mathrm{T}} = 0.25\ \mathrm{TeV}/p_{\mathrm{T}} \oplus 0.168\ \mathrm{TeV}^{-1} \cdot p_{\mathrm{T}} \oplus 3.27\%$
	$\sigma_{\mu}^{\mathrm{ID}}/p_{\mathrm{T}} = 0.417\ \mathrm{TeV}^{-1} \cdot p_{\mathrm{T}} \oplus 1.55\%$
	$\sigma_{\mu}/p_{\mathrm{T}} = \min\left(\sigma_{\mu}^{\mathrm{MS}}/p_{\mathrm{T}}, \sigma_{\mu}^{\mathrm{ID}}/p_{\mathrm{T}}\right)$
missing transverse momentum	$\sigma_{E_{\mathrm{T}}^{\mathrm{miss}}} = 0.5 \cdot \sqrt{\sum E_{\mathrm{T}}\ [\mathrm{GeV}]}$

5.5.3 Scan algorithm

For each event class, the scan algorithm identifies one region having the largest upward or downward deviation in a binned distribution, provided in the form of a histogram, as the Region-of-Interest (RoI). A region is defined as one or several contiguous bins in a histogram[3]. Table 5.8 summarizes the number of bins and regions.

For each region with an SM expectation larger than 0.01, the statistical estimator p_0, defined in Eqs. 4.36–4.38, is computed. Here, p_0 is to be interpreted as a local p_0-value and the region of largest deviation identified by the algorithm is the region with the smallest p_0-value. The smallest p_0 in an event class is referred to as p_{class}. Such a method can in principle find narrow resonances, single outstanding events, as well as signals spread over large regions of phase space in distributions of any shape.

[3]When combining bins, background uncertainties are treated as correlated among the bins with the exception of the MC statistical uncertainties and uncorrelated shape uncertainties.

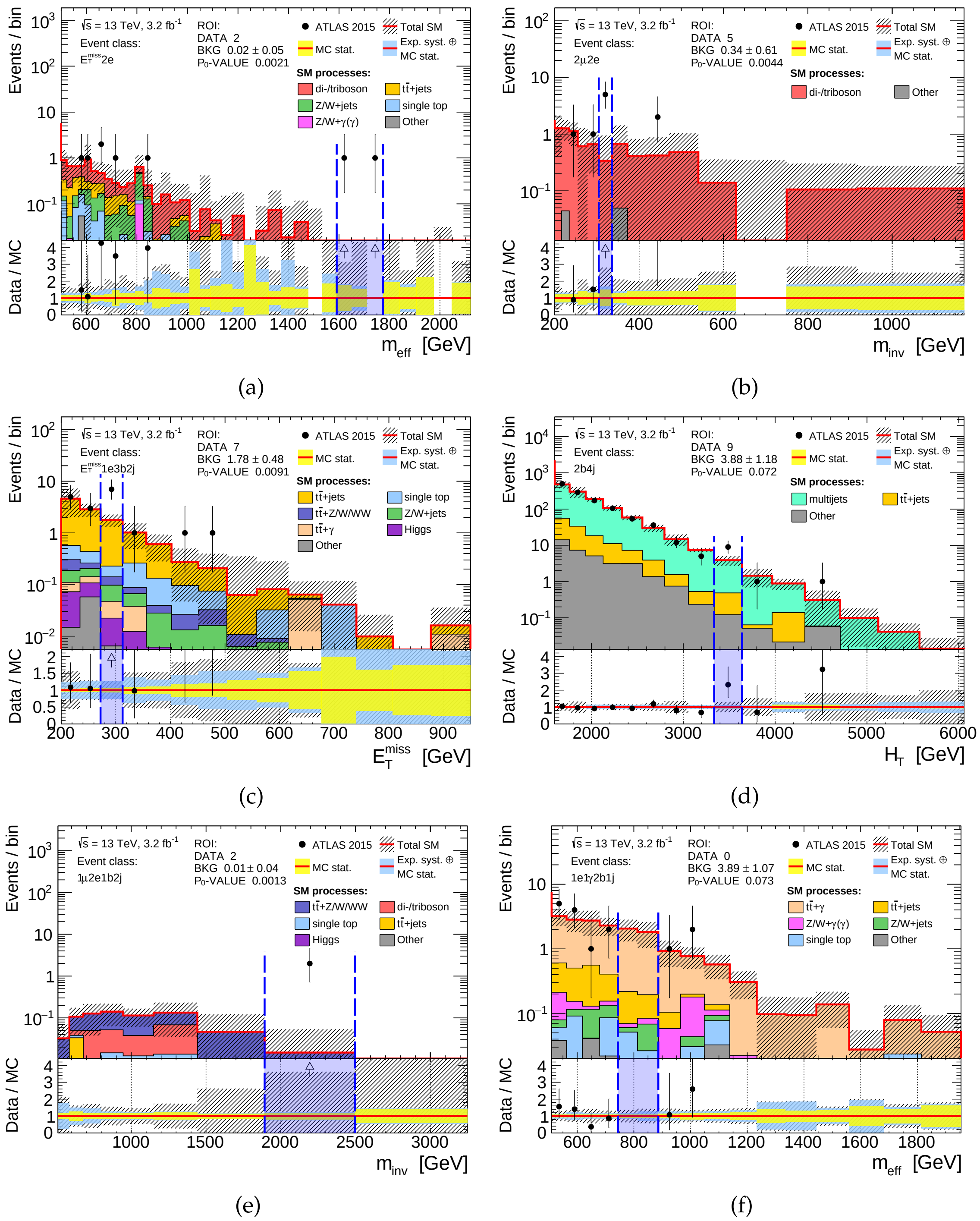

Figure 5.2: Example distributions showing the Region-of-Interest (RoI), i.e. the region with the smallest p_0-value, between the vertical blue dashed lines. The event class is listed in the top left corner and the observable is labelled on the horizontal axis. Figures (a) to (e) show excesses while (f) shows a deficit as largest deviation. The hatched band includes all uncertainties on the SM expectation. In the ratio plots, the yellow band shows the statistical uncertainty from MC simulations, the blue band includes the experimental uncertainties, and the hatched band includes the theory uncertainties.

Table 5.8: Summary of the numbers of regions and bins in the scans. Regions are built from one or more contiguous bins and are tested only if $C_{\mathrm{SM}} > 0.01$ such that multiple bins with $C_{\mathrm{SM}} < 0.01$ can form a region for hypothesis testing. Regions with $C_{\mathrm{SM}} < 0.01$ and $C_{\mathrm{obs}} \geq 3$ do not qualify for testing but are being monitored, since such a region could be considered for a DDSR. Numbers for 'all bins' and 'all regions' depend only the binning and the intervals covered in the histograms.

Scan observable	m_{eff}	m_{inv}	H_{T}	$E_{\mathrm{T}}^{\mathrm{miss}}$
All bins	18 910	20 162	20 266	8 188
Bins with $C_{\mathrm{SM}} > 0.01$	7 724	10 370	8 181	3 371
Bins with $C_{\mathrm{SM}} > 0.01$ and $C_{\mathrm{obs}} \geq 1$	3 455	4 908	3 647	1 206
All regions	375 336	432 900	438 360	133 638
Regions with $C_{\mathrm{SM}} > 0.01$	245 449	328 167	288 266	93 994
Regions with $C_{\mathrm{SM}} > 0.01$ and $C_{\mathrm{obs}} \geq 1$	138 244	200 839	163 908	45 636
Regions with $C_{\mathrm{SM}} < 0.01$ and $C_{\mathrm{obs}} \geq 3$	2	2	1	1

To illustrate the operation of the algorithm, some example distributions are presented. Figure 5.2(a) shows the effective mass distribution of the event class with two electrons and large missing transverse momentum ($E_{\mathrm{T}}^{\mathrm{miss}}\,2e$). Figure 5.2(b) shows the invariant mass distribution of the event class with two muons and two electrons ($2\mu\,2e$). Figure 5.2(c) shows the missing transverse momentum distribution of the event class with one electron, three b-jets, two light jets and large missing transverse momentum ($E_{\mathrm{T}}^{\mathrm{miss}}\,1e\,3b\,2j$). Figure 5.2(d) shows the H_{T} distribution of the event class with two b-jets and four light jets ($2b\,4j$). Figure 5.2(e) shows the invariant mass distribution of the event class with one muon, two electrons, one b-jet and two light jets ($1\mu\,2e\,1b\,2j$) and Figure 5.2(f) shows the effective mass distribution of the event class with one electron, one photon, two b-jets and one light jet ($1e\,1\gamma\,2b\,1j$). The regions with the largest deviation found by the search algorithm in these distributions (RoI), an excess in Figures 5.2(a), 5.2(b), 5.2(c), 5.2(d) and 5.2(e), and a deficit in Figure 5.2(f), are indicated by vertical blue dashed lines. The observed and expected number of events[4] in the RoI, as well as the corresponding p_0, are given in the figure.

Requiring $C_{\mathrm{SM}} > 0.01$ in order for p_0 to be computed, avoids sensitivity to spurious deviations arising from too few or no MC events to properly model the expectation value in a too finely binned histogram, and forces the algorithm to combine multiple bins. However, it can also reduce the significance of a signal, for instance, in the tail of a distribution where the algorithm can be forced to vastly enlarge the region. Therefore, regions having $C_{\mathrm{SM}} < 0.01$ and $C_{\mathrm{obs}} \geq 3$, which can potentially deviate enough for a DDSR, are investigated and a p_0-value is computed and compared to the distribution of p_{class}-values from the scan. Table 5.8 lists six regions having $C_{\mathrm{SM}} < 0.01$ and $C_{\mathrm{obs}} \geq 3$, five of which occur in the 2μ and $E_{\mathrm{T}}^{\mathrm{miss}}\,1e\,1j$ event classes as a result of MC events with a large negative weight entering a bin and strongly reducing the SM expectation value. In these cases the expectation value has a large statistical MC uncertainty and hence the smallest p_0 is only 0.39. The other region occurs in the $1\gamma\,2b\,2j$ event class with $C_{\mathrm{SM}} = 0.008 \pm 0.302$ and $C_{\mathrm{obs}} = 3$ resulting in $p_0 = 5.1 \cdot 10^{-3}$. None of these deviations are large enough to meet the criteria for a DDSR.

[4]Occasionally, an uncertainty on the expected number of events larger than 100% is quoted. Since negative expectation values are unphysical, these should be interpreted according to their treatment in Eq. 4.37, i.e. as the probability of observing no events.

5.5.4 Pseudo experiments

As described in Section 4.3.5, pseudo-experiments are generated to derive the probability of finding a p_0-value of a given size, for a given observable and algorithm. The p_{class}-value distributions of the pseudo-experiments and their properties can be compared with the p_{class}-value distribution obtained from experiment. Correlations in the uncertainties of the SM expectation affect this probability and their effect is taken into account in the generation of pseudo-data as outlined in the following.

For the experimental uncertainties, each of the 35 nuisance parameters, associated with a different source of uncertainty, are varied independently by drawing a value at random from a Gaussian pdf. The variation of a given nuisance parameter is identical (i.e. correlated) across all bins and event classes. Uncertainties in the cross-sections of the various backgrounds and the integrated luminosity are also treated as correlated across all bins and event classes. Likewise, theoretical shape uncertainties estimated from scale variations or from the differences with alternative generators, are treated as correlated. The only exceptions are uncertainties used for some SM processes that are not derived from explicit variations. These are treated as uncorrelated, both between event classes and between bins of the same event class. Scale variations are applied in the generation of pseudo-experiments by varying the renormalization, factorization, resummation and merging scales independently. The value of each scale variation is again correlated between all bins and event classes and varied only between different pseudo-experiments. The scales are correlated between processes of the same type that are generated with a similar generator set-up, i.e. scales are correlated among the $W/Z/\gamma+$jets processes, among all the diboson processes, among the $t\bar{t}+W/Z$ processes, and among the single-top processes.

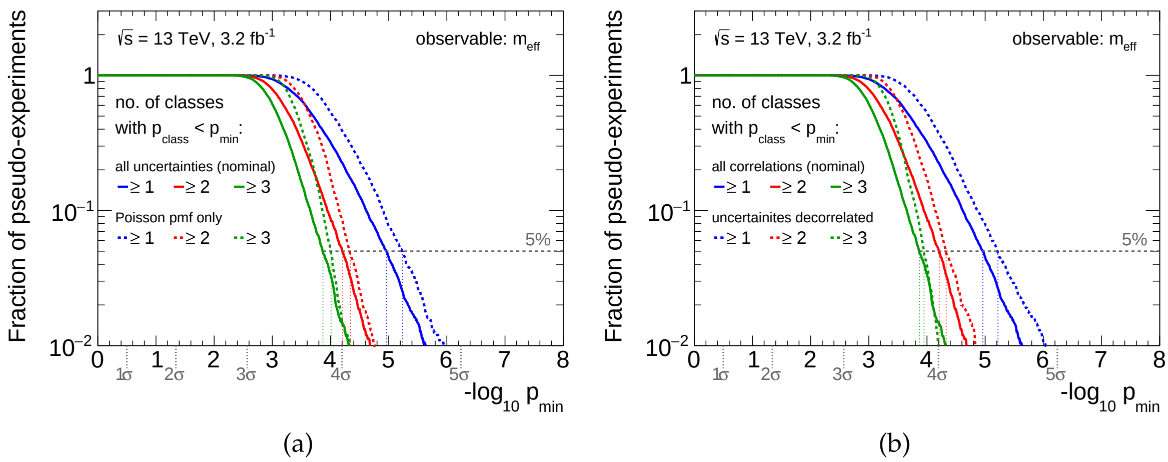

Figure 5.3: Comparison of the fractions of pseudo-experiments which have at least one, two and three p_{class}-values below a given p_{min} in the scan of the m_{eff} observable. In (a) a background model without *any* experimental or theory uncertainties (dashed curves) is compared to the nominal background model (solid curves). In (b) a background model in which all bin-by-bin correlations in the uncertainties are decorrelated (dashed curves) is compared to the nominal background model (solid curves). For both background models the resulting thresholds for which $P_{\text{exp},i} < 5\%$ are marked by vertical dotted lines.

It should be noted that while the size of the systematic uncertainties and the correlations in the uncertainty affect the (cumulative) distribution of the expected p_{class}-values, this is only a small effect, as changing the correlation model or the size of the uncertainties in the background model affects both the variations in the pseudo-data and the size of the uncertainty used in the computation of the p_0-value. To illustrate this, Figure 5.3(a) compares the fraction of pseudo-experiments which have at least one, two or three p_{class}-values below a given $p_{\min}$, for both: a background model without *any* experimental or theory uncertainties, i.e. using only the Poisson pmf to generate the pseudo-data and compute the p_0-values (dashed curves); and the nominal background model where all uncertainties are included (solid curves), for the m_{eff} scan. The differences between the thresholds for which $P_{\text{exp},i} < 5\%$ can be seen to be relatively small and demonstrate the important property that the thresholds are predominantly determined by the number of event classes and regions therein. Removing all experimental and theory uncertainties can, obviously, have a very large effect on the computed p_0-value of any given deviation, e.g. from the experiment.

Similarly, Figure 5.3(b) compares the fraction of pseudo-experiments for both: a background model decorrelating all the bin-by-bin variations due to experimental and theory uncertainties (dashed curves); and the nominal background model where all correlations in the uncertainties are as described above (solid curves). Again, the differences in the thresholds are relatively small, but the effect on the computed p_0-value of any given deviation in a region consisting of multiple bins can be large.

The same tests have been performed for the scans of the other observables with similar results. The results can be found in Appendix G.

5.5.5 Sensitivity tests

In the following section the sensitivity of the scan algorithm to possible signals is evaluated. It should be stressed that these tests show the sensitivity to signals for which no optimizations have been made in the analysis to discover them. The sensitivity of the procedure is evaluated with two different methods that either use:

- A modified background expectation value through the removal of an SM process or
- Pseudo-data samples generated from an SM plus signal expectation value.

As a figure of merit, the fraction of *signal* pseudo-experiments, i.e. those generated from an expectation value that differs from the one in the background model, with $P_{\text{exp},i} < 5\%$ is computed for $i = 1, 2$ and 3.

Sensitivity to Standard Model processes

Sensitivity to the WZ diboson process In order to test the sensitivity to known SM processes, the analysis can be performed with an SM process removed from the background prediction, while generating pseudo-data from the complete SM prediction to simulate the experimental data. Here, the sensitivity to the WZ diboson process is tested. It is removed from the background prediction which is denoted as 'SM-WZ' with expectation value $C_{\text{SM-}WZ} = C_{\text{SM}} - C_{WZ}$. The number of event classes satisfying $C_{\text{SM-}WZ} > 0.1$ and thereby entering the scan is 712, i.e. 18 less than in the nominal case as listed in Table F.2 of Appendix F.

In Figure 5.4, the solid curves show the expected p_{class} distributions in an analysis using a background prediction not containing the WZ process. It is obtained from pseudo-experiments in which pseudo-data are generated from the 'SM-WZ' background prediction and which are tested against the same 'SM-WZ' background prediction. These define the $p_{\min}$ thresholds at

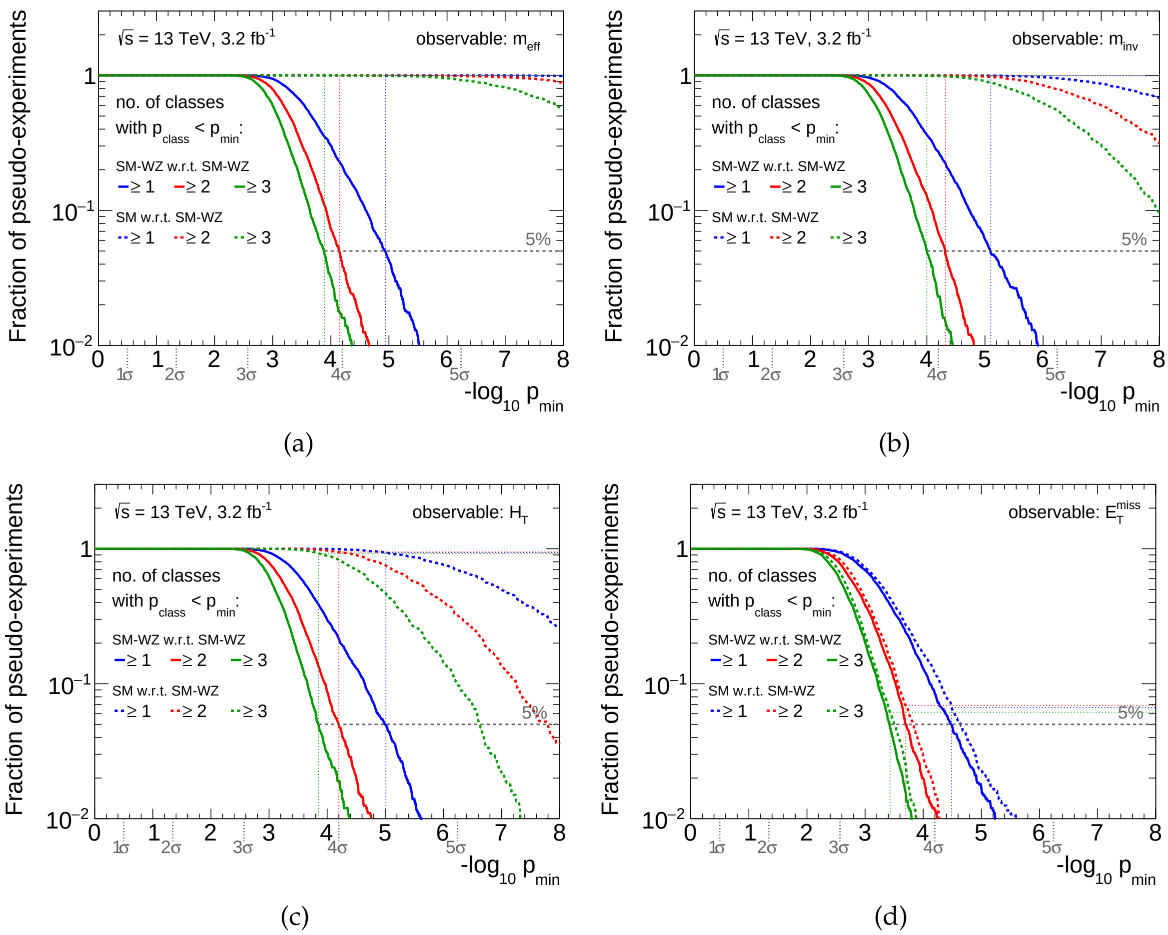

Figure 5.4: The fraction of pseudo-experiments which have at least one, two and three p_{class}-values below a given p_{min}, given for both: pseudo-experiments generated from a modified expectation and tested against the modified expectation (solid); and pseudo-experiments generated from the nominal expectation and tested against the modified expectation (dashed). The modified expectation consists of all contributions from SM processes except the WZ diboson process and is denoted 'SM-WZ'. The m_{inv} scan is shown in (a), the m_{eff} scan in (b), the H_{T} scan in (c) and the $E_{\text{T}}^{\text{miss}}$ scan in (d). The horizontal dotted lines mark the fractions of signal pseudo-experiments having $P_{\text{exp},i} < 5\%$ when tested against the modified background prediction.

which $P_{\text{exp},i} < 5\%$. Vertical dotted lines are drawn at the threshold values. The dashed curves show the p_{class} distributions obtained from pseudo-experiments in which pseudo-data are generated from the complete SM prediction (including the WZ process) and which are tested against the 'SM-WZ' background prediction. The horizontal dotted lines mark the fraction of *signal* pseudo-experiments that meet the $P_{\text{exp},i} < 5\%$ requirement for one or more DDSRs. In the m_{eff} and m_{inv} scan, the fraction is about 100% in all three cases $i = 1, 2$ and 3. In the H_{T} scan the fraction is more than 90% in all three cases $i = 1, 2$ and 3; while the $E_{\text{T}}^{\text{miss}}$ scan, which only considers classes with $E_{\text{T}}^{\text{miss}} > 200$ GeV, shows very low sensitivity with less than 7% of the *signal* pseudo-experiments having $P_{\text{exp},i} < 5\%$ for $i = 1, 2$ and 3. In conclusion, diboson WZ production can be found with this analysis, leading to its discovery in one or more DDSRs had its existence been unknown so far.

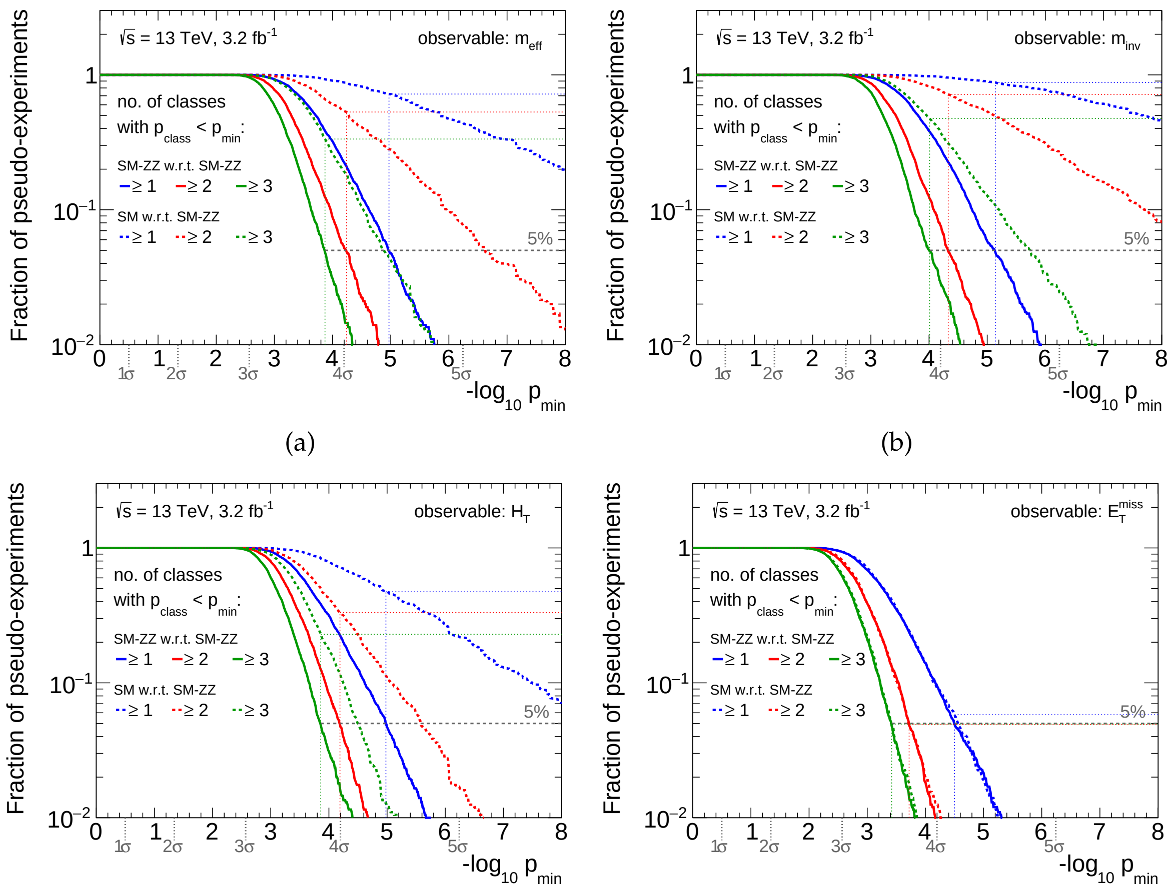

(a) (b) (c) (d)

Figure 5.5: The fraction of pseudo-experiments which have at least one, two and three p_{class}-values below a given p_{min}, given for both: pseudo-experiments generated from a modified expectation and tested against the modified expectation (solid); and pseudo-experiments generated from the nominal expectation and tested against the modified expectation (dashed). The modified expectation consists of all contributions from SM processes except the ZZ diboson process and is denoted 'SM-ZZ'. The m_{inv} scan is shown in (a), the m_{eff} scan in (b), the H_{T} scan in (c) and the $E_{\text{T}}^{\text{miss}}$ scan in (d). The horizontal dotted lines mark the fractions of signal pseudo-experiments having $P_{\text{exp},i} < 5\%$ when tested against the modified background prediction.

Sensitivity to the ZZ diboson process Figure 5.5 shows the sensitivity to the ZZ diboson process. After removing the process from the background prediction, the number of event classes active in the scan is 719, i.e. 11 less than in the nominal case as listed in Table F.2 of Appendix F.

The m_{inv} is the most sensitive, with a fraction of *signal* pseudo-experiments having $P_{\mathrm{exp},1} < 5\%$ close to 90%. Therefore, diboson ZZ production can be found with this analysis in 90% of the cases, leading to its discovery in one or more DDSRs had its existence been unknown so far.

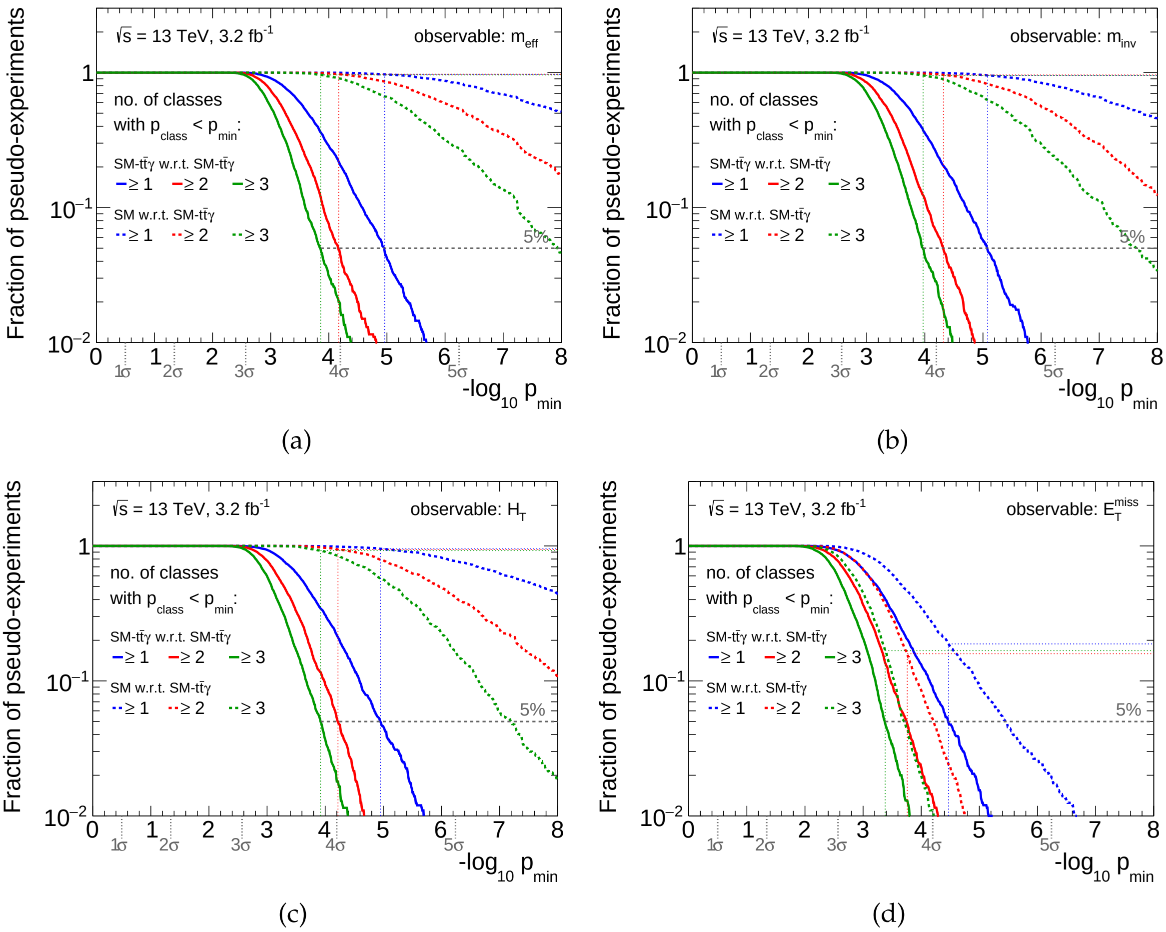

Figure 5.6: The fraction of pseudo-experiments which have at least one, two and three p_{class}-values below a given p_{min}, given for both: pseudo-experiments generated from a modified expectation and tested against the modified expectation (solid); and pseudo-experiments generated from the nominal expectation and tested against the modified expectation (dashed). The modified expectation consists of all contributions from SM processes except the $t\bar{t}+\gamma$ process and is denoted 'SM-$t\bar{t}\gamma$'. The m_{inv} scan is shown in (a), the m_{eff} scan in (b), the H_{T} scan in (c) and the $E_{\mathrm{T}}^{\mathrm{miss}}$ scan in (d). The horizontal dotted lines mark the fractions of signal pseudo-experiments having $P_{\mathrm{exp},i} < 5\%$ when tested against the modified background prediction.

Sensitivity to the $t\bar{t}+\gamma$ process Figure 5.6 shows the sensitivity to the $t\bar{t}+\gamma$ process. After removing the process from the background prediction, the number of event classes active in the scan is 681, i.e. 49 less than in the nominal case as listed in Table F.2 of Appendix F.

The m_{eff} scan is the most sensitive, with a fraction of *signal* pseudo-experiments having $P_{\mathrm{exp},i} < 5\%$ for $i = 1$, 2 and 3 close to 100%. Therefore, $t\bar{t}+\gamma$ production can be found with this analysis, leading to its discovery in one or more DDSRs had its existence been unknown so far.

Sensitivity to the $t\bar{t} + W/Z$ process The removal of any of three SM processes listed above leads to at least one DDSR with a large probability. The sensitivity to the $t\bar{t} + W/Z$ process has also been tested but in none of the scanned observables the ratio of *signal* pseudo-experiments with $P_{\mathrm{exp},i} < 5\%$ for $i = 1, 2$ or 3 exceeds 7%, indicating that the current analysis, i.e. integrated luminosity of the dataset, acceptance and choice of observables, has no sensitivity to this process.

Sensitivity to new-physics signals

Table 5.9: List of the Z' and $\tilde{g}$ benchmark signals used to generate signal pseudo-experiments. The predicted cross-section of each of the signals is given. As a figure of merit for the sensitivity of the search the percentage of signal pseudo-experiments having $P_{\mathrm{exp},i} < 5\%$ are given for $i = 1, 2$ and 3. No sensitivity to a signal (or absence of a signal) results by definition in a percentage of 5%. The statistical uncertainty on the percentage from the finite number of pseudo-experiments is approximately 1%.

Signal	Cross-section [fb]	Observable	$P_{\mathrm{exp},1} < 5\%$	$P_{\mathrm{exp},2} < 5\%$	$P_{\mathrm{exp},3} < 5\%$
Z' (2.0 TeV) $\to f\bar{f}$	743	m_{eff}	100%	98%	85%
		m_{inv}	100%	100%	88%
		H_{T}	100%	98%	88%
		$E_{\mathrm{T}}^{\mathrm{miss}}$	6%	5%	5%
Z' (2.5 TeV) $\to f\bar{f}$	216	m_{eff}	81%	42%	22%
		m_{inv}	95%	50%	25%
		H_{T}	81%	42%	23%
		$E_{\mathrm{T}}^{\mathrm{miss}}$	5%	5%	4%
Z' (3.0 TeV) $\to f\bar{f}$	71	m_{eff}	17%	8%	7%
		m_{inv}	38%	12%	7%
		H_{T}	17%	8%	7%
		$E_{\mathrm{T}}^{\mathrm{miss}}$	5%	4%	5%
Z' (3.5 TeV) $\to f\bar{f}$	26	m_{eff}	6%	5%	5%
		m_{inv}	8%	5%	4%
		H_{T}	6%	5%	4%
		$E_{\mathrm{T}}^{\mathrm{miss}}$	5%	4%	5%
$\tilde{g}$ (1.0 TeV) $\to t\bar{t}\tilde{\chi}_1^0$	232	m_{eff}	92%	91%	88%
		m_{inv}	84%	83%	80%
		H_{T}	86%	85%	82%
		$E_{\mathrm{T}}^{\mathrm{miss}}$	99%	99%	99%
$\tilde{g}$ (1.2 TeV) $\to t\bar{t}\tilde{\chi}_1^0$	57	m_{eff}	17%	13%	10%
		m_{inv}	8%	7%	6%
		H_{T}	13%	10%	8%
		$E_{\mathrm{T}}^{\mathrm{miss}}$	31%	25%	22%
$\tilde{g}$ (1.4 TeV) $\to t\bar{t}\tilde{\chi}_1^0$	16	m_{eff}	5%	5%	5%
		m_{inv}	4%	5%	5%
		H_{T}	5%	5%	5%
		$E_{\mathrm{T}}^{\mathrm{miss}}$	8%	6%	5%
$\tilde{g}$ (1.6 TeV) $\to t\bar{t}\tilde{\chi}_1^0$	5	m_{eff}	5%	4%	4%
		m_{inv}	4%	5%	5%
		H_{T}	6%	5%	4%
		$E_{\mathrm{T}}^{\mathrm{miss}}$	5%	5%	5%

In order to test the sensitivity to possible BSM signals, the analysis can be performed with the nominal SM background prediction, while generating pseudo-data from an SM-plus-signal prediction to simulate the experimental data. Two types of signals are used in this test,

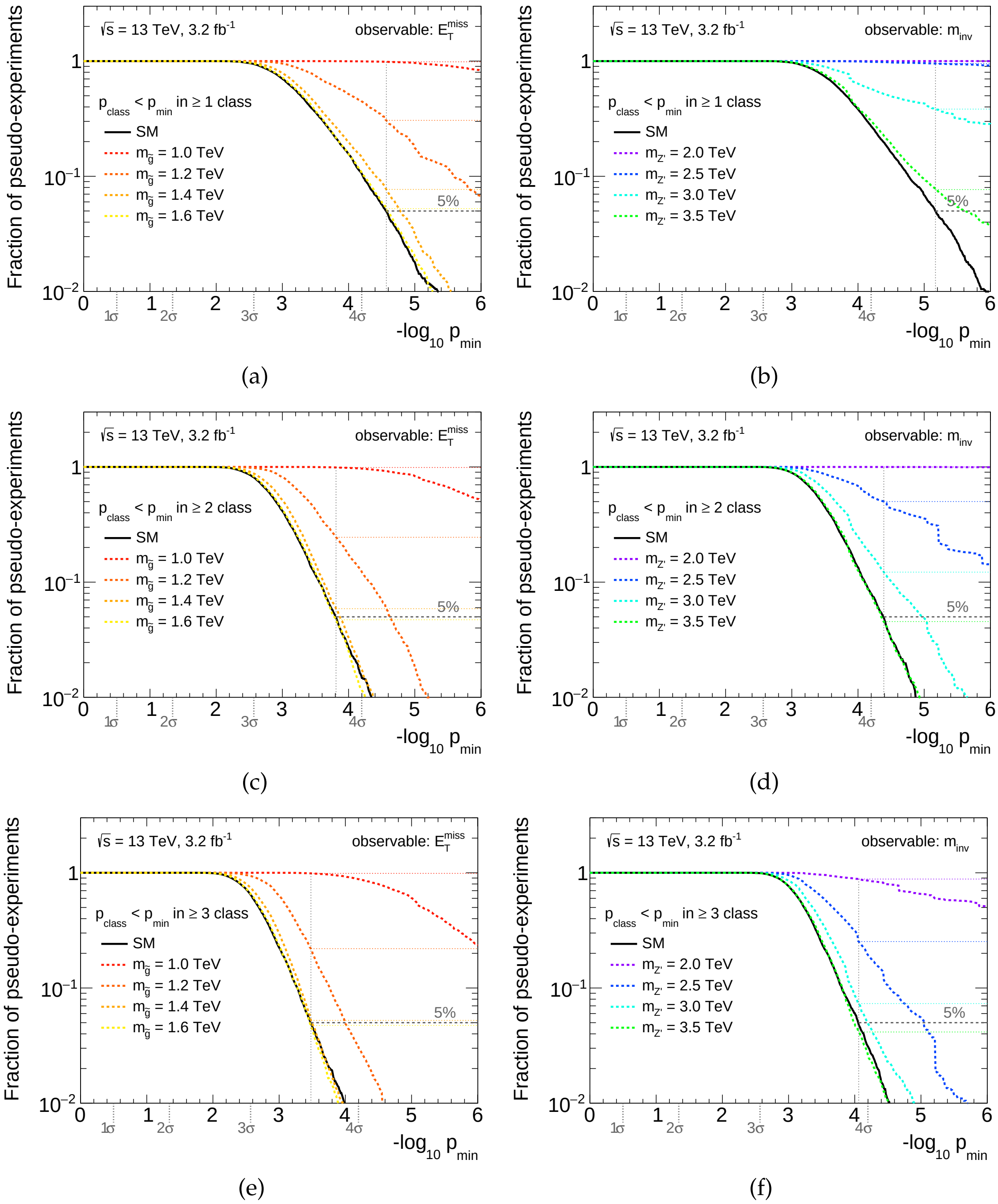

Figure 5.7: The fraction of pseudo-experiments that have at least one (top row), two (middle row) or three (bottom row) p_{class}-values below a given p_{min}. The fraction of signal pseudo-experiments are shown by the dashed curves and the solid black curve shows the fraction of nominal pseudo-experiments. In the left column, the signal pseudo-experiments assume gluino pair production with $\tilde{g} \rightarrow t\bar{t}\tilde{\chi}_1^0$ and the fractions are shown for the $E_{\text{T}}^{\text{miss}}$ scan which has the highest sensitivity. In the right column, the signal pseudo-experiments assume the production of an SSM Z' decaying into fermions and the fractions are shown for the m_{inv} scan which has the highest sensitivity to this type of signal. The horizontal dotted lines mark the fractions of signal pseudo-experiments having $P_{\text{exp},i} < 5\%$ when tested against the nominal SM background prediction.

the first one is the production of an SSM Z' boson decaying into fermions and having the same couplings as the SM Z boson. The second signal is the supersymmetric production of gluino pairs, each promptly decaying into a pair of top quarks and a nearly massless (1 GeV) neutralino. Table 5.9 lists the cross-sections of the injected signals for each of the assumed masses of the Z' or $\tilde{g}$ particle(s). The percentage of signal pseudo-experiments having $P_{\mathrm{exp},i} < 5\%$ for $i = 1$, 2 and 3 are also listed for all four observables. The statistical uncertainty on the percentage from the finite number of pseudo-experiments is about 1% which occasionally results in a percentage smaller than 5% when there is no sensitivity to a signal.

Figure 5.7 shows the sensitivity to the two benchmark signals considered as a function of the mass of the produced particle. For the Z' signal, where the mass of the resonance can be reconstructed from its decay products, the sensitivity to the signal is observed to be the largest in the scan of the m_{inv} distributions. Gluinos undergo a cascade decay process to the lightest neutralino, which is undetected and leads to missing transverse momentum. The sensitivity to the gluino signal is therefore found to be the largest in the scan of the $E_{\mathrm{T}}^{\mathrm{miss}}$ distributions.

A deviation for which $P_{\mathrm{exp},i} < 5\%$ promotes the selection to a DDSR. By applying this criterion, it can be seen in Figure 5.9 that the search is sensitive to a Z' boson with a mass of about 2.5 TeV as 95% of the signal pseudo-experiments show a deviation for which $P_{\mathrm{exp},1} < 5\%$. Similarly, the search is sensitive to the 1.0 TeV gluino signal used, with almost all signal pseudo-experiments showing a deviation for which $P_{\mathrm{exp},i} < 5\%$. It should be noted that these are tests of the discovery sensitivity and should therefore not be compared to the exclusion sensitivity of model-based searches.

5.6 Results of search algorithm applied to 2015 dataset

Table 5.10: List of the three event classes with the smallest p_{class}-values in each of the scans. The fraction of pseudo-experiments having smaller p_{class}-values than those observed from experiment are listed under $P_{\mathrm{exp},i}(p_{\mathrm{class}})$ for $i = 1$, 2 and 3, as well as the observed and expected number of events in the region selected by the scan algorithm as the RoI.

Observable	Class	p_{class} $(\cdot 10^{-3})$	$P_{\mathrm{exp},i}(p_{\mathrm{class}})$	C_{obs}	$C_{\mathrm{SM}} \pm \delta C_{\mathrm{SM}}$	Region [GeV]
m_{eff}	$1e\,1g\,7j$	0.19	49%	2	0.0106 ± 0.0089	1251–1743
	$E_{\mathrm{T}}^{\mathrm{miss}}\,2e$	2.08	97%	2	0.020 ± 0.049	1591–1774
	$1\mu\,1e\,4b\,2j$	2.66	97%	2	0.040 ± 0.036	992–1227
m_{inv}	$1e\,1g\,7j$	0.22	63%	2	0.0122 ± 0.0084	1743–2925
	$1\mu\,2e\,1b\,2j$	1.28	94%	2	0.015 ± 0.039	1892–2496
	$1\gamma\,2b\,2j$	2.23	98%	5	0.36 ± 0.46	3960–5301
H_{T}	$1e\,1g\,7j$	0.15	43%	2	0.0106 ± 0.0065	1251–1743
	$E_{\mathrm{T}}^{\mathrm{miss}}\,1\mu\,1\gamma\,1b\,3j$	2.52	99%	3	0.169 ± 0.093	630–737
	$1\mu\,2e\,1b\,2j$	3.41	99%	2	0.019 ± 0.070	1150–1892
$E_{\mathrm{T}}^{\mathrm{miss}}$	$E_{\mathrm{T}}^{\mathrm{miss}}\,2e\,3b$	3.53	97%	2	0.042 ± 0.047	266–341
	$E_{\mathrm{T}}^{\mathrm{miss}}\,1\mu\,3b$	4.38	93%	9	1.8 ± 1.1	325–570
	$E_{\mathrm{T}}^{\mathrm{miss}}\,1\mu\,1j$	6.11	94%	3	0.24 ± 0.12	1039–1085

Figure 5.8 shows the three smallest p_{class}-values observed from experiment in the 2015 ATLAS dataset, for each of the scanned observables, in comparison to the expected cumulative distribution of p_{class}-values from pseudo-experiments. The $P_{\mathrm{exp},i}(p_{\mathrm{class}})$-values of the deviations

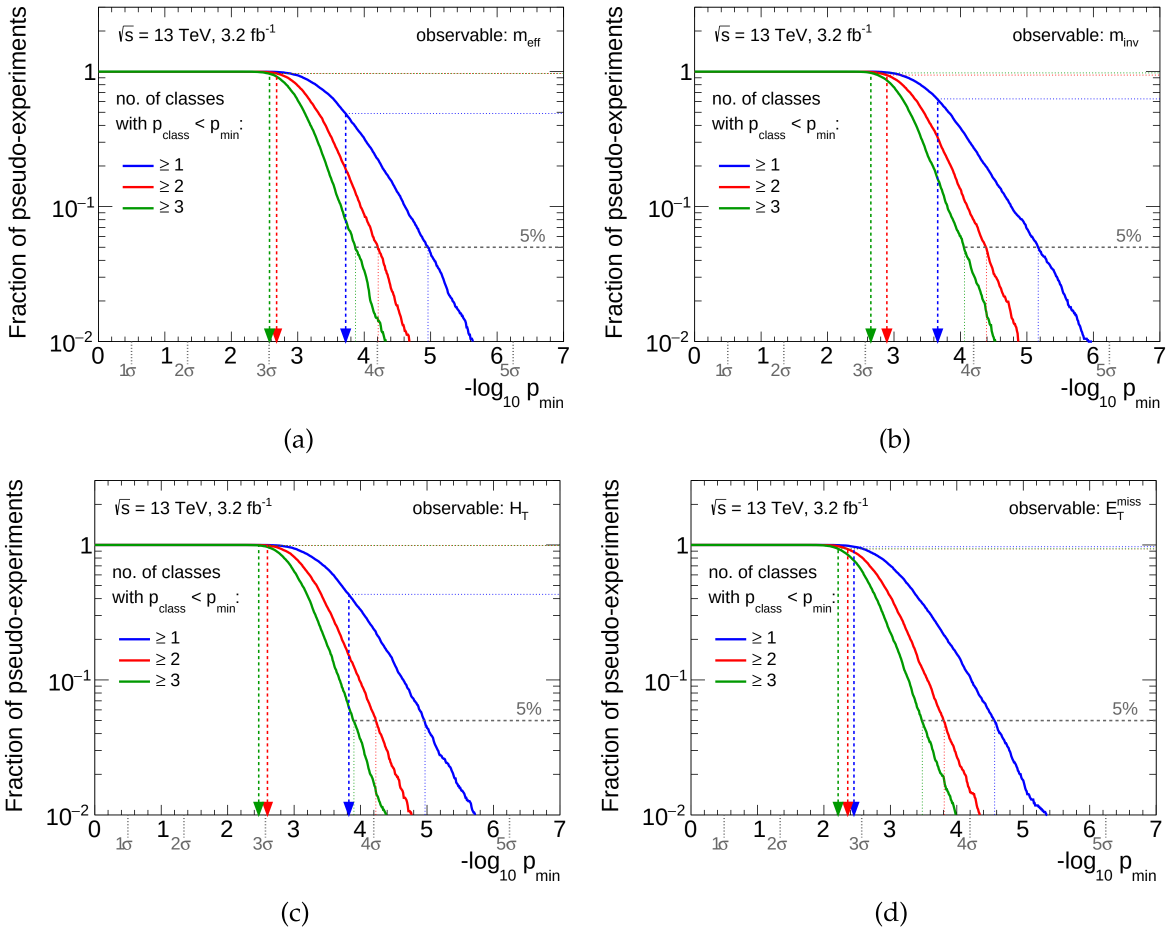

Figure 5.8: The fraction of pseudo-experiments that have at least one, two or three p_{class}-values below a given $p_{\min}$. The fraction of pseudo-experiments are shown by the solid curves and the three smallest p_{class}-values observed from the experiment are indicated by dashed arrows. The m_{eff} scan is shown in (a), the m_{inv} scan in (b), the H_{T} scan in (c) and the $E_{\text{T}}^{\text{miss}}$ scan in (d). The horizontal dotted lines mark the fractions of pseudo-experiments having p_{class}-values smaller than those observed from experiment. The vertical dotted lines mark the p_{class}-values for which $P_{\text{exp},i} < 5\%$ indicating the threshold for a DDSR.

observed from experiment are all larger than 5% and hence no DDSRs are defined. Table 5.10 summarizes the scan results for the three largest deviations per scanned observable.

The largest deviation reported by a dedicated search using the same dataset was observed in an inclusive diphoton data selection at a diphoton mass of around 750 GeV with a local significance of 3.9σ [206]. Due to the different event selections and background estimates the excess has a lower significance in this analysis. The excess was not confirmed in a dedicated analysis with 2016 data [207].

To ensure that the result in Figure 5.8 does not crucially depend on the correct estimate of the size of the theory uncertainties, experimental uncertainties or MC statistical uncertainties, the scans are repeated with: a background model in which *all* theory uncertainties are simultaneously reduced by a factor of two; a background model in which all MC statistical uncertainties are set to zero; and a background model in which *all* experimental uncertainties are simultaneously reduced by a factor of two. For all three cases, the three smallest p_{class}-values of each scanned observable are compared to the thresholds for which $P_{\text{exp},i} < 5\%$ as determined from the nominal background model. This can be done because it has been shown

Table 5.11: List of the three event classes with the smallest p_{class}-values in each of the scans. The fraction of pseudo-experiments having smaller p_{class}-values than those observed from experiment are listed under $P_{\text{exp},i}(p_{\text{class}})$ for $i = 1$, 2 and 3, as well as the observed and expected number of events in the region selected by the scan algorithm as the RoI.

	50% theory unc.		**no MC stat. unc.**		**50% experimental unc.**	
Observable	p_{class} $(\cdot 10^{-3})$	$P_{\text{exp},i}(p_{\text{class}})$	p_{class} $(\cdot 10^{-3})$	$P_{\text{exp},i}(p_{\text{class}})$	p_{class} $(\cdot 10^{-3})$	$P_{\text{exp},i}(p_{\text{class}})$
m_{eff}	0.18	47%	0.16	44%	0.15	42%
	0.87	74%	2.00	97%	1.23	86%
	1.00	61%	2.38	95%	1.46	80%
m_{inv}	0.21	61%	0.19	57%	0.19	57%
	0.31	45%	1.27	94%	0.36	51%
	0.55	48%	1.64	93%	0.55	48%
H_{T}	0.15	43%	0.13	40%	0.14	41%
	1.25	89%	2.28	99%	2.12	98%
	1.31	77%	3.41	99%	3.19	99%
$E_{\text{T}}^{\text{miss}}$	2.25	92%	3.09	96%	2.57	94%
	2.81	82%	4.28	93%	3.31	87%
	5.12	89%	5.70	92%	5.69	92%

in Section 5.5.4 that reducing the uncertainties does not significantly change the thresholds, and only shifts the thresholds to somewhat smaller p_0-values (i.e. larger $-\log_{10} p_0$). The results are summarized in Table 5.11. None of the tests result in a $P_{\text{exp},i} < 5\%$ and it can be concluded that the scan results do not crucially depend on the estimates of these uncertainties.

In conclusion, no significant deviations are found in the 2015 dataset and consequently no dedicated analysis using DDSRs is initiated.

6 Application to the combined 2015 & 2016 dataset

This chapter documents the preliminary version of the analysis using the 2015 & 2016 ATLAS datasets. The analysis is based on the analysis described in Chapter 5. Where appropriate, references are made to passages in Chapter 5 and the discussion is focussed on the differences and the results.

6.1 Data selection

6.1.1 Dataset

The data used in this chapter were collected by the ATLAS detector during 2015 and 2016 in pp collisions at the LHC with a centre-of-mass energy of 13 TeV and a 25 ns bunch crossing interval. After applying quality criteria for the beam, data and detector, the available dataset corresponds to an integrated luminosity of 36.2 fb^{-1}.

In this dataset, the average number of inelastic pp collisions per bunch crossing is 24, 14 for the data recorded in 2015 and 25 for the data recorded in 2016.

As in Chapter 5, all candidate events are required to have a reconstructed vertex.

6.1.2 Definition of objects

Signal objects The definitions of the objects are largely the same to those in Chapter 5 with some exceptions. Criteria are updated to be inline with the latests recommendations from the ATLAS Combined Performance groups and analysis groups. The differences are summarized below:

- *Baseline electron* candidates are required to pass the *LooseAndBLayer* likelihood-based identification requirement [208], requiring in addition to the *Loose* requirements (see Section 3.2) a hit in the innermost pixel layer of the ID to reduce the background from photon conversions.
- Electron candidates within the transition region between the barrel and endcap electromagnetic calorimeters, $1.37 < |\eta| < 1.52$, are *not* removed, as the additional uncertainty associated with the measurement of the electron energy in this region is negligible for this analysis.
- The updated isolation requirements applied to the signal electrons target E_{T}-dependent efficiencies increasing with the electron transverse momentum to 90% at 25 GeV and 99% at 60 GeV.

- The updated isolation requirement applied to signal muons is based on track isolation and optimised for high-p_{T} muons, requiring $p_{\mathrm{T}}^{\mathrm{cone0.2}} < 1.25$ GeV.
- Tighter quality criteria for (b-)jets against non-collision backgrounds are *only* applied to events with (b-)jets (and $E_{\mathrm{T}}^{\mathrm{miss}}$). The presence of other signal objects obsoletes this requirement.
- The b-tagging is performed with the recommended MV2C10 multivariate discriminant, which is trained on simulated $t\bar{t}$ events and a background in which 7% of the jets contain c-hadrons (c-jets). It has a similar light-flavour jet rejection as the 2015 MV2C20 configuration (but an improved c-jet rejection) [209].

Table 6.1 lists the reconstructed signal objects, along with their p_{T} and pseudorapidity requirements, used for the analysis in this chapter.

***Z* and Higgs boson objects** In this chapter, three additional objects are considered in special iterations of the scan algorithm: a Higgs boson decaying to two photons (h); a Higgs boson decaying to four leptons (H); and a Z boson decaying to two leptons (Z). The Higgs boson and Z boson objects are reconstructed from their decay products which need to pass the signal object requirements listed in Table 6.1.

A $h \to \gamma\gamma$ candidate is identified by requiring a signal photon pair with an invariant mass between 120 and 130 GeV. If such a pair is found, the two photons are removed and replaced by a Higgs boson, labelled h, with as its four-vector the sum of the four-vectors of the two photons. All photon pairs with a diphoton mass in the required range are replaced, where each photon can only be part of one pair. In case combinatorics allow a photon to be part of multiple diphoton pairs that satisfy the Higgs mass, the pair closest to the Higgs mass takes precedence.

A $h \to \ell\ell\ell\ell$ candidate is identified by requiring two oppositely charged same flavour signal lepton pairs, i.e. $\ell\ell\ell\ell = \{e^-e^+e^-e^+,\ \mu^-\mu^+\mu^-\mu^+,\ e^-e^+\mu^-\mu^+\}$, with an invariant mass between 110 and 135 GeV, and an invariant mass for one of the two pairs compatible with the Z mass (between 66 and 116 GeV). As for photon pairs, if four leptons are found satisfying the requirement, the four leptons are removed and replaced by a Higgs boson object, labelled H, with as its four-vector the sum of the four lepton four-vectors. Ambiguities would be treated in a similar way as for photons, however, none of the event classes defined by data or expectation contain more than four leptons as will be shown in Section 6.5.1 and so no ambiguities are present.

Finally, a $Z \to \ell\ell$ candidate is identified by requiring an oppositely charged same flavour signal lepton pair, i.e. $\ell\ell = \{e^-e^+,\ \mu^-\mu^+\}$, with an invariant mass between 66 and 116 GeV. All pairs with the required dilepton mass are replaced by a Z boson, except when the lepton pair satisfies the H requirements together with another signal lepton pair in which case the H object takes precedence. As for photon pairs, in case combinatorics allow a lepton to be part of multiple dilepton pairs that satisfy the Z mass, the pair closest to the Z mass takes precedence.

Table 6.1 lists the composite objects, along with the required signal objects and mass requirements. The relatively large p_{T} requirements on the signal leptons and photons, can only be produced by boosted Higgs bosons.

Table 6.1: Physics objects used for classifying events. For each signal object the corresponding label, minimum p_{T} requirement, and pseudorapidity requirement is given, and for composite objects the constituents and mass requirements are given.

Signal object	Label	p_{T} (min) [GeV]	Pseudorapidity
Isolated electron	e	25	$\lvert\eta\rvert < 2.47$
Isolated muon	μ	25	$\lvert\eta\rvert < 2.70$
Isolated photon	γ	50	$\lvert\eta\rvert < 1.37$ or $1.52 < \lvert\eta\rvert < 2.37$
b-tagged jet	b	60	$\lvert\eta\rvert < 2.50$
Light (non-b-tagged) jet	j	60	$\lvert\eta\rvert < 2.80$
Missing transverse momentum	$E_{\mathrm{T}}^{\mathrm{miss}}$	200	
Composite object	**Label**	**Signal objects**	**Mass requirement [GeV]**
Z boson candidate	Z	e^-e^+	$66 < m_{\mathrm{inv}}(\ell\ell) < 116$
		$\mu^-\mu^+$	
Higgs boson candidate	h	$\gamma\gamma$	$120 < m_{\mathrm{inv}}(\gamma\gamma) < 130$
Higgs boson candidate	H	$Z + e^-e^+$	$110 < m_{\mathrm{inv}}(Z + \ell\ell) < 135$
		$Z + \mu^-\mu^+$	

6.1.3 Definition of event classes

Exclusive event classes Events are divided into mutually exclusive classes that are labelled with the number and type of reconstructed objects listed in Table 6.1 similarly to the classification in Chapter 5. When the composite h, H, and Z objects are considered, they are used to define classes in the same manner as any other signal object.

Merged event classes Applying the search algorithm to event classes that are exclusive in the number of jets can be advantageous as it can enhance the sensitivity to, for instance, signal processes that produce events with a large number of jets. However, in other cases, a contribution from a possible signal might be spread out over several event classes with a different jet count or lepton flavour. To avoid missing such contributions, the scan algorithm can be applied to event classes that use a more inclusive class definition, but are still mutually exclusive. Using a procedure to merge classes also reduces the total number of event classes and hence the number of tests performed, thereby reducing the LEE. In addition to the exclusive event classes this chapter also considers *merged* event classes that are:

- Inclusive in the number of non-b-tagged jets, e.g.: $2\gamma\,3j \rightarrow 2\gamma$ (i).
- Inclusive in the number of b-tagged jets if there are two or more, e.g.: $2\gamma\,1b\,1j \rightarrow 2\gamma\,1b$ (i) and $2\gamma\,3b\,1j \rightarrow 2\gamma\,2{+}b$ (i).
- Inclusive in different lepton flavours (e or μ), e.g.: $2e\,3b\,1j \rightarrow 2l\,2{+}b$ (i) and $2\mu\,1e\,1j \rightarrow 2l\,1l'$ (i).

where '(i)' indicates that the class is *inclusive* in non-b-tagged jets. The lepton label l is used to count the dominant lepton flavour in the event and l' is used to count the remaining leptons of the other flavour.

6.1.4 Triggers and event selection

The trigger and offline event selections are similar to the selection procedure in Chapter 5 with some exceptions:

- The increase in instantaneous luminosity provided by the LHC in 2016 requires more stringent trigger requirements in order not to exceed to maximum trigger bandwidth. A reconstruction-level p_{T} requirement is added for single lepton trigger selections to avoid trigger inefficiencies as a result of the large lepton p_{T} required by the trigger.
- The single-photon reconstruction-level p_{T} requirement is increased for the same reason mentioned above.
- The diphoton trigger selection requirement is removed since these triggers are no longer included in the derivation being used.
- The single jet trigger selection requirement is removed since also these triggers are no longer included in the derivation being used.

The acceptance has thus been limited in this preliminary version of the analysis as a result of changes to the derivation selection[1]. To obtain the same (or a larger) acceptance level in the future as the analysis in Chapter 5, multiple derivations would need to be used. Figure 6.1 summarizes the trigger and event selection used in this chapter.

Events subject to additional cuts are marked in Figure 6.1 as 'Accepted*'. For event classes with $1\mu + X$, $1e + X$ and $1\mu 1e + X$, where X can be photons, jets or $E_{\mathrm{T}}^{\mathrm{miss}}$, an additional reconstruction-level cut is applied requiring at least one of the following conditions:

- $H_{\mathrm{T}}(\mathrm{jets}) > 150$ GeV
- $p_{\mathrm{T}}(\ell) > 100$ GeV

Event classes with $E_{\mathrm{T}}^{\mathrm{miss}} > 200$ GeV and photons or jets are required to pass at least one of the following conditions:

- $H_{\mathrm{T}}(\mathrm{jets}) > 150$ GeV
- $p_{\mathrm{T}}(\gamma) > 100$ GeV

The full selection requirements per event class are discussed in Appendix C.

The quality cuts are identical to those applied in Chapter 5 and are listed in Table 5.2.

6.2 Monte Carlo simulation

6.2.1 Monte Carlo samples for Standard Model processes

For all SM processes, the MC simulated event samples are updated with respect to those used in Chapter 5 to include the correct average pile-up and detector conditions (i.e. triggers, calibrations, alignments, disabled readout channels, etc.) for each of the data-taking time periods in the years 2015 and 2016, and to include the latest developments in detector simulation and object reconstruction. Additionally, the latest techniques are used in the MC event generators to improve the formal accuracy, PDF sets and PS predictions.

The pile-up for this dataset is modelled with a set of minimum-bias interactions generated using PYTHIA 8.210 [107], the `NNPDF2.3LO` PDF set and the updated A3 [210] tune. SM processes generated with SHERPA use the upgraded SHERPA 2.2 [104] series and the

[1] The derivation used in this chapter applies an additional *trigger skimming*, meaning it requires events to pass at least one of the triggers in a predefined list. This list does not include diphoton and jet triggers.

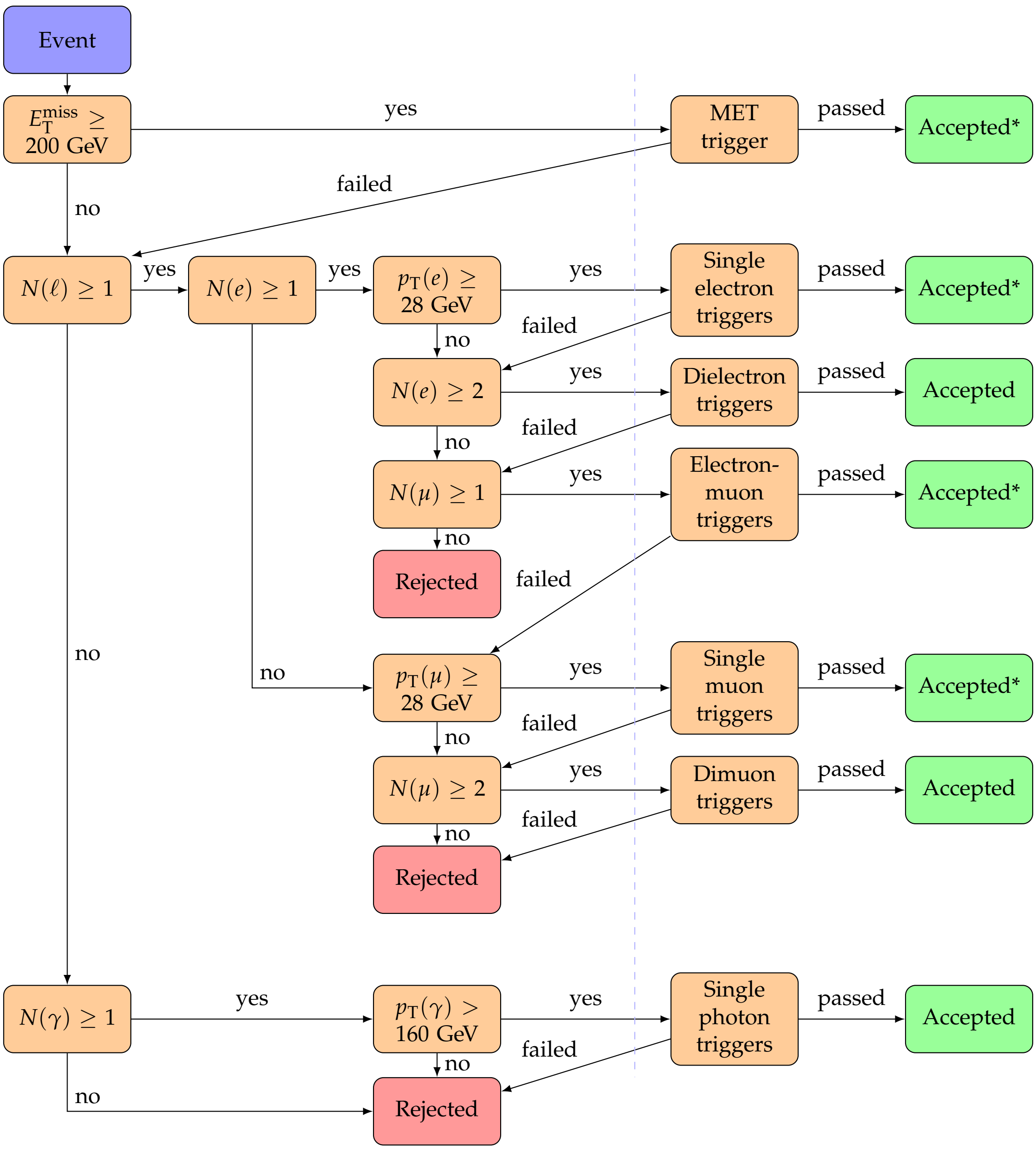

Figure 6.1: Flow diagram of the trigger and offline event selection strategy. The offline requirements are shown on the left of the dashed line and the trigger requirements are shown on the right of the dashed line. N is the object multiplicity of the object between brackets and ℓ stands for e or μ as defined in Table 6.1. Events accepted by a box marked with an asterisk (*) can be subject to additional cuts which are discussed in detail in Appendix C. Note that no diphoton and single-jet triggers are used and hence jet-only events (without ℓ, γ or E_T^{miss}) are not analysed.

NNPDF3.0NNLO [211] PDF set. The generator setup is described in Refs. [212] and [213] for boson plus jets and multiboson production respectively. Top-quark pairs and single top-quarks in the Wt-, t- and s-channels are simulated using the POWHEG-BOX v2 generator with the NNPDF3.0NLO PDF set (NNPDF3.0NLOf4 fixed four-flavour PDF set for t-channel); interfaced to PYTHIA 8.230 using the A14 tune with the NNPDF2.3LO PDF set for the PS, fragmentation, and the underlying event; and an updated value of the h_{damp} parameter to 1.5 times the mass of the top-quark, as detailed in Ref. [214]. Samples of the production of top-quark pairs in association with massive bosons (H, W, Z) are generated at NLO with MG5_aMC@NLO using the NNPDF3.0NLO PDF set and interfaced to PYTHIA 8.210 with the A14 tune, as detailed in Ref. [188].

The updated SM MC programs used for the background model in this chapter are listed in Table 6.2. At the moment of writing, samples of triple-photon ($\gamma\gamma\gamma$) production and Higgs boson production via gluon fusion (ggF) and W/Z boson fusion (VBF) where not yet available and are therefore missing from the SM background prediction used in this preliminary analysis[2]. For Higgs boson production in association with a $t\bar{t}$ pair ($t\bar{t}H$), samples of the decay channel to a pair of photons are also missing. Samples of several processes with a small cross-section ($O(10$ fb$)$ or smaller) are also not yet available such as e.g. $t\bar{t}+WZ$, $t\bar{t}+ZZ$, $t\bar{t}+Z\gamma$, $t\bar{t}+W\gamma$, $t\bar{t}+\gamma\gamma$, tH, $Wt+H$, $Wt+Z$, $WW\gamma$, $WZ\gamma$, etc. although for some processes the phase-space is already (partially) included in other samples listed in Table 6.2. The (preliminary) search strategy, which will be described in Section 6.4, is adapted to allow the use of an incomplete background model.

Whereas in Chapter 5 a single background model is constructed for all event classes, in this chapter different subsets of samples and different overlap removal procedures are applied to model the SM expectation depending on the event class or validation selection being considered. The overlap between $W/Z+$jets and $W/Z+\gamma(\gamma)$ samples is addressed as follows: for event classes without photons or validation selections without a photon requirement (i.e. inclusive in additional photons) the inclusive $W/Z+$jets samples are used and no overlap removal is applied; for event classes / validation selections requiring one photon, the $W/Z+\gamma$ and inclusive samples are used after removing events in the overlapping phase-space from the inclusive sample; for event classes / validation selections requiring two or more photons, the $W/Z+\gamma\gamma$, $W/Z+\gamma$ and inclusive samples are used after removing events in the overlapping phase-space from the inclusive and $W/Z+\gamma$ samples. This method ensures that the samples generated with the highest formal accuracy are being used to model the SM expectation whenever MC statistics are sufficient. The same approach is applied to the $t\bar{t}$ and $t\bar{t}+\gamma$ samples.

Since the multijet event classes are not part of the selection, the QCD multijet samples are not used in the background model. Possible contributions from QCD events, in event classes containing other objects than jets, through misreconstructed objects (fakes) cannot be estimated reliably using MC since the number of simulated events is too small. The absence of possible QCD contributions (fake contributions) in the background model can lead to an underestimation of the number of expected events and is discussed further in Section 6.4.

[2] Although gluon fusion and W/Z boson fusion are the dominant Higgs production modes, the acceptance of the analysis for these events is very low due to the high p_{T} requirements on the signal leptons and on the leading photon for $\gamma\gamma(+$jets$)$ final states (see Figure 6.1). Events selected by the $E_{\mathrm{T}}^{\mathrm{miss}}$ or lepton triggers and containing a Higgs boson decaying to two photons have a much larger acceptance.

Table 6.2: A summary of the MC samples used in this chapter to model SM background processes. For each sample the corresponding generator, matrix element (ME) accuracy, parton shower (PS), cross-section normalization accuracy, parton density function (PDF) set and tune are indicated. Z refers to γ^* / Z.

Physics process	Generator	ME accuracy	Parton shower	Cross-section normalization	PDF set	Tune
$W (\to \ell\nu)$ + jets	Sherpa 2.2.1	0,1,2j@NLO + 3,4j@LO	Sherpa 2.2.1	NNLO	NNPDF3.0NNLO	Sherpa
$Z (\to \ell^+\ell^-)$ + jets	Sherpa 2.2.1	0,1,2j@NLO + 3,4j@LO	Sherpa 2.2.1	NNLO	NNPDF3.0NNLO	Sherpa
$Z (\to \nu\bar{\nu})$ + jets	Sherpa 2.2.1	0,1,2j@NLO + 3,4j@LO	Sherpa 2.2.1	NNLO	NNPDF3.0NNLO	Sherpa
Z / $W + \gamma$	Sherpa 2.2.2	0,1j@NLO + 2,3j@LO	Sherpa 2.2.2	NLO	NNPDF3.0NNLO	Sherpa
Z / $W + \gamma\gamma$	Sherpa 2.2.2	0j@NLO + 1,2j@LO	Sherpa 2.2.2	NLO	NNPDF3.0NNLO	Sherpa
γ + jets	Sherpa 2.2.2	0,1,2j@NLO + 3,4j@LO	Sherpa 2.2.2	NLO	NNPDF3.0NNLO	Sherpa
$\gamma\gamma$ + jets	Sherpa 2.2.4	0,1j@NLO + 2,3j@LO	Sherpa 2.2.4	NLO	NNPDF3.0NNLO	Sherpa
$t\bar{t}$	Powheg-Box v2	NLO	Pythia 8.230	NNLO+NNLL	NNPDF3.0NLO	A14
$t\bar{t} + W$	MG5_aMC@NLO 2.3.3	NLO	Pythia 8.210	NLO	NNPDF3.0NLO	A14
$t\bar{t} + Z$	MG5_aMC@NLO 2.3.3	NLO	Pythia 8.210	NLO	NNPDF3.0NLO	A14
$t\bar{t} + WW$	MG5_aMC@NLO 2.2.2	LO	Pythia 8.186	NLO	NNPDF2.3LO	A14
$t\bar{t} + \gamma$	MG5_aMC@NLO 2.2.3	LO	Pythia 8.186	NLO	NNPDF2.3LO	A14
Single-top (t-channel)	Powheg-Box v2	NLO	Pythia 8.230	app. NNLO	NNPDF3.0NLOf4	A14
Single-top (s- and Wt-channel)	Powheg-Box v2	NLO	Pythia 8.230	app. NNLO	NNPDF3.0NLO	A14
tZ	MG5_aMC@NLO 2.2.2	LO	Pythia 8.186	NLO	NNPDF3.0LO	A14
3-top	MG5_aMC@NLO 2.2.2	LO	Pythia 8.186	LO	NNPDF2.3LO	A14
4-top	MG5_aMC@NLO 2.2.2	LO	Pythia 8.186	NLO	NNPDF2.3LO	A14
WW / WZ / ZZ (semi-lept.)	Sherpa 2.2.1	0,1j@NLO + 2,3j@LO	Sherpa 2.2.1	NLO	NNPDF3.0NNLO	Sherpa
WW / WZ / ZZ (fully-lept.)	Sherpa 2.2.2	0,1j@NLO + 2,3j@LO	Sherpa 2.2.2	NLO	NNPDF3.0NNLO	Sherpa
$ZZ (\to \nu\bar{\nu}\nu\bar{\nu})$	Sherpa 2.2.1	0,1j@NLO + 2,3j@LO	Sherpa 2.2.1	NLO	NNPDF3.0NNLO	Sherpa
$gg \to ZZ$ / WW (semi-lept.)	Sherpa 2.2.2	0,1j@LO	Sherpa 2.2.2	LO	NNPDF3.0NNLO	Sherpa
Higgs ($t\bar{t}H$)	MG5_aMC@NLO 2.2.3	NLO	Pythia 8.210	NLO	NNPDF3.0NLO	A14
Higgs (W/ZH)	Pythia 8.186	LO	Pythia 8.186	NNLO	NNPDF2.3LO	A14
Tribosons (fully-lept., on shell)	Sherpa 2.2.2	0j@NLO + 1,2,3j@LO	Sherpa 2.2.2	NLO	NNPDF3.0NNLO	Sherpa
Tribosons (fully-lept., off shell)	Sherpa 2.2.1	0,1j@LO	Sherpa 2.2.1	LO	NNPDF3.0NNLO	Sherpa
Tribosons (semi-lept.)	Sherpa 2.2.2	0(,1)j@LO	Sherpa 2.2.2	LO	NNPDF3.0NNLO	Sherpa

6.2.2 Systematic uncertainties

Experimental uncertainties Experimental systematic uncertainties are determined and treated as described in Section 5.2.3. A total of 53 sources of experimental uncertainties are identified pertaining to one or more physics objects considered and for each source, the one-standard-deviation (1σ) CI is propagated to a 1σ CI around the nominal SM expectation. The total experimental uncertainty of the SM expectation is obtained from the sum in quadrature of all 53 1σ CIs and the uncertainty of the luminosity measurement which for the combined 2015 and 2016 dataset is determined at 2.1% [202].

Theoretical modelling uncertainties To estimate the dominant theory uncertainties, several variations are applied at the generator level and propagated to uncertainties on the final expectation values.

Modelling uncertainties for all processes generated with SHERPA are determined by varying the renormalization and factorization scales by factors of 0.5 and 2; by using two alternative PDF sets (`CT14NNLO` [215] and `MMHT2014NNLO` [216]); and by varying α_S by ± 0.001 around the nominal value of 0.118[3]. The different uncertainty components and the statistical uncertainty of the prediction are summed in quadrature to get the combined theory uncertainty.

For top-quark pair or single-top production, the modelling uncertainty is determined by constructing a two-point variation, varying the renormalization and factorization scales, and simultaneously applying variations of α_S for initial state radiation in the A14 shower tune. Furthermore, two alternative PDF sets (`CT14NLO` and `MMHT2014NLO`) are used as a source of uncertainty, and α_S is varied by ± 0.001 around the nominal value of 0.118[4]. As in Chapter 5, an uncertainty in the interference between the Wt and $t\bar{t}$ production is estimated by comparing *diagram-removed* samples to *cross-section-subtracted* samples.

Explicit variations are not yet available for samples generated with MG5_aMC@NLO. For processes with a cross-section normalisation known at NLO an uncorrelated uncertainty is applied to the normalisation based on the variation of the scales, PDFs sets and α_S. For the $t\bar{t} + W/Z/H$ processes a 13% uncertainty is assigned to the cross-section normalisation [175], while for the $t\bar{t} + WW/\gamma$, tZ, 3-top and 4-top samples, generated a LO, a more conservative uncertainty estimate of 50% is assigned to the cross-section normalisation, as in Chapter 5.

6.3 Validation of the background model

The modelling of the dominant SM processes is validated, as described in Chapter 5, by producing the validation distributions summarized in Table 5.4. A total of 442 validation distributions are made of which a selection of 133 is shown in Figures H.1–H.18 of Appendix H.

In this preliminary version of the analysis, no event classes are discarded and no corrections have been made to the background model, i.e. the sum of the nominal generator predictions is used as an estimate of the SM expectation in all event classes. However, the change in the selection procedure summarized in Figure 6.1, in comparison to the selection in Chapter 5 means that there are no jet-only event classes with $E_{\mathrm{T}}^{\mathrm{miss}} < 200$ GeV. In Chapter 5, event

[3]The α_S variations are not available/applied in samples of the $Z \to \mu\mu$ process.

[4]The α_S variations are not available/applied in samples of single top production.

classes with one electron and several (b-)jets were discarded due to the large contribution of multijet events (fake contribution). In Figure H.1 of Appendix H it can be observed that also the analysis presented in this chapter has a large fake contribution in these event classes.

6.4 Search strategy and algorithm

The preliminary background model is incomplete due to the following shortcomings:

- the absence of MC samples for several SM processes with a small cross section
- the absence of an estimation of the fake contributions from QCD events
- the absence of estimations for several theoretical modelling uncertainties

These shortcomings can lead to an underestimation of the true SM expectation value and/or an underestimation of its (theory) uncertainty. This in turn can lead to an underestimation, or overestimation, of the significance of an observed deviation. For an observed *deficit*, the underestimation of the SM expectation value diminishes the significance ($Z^{\text{obs}}_{\text{deficit}} \leq Z^{\text{true}}_{\text{deficit}}$), while the underestimation of its uncertainty overestimates the significance ($Z^{\text{obs}}_{\text{deficit}} \geq Z^{\text{true}}_{\text{deficit}}$). Therefore, no conclusions can be drawn for observed deficits based on an incomplete background model.

For observed excesses, however, both cases lead to $Z^{\text{obs}}_{\text{excess}} \geq Z^{\text{true}}_{\text{excess}}$, so any region that has an excess with an estimated significance smaller than that required for a DDSR ($Z^{\text{obs}}_{\text{excess}} \leq Z_{\text{DDSR}}$) can be (permanently) excluded as a DDSR candidate since in this case the inequality $Z^{\text{true}}_{\text{excess}} \leq Z^{\text{obs}}_{\text{excess}} \leq Z_{\text{DDSR}}$ holds. In terms of the test-statistics used, this amounts to $P_{\text{exp},1}(p^{\text{true}}_{\text{class}}) \geq P_{\text{exp},1}(p^{\text{obs}}_{\text{class}})$ and hence if $P_{\text{exp},1}(p^{\text{obs}}_{\text{class}}) > 5\%$ then also $P_{\text{exp},1}(p^{\text{true}}_{\text{class}}) > 5\%$ and the region can be excluded as a DDSR candidate.

The strategy is therefore to eliminate as many DDSR candidates as possible based on the observed excesses over the incomplete background model. No definitive conclusions will be drawn for any regions with an observed deficit, or regions with an observed excess for which $P_{\text{exp},1}(p_{\text{class}}) < 5\%$. In order to qualify a possible excess that cannot be eliminated as a DDSR, any of the shortcomings mentioned above affecting the background(s) in that region need to be addressed first.

As in Chapter 5, one region of largest deviation (RoI) in a binned distribution of an observable is identified for each of the selected event classes and the associated p_0-value (p_{class}) is used as a test-statistic. Since only excesses are being considered, the definition of p_0 is modified to:

$$p_0 = P(n \geq C_{\text{obs}}) = \int_0^{\infty} \mathrm{d}x\, G\left(x; C_{\text{SM}}, \delta C_{\text{SM}}\right) \cdot \sum_{n=C_{\text{obs}}}^{\infty} \frac{\mathrm{e}^{-x} x^n}{n!} \tag{6.1}$$

For the exclusive event classes, the scan is applied to the same observables (m_{eff}, m_{inv}, H_{T}, and $E^{\text{miss}}_{\text{T}}$) used in Chapter 5. Only the event classes having $E^{\text{miss}}_{\text{T}} > 200$ GeV are considered for the $E^{\text{miss}}_{\text{T}}$ observable. For the merged event classes, some of the observables are redefined:

- The m_{inv} is computed by only summing the four-vectors of the objects explicitly labelled in the event class, i.e. excluding the four-vectors of any additional jets in the event.
- The H_{T} is replaced by the scalar p_{T}-sum ($\sum p_{\text{T}}(X)$) of all objects (X) labelled in the event class, i.e. excluding the four-vectors of any additional jets in the event; and by

the $\sum p_{\mathrm{T}}(\text{jets})$ observable, computed as the scalar p_{T}-sum of *all* (b-)jets in the event. For classes without b-jets these observables are related as $H_{\mathrm{T}} = \sum p_{\mathrm{T}}(X) + \sum p_{\mathrm{T}}(\text{jets})$.

- The m_{eff} is defined as the scalar p_{T}-sum of *all* objects in the event, i.e. including the four-vectors of any additional jets in the event, plus $E_{\mathrm{T}}^{\text{miss}}$.
- The definition of $E_{\mathrm{T}}^{\text{miss}}$ is identical.

Note that both the m_{eff} and $E_{\mathrm{T}}^{\text{miss}}$ are identical to the definition for exclusive event classes and yield the same value per event, while m_{inv} and $\sum p_{\mathrm{T}}(X)$ only consider the objects explicitly listed in the merged event class label.

Updated trigger thresholds and the absence of the diphoton trigger selection are propagated to the threshold abscissa value of the binned distribution at which the search algorithm starts as described in Section 5.5.2. The binning of the histograms is also similar to that in Chapter 5 but using a $\pm 5\sigma$ interval ($k_{e,\gamma} = 10$) for photons and electrons to avoid having bins with (too) few MC events.

6.5 Classification results

Three iterations of the analysis are performed using different types of event classes:

- Exclusive event classes: these classes are similar to those used in Chapter 5. Z and Higgs boson objects are *not* considered.
- Merged event classes: these classes are obtained by merging certain exclusive event classes as described in Section 6.1.3. Z and Higgs boson objects are *not* considered.
- Merged event classes with Z and Higgs boson objects: Z and Higgs boson objects are considered in this iteration only. Event classes are merged using the same procedure as for the event classes in the aforementioned iteration. Of the resulting event classes only those have at least one Z, H, or h object are kept.

6.5.1 Exclusive event classes

Table 6.3 summarizes the number of event classes after classification. In total 1089 exclusive event classes are found to have at least one observed event or an SM expectation greater than 0.1 events. The number of observed events and the predictions from MC simulations for these classes are shown in Appendix I. Events from experiment are observed in 812 out of 1089 event classes. These include events with up to four leptons (muons and/or electrons), three photons, twelve jets and six b-jets.

There are 31 event classes, listed in Table 6.4, with an SM expectation of less than 0.1 events. No more than two data events are observed in any of the event classes having $C_{\text{SM}} < 0.1$. The remaining 1058 classes are retained for further analysis.

Several very large excesses can be noticed in Figure I.3 of Appendix I in the three-photon event classes for which MC samples for SM triple-photon production are not available at the time of writing and the contribution from these processes are missing from the background model.

Table 6.3: Number of event classes after classification of all accepted events.

Event classes with	Exclusive	Merged	Merged and $N(Z, h, H) \geq 1$
$C_{SM} > 0.1$ and $C_{obs} \geq 1$	781	84	36
$C_{SM} > 0.1$ and $C_{obs} = 0$	277	12	16
$C_{SM} > 0.1$	1058	96	52
$C_{SM} < 0.1$ and $C_{obs} \geq 1$	31	2	4
$C_{SM} > 0.1$ or $C_{obs} \geq 1$	1089	98	56

Table 6.4: Event classes with at least one observed event from experiment and an SM expectation smaller than 0.1. The UL at a 95% CL on the expected number of events, as obtained from the MC background, is given. For four event classes (indicated with a '−') there are no MC events in the background model and no UL can be estimated.

Event class	Observed events	Expected events (95% CL UL)
$2\gamma\ 2b\ 6j$	1	–
$3\gamma\ 4j$	1	$2.1 \cdot 10^{-2}$
$3\gamma\ 1b$	1	$5.3 \cdot 10^{-7}$
$1e\ 4b\ 7j$	1	$7.5 \cdot 10^{-2}$
$1e\ 1\gamma\ 4b\ 4j$	1	$5.5 \cdot 10^{-2}$
$2e\ 1\gamma\ 7j$	1	$1.3 \cdot 10^{-1}$
$3e\ 1\gamma\ 3j$	2	$1.7 \cdot 10^{-1}$
$4e\ 4j$	1	$9.4 \cdot 10^{-2}$
$1\mu\ 5b\ 6j$	1	$5.7 \cdot 10^{-2}$
$1\mu\ 1e\ 3b\ 7j$	1	$1.8 \cdot 10^{-2}$
$1\mu\ 2e\ 3b\ 5j$	1	$1.4 \cdot 10^{-2}$
$1\mu\ 2e\ 4b$	1	$2.9 \cdot 10^{-2}$
$1\mu\ 2e\ 1\gamma\ 2j$	1	$1.2 \cdot 10^{-1}$
$1\mu\ 2e\ 1\gamma\ 3j$	1	$6.1 \cdot 10^{-2}$
$2\mu\ 6b\ 3j$	1	–
$2\mu\ 1\gamma\ 3b$	1	$5.7 \cdot 10^{-2}$
$3\mu\ 4b\ 1j$	1	$2.4 \cdot 10^{-2}$
$4\mu\ 1b\ 3j$	1	$1.2 \cdot 10^{-1}$
$E_T^{miss}\ 1\gamma\ 4b\ 1j$	1	$1.1 \cdot 10^{-1}$
$E_T^{miss}\ 1e\ 1b\ 11j$	1	–
$E_T^{miss}\ 2e\ 4b\ 3j$	1	$7.8 \cdot 10^{-2}$
$E_T^{miss}\ 2e\ 5b\ 2j$	1	$3.7 \cdot 10^{-2}$
$E_T^{miss}\ 1\mu\ 1\gamma\ 4b$	1	$1.6 \cdot 10^{-2}$
$E_T^{miss}\ 1\mu\ 2\gamma\ 1b$	1	$5.4 \cdot 10^{-2}$
$E_T^{miss}\ 1\mu\ 1e\ 2b\ 8j$	1	$2.4 \cdot 10^{-2}$
$E_T^{miss}\ 1\mu\ 2e\ 5j$	1	$1.3 \cdot 10^{-1}$
$E_T^{miss}\ 2\mu\ 9j$	1	$6.8 \cdot 10^{-3}$
$E_T^{miss}\ 2\mu\ 2e\ 1j$	1	$1.3 \cdot 10^{-1}$
$E_T^{miss}\ 3\mu\ 1\gamma\ 1j$	1	$2.7 \cdot 10^{-2}$
$E_T^{miss}\ 3\mu\ 1\gamma\ 3b$	1	–
$E_T^{miss}\ 4\mu\ 2j$	1	$3.3 \cdot 10^{-2}$

6.5.2 Merged event classes

The third column of Table 6.3 gives the number of merged event classes after classification. The two event classes excluded from the scan algorithm are $E_{\mathrm{T}}^{\mathrm{miss}}\,3l\,1\gamma$ (i) and $E_{\mathrm{T}}^{\mathrm{miss}}\,3l\,1\gamma\,2{+}b$ (i), both having one observed event and a 95% CL UL on the expectation value of $1.3 \cdot 10^{-1}$ and $2.3 \cdot 10^{-2}$ respectively. The event yields for all 98 event classes are shown in Figure 6.2.

6.5.3 Merged event classes with Z and Higgs boson objects

This section demonstrates the introduction of Z and Higgs boson objects, as defined in Section 6.1.2. Event classes are defined after replacing signal lepton or photon pairs with a Z, H or h object when they meet the conditions. The exclusive event classes with an h object are therefore subsets of the event classes defined in Section 6.5.1, e.g. $1h\,1b\,1j \subset 2\gamma\,1b\,1j$. The exclusive event classes with an H or Z object are subsets of the union of the two/three classes with different lepton flavour content, e.g. $1Z\,1e\,1j \subset (3e\,1j \cup 2\mu\,1e\,1j)$ and $1H\,1b\,1j \subset (4e\,1b\,1j \cup 4\mu\,1b\,1j \cup 2\mu\,2e\,1b\,1j)$. The resulting event classes are then merged following the same procedure as in the previous section. Only the merged event classes containing at least one Z, H or h signal object are kept.

The classification results are shown in the fourth column of Table 6.3 and the event yields are shown in Figure 6.3. The four event classes that do not participate in the scan are: $1Z\,1h\,2{+}b$ (i), $E_{\mathrm{T}}^{\mathrm{miss}}\,1Z\,1l\,1\gamma$ (i), $E_{\mathrm{T}}^{\mathrm{miss}}\,1Z\,1l\,1\gamma\,2{+}b$ (i) and $E_{\mathrm{T}}^{\mathrm{miss}}\,1h\,1b$ (i). All four excluded classes have one observed event and a 95% CL UL on the expectation value of $2.4 \cdot 10^{-2}$, $2.0 \cdot 10^{-1}$, $3.6 \cdot 10^{-2}$ and $1.5 \cdot 10^{-1}$ respectively.

6.6 Application of search algorithm

6.6.1 Exclusive event classes

Table 6.5 summarizes the number of bins and regions obtained using the current version of the background model.

The last row underneath 'exclusive event classes' in Table 6.5 lists again all regions having $C_{\mathrm{SM}} < 0.01$ and $C_{\mathrm{obs}} \geq 3$ which are discarded in the scan. All of the discarded regions in the m_{eff}, H_{T} and $E_{\mathrm{T}}^{\mathrm{miss}}$ scan, as well as seven regions in the m_{inv} scan, are (overlapping) regions containing a bin with a negative SM expectation value and a large MC statistical uncertainty as a result of an MC event with a large negative weight. The p_0-values for these regions range from 0.003 to 0.4 (average $p_0 = 0.3$).

Three of the remaining regions in the m_{inv} scan are overlapping regions in the $2\gamma\,1b\,5j$ event class with $C_{\mathrm{SM}} = 0.008 \pm 0.328$ and $C_{\mathrm{obs}} = 4$ resulting in $p_0 = 4.4 \cdot 10^{-4}$. A larger overlapping region in the $2\gamma\,1b\,5j$ event class is accepted in the scan as RoI. None of these deviations are large enough to meet the criteria for a DDSR.

The remaining 78 regions seen in the m_{inv} scan are overlapping regions in the 3γ event class with the most deviating region having $C_{\mathrm{SM}} = (8 \pm 9) \cdot 10^{-4}$ and $C_{\mathrm{obs}} = 4$ resulting in $p_0 < 10^{-9}$ thereby meeting the criteria for a DDSR by a wide margin. This is a clear 'observation' of SM triple-photon production for which the MC samples are missing from the background model,

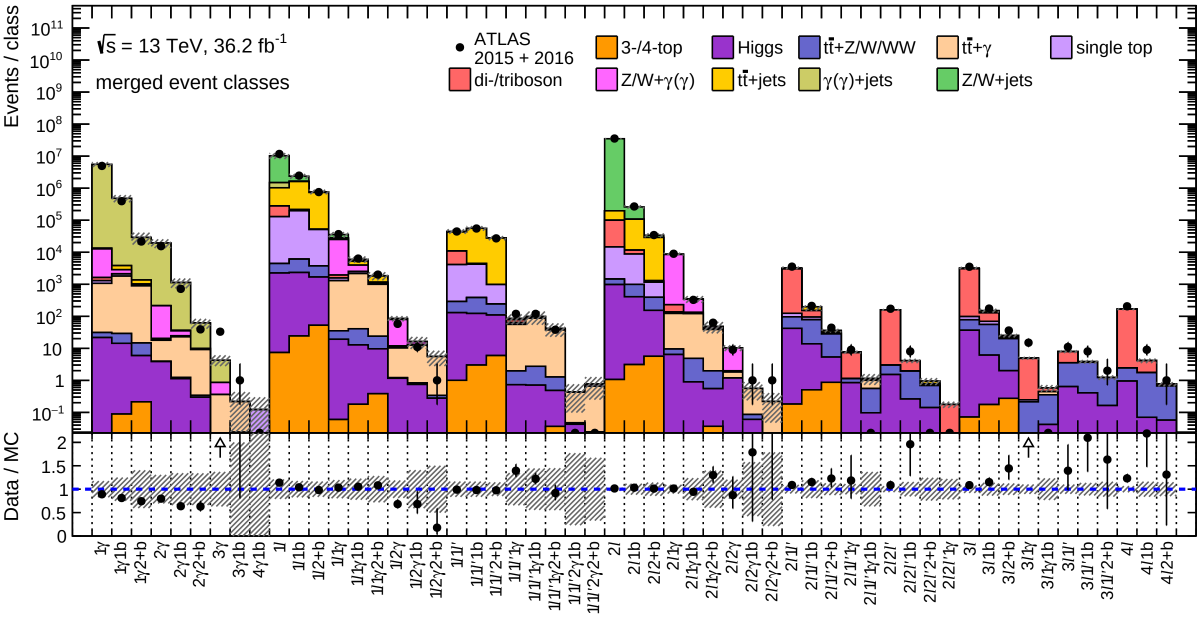

(a)

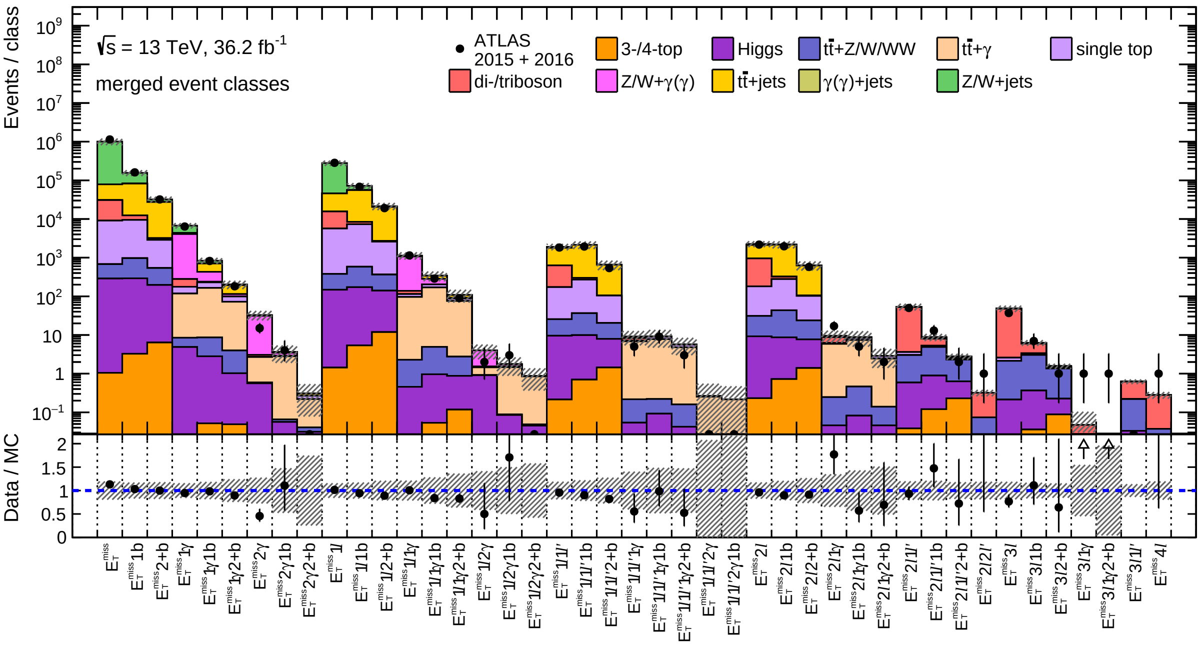

(b)

Figure 6.2: Expected and observed number of events in all merged event classes. The class labels list the type and multiplicity of reconstructed objects in the events. All classes are inclusive in additional non-b-tagged jets (note '(i)' in labels has been omitted), and inclusive for two or more b-tagged jets. The l is used to indicate the largest number of leptons of a single flavour, while l' is used only when both lepton flavours (electron and muon) are present. The total uncertainty on the SM prediction is indicated by hatched bands.

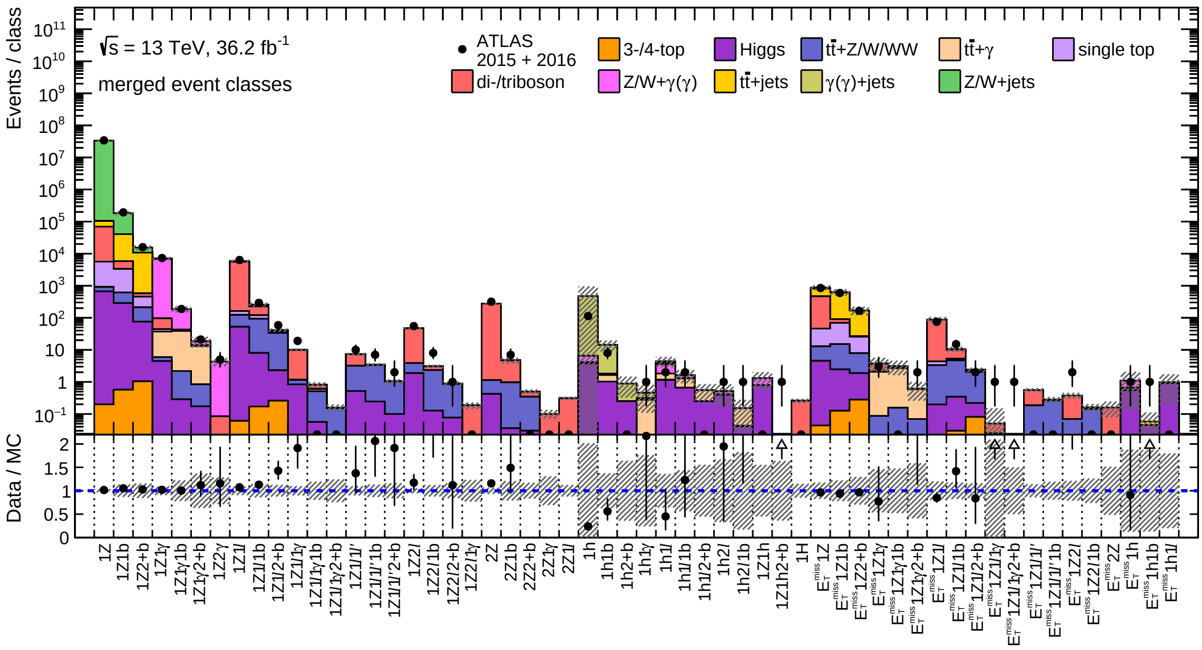

Figure 6.3: Expected and observed number of events in all merged event classes. The class labels list the type and multiplicity of reconstructed objects in the events, including Z, H, and h objects. All classes are inclusive in additional non-b-tagged jets (note '(i)' in labels has been omitted), and inclusive for two or more b-tagged jets. The l is used to indicate the largest number of leptons of a single flavour, while l' is used only when both lepton flavours (electron and muon) are present. The total uncertainty on the SM prediction is indicated by hatched bands.

as mentioned in Section 6.3. Consequently, no conclusions can be drawn from these excesses other than the inability to exclude the entire 3γ class as a potential DDSR candidate.

6.6.2 Merged event classes

As for the exclusive classes, the algorithm only identifies RoIs with excesses. The number of bins and regions are summarized in Table 6.5. In total, 14 regions have $C_{\text{SM}} < 0.01$ and $C_{\text{obs}} \geq 3$. Six regions are in the 3γ event classes with $p_0 < 10^{-9}$. The remaining eight regions are overlapping regions in $2l$ and $E_{\text{T}}^{\text{miss}}\,2l$ classes due to contributions of MC events with negative weights and the smallest p_0 is 0.1.

6.6.3 Merged event classes with Z and Higgs boson objects

The same observables as used in the previous section are scanned and a summary of the regions can be found in Table 6.5.

6.7 Estimation of DDSR thresholds

6.7.1 Exclusive event classes

As in Chapter 5, pseudo-experiments are generated to model the cdf of the p_{class} test-statistic. Figure 6.4 shows the cumulative p_{class} distributions $P_{\text{exp},i}$ (with $i = 1$, 2 and 3) for all the

Table 6.5: Summary of the numbers of regions and bins in the scans. Regions are built from one or more contiguous bins and are tested only if $C_{SM} > 0.01$ such that multiple bins with $C_{SM} < 0.01$ can form a region for hypothesis testing. Regions with $C_{SM} < 0.01$ and $C_{obs} \geq 3$ do not qualify for testing but are being monitored, since such a region could be considered for a DDSR. Numbers for 'all bins' and 'all regions' depend only the binning and the intervals covered by the histograms.

Exclusive event classes				
Scan observable	m_{eff}	m_{inv}	H_{T}	$E_{\text{T}}^{\text{miss}}$
All bins	22 281	23 519	23 223	38 336
Bins with $C_{SM} > 0.01$	9 847	12 983	9 983	5 609
Bins with $C_{SM} > 0.01$ and $C_{obs} \geq 1$	5 101	7 042	5 136	2 372
All regions	330 249	368 390	357 747	1 753 776
Regions with $C_{SM} > 0.01$	230 167	297 412	243 386	577 988
Regions with $C_{SM} > 0.01$ and $C_{obs} \geq 1$	147 448	204 728	153 920	291 111
Regions with $C_{SM} < 0.01$ and $C_{obs} \geq 3$	8	88	9	3

Merged event classes					
Scan observable	m_{eff}	m_{inv}	$\sum p_{\text{T}}(X)$	$\sum p_{\text{T}}(\text{jets})$	$E_{\text{T}}^{\text{miss}}$
All bins	2 050	2 024	1 904	5 342	2 244
Bins with $C_{SM} > 0.01$	1 233	1 157	919	2 313	822
Bins with $C_{SM} > 0.01$ and $C_{obs} \geq 1$	868	755	558	1 368	423
All regions	32 307	32 556	29 469	157 044	60 276
Regions with $C_{SM} > 0.01$	25 957	25 116	19 622	119 005	37 979
Regions with $C_{SM} > 0.01$ and $C_{obs} \geq 1$	21 669	19 115	13 923	86 036	23 908
Regions with $C_{SM} < 0.01$ and $C_{obs} \geq 3$	1	5	6	2	0

Merged event classes and $N(Z,h,H) \geq 1$					
Scan observable	m_{eff}	m_{inv}	$\sum p_{\text{T}}(X)$	$\sum p_{\text{T}}(\text{jets})$	$E_{\text{T}}^{\text{miss}}$
All bins	2 048	1 799	2 107	2 973	880
Bins with $C_{SM} > 0.01$	695	680	605	875	185
Bins with $C_{SM} > 0.01$ and $C_{obs} \geq 1$	358	309	282	369	66
All regions	58 548	50 558	61 684	91 074	24 736
Regions with $C_{SM} > 0.01$	32 682	32 345	30 240	59 474	10 952
Regions with $C_{SM} > 0.01$ and $C_{obs} \geq 1$	18 908	16 869	16 714	30 599	4 940
Regions with $C_{SM} < 0.01$ and $C_{obs} \geq 3$	0	0	0	0	0

scanned observables. The p_{class}-values for which $P_{\text{exp},i} < 5\%$ are indicated by dotted vertical lines and given in Table 6.6.

6.7.2 Merged event classes

Figure 6.5 shows the $P_{\text{exp},i}$ distribution (with $i = 1, 2$ and 3) for each of the scanned observables in the merged event classes. The p_{class}-values for which $P_{\text{exp},i} < 5\%$ are also given in Table 6.6.

6.7.3 Merged event classes with Z and Higgs boson objects

Thresholds for DDSRs are again defined using pseudo-experiments and listed in Table 6.6.

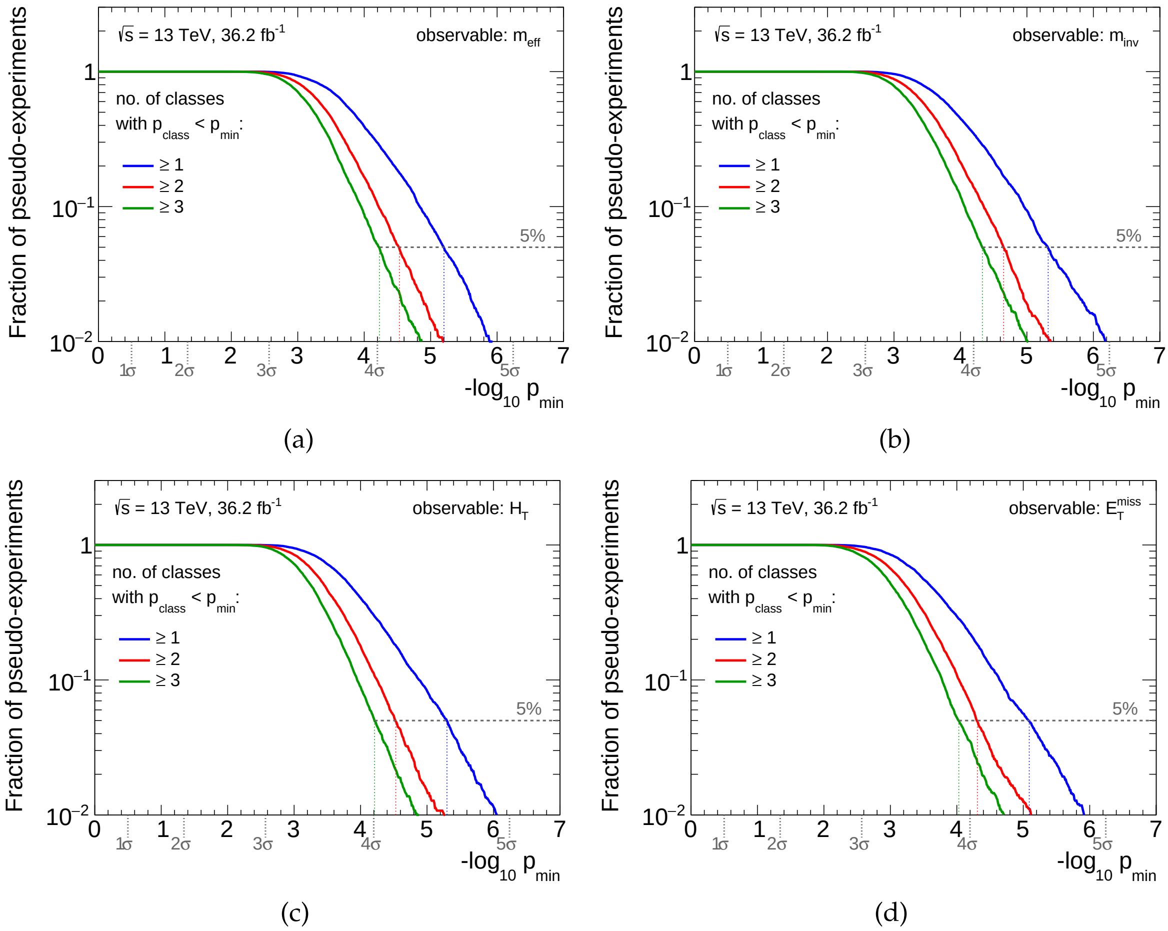

Figure 6.4: The fraction of pseudo-experiments that have at least one, two or three p_{class}-values below a given p_{min} in scans performed on *exclusive* event classes. The fractions of pseudo-experiments are shown by the solid curves. The m_{eff} scan is shown in (a), the m_{inv} scan in (b), the H_{T} scan in (c) and the $E_{\text{T}}^{\text{miss}}$ scan in (d). The vertical dotted lines mark the p_{class}-values for which $P_{\text{exp},i} < 5\%$ indicating the threshold for a DDSR.

6.8 Results of search algorithm applied to 2015+2016 dataset

6.8.1 Exclusive event classes

The results from the scans are summarized in Table 6.7 showing the details of the RoIs with the largest excesses in each of the scans. Event classes that are affected by the known deficiencies of the background model are annotated as they appear among the largest excesses. The three-photon event classes 3γ and $3\gamma\,1j$ appear among the largest excesses in all three scans. Similarly, the $1e\,1j$ event class, an event class that was discarded in Chapter 5 due to its large contribution from QCD events, appears among the largest excesses in all three scans. The 3γ, $3\gamma\,1j$ and $1e\,1j$ all three pass the DDSR threshold and can thus not (yet) be eliminated from DDSR candidacy.

For the $2e$ event class, appearing in the H_{T} scan as having one of the largest excesses, it should be noted that the current $Z+$jets MC samples do not contain enough simulated events with a high-p_{T} Z boson to populate the tails at high H_{T}, m_{eff} and m_{inv}[5]. The excesses are discussed in

[5] The 2μ event class also suffers from large statistical MC uncertainties in the tail of the distributions, but the

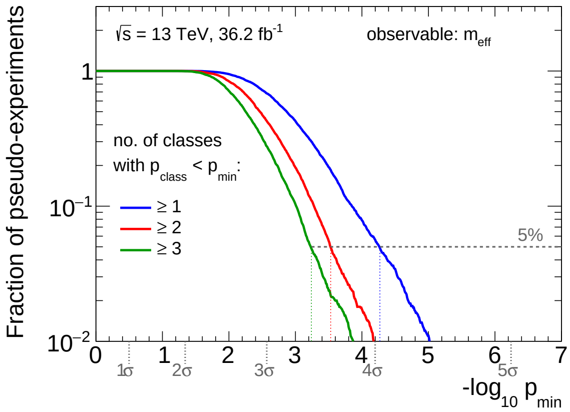

(a)

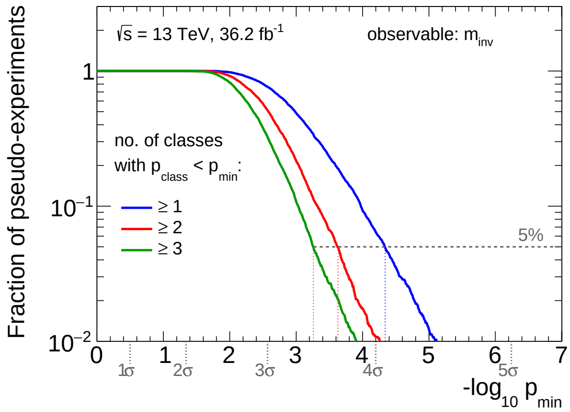

(b)

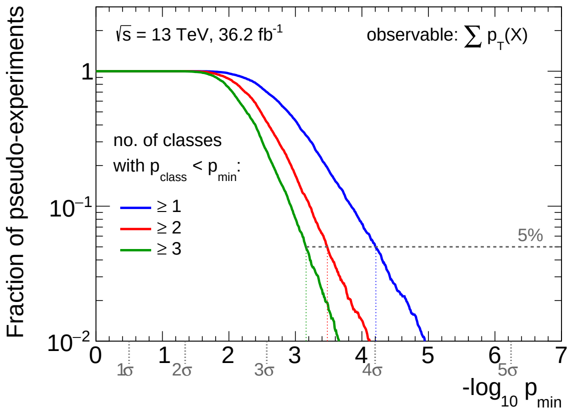

(c)

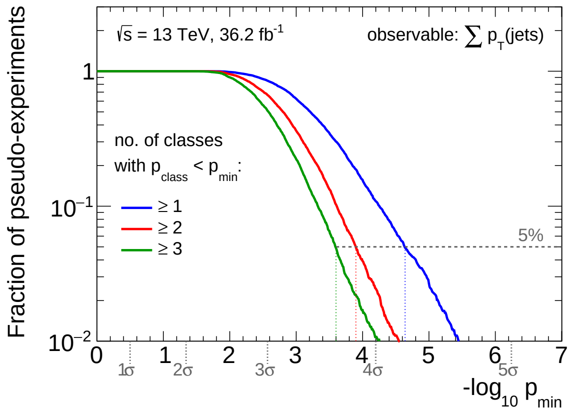

(d)

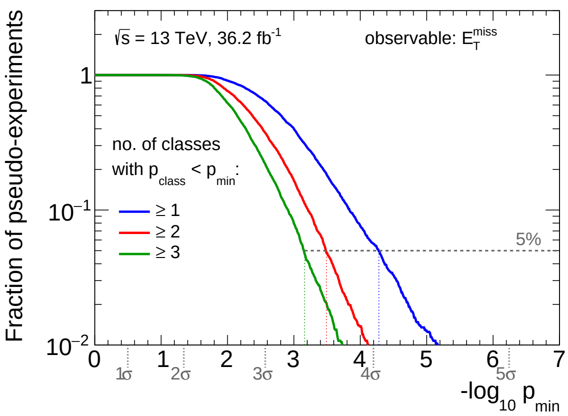

(e)

Figure 6.5: The fraction of pseudo-experiments that have at least one, two or three p_{class}-values below a given p_{min} in scans performed on *merged* event classes. The fractions of pseudo-experiments are shown by the solid curves. The m_{eff} scan is shown in (a), the m_{inv} scan in (b), the $\sum p_{\mathrm{T}}(X)$ scan in (c), where X are the objects in the event class label, the $\sum p_{\mathrm{T}}(\mathrm{jets})$ scan in (d), and the $E_{\mathrm{T}}^{\mathrm{miss}}$ scan in (e). The vertical dotted lines mark the p_{class}-values for which $P_{\mathrm{exp},i} < 5\%$ indicating the threshold for a DDSR.

Table 6.6: The p_{class}-values for which $P_{\text{exp},i} < 5\%$ defining the threshold for a DDSR.

Observable	$P^{-1}_{\text{exp},1}(5\%)$	$P^{-1}_{\text{exp},2}(5\%)$	$P^{-1}_{\text{exp},3}(5\%)$
Exclusive event classes			
m_{eff}	$6.3 \cdot 10^{-6}$	$2.9 \cdot 10^{-5}$	$5.9 \cdot 10^{-5}$
m_{inv}	$4.8 \cdot 10^{-6}$	$2.2 \cdot 10^{-5}$	$4.7 \cdot 10^{-5}$
H_{T}	$5.0 \cdot 10^{-6}$	$2.9 \cdot 10^{-5}$	$6.2 \cdot 10^{-5}$
$E_{\text{T}}^{\text{miss}}$	$8.1 \cdot 10^{-6}$	$4.9 \cdot 10^{-5}$	$9.3 \cdot 10^{-5}$
Merged event classes			
m_{eff}	$5.4 \cdot 10^{-5}$	$2.9 \cdot 10^{-4}$	$5.7 \cdot 10^{-4}$
m_{inv}	$4.6 \cdot 10^{-5}$	$2.3 \cdot 10^{-4}$	$5.5 \cdot 10^{-4}$
$\sum p_{\text{T}}(X)$	$6.2 \cdot 10^{-5}$	$3.3 \cdot 10^{-4}$	$6.9 \cdot 10^{-4}$
$\sum p_{\text{T}}(\text{jets})$	$2.3 \cdot 10^{-5}$	$1.3 \cdot 10^{-4}$	$2.5 \cdot 10^{-4}$
$E_{\text{T}}^{\text{miss}}$	$5.2 \cdot 10^{-5}$	$3.2 \cdot 10^{-4}$	$6.9 \cdot 10^{-4}$
Merged event classes and $N(Z,h,H) \geq 1$			
m_{eff}	$8.1 \cdot 10^{-5}$	$4.5 \cdot 10^{-4}$	$1.0 \cdot 10^{-3}$
m_{inv}	$6.6 \cdot 10^{-5}$	$4.1 \cdot 10^{-4}$	$9.1 \cdot 10^{-4}$
$\sum p_{\text{T}}(X)$	$9.1 \cdot 10^{-5}$	$5.2 \cdot 10^{-4}$	$1.2 \cdot 10^{-3}$
$\sum p_{\text{T}}(\text{jets})$	$6.3 \cdot 10^{-5}$	$3.3 \cdot 10^{-4}$	$7.8 \cdot 10^{-4}$
$E_{\text{T}}^{\text{miss}}$	$2.3 \cdot 10^{-4}$	$1.9 \cdot 10^{-3}$	$5.0 \cdot 10^{-3}$

more detail in Section 6.9.

6.8.2 Merged event classes

The results from the scans in merged event classes are summarized in Table 6.8. As for the scans in the exclusive classes, the three-photon classes exhibit the largest excesses and pass the DDSR threshold. The excess observed in the m_{eff} scan in the $2l\,1l'\,1\gamma$ (i) class is also near the $P_{\text{exp},1} < 5\%$ threshold. This class, as well as the $3l\,1\gamma$ (i) event class which is also among the largest excesses in all scans, contribute to the $1Z\,1l\,1\gamma$ (i) which passes the DDSR threshold and is discussed in the next section.

6.8.3 Merged event classes with Z and Higgs boson objects

The largest deviations found in the scan of each of the observables are listed in Table 6.9.

With the preliminary background model used in this chapter, the search algorithm identifies regions in the scans of the m_{eff}, and $\sum p_{\text{T}}(\text{jets})$ observables satisfying the conditions for a DDSR. This RoI is in the $1Z\,1l\,1\gamma$ (i) event class, which also contains the RoI with the largest deviation in the $\sum p_{\text{T}}(X)$ scan. As such, the event classes $1Z\,1l\,1\gamma$ (i) is not excluded from containing DDSR candidates. The class is expected to receive significant contributions from the fully-leptonic $WZ\gamma$ SM process which is not included in the background model as discussed in the next section.

wider binning for high-p_{T} muons ensures all bins are populated.

Table 6.7: List of the six event classes with the smallest p_{class}-values in each of the scans in exclusive event classes. The observed and expected number of events in the region selected by the scan algorithm as the RoI are given. If $P_{\text{exp},i}(p_0) < 5\%$ for $i = 1, 2$ and/or 3, it is indicated by giving all values of i for which it is true.

Observable	Class	p_{class}	$P_{\text{exp},i} < 5\%$	C_{obs}	$C_{\text{SM}} \pm \delta C_{\text{SM}}$	Region [GeV]
m_{eff}	3γ [a]	$9.3 \cdot 10^{-5}$		6	0.40 ± 0.34	653–1584
	$3\gamma\,1j$ [a]	$2.3 \cdot 10^{-4}$		4	0.18 ± 0.16	640–828
	$1e\,1j$ [b]	$9.6 \cdot 10^{-4}$		106 814	$(83.9 \pm 7.4) \cdot 10^{3}$	420–456
	$2\mu\,1e\,1\gamma\,1j$ [c]	$1.0 \cdot 10^{-3}$		2	0.041 ± 0.021	853–1430
	$3\mu\,2b\,1j$	$1.1 \cdot 10^{-3}$		9	2.34 ± 0.35	510–766
	$1\mu\,1e\,1\gamma\,1b$	$1.4 \cdot 10^{-3}$		17	4.3 ± 2.5	470–534
m_{inv}	3γ [a]	$3.3 \cdot 10^{-9}$	$i = 1$	15	1.09 ± 0.59	520–1690
	$3\gamma\,1j$ [a]	$1.9 \cdot 10^{-5}$	$i = 2$	5	0.14 ± 0.18	828–1058
	$2e\,1\gamma\,3b$	$1.1 \cdot 10^{-4}$		2	0.011 ± 0.011	781–1065
	$1e\,1j$ [b]	$1.4 \cdot 10^{-4}$		101 181	$(76.1 \pm 6.9) \cdot 10^{3}$	420–456
	$1\gamma\,4b\,3j$	$6.4 \cdot 10^{-4}$		2	0.013 ± 0.041	1303–1632
	$1\mu\,1e\,1\gamma$	$7.9 \cdot 10^{-4}$		10	2.23 ± 0.81	442–497
H_{T}	$1e\,1j$ [b]	$4.9 \cdot 10^{-9}$	$i = 1$	71 427	$(50.8 \pm 3.6) \cdot 10^{3}$	386–420
	3γ [a]	$5.5 \cdot 10^{-5}$		6	0.40 ± 0.28	607–1584
	$2e$ [d]	$1.5 \cdot 10^{-4}$		4	0.16 ± 0.14	1552–3050
	$3\gamma\,1j$ [a]	$2.3 \cdot 10^{-4}$		4	0.18 ± 0.16	640–828
	$3\mu\,2b\,1j$	$2.4 \cdot 10^{-4}$		7	1.12 ± 0.18	510–617
	$E_{\text{T}}^{\text{miss}}\,2\mu$	$7.7 \cdot 10^{-4}$		10	1.2 ± 1.4	687–1028
$E_{\text{T}}^{\text{miss}}$	$E_{\text{T}}^{\text{miss}}\,1e\,1b$	$1.5 \cdot 10^{-3}$		2	0.013 ± 0.069	1328–1379
	$E_{\text{T}}^{\text{miss}}\,2\mu$	$2.1 \cdot 10^{-3}$		4	0.14 ± 0.44	536–638
	$E_{\text{T}}^{\text{miss}}\,2e\,1\gamma\,3j$	$2.8 \cdot 10^{-3}$		2	0.063 ± 0.046	200–235
	$E_{\text{T}}^{\text{miss}}\,1\mu\,5b\,2j$	$2.9 \cdot 10^{-3}$		2	0.046 ± 0.072	331–498
	$E_{\text{T}}^{\text{miss}}\,1e\,1\gamma\,2b\,3j$	$4.0 \cdot 10^{-3}$		2	0.054 ± 0.084	421–533
	$E_{\text{T}}^{\text{miss}}\,1\mu\,1j$	$4.7 \cdot 10^{-3}$		2	0.064 ± 0.085	1595–1652

[a] Contribution from SM triple-photon production missing from background model.
[b] Contribution from misreconstructed multijet events missing from background model.
[c] Contribution from SM $WZ\gamma$ production missing from background model.
[d] Contribution from events with a high-p_{T} $Z/\gamma^{*}(\rightarrow \ell\ell)$ missing from background model.

The largest excess in the m_{inv} scan appearing in the 2Z (i) class (with $p_0 = 1.4 \cdot 10^{-4}$, i.e. a local significance of 3.6σ) has also been reported in Ref. [217] in which the reported local 3.6σ excess at 700 GeV corresponds to a global significance of 2.2σ. It does not qualify as a DDSR in this analysis.

6.9 Discussion of observed excesses

Several excesses are observed that have $P_{\text{exp},i} < 5\%$ for $i = 1, 2$ or 3 and are therefore large enough to be DDSR candidates. As discussed in Section 6.3, given the fact that several SM processes are not included in the background and that not all theory uncertainties have been estimated, at best, a process of elimination can be started in which regions not having an excess large enough to meet the criteria for a DDSR can be eliminated from candidacy. All but a few regions can indeed be eliminated and the remaining regions are discussed in this section. Although no definitive conclusions can be drawn for these regions, it helps to gauge whether it

Table 6.8: List of the six event classes with the smallest p_{class}-values in each of the scans. The observed and expected number of events in the region selected by the scan algorithm as the RoI are given. If $P_{\mathrm{exp},i}(p_0) < 5\%$ for $i = 1, 2$ and/or 3, it is indicated by giving all values for i for which it is true.

Observable	Merged class	p_{class}	$P_{\mathrm{exp},i} < 5\%$	C_{obs}	$C_{\mathrm{SM}} \pm \delta C_{\mathrm{SM}}$	Region [GeV]
m_{eff}	3γ [a]	$2.9 \cdot 10^{-7}$	$i = 1$	10	0.58 ± 0.42	653–867
	$2l\,1l'\,1\gamma$ [b]	$6.2 \cdot 10^{-5}$	$i = 2$	4	0.170 ± 0.072	888–1508
	$3l\,1\gamma$ [b]	$3.3 \cdot 10^{-4}$	$i = 3$	13	3.56 ± 0.76	250–1072
	$E_{\mathrm{T}}^{\mathrm{miss}}\,1\gamma$	$2.2 \cdot 10^{-3}$		2	0.040 ± 0.061	4089–4679
	$2l\,1l'\,2{+}b$	$2.4 \cdot 10^{-3}$		24	11.0 ± 2.0	750–2405
	$4l\,1b$	$6.4 \cdot 10^{-3}$		5	1.09 ± 0.21	320–438
m_{inv}	3γ [a]	$1.0 \cdot 10^{-9}$	$i = 1$	20	1.75 ± 0.88	520–1300
	$3l\,1\gamma$ [b]	$3.0 \cdot 10^{-4}$		12	3.36 ± 0.38	250–824
	$4l\,1b$	$4.0 \cdot 10^{-4}$	$i = 3$	7	1.21 ± 0.22	320–438
	$4l$	$2.2 \cdot 10^{-3}$		84	57.8 ± 3.8	200–250
	$E_{\mathrm{T}}^{\mathrm{miss}}\,2\gamma\,1b$	$2.3 \cdot 10^{-3}$		2	0.042 ± 0.061	914–1485
	$2l\,2l'$	$2.8 \cdot 10^{-3}$		80	55.1 ± 3.7	278–800
$\sum p_{\mathrm{T}}(X)$	3γ [a]	$5.6 \cdot 10^{-5}$	$i = 1$	8	0.80 ± 0.49	563–1584
	$2l\,1l'\,1\gamma$ [b]	$1.2 \cdot 10^{-3}$		4	0.40 ± 0.14	521–1127
	$3l\,1\gamma$ [b]	$3.0 \cdot 10^{-3}$		3	0.272 ± 0.056	402–466
	$2l\,1l'\,2{+}b$	$3.2 \cdot 10^{-3}$		13	4.95 ± 0.74	527–623
	$2l\,2l'$	$5.9 \cdot 10^{-3}$		30	17.1 ± 1.7	320–563
	$E_{\mathrm{T}}^{\mathrm{miss}}\,2l\,1l'\,1b$	$6.8 \cdot 10^{-3}$		5	1.07 ± 0.29	532–624
$\sum p_{\mathrm{T}}(\text{jets})$	3γ [a]	$9.2 \cdot 10^{-5}$		6	0.33 ± 0.38	166–355
	$2l\,1l'\,1\gamma$ [b]	$1.2 \cdot 10^{-4}$	$i = 2$	5	0.36 ± 0.17	235–469
	$2l\,1l'\,2{+}b$	$1.0 \cdot 10^{-3}$		12	3.7 ± 0.63	606–1177
	$3l\,1\gamma$ [b]	$1.4 \cdot 10^{-3}$		3	0.188 ± 0.077	322–428
	$E_{\mathrm{T}}^{\mathrm{miss}}\,2l\,1l'$	$2.9 \cdot 10^{-3}$		2	0.068 ± 0.039	1916–2366
	$4l\,1b$	$3.4 \cdot 10^{-3}$		2	0.081 ± 0.027	492–537
$E_{\mathrm{T}}^{\mathrm{miss}}$	$E_{\mathrm{T}}^{\mathrm{miss}}\,2\gamma\,1b$	$1.5 \cdot 10^{-2}$		1	0.015 ± 0.012	437–633
	$E_{\mathrm{T}}^{\mathrm{miss}}\,3l$	$1.6 \cdot 10^{-2}$		1	0.015 ± 0.015	969–1022
	$E_{\mathrm{T}}^{\mathrm{miss}}\,2l\,1\gamma$	$2.6 \cdot 10^{-2}$		14	5.6 ± 2.7	200–278
	$E_{\mathrm{T}}^{\mathrm{miss}}\,2l\,1l'\,1b$	$2.7 \cdot 10^{-2}$		4	1.08 ± 0.23	325–399
	$E_{\mathrm{T}}^{\mathrm{miss}}\,1l\,1b$	$2.8 \cdot 10^{-2}$		5	1.09 ± 0.95	1314–1507
	$E_{\mathrm{T}}^{\mathrm{miss}}\,1\gamma$	$2.9 \cdot 10^{-2}$		1	0.024 ± 0.040	1785–1858

[a] Contribution from SM triple-photon production missing from background model.
[b] Contribution from SM $WZ\gamma$ production missing from background model.

Table 6.9: List of the six event classes with the smallest p_{class}-values in each of the scans. The observed and expected number of events in the region selected by the scan algorithm as the RoI are given. If $P_{\text{exp},i}(p_0) < 5\%$ for $i = 1, 2$ and/or 3, it is indicated by giving all values for i for which it is true.

Observable	Merged class	p_{class}	$P_{\text{exp},i} < 5\%$	C_{obs}	$C_{\text{SM}} \pm \delta C_{\text{SM}}$	Region [GeV]
m_{eff}	$1Z\,1l\,1\gamma$ [a]	$2.7 \cdot 10^{-6}$	$i = 1$	7	0.48 ± 0.16	563–1017
	$E_{\text{T}}^{\text{miss}}\,1Z\,1l$	$6.8 \cdot 10^{-3}$		5	0.99 ± 0.38	1923–3163
	$1Z\,1l\,1l'\,1b$	$7.0 \cdot 10^{-3}$		5	1.08 ± 0.27	362–519
	$2Z\,1b$	$9.4 \cdot 10^{-3}$		2	0.137 ± 0.047	511–595
	$1Z\,1\gamma\,2{+}b$	$1.3 \cdot 10^{-2}$		1	0.012 ± 0.011	1595–1845
	$1Z\,2l$	$1.5 \cdot 10^{-2}$		14	6.82 ± 0.95	276–441
m_{inv}	$2Z$ [b]	$1.4 \cdot 10^{-4}$		12	3.04 ± 0.41	644–788
	$1Z\,2l\,1b$	$8.3 \cdot 10^{-4}$		6	0.99 ± 0.20	320–469
	$1Z\,1l\,1\gamma$ [a]	$1.5 \cdot 10^{-3}$		10	2.99 ± 0.38	364–2085
	$1Z\,1\gamma$	$4.5 \cdot 10^{-3}$		7	1.68 ± 0.58	1228–1290
	$E_{\text{T}}^{\text{miss}}\,1Z\,1l\,1b$	$5.5 \cdot 10^{-3}$		5	1.05 ± 0.21	584–666
	$E_{\text{T}}^{\text{miss}}\,1Z\,1\gamma\,2{+}b$	$8.1 \cdot 10^{-3}$		2	0.09 ± 0.10	589–647
$\sum p_{\text{T}}(X)$	$1Z\,1l\,1\gamma$ [a]	$1.3 \cdot 10^{-4}$		8	1.35 ± 0.22	364–1017
	$E_{\text{T}}^{\text{miss}}\,1Z\,1\gamma\,2{+}b$	$6.1 \cdot 10^{-3}$		2	0.085 ± 0.084	486–589
	$1Z\,1l\,1l'\,1b$	$8.2 \cdot 10^{-3}$		3	0.396 ± 0.070	408–459
	$2Z\,1b$	$9.9 \cdot 10^{-3}$		3	0.41 ± 0.13	511–644
	$1Z\,1l\,2{+}b$	$1.1 \cdot 10^{-2}$		26	14.8 ± 2.0	495–2239
	$1Z\,1l\,1l'\,2{+}b$	$1.4 \cdot 10^{-2}$		2	0.172 ± 0.042	502–575
$\sum p_{\text{T}}(\text{jets})$	$1Z\,1l\,1\gamma$ [a]	$8.1 \cdot 10^{-6}$	$i = 1$	6	0.35 ± 0.15	291–469
	$2Z\,1b$	$2.9 \cdot 10^{-3}$		2	0.074 ± 0.026	492–537
	$E_{\text{T}}^{\text{miss}}\,1Z\,2l$	$3.6 \cdot 10^{-3}$		2	0.065 ± 0.063	111–322
	$E_{\text{T}}^{\text{miss}}\,1Z\,1l$	$5.9 \cdot 10^{-3}$		2	0.104 ± 0.048	1916–2366
	$1Z\,1l\,1l'\,1b$	$6.4 \cdot 10^{-3}$		3	0.355 ± 0.084	200–250
	$E_{\text{T}}^{\text{miss}}\,1Z\,1l\,1b$	$6.5 \cdot 10^{-3}$		3	0.33 ± 0.14	157–177
$E_{\text{T}}^{\text{miss}}$	$E_{\text{T}}^{\text{miss}}\,1Z\,2l$	$1.4 \cdot 10^{-2}$		2	0.169 ± 0.061	224–307
	$E_{\text{T}}^{\text{miss}}\,1Z\,1l$	$2.6 \cdot 10^{-2}$		1	0.026 ± 0.022	969–1022
	$E_{\text{T}}^{\text{miss}}\,1Z\,1\gamma\,2{+}b$	$2.6 \cdot 10^{-2}$		2	0.20 ± 0.16	228–259
	$E_{\text{T}}^{\text{miss}}\,1Z\,1l\,1b$	$4.2 \cdot 10^{-2}$		6	2.32 ± 0.60	307–511
	$E_{\text{T}}^{\text{miss}}\,1Z$	$5.0 \cdot 10^{-2}$		3	0.74 ± 0.32	721–768
	$E_{\text{T}}^{\text{miss}}\,1Z\,1l\,2{+}b$	$5.6 \cdot 10^{-2}$		1	0.056 ± 0.046	361–399

[a] Contribution from SM $WZ\gamma$ production missing from background model.
[b] This region has also been reported in Ref. [217] as having a global 2.2σ excess (3.6σ local).

is worthwhile to continue with an effort of realizing a complete enough background model and for which classes additional efforts are needed to estimate contributions from misidentified objects in a data-driven way.

6.9.1 Three-photon events

The production of three isolated photons, for which the SM contribution is missing from the background model, is 'observed' in the analysis at several stages:

- At the classification stage, the $3\gamma\,4j$ and $3\gamma\,1b$ event classes are excluded from further analysis because the expectation value is below 0.1. Since they each have an observed event, they are reported in Table 6.4.
- The search algorithm discards regions with $C_{\mathrm{SM}} < 0.01$ (see Section 5.5.3). As a safety net against missing large local excesses in a background-free region, regions having $C_{\mathrm{SM}} < 0.01$ and $C_{\mathrm{obs}} \geq 3$ are reported (Table 6.5) which, in this case, leads to 78 (overlapping) regions being reported in the m_{inv} scan of the exclusive 3γ class. The most deviating reported region has $C_{\mathrm{SM}} = (8 \pm 9) \cdot 10^{-4}$ corresponding to a $p_0 < 10^{-9}$ and thereby meeting the criteria for a DDSR. Excluded regions similarly resulting in $p_0 < 10^{-9}$ have also been reported from scanning the 3γ (i) class.
- The $3\gamma(1j)$ class(es) appear(s) as (one of the) largest excesses in the scan results of all observables. Criteria for a DDSR are met in the scan of merged event classes for all observables scanned (in the $\sum p_{\mathrm{T}}(\mathrm{jets})$ observable only in combination with the $2l\,1l'\,1\gamma$ (i) class), and in the scan of exclusive event classes for the m_{inv} observable where the 3γ class yields a DDSR and the 3γ plus $3\gamma\,1j$ classes together yield a DDSR.

These event classes should be re-evaluated once MC samples have been produced, e.g. by following the procedures in Ref. [218]. The NLO prediction of the triple-photon production cross section is approximately 3 fb for isolated photons with $p_{\mathrm{T}} > 50$ GeV [219][6]. It can therefore be expected that adding the SM expectation for triple-photon production to the background model significantly reduces the observed excesses in the 3γ(+jets) event classes.

6.9.2 Three-lepton plus photon events

As for the three-photon events, the production of three isolated leptons and an isolated photon, for which the SM $WZ\gamma$ contribution is missing from the background model, is 'observed' in the analysis at several stages. It is however most clearly visible in the scans of *merged* event classes with Z and Higgs boson objects where the $1Z\,1l\,1\gamma$ (i) class satisfies the conditions for a DDSR in the m_{eff} and $\sum p_{\mathrm{T}}(\mathrm{jets})$ observable. In the scans of *merged* event classes *without* Z and Higgs boson objects, the excess is diluted in the $2l\,1l'\,1\gamma$ (i) and $3l\,1\gamma$ (i) classes, both of which appear among the largest excesses in all observables and in some cases yield a DDSR, albeit in combination with other classes. In the scans of *exclusive* event classes, the excess is diluted even further over classes differing in lepton flavour composition and jet multiplicity. The $2\mu\,1e\,1\gamma\,1j$ (i) class still appears as one of the largest excesses in the m_{eff} scan.

Among the excluded event classes at the classification stage similar classes appear such as the $E_{\mathrm{T}}^{\mathrm{miss}}\,1Z\,1l\,1\gamma$ (i) and $E_{\mathrm{T}}^{\mathrm{miss}}\,3l\,1\gamma$ (i) merged classes and the exclusive $3e\,1\gamma\,3j$, $1\mu\,2e\,1\gamma\,2j$,

[6] Note that in this chapter all 3γ(+jets) event classes require a leading photon of $p_{\mathrm{T}} > 160$ GeV.

$1\mu\, 2e\, 1\gamma\, 3j$ and $E_{\mathrm{T}}^{\mathrm{miss}}\, 3\mu\, 1\gamma\, 1j$ classes. This case illustrates how multiple small excesses in several exclusive classes can be enhance the excess by using composite objects such as Z or Higgs boson objects and merging event classes.

These event classes, particularly the $1Z\, 1l\, 1\gamma$ (i) class, should be re-evaluated once a MC estimation is obtained for the SM $WZ\gamma$ (and $WW\gamma$) production and any other contributing processes. A LO estimate of the $WZ\gamma$ cross-section (including processes with quartic gauge boson interactions) times branching ratio to three leptons, using MG5_aMC@NLO 2.6.3 and requiring $p_{\mathrm{T}}(\ell) > 25\,\mathrm{GeV}$ and $p_{\mathrm{T}}(\gamma) > 50\,\mathrm{GeV}$, yields approximately 0.26 fb. This would make it the dominant background process in this event class and likely reduces the excess to some degree or entirely. Previous studies of the $WZ\gamma$ process were performed with $\sqrt{s} = 8$ TeV pp collision data using the semi-leptonic channel [220, 221]. Studies of the fully leptonic channel have not yet been reported.

6.9.3 Electron plus jet(s) events

In the H_{T} scan, the exclusive $1e\, 1j$ event class shows an excess with $P_{\mathrm{exp},1} < 5\%$. This event class is among the event classes discarded in the analysis of the 2015 data (Chapter 5) because of the large contribution from misreconstructed QCD events. As the background model used in this chapter does not include any estimation of misreconstructed QCD events (fakes) through MC simulation or otherwise, it leads to an significant underestimation of the expectation value in this class as anticipated from the validation procedure. An initial estimate based on multijet MC samples can be shown to cover the discrepancy and it is therefore likely that the excess is the result entirely of fakes. However, a proper estimation of this fake contribution requires a data-driven method since the number of simulated multijet MC events are generally too few for this purpose.

6.9.4 Four leptons and a b-jet

The $4l\, 1b$ (i) and $2Z\, 1b$ (i) event classes appear among the largest deviations. In most cases the excesses are too small to qualify as a DDSR. In the m_{inv} scan, however, the $4l\, 1b$ (i) class qualifies as a DDSR, but only *in combination with* the 3γ (i) and $3l\, 1\gamma$ (i) classes ($P_{\mathrm{exp},3} < 5\%$). As discussed above, the excesses in these classes will likely diminish when the missing background contributions are accounted for, in which case the $4l\, 1b$ (i) will also no longer qualify as a DDSR. Additionally, it is expected to receive contributions from several of the listed missing samples in Section 6.2.1 such as $t\bar{t} + WZ$, $t\bar{t} + ZZ$, $Wt + Z$, etc.

6.9.5 Data-derived signal region

If, after addressing the current deficiencies of the background model, one of the excesses in the DDSR candidates still has a $P_{\mathrm{exp},i} < 5\%$ it should be followed-up by designing an analysis with a background model tailored to the DDSR. At this stage, control regions as well as BSM models can be introduced for interpretation and the signal region can be optimized using simulated signals or the current ($36.2\,\mathrm{fb}^{-1}$) dataset, while keeping it *blinded* upon application to an independent dataset until the unblinding stage, as is common practice with this kind of analysis. It is important that the analysis of the DDSR is applied to an *independent* dataset, i.e. not containing any events used to search for and define the DDSR, as doing so will introduce a strong bias. A result obtained with an independent dataset is free from a LEE and needs no correcting for the method used to find the DDSR. However, as discussed in Section 4.2.3, it is possible to use a test-statistic that combines the initial P_{exp}-value leading to the DDSR and the local p_0-value obtained from the analysis of the DDSR using an independent dataset ($p_{0_{\text{DS2}}}$), e.g. $t_p = P_{\text{exp}}(p_{\text{class}}) \cdot p_{0_{\text{DS2}}}$. By definition $P_{\text{exp}} < 0.05$ for a DDSR and, while this can simply be used as the upper limit (i.e. construct the p_0-value of for the combined dataset as $p_{0_{\text{comb}}} = 0.05 \cdot p_{0_{\text{DS2}}}$), smaller P_{exp} values are additional evidence against H_0 taken into account by t_p. Pseudo-experiments taking into account any correlated effects between the two analysis can then be used to model the cdf of t_p and determine the overall significance of the excess.

7 Conclusion & outlook

This thesis presents a BSM-model-independent search strategy to look for unanticipated signals for new physics. Events are classified according to their final state into event classes. For each event class an automated search algorithm tests whether the observed event counts are compatible with the Monte Carlo (MC) simulated Standard Model (SM) expected event counts in many regions of several different distributions sensitive to the effects of new physics. For each distribution the search algorithm is repeated on a large number of pseudo-experiments to make a frequentist estimate of the statistical significance of the three most deviating regions in different event classes. A region in which a significant deviation is observed defines a data-derived signal region (DDSR). The allowed false positive rate, i.e. the probability to define a DDSR in the absence of a signal, is fixed a priori. Any region in which a deviation is observed that is larger than the threshold imposed by this condition is significant. Any DDSR found will need to be tested with a statistically independent dataset in a dedicated analysis using an improved background model.

In Chapter 4, several aspects of this strategy are compared using simplified examples to the statistically more powerful 'global' method of combining the datasets and correcting to local significance for the amount of tests performed. It is concluded that the DDSR method can potentially perform better than the global method for the practical reason that it allows the construction of a background model for a single test region (possibly with control regions for instance) rather than for many. The significance to a given signal as function of the number of tests, the false positive rate, and the signal strength is also studied using simplified examples. It is demonstrated that the data should be analysed in both very exclusive (many test regions) and very inclusive (few test regions) representations in order to maximize the potential to find an unanticipated signal for new physics. The analyses steps are outlined and the advantaged and disadvantaged of the DDSR strategy are summarized.

In Chapter 5, the strategy has been applied to the data collected by the ATLAS experiment at the LHC during 2015, corresponding to a total of 3.2 fb^{-1} of $\sqrt{s} = 13$ TeV pp collisions. With this dataset, the effective mass, invariant mass, missing transverse momentum and scalar sum of transverse momentum distributions of exclusive event classes containing electrons, muons, photons, b-tagged jets, non-b-tagged jets and missing transverse momentum have been scanned for deviations from the MC-based SM prediction. Sensitivity studies have been performed with various toy signals ($t\bar{t}+\gamma$, $t\bar{t}+W/Z$, WZ, ZZ, gluino, and Z' production) showing that the strategy can potentially discover signals for new physics without a priori knowledge of the processes.

No significant deviations are found in the 2015 dataset and consequently no dedicated analysis of DDSRs is performed.

In Chapter 6, the strategy has subsequently been applied to the ATLAS dataset collected during 2015 and 2016 corresponding to a total of 36.2 fb^{-1} of $\sqrt{s} = 13$ TeV pp collisions in a preliminary version of the analysis. In addition to scanning the data in exclusive event classes, the data is also scanned in event classes that are more inclusive in (b-)jets and lepton flavour. In a separate iteration of the scan Z and Higgs boson candidates are reconstructed from leptons or photons and used for the definition of event classes and in the computation of the scanned observables. Multijet event classes of the 2015 plus 2016 dataset are, in contrast to the analysis of the 2015 dataset, not analysed. The preliminary version of the analysis presented in Chapter 6 uses an incomplete background model in which several background processes with a small cross section remain missing as well as estimates of contributions from misreconstructed QCD events and theoretical modelling uncertainties for some processes. Therefore, a process of elimination has been adopted by which regions can be excluded as having an excess large enough to potentially define a DDSR. All but a few of the large number of regions scanned are eliminated. The regions not eliminated correspond to the final states of processes that are not included in the background model, notably triple-photon production, the fully-leptonic channel of $WZ\gamma$ production, and misreconstructed QCD events in the electron-plus-jet final state. These event classes should be re-evaluated once the deficiencies in the background model are addressed but are expected to be eliminated as well based on initial estimates of the missing contributions.

The application of the strategy discussed in this work will be useful to search for signals of unknown particles and interactions in the full Run 2 and other future datasets. As the size of the dataset grows so does the complexity of analysis in terms of derivation formats needed, disk space and bookkeeping requirements, the number of rare SM processes to be included in the background model, the removal of overlapping phase-space regions between processes, etc. At the same time, the growing look-elsewhere effect might also prohibit the use of exclusive event classes. A more modular approach in which subsets of similar final states with the same contributing background processes are analysed in series is recommended to allow separate background models to be used for each subset and to address some of the technical issues regarding derivations. It is important though that in a more modular approach the data-driven inclusiveness of the event classes considered is maintained as it is one of the unique features of this approach. For future developments, it might also be interesting to look into the possibility of providing exclusion limits for the fast exclusion of exotic BSM models predicting high-multiplicity final states. In particular, the classification of all selected (observed and simulated) events into exclusive classes allows a uniform exclusion limit for all event classes *not* observed (within the selection) at the classification stage (i.e. having $C_{\mathrm{SM}} < 0.1$ and $C_{\mathrm{obs}} = 0$). This could similarly be extended to regions in the tails of the scanned distributions.

A Derivation of background efficiency for alternative test statistics

Two options for more powerful test statistics are discussed in Section 4.2.3. Here, the background efficiencies for these test statistics are derived analytically and verified with toy experiments.

A.1 Multiplying p_0-values

The first of the two alternative test statistics is defined in Eq. 4.20 as[1]:

$$t_p \equiv \bar{p}_{0_1} \cdot p_{0_2}$$

where $\bar{p}_{0_1}$ is the global p_0-value after the initial tests on the first of the two equally-sized data samples as defined in Eq. 4.8. Both $\bar{p}_{0_1} \sim \mathcal{U}(0,1)$ and $p_{0_2} \sim \mathcal{U}(0,1)$ under H_0 which is used to determine ϵ_{bkg}. Under the condition that a DDSR is found, i.e. $\bar{p}_{0_1} \leq \bar{\alpha}_1$, the pdf of $\bar{p}_{0_1}$ ($f_{\bar{p}_{0_1}}$) becomes a uniform distribution between 0 and $\bar{\alpha}_1$:

$$f_{\bar{p}_{0_1}}(x \mid \bar{\alpha}_1) = \begin{cases} 1/\bar{\alpha}_1 & \text{if } 0 \leq x \leq \bar{\alpha}_1 \\ 0 & \text{else} \end{cases} \tag{A.1}$$

such that it is normalized to unity.

In Eq. 4.17 it is concluded that ϵ_{bkg} can be well approximated by $\bar{\alpha}_1 \alpha_2$ when p_{0_2} is used as the test statistic. Note that this approximation is the exact solution for the probability to find at least one DDSR times the probability that $p_{0_2} \leq \alpha_2$ for exactly one DDSR, i.e. $\Pr(n_{\text{FP}} \geq 1 \mid H_0) \cdot \Pr(p_{0_2} \leq \alpha_2 \mid H_0)$. In other words, the probability $\Pr(n_{\text{FP}} \geq 2 \mid H_0)$ must be small enough to be negligible. The probability to find more than one DDSR is (smaller than) $\frac{\bar{\alpha}_1^2}{2}$:

$$\begin{aligned} \Pr(n_{\text{FP}} \geq 2 \mid H_0) &= 1 - \Pr(n_{\text{FP}} = 0 \mid H_0) - \Pr(n_{\text{FP}} = 1 \mid H_0) \\ &= 1 - \binom{n}{0} \alpha_1^0 (1-\alpha_1)^{n-0} - \binom{n}{1} \alpha_1^1 (1-\alpha_1)^{n-1} \\ &= 1 - (1-\bar{\alpha}_1) - n\left(1-(1-\bar{\alpha}_1)^{\frac{1}{n}}\right)(1-\bar{\alpha}_1)^{\frac{n-1}{n}} \\ &= \frac{n-1}{n} \cdot \frac{\bar{\alpha}_1^2}{2} + \mathrm{O}\left(\bar{\alpha}_1^3\right) < \frac{\bar{\alpha}_1^2}{2} + \mathrm{O}\left(\bar{\alpha}_1^3\right) \end{aligned} \tag{A.2}$$

[1] Note that this is rather similar to the commonly used Fisher's method, in which independent p_0-values are combined by taking the sum of the logarithm of the p_0-values, i.e. $t'_p \equiv -2\sum_{i=1}^{k} \ln p_{0_i}$. In this case, t'_p can be shown to follow the well-known χ^2 distribution with $2k$ degrees of freedom.

This result can be used to simplify to calculation of ϵ_{bkg} for the alternative test statistics knowing that the error is of $\mathrm{O}\left(\bar{\alpha}_1^2\right)$. Using the critical value c_p against which t_p is compared as the parameter for ϵ_{bkg}, it can calculated as:

$$\begin{aligned}
\epsilon_{\text{bkg}}(c_p \mid \bar{\alpha}_1) &= \Pr\left(\bar{p}_{01} \le \bar{\alpha}_1 \,\cap\, t_p \le c_p \mid H_0\right) \\
&= \Pr\left(\bar{p}_{01} \le \bar{\alpha}_1 \mid H_0\right) \cdot \Pr\left(t_p \le c_p \,\middle|\, \bar{p}_{01} \le \bar{\alpha}_1 \text{ and } H_0\right) \\
&= \bar{\alpha}_1 \cdot \int_0^1 \Pr\left(p_{02} \le \frac{c_p}{x} \,\middle|\, H_0\right) \cdot f_{\bar{p}_{01}}(x|\bar{\alpha}_1)\,\mathrm{d}x \\
&= \bar{\alpha}_1 \left[\int_0^{c_p} \Pr\left(p_{02} \le \frac{c_p}{x} \,\middle|\, H_0\right) f_{\bar{p}_{01}}(x|\bar{\alpha}_1)\,\mathrm{d}x + \int_{c_p}^1 \Pr\left(p_{02} \le \frac{c_p}{x'} \,\middle|\, H_0\right) f_{\bar{p}_{01}}(x'|\bar{\alpha}_1)\,\mathrm{d}x'\right] \\
&= \bar{\alpha}_1 \left[\int_0^{c_p} f_{\bar{p}_{01}}(x|\bar{\alpha}_1)\,\mathrm{d}x + \int_{c_p}^1 \frac{c_p}{x'} f_{\bar{p}_{01}}(x'|\bar{\alpha}_1)\,\mathrm{d}x'\right] \\
&= \int\limits_0^{c_p} \begin{cases} 1 & \text{if } x \le \bar{\alpha}_1 \\ 0 & \text{if } x > \bar{\alpha}_1 \end{cases} \mathrm{d}x + \int\limits_{c_p}^1 \frac{c_p}{x'} \begin{cases} 1 & \text{if } x' \le \bar{\alpha}_1 \\ 0 & \text{if } x' > \bar{\alpha}_1 \end{cases} \mathrm{d}x' \\
&= \begin{cases} \int_0^{c_p} \mathrm{d}x + \int_{c_p}^{\bar{\alpha}_1} c_p/x'\,\mathrm{d}x' & \text{if } c_p \le \bar{\alpha}_1 \\ \int_0^{\bar{\alpha}_1} \mathrm{d}x & \text{if } c_p > \bar{\alpha}_1 \end{cases} \\
&= \begin{cases} c_p\left(1 + \ln\bar{\alpha}_1 - \ln c_p\right) & \text{if } c_p \le \bar{\alpha}_1 \\ \bar{\alpha}_1 & \text{if } c_p > \bar{\alpha}_1 \end{cases}
\end{aligned} \tag{A.3}$$

A.2 Adding z-scores

Similarly, ϵ_{bkg} can be determined for the test statistic defined in Eq. 4.21 as[2]:

$$t_z \equiv \bar{z}_1 + z_2$$

where $\bar{z}_1$ is the global z-score after the initial tests on the first of the two equally-sized data samples and it is defined as $\bar{z}_1 \equiv z\left(\bar{p}_{01}\right)$. Both $\bar{z}_1 \sim \phi$ and $z_2 \sim \phi$ under H_0. Under the condition that a DDSR is found, i.e. $\bar{z}_1 \ge z(\bar{\alpha}_1)$, the pdf of $\bar{z}_1$ becomes:

$$f_{\bar{z}_1}(x \mid \bar{\alpha}_1) = \begin{cases} 0 & \text{if } x < z(\bar{\alpha}_1) \\ \phi(x) / \int_{z(\bar{\alpha}_1)}^{\infty} \phi(x')\,\mathrm{d}x' = \phi(x)/Q(z(\bar{\alpha}_1)) = \phi(x)/\bar{\alpha}_1 & \text{if } x \ge z(\bar{\alpha}_1) \end{cases} \tag{A.4}$$

[2]Note that this is also rather similar to the commonly used Stouffer's z-score method, in which independent z-scores ($\sim \phi$) are combined as $z_{\text{comb}} \equiv \sum_{i=1}^{k} z_i/\sqrt{k} \sim \phi$ to get a z-score of the combined results.

such that it is normalized to unity. The ccdf of t_z ($\bar{F}_{t_z}$), parametrized using the critical value c_z against which t_z is compared, and under the condition that a DDSR has been found is then:

$$
\begin{aligned}
\bar{F}_{t_z}(c_z \mid \bar{\alpha}_1) &= \Pr\left(t_z \geq c_z \mid \bar{z}_1 \geq z(\bar{\alpha}_1) \text{ and } H_0\right) \\
&= \int_{c_z}^{\infty} \mathrm{d}t_z \int_{-\infty}^{\infty} \mathrm{d}y \int_{-\infty}^{\infty} \mathrm{d}x \, f_{\bar{z}_1}(x|\bar{\alpha}_1) \cdot f_{z_2}(y) \cdot \delta\left(x + y - t_z\right) \\
&= \frac{1}{\bar{\alpha}_1} \int_{c_z}^{\infty} \mathrm{d}t_z \int_{-\infty}^{\infty} \mathrm{d}y \int_{z(\bar{\alpha}_1)}^{\infty} \mathrm{d}x \, \phi(x) \cdot \phi(y) \cdot \delta\left(x + y - t_z\right) \\
&= \int_{c_z}^{\infty} \mathrm{d}t_z \, \frac{\mathcal{N}(t_z \mid 0, 2)}{\bar{\alpha}_1} \cdot Q\left(\frac{2 \cdot z(\bar{\alpha}_1) - t_z}{\sqrt{2}}\right)
\end{aligned}
\tag{A.5}
$$

The ϵ_{bkg} for small $\bar{\alpha}_1$ then becomes:

$$
\begin{aligned}
\epsilon_{\text{bkg}}(c_z \mid \bar{\alpha}_1) &= \Pr\left(\bar{z}_1 \geq z(\bar{\alpha}_1) \,\cap\, t_z \geq c_z \mid H_0\right) \\
&= \Pr\left(\bar{z}_1 \geq z(\bar{\alpha}_1) \mid H_0\right) \cdot \Pr\left(t_z \geq z \mid \bar{z}_1 \geq z(\bar{\alpha}_1) \text{ and } H_0\right) \\
&= \bar{\alpha}_1 \cdot F_{t_z}(c_z \mid \bar{\alpha}_1) \\
&= \int_{c_z}^{\infty} \mathrm{d}t_z \, \mathcal{N}(t_z \mid 0, 2) \cdot Q\left(\frac{2 \cdot z(\bar{\alpha}_1) - t_z}{\sqrt{2}}\right)
\end{aligned}
\tag{A.6}
$$

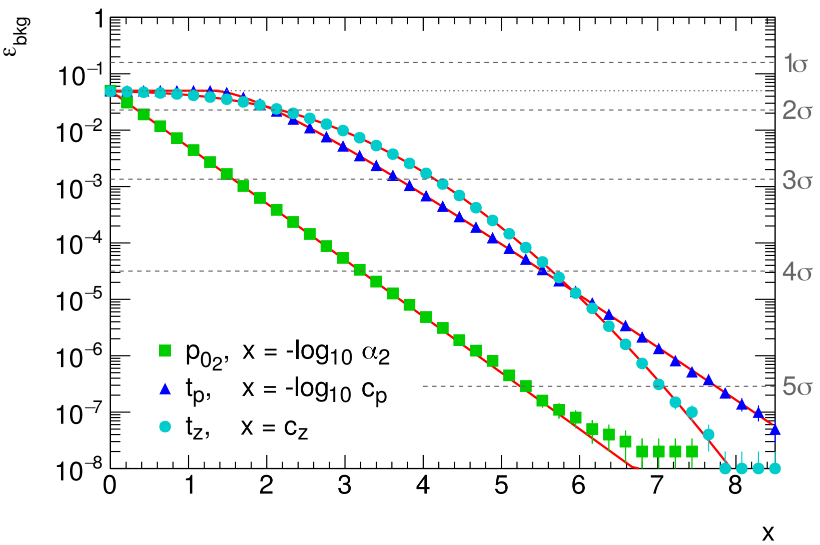

Figure A.1: Background efficiencies for the three different test statistics as a function of x, where x is (the logarithmic form of) the critical parameter to which the test statistic is compared. The markers show the numerical results obtained using toy experiments, while the solid red lines are the analytical results. The dashed lines show the corresponding global significances. The $\bar{\alpha}_1$ is set to 0.05 and the number of bins n is set to 10^5. A dotted line is drawn at $\epsilon_{\text{bkg}} = \bar{\alpha}_1$ which is the maximum background efficiency by construction.

A.3 Verification using toy experiments

Figure A.1 shows the background efficiencies for each of the three test statistics (p_{0_2}, t_p and t_z) discussed as a function of the critical value against which the test statistics are compared (α_2, c_p and c_z). For α_2 and c_p the $-\log_{10}$-values are used on the x-axis. As a verification, an MC method to generate toy experiments is used to estimate ϵ_{bkg} in a frequentist way from the fraction of toys having $p_{0_2} \leq \alpha_2$, $t_p \leq c_p$, or $t_z \geq c_z$ respectively. The functions are given by Eqs. 4.16, 4.22 and 4.23 and shown in Figure A.1 with the red solid lines. The markers show the ϵ_{bkg} as obtained from MC simulations. The particular parameters used in the comparison are $\bar{\alpha} = 0.05$ and $n = 10^5$. The functions agree with the MC simulations within the statistical uncertainties.

B Developments in the analysis

The analysis described in Chapter 5 is based on an early version of the analysis of the 2015 dataset that was used as an example in Ref. [11] which describes the method and search strategy. Several improvements have been made to the analysis presented in Ref. [11] which have been incorporated in Chapter 5. The changes and their effects are summarized in this appendix.

B.1 Event selection

Events with large offline $E_{\mathrm{T}}^{\mathrm{miss}}$ The event selection, as shown in Figure 5.1, allows events with an offline reconstructed $E_{\mathrm{T}}^{\mathrm{miss}} > 200$ GeV that do not pass the online $E_{\mathrm{T}}^{\mathrm{miss}}$ trigger to be selected by any of the other requirements rather than discarding them. In other words, the selection requirement for events with large $E_{\mathrm{T}}^{\mathrm{miss}}$ is placed in a logical *OR* with the remaining requirements. As the online $E_{\mathrm{T}}^{\mathrm{miss}}$ reconstruction is based solely on calorimeter information and does not take into account the presence of any muons in the event, discarding events with an offline reconstructed $E_{\mathrm{T}}^{\mathrm{miss}} > 200$ GeV failing to pass the online $E_{\mathrm{T}}^{\mathrm{miss}}$ trigger can lead to inefficiencies in event classes such as $E_{\mathrm{T}}^{\mathrm{miss}}\,2\mu$ where the $E_{\mathrm{T}}^{\mathrm{miss}}$ arises from, for instance, neutrinos recoiling against muons. The observed (expected) number of events in the $E_{\mathrm{T}}^{\mathrm{miss}}\,2\mu$ event class increases from 1 (5.4) in Ref. [11], to 17 (18.0) in Chapter 5, and a new ($E_{\mathrm{T}}^{\mathrm{miss}}\,3\mu$) event class is added to the scan with 1 (0.65) events.

Triggers for electron(s) plus muon(s) events The event selection in Ref. [11] required events containing both one or more electrons and one or more muons to pass the electron trigger requirement or the electron-plus-muon trigger requirement. In Figure 5.1, any event containing both electrons and muons is required to *either* pass the muon *or* the electron trigger requirements (or the electron-plus-muon requirement). In other words, the lepton requirements are placed in a logical *OR* rather than in a hierarchical order, such that mixed-lepton-flavour events that fail the electron and mixed-lepton triggers can be selected by the single/di-muon trigger. This improves the acceptance of event classes with one electron plus one or more muons with up to approximately 5%.

Derivation cuts Table C.1 in Appendix C presents a complete overview of the impact of the derivation requirements on the event selection. While in Ref. [11] it is implicitly assumed that the $H_{\mathrm{T}}(\mathrm{jets}_{20}) > 150$ GeV requirement is satisfied for events with $E_{\mathrm{T}}^{\mathrm{miss}} > 200$ GeV, the effect of this cut on the acceptance has not been estimated.

For the remaining event classes in Table C.1 with no large $E_{\mathrm{T}}^{\mathrm{miss}}$, the requirement in Ref. [11] is a lepton with a p_{T} larger than 100 GeV. This requirement has been changed to a lepton with $p_{\mathrm{T}} > 100$ GeV *OR* $H_{\mathrm{T}}(\mathrm{jets}_{60}) > 150$ GeV. This increases the acceptance of e.g. the $1\mu\,2b$ event classes with more than 800% to 14 159 observed events, and adds five new event classes to the scan. The total number of accepted events increases by approximately 4.5%.

B.2 Cleaning cuts

The $E_{\mathrm{T}}^{\mathrm{miss}}$ cleaning cuts listed in Table 5.2 are applied to all event classes with $E_{\mathrm{T}}^{\mathrm{miss}} > 200$ GeV in Ref. [11]. These cuts are very effective in removing fake $E_{\mathrm{T}}^{\mathrm{miss}}$ contamination in $E_{\mathrm{T}}^{\mathrm{miss}}$ + jets event classes where the fake $E_{\mathrm{T}}^{\mathrm{miss}}$ arises from jet mismeasurements. However, in event classes with additional leptons the regions removed by these cuts are dominated by events with real $E_{\mathrm{T}}^{\mathrm{miss}}$ final-states from W, $t\bar{t}$ and diboson events, and contain a negligible fake $E_{\mathrm{T}}^{\mathrm{miss}}$ contribution. In this work, the $E_{\mathrm{T}}^{\mathrm{miss}}$ cleaning cuts have only been applied to event classes with $E_{\mathrm{T}}^{\mathrm{miss}} > 200$ GeV having *no* leptons. This increases the acceptance in all $E_{\mathrm{T}}^{\mathrm{miss}}$-plus-lepton(s) event classes and the number of active event classes (i.e. $C_{\mathrm{SM}} > 0.1$) increases by 40.

B.3 MC corrections

In Ref. [11], a reweighting procedure as a function of $E_{\mathrm{T}}^{\mathrm{miss}}$ and of the number of signal jets is applied to event classes with two photons and jets ($E_{\mathrm{T}}^{\mathrm{miss}} < 200$ GeV and no leptons) to correct a known deficiency in the modelling of the $E_{\mathrm{T}}^{\mathrm{miss}}$ distribution due to a too large forward jet activity in the SHERPA 2.1.1 samples. After extensive studies of the impact of this modelling issue on the scan results, it had been concluded that this modelling deficiency has no impact, but the background model with the reweighting procedure for the diphoton event classes was kept. Since there is no impact of this mismodelling on the results and since it affects all SHERPA 2.1.1 samples, this work treats all SHERPA 2.1.1 samples consistently by *not* reapplying the reweighting procedure as a function of $E_{\mathrm{T}}^{\mathrm{miss}}$ and jets in the diphoton event classes.

B.4 Classification

The aforementioned changes lead to an increase of the number of event classes. The number of event classes having $C_{\mathrm{SM}} < 0.1$ and $C_{\mathrm{obs}} \geq 1$ increases from 18 event classes to 20, and the number of event classes subjected to the search algorithm from 686 event classes to 730.

B.5 Scanned observables

In addition to the m_{eff} and m_{inv} observables scanned in Ref. [11], the H_{T} observable is scanned, as well as the $E_{\mathrm{T}}^{\mathrm{miss}}$ observable in classes with $E_{\mathrm{T}}^{\mathrm{miss}} > 200$ GeV.

B.6 Scan algorithm

Formation of regions The scan algorithm used in Ref. [11] combines multiple bins into a region by summing together the observed and expected number of events, and the total uncertainties on the expected number of events of each of the bins, as follows:

1. Each systematic variation is symmetrized[1] around the nominal expectation value in the bin;
2. The total uncertainty on the expectation value in the bin is computed from summing together all contributions quadratically.
3. The total (uncertainty on the) expectation value in the region is computed from linearly summing together the contributions of the bins in the region.

The linear addition of the total uncertainties of the bins implicitly assumes that these uncertainties are fully correlated among the bins, which is the case for the majority of the systematic uncertainties but not for MC statistical uncertainties (or some of the theory uncertainties that are explicitly assumed to be uncorrelated). In this work, the algorithm has been modified to effectively produce a rebinning of the histogram where the entire region is one bin. To achieve this the following procedure is used:

1. Each systematic up (and down) variation separately is summed linearly over the region;
2. Each systematic variation is symmetrized around the nominal expectation value in the region;
3. Any additional correlated sources of uncertainty are linearly summed together over the region;
4. All uncorrelated sources of uncertainty are summed quadratically;
5. The total uncertainty on the expectation value in the region is computed from summing together all contributions quadratically.

This has a few consequences, the most straightforward one being a reduction in the total uncertainty of a multi-bin region due to the over-pessimistic treatment of the uncorrelated sources of uncertainty in Ref. [11]. A second effect results from the symmetrization *after* the systematic up/down variations are summed over the entire region. A systematic up/down variation can have an expectation value above the nominal in one bin and below the nominal in an adjacent bin. Such bin-by-bin correlations are lost when the uncertainties are symmetrized before they are summed, leading to an over-pessimistic estimate of the total uncertainty in multi-bin regions.

Exclusion of regions In Ref. [11], regions having a total uncertainty on the expectation value larger than 100% are discarded by the algorithm. This, however, allows the possibility for a region with a number of observed events far larger than the uncertainty (e.g. $C_{\mathrm{SM}} = 0.5 \pm 1$ and $C_{\mathrm{obs}} = 10$) to be discarded which is obviously undesirable and is therefore not applied in this work.

B.7 Sensitivity tests

In Ref. [11], several sensitivity tests for a known SM process (X) were performed. The tests were performed by either removing the WZ diboson process or the $t\bar{t}+\gamma$ process. In this work additional tests are included using the ZZ diboson process and $t\bar{t}+W/Z$ processes.

[1] A two-sided systematic variation i is symmetrized as: $\sigma_i = \max\left(|C^{\mathrm{up}}_{\mathrm{SM},i} - C_{\mathrm{SM}}|, |C^{\mathrm{down}}_{\mathrm{SM},i} - C_{\mathrm{SM}}|, |C^{\mathrm{up}}_{\mathrm{SM},i} - C^{\mathrm{down}}_{\mathrm{SM},i}|/2\right)$ where $C^{\mathrm{up/down}}_{\mathrm{SM},i}$ is the total C_{SM} expectation after a 1σ up/down variation of source i. For one-sided (up) variations the same is applied using: $C^{\mathrm{down}}_{\mathrm{SM},i} = 2C_{\mathrm{SM}} - C^{\mathrm{up}}_{\mathrm{SM},i}$.

The sensitivity tests for a known SM process (X) were performed in Ref. [11] by comparing the fraction of pseudo-experiments having a p_{class}-value below a certain threshold for pseudo-experiments with:

1. SM pseudo-data tested against a 'SM-X' background model (signal case)
2. SM pseudo-data tested against the SM background model (background case)

In both cases the same number of active event classes, those having $C_{\text{SM}} > 0.1$ in the SM background model, is used. This therefore implicitly covers the possibility of finding the signal at the classification stage in one of the discarded event classes, i.e. classes having $C_{\text{obs}} > 0$, $C_{\text{SM}-X} < 0.1$ and $C_{\text{SM}} > 0.1$. In this work, the two or strictly separated by evaluating the sensitivity of the classification stage (Appendix F) and the search algorithm separately. The sensitivity tests in this work are therefore performed with pseudo-experiments with:

1. SM pseudo-data tested against a 'SM-X' background model (signal case)
2. 'SM-X' pseudo-data tested against a 'SM-X' background model (background case)

where in both cases the same number of active event classes, those having $C_{\text{SM}-X} > 0.1$, are used. By comparing Figures 5.4–5.6 against Figure 5.8 it can be seen that the effect on the DDSR threshold is negligible. It is expected to make a significant difference only when the number of classes having $C_{\text{SM}-X} > 0.1$ is far smaller than the number of classes having $C_{\text{SM}} > 0.1$, e.g. far a process X with a relatively large cross section.

C Derivation and event selection

C.1 Analysis of 2015 dataset

C.1.1 Derivation

The acceptance is limited by the derivation selection cuts, which requires all events to satisfy at least one of the following conditions:

- $H_\mathrm{T}(\mathrm{jets}_{20}) > 150$ GeV
- $p_\mathrm{T}(1e) > 100$ GeV
- $p_\mathrm{T}(1\mu) > 100$ GeV
- $p_\mathrm{T}(1\gamma) > 100$ GeV
- $p_\mathrm{T}(2e) > 20$ GeV
- $p_\mathrm{T}(2\mu) > 20$ GeV
- $p_\mathrm{T}(2\gamma) > 50$ GeV

where $H_\mathrm{T}(\mathrm{jets}_{20})$ is the scalar sum of transverse momenta of all reconstructed jets based on a jet definition that is similar to signal jets in Table 5.1 but with a lowered $p_\mathrm{T} > 20$ GeV requirement, and where, for instance, $p_\mathrm{T}(1e)$ and $p_\mathrm{T}(2e)$ refer to first and second leading (in p_T) electron in the event. These requirements affect the event classes marked in Figure 5.1 as 'Accepted*'.

C.1.2 Classes without large $E_\mathrm{T}^\mathrm{miss}$

For event classes with $1\mu + X$, $1e + X$ and $1\mu 1e + X$, where X can be photons or jets, an additional reconstruction-level cut is applied requiring at least one of the following conditions:

- $H_\mathrm{T}(\mathrm{jets}_{60}) > 150$ GeV
- $p_\mathrm{T}(1e) > 100$ GeV
- $p_\mathrm{T}(1\mu) > 100$ GeV

as described in Section 5.1.4. The relevant requirements are summarized per event class in the top-half of Table C.1.

C.1.3 Classes with large $E_\mathrm{T}^\mathrm{miss}$

For event classes with $E_\mathrm{T}^\mathrm{miss} > 200$ GeV, one of the derivation requirements is likely to be met, especially the $H_\mathrm{T}(\mathrm{jets}_{20}) > 150$ GeV derivation requirement, so no reconstruction-level cuts are applied. However, a small fraction of events having $E_\mathrm{T}^\mathrm{miss} > 200$ GeV but simultaneously failing all derivation requirements are not accepted. All relevant selection cuts, reconstruction-level or derivation, are therefore summarized in the bottom-half of Table C.1 per event class.

Note that, any event class having three or more signal jets always satisfies the $H_T(\text{jets}_{20/60}) >$ 150 GeV requirement by definition.

Table C.1: Additional selection requirements imposed on events passing the initial trigger selection requirements. Two jet collections are used: jets_{20} is the collection of jets having $p_T > 20$ GeV stemming from the derivation cuts; and jets_{60} is the collection of signal jets. All relevant event classes are listed, using $(X\gamma)$ to denote zero or more photons.

	$E_T^{miss} < 200$ GeV		
Events with	Requirements	Relevant event classes	
1 electron + 0, 1 or 2 (b-)jet(s) + any number of photons	$H_T(\text{jets}_{60}) > 150$ GeV or $p_T(e) > 100$ GeV	$1e\,(X\gamma)$ $1e\,(X\gamma)\,1j$ $1e\,(X\gamma)\,1b$	$1e\,(X\gamma)\,2j$ $1e\,(X\gamma)\,1b\,1j$ $1e\,(X\gamma)\,2b$
1 muon + 0, 1 or 2 (b-)jet(s) + any number of photons	$H_T(\text{jets}_{60}) > 150$ GeV or $p_T(\mu) > 100$ GeV	$1\mu\,(X\gamma)$ $1\mu\,(X\gamma)\,1j$ $1\mu\,(X\gamma)\,1b$	$1\mu\,(X\gamma)\,2j$ $1\mu\,(X\gamma)\,1b\,1j$ $1\mu\,(X\gamma)\,2b$
1 electron + 1 muon + 0, 1 or 2 (b-)jet(s) + any number of photons	$H_T(\text{jets}_{60}) > 150$ GeV or $p_T(e) > 100$ GeV or $p_T(\mu) > 100$ GeV	$1e\,1\mu\,(X\gamma)$ $1e\,1\mu\,(X\gamma)\,1j$ $1e\,1\mu\,(X\gamma)\,1b$	$1e\,1\mu\,(X\gamma)\,2j$ $1e\,1\mu\,(X\gamma)\,1b\,1j$ $1e\,1\mu\,(X\gamma)\,2b$
	$E_T^{miss} > 200$ GeV		
Events with	Requirements	Relevant event classes	
$E_T^{miss} > 200$ GeV + 1 or 2 (b-)jet(s)	$H_T(\text{jets}_{20}) > 150$ GeV	$E_T^{miss}\,1j$ $E_T^{miss}\,1b$	$E_T^{miss}\,2j$ $E_T^{miss}\,1b\,1j$ $E_T^{miss}\,2b$
$E_T^{miss} > 200$ GeV + 1 photon + 0, 1 or 2 (b-)jet(s)	$H_T(\text{jets}_{20}) > 150$ GeV or $p_T(\gamma) > 100$ GeV	$E_T^{miss}\,1\gamma$ $E_T^{miss}\,1\gamma\,1j$ $E_T^{miss}\,1\gamma\,1b$	$E_T^{miss}\,1\gamma\,2j$ $E_T^{miss}\,1\gamma\,1b\,1j$ $E_T^{miss}\,1\gamma\,2b$
$E_T^{miss} > 200$ GeV + 1 electron + 0, 1 or 2 (b-)jet(s) + any number of photons	$H_T(\text{jets}_{20}) > 150$ GeV or $p_T(e) > 100$ GeV	$E_T^{miss}\,1e\,(X\gamma)$ $E_T^{miss}\,1e\,(X\gamma)\,1j$ $E_T^{miss}\,1e\,(X\gamma)\,1b$	$E_T^{miss}\,1e\,(X\gamma)\,2j$ $E_T^{miss}\,1e\,(X\gamma)\,1b\,1j$ $E_T^{miss}\,1e\,(X\gamma)\,2b$
$E_T^{miss} > 200$ GeV + 1 muon + 0, 1 or 2 (b-)jet(s) + any number of photons	$H_T(\text{jets}_{20}) > 150$ GeV or $p_T(\mu) > 100$ GeV	$E_T^{miss}\,1\mu\,(X\gamma)$ $E_T^{miss}\,1\mu\,(X\gamma)\,1j$ $E_T^{miss}\,1\mu\,(X\gamma)\,1b$	$E_T^{miss}\,1\mu\,(X\gamma)\,2j$ $E_T^{miss}\,1\mu\,(X\gamma)\,1b\,1j$ $E_T^{miss}\,1\mu\,(X\gamma)\,2b$
$E_T^{miss} > 200$ GeV + 1 electron + 1 muon + 0, 1 or 2 (b-)jet(s) + any number of photons	$H_T(\text{jets}_{20}) > 150$ GeV or $p_T(e) > 100$ GeV or $p_T(\mu) > 100$ GeV	$E_T^{miss}\,1e\,1\mu\,(X\gamma)$ $E_T^{miss}\,1e\,1\mu\,(X\gamma)\,1j$ $E_T^{miss}\,1e\,1\mu\,(X\gamma)\,1b$	$E_T^{miss}\,1e\,1\mu\,(X\gamma)\,2j$ $E_T^{miss}\,1e\,1\mu\,(X\gamma)\,1b\,1j$ $E_T^{miss}\,1e\,1\mu\,(X\gamma)\,2b$

C.2 Analysis of 2015 & 2016 dataset

As for the analysis of the 2015 dataset, the acceptance is limited by the derivation. The reconstruction level requirements have been simplified to avoid a description of the cuts in terms of two different jet collections.

C.2.1 $1\mu + X$, $1e + X$ and $1\mu 1e + X$ classes

For event classes with $1\mu + X$, $1e + X$ and $1\mu 1e + X$, where X can be photons or jets, an additional reconstruction-level cut is applied requiring at least one of the following conditions:

- $H_{\mathrm{T}}(\mathrm{jets}) > 150$ GeV
- $p_{\mathrm{T}}(1e) > 100$ GeV
- $p_{\mathrm{T}}(1\mu) > 100$ GeV

as described in Section 6.1.4. The cuts are also applied for events with $E_{\mathrm{T}}^{\mathrm{miss}} > 200$ GeV. The relevant requirements are summarized per event class in Table C.2.

C.2.2 Classes with large $E_{\mathrm{T}}^{\mathrm{miss}}$ plus jets and/or photons

For event classes with $E_{\mathrm{T}}^{\mathrm{miss}} + X$, where X can be photons or jets, an additional reconstruction-level cut is applied requiring at least one of the following conditions:

- $H_{\mathrm{T}}(\mathrm{jets}) > 150$ GeV
- $p_{\mathrm{T}}(1\gamma) > 100$ GeV

as described in Section 6.1.4. The relevant requirements are also summarized per event class in Table C.2.

Note that, any event class having three or more signal jets always satisfies the $H_{\mathrm{T}}(\mathrm{jets}) > 150$ GeV requirement by definition.

Table C.2: Additional selection requirements imposed on events passing the initial trigger selection requirements. Only the collection of signal jets is used in the H_{T} requirements. All affected event classes are listed, using $(X\gamma)$ to denote zero or more photons.

Events with	Requirements	Affected event classes	
$E_{\mathrm{T}}^{\mathrm{miss}} > 200$ GeV + 1 or 2 (b-)jet(s)	$H_{\mathrm{T}}(\text{jets}) \geq 150$ GeV	$E_{\mathrm{T}}^{\mathrm{miss}}\,1j$ $E_{\mathrm{T}}^{\mathrm{miss}}\,1b$	$E_{\mathrm{T}}^{\mathrm{miss}}\,2j$ $E_{\mathrm{T}}^{\mathrm{miss}}\,1b\,1j$ $E_{\mathrm{T}}^{\mathrm{miss}}\,2b$
$E_{\mathrm{T}}^{\mathrm{miss}} > 200$ GeV + 1 photon + 0, 1 or 2 (b-)jet(s)	$H_{\mathrm{T}}(\text{jets}) \geq 150$ GeV or $p_{\mathrm{T}}(\gamma) \geq 100$ GeV	$E_{\mathrm{T}}^{\mathrm{miss}}\,1\gamma$ $E_{\mathrm{T}}^{\mathrm{miss}}\,1\gamma\,1j$ $E_{\mathrm{T}}^{\mathrm{miss}}\,1\gamma\,1b$	$E_{\mathrm{T}}^{\mathrm{miss}}\,1\gamma\,2j$ $E_{\mathrm{T}}^{\mathrm{miss}}\,1\gamma\,1b\,1j$ $E_{\mathrm{T}}^{\mathrm{miss}}\,1\gamma\,2b$
1 electron + 0, 1 or 2 (b-)jet(s) + any number of photons	$H_{\mathrm{T}}(\text{jets}) \geq 150$ GeV or $p_{\mathrm{T}}(e) \geq 100$ GeV	$1e\,(X\gamma)$ $1e\,(X\gamma)\,1j$ $1e\,(X\gamma)\,1b$ $E_{\mathrm{T}}^{\mathrm{miss}}\,1e\,(X\gamma)$ $E_{\mathrm{T}}^{\mathrm{miss}}\,1e\,(X\gamma)\,1j$ $E_{\mathrm{T}}^{\mathrm{miss}}\,1e\,(X\gamma)\,1b$	$1e\,(X\gamma)\,2j$ $1e\,(X\gamma)\,1b\,1j$ $1e\,(X\gamma)\,2b$ $E_{\mathrm{T}}^{\mathrm{miss}}\,1e\,(X\gamma)\,2j$ $E_{\mathrm{T}}^{\mathrm{miss}}\,1e\,(X\gamma)\,1b\,1j$ $E_{\mathrm{T}}^{\mathrm{miss}}\,1e\,(X\gamma)\,2b$
1 muon + 0, 1 or 2 (b-)jet(s) + any number of photons	$H_{\mathrm{T}}(\text{jets}) \geq 150$ GeV or $p_{\mathrm{T}}(\mu) \geq 100$ GeV	$1\mu\,(X\gamma)$ $1\mu\,(X\gamma)\,1j$ $1\mu\,(X\gamma)\,1b$ $E_{\mathrm{T}}^{\mathrm{miss}}\,1\mu\,(X\gamma)$ $E_{\mathrm{T}}^{\mathrm{miss}}\,1\mu\,(X\gamma)\,1j$ $E_{\mathrm{T}}^{\mathrm{miss}}\,1\mu\,(X\gamma)\,1b$	$1\mu\,(X\gamma)\,2j$ $1\mu\,(X\gamma)\,1b\,1j$ $1\mu\,(X\gamma)\,2b$ $E_{\mathrm{T}}^{\mathrm{miss}}\,1\mu\,(X\gamma)\,2j$ $E_{\mathrm{T}}^{\mathrm{miss}}\,1\mu\,(X\gamma)\,1b\,1j$ $E_{\mathrm{T}}^{\mathrm{miss}}\,1\mu\,(X\gamma)\,2b$
1 electron + 1 muon + 0, 1 or 2 (b-)jet(s) + any number of photons	$H_{\mathrm{T}}(\text{jets}) \geq 150$ GeV or $p_{\mathrm{T}}(e) \geq 100$ GeV or $p_{\mathrm{T}}(\mu) \geq 100$ GeV	$1e\,1\mu\,(X\gamma)$ $1e\,1\mu\,(X\gamma)\,1j$ $1e\,1\mu\,(X\gamma)\,1b$ $E_{\mathrm{T}}^{\mathrm{miss}}\,1e\,1\mu\,(X\gamma)$ $E_{\mathrm{T}}^{\mathrm{miss}}\,1e\,1\mu\,(X\gamma)\,1j$ $E_{\mathrm{T}}^{\mathrm{miss}}\,1e\,1\mu\,(X\gamma)\,1b$	$1e\,1\mu\,(X\gamma)\,2j$ $1e\,1\mu\,(X\gamma)\,1b\,1j$ $1e\,1\mu\,(X\gamma)\,2b$ $E_{\mathrm{T}}^{\mathrm{miss}}\,1e\,1\mu\,(X\gamma)\,2j$ $E_{\mathrm{T}}^{\mathrm{miss}}\,1e\,1\mu\,(X\gamma)\,1b\,1j$ $E_{\mathrm{T}}^{\mathrm{miss}}\,1e\,1\mu\,(X\gamma)\,2b$

D Normalisation of multijet, photon+jet and diphoton MC samples

Table D.1: Normalisation factors (N.F.) applied to the multijet MC normalisation in event classes having only j and b objects. The blank entries correspond to event classes for which no rescaling has been applied, as those event classes have $C_{obs} \leq 4$. Note that C_{SM} includes the multijet and other possible background contributions.

Event class	C_{SM}	C_{obs}	N.F.
$2j$	$8.15 \cdot 10^5$	$6.61 \cdot 10^5$	0.81
$3j$	$9.33 \cdot 10^5$	$7.00 \cdot 10^5$	0.75
$4j$	$4.96 \cdot 10^5$	$3.52 \cdot 10^5$	0.71
$5j$	$1.74 \cdot 10^5$	$1.20 \cdot 10^5$	0.69
$6j$	$4.66 \cdot 10^4$	$3.18 \cdot 10^4$	0.68
$7j$	$1.04 \cdot 10^4$	$7.02 \cdot 10^3$	0.67
$8j$	$2.06 \cdot 10^3$	$1.36 \cdot 10^3$	0.65
$9j$	343	260	0.75
$10j$	48.0	50	1.04
$11j$	14.2	9	0.61
$12j$	1.68	2	
$13j$	0.429	0	
$1b1j$	$8.37 \cdot 10^4$	$7.42 \cdot 10^4$	0.89
$14j$	0.345	0	
$1b2j$	$1.45 \cdot 10^5$	$1.28 \cdot 10^5$	0.88
$1b3j$	$1.01 \cdot 10^5$	$8.95 \cdot 10^4$	0.88
$1b4j$	$4.38 \cdot 10^4$	$3.86 \cdot 10^4$	0.88
$1b5j$	$1.43 \cdot 10^4$	$1.25 \cdot 10^4$	0.87
$1b7j$	819	759	0.92
$1b6j$	$3.69 \cdot 10^3$	$3.14 \cdot 10^3$	0.84
$1b8j$	169	142	0.82
$1b9j$	36.3	28	0.76
$1b10j$	7.01	2	
$1b11j$	1.18	0	
$2b$	$3.41 \cdot 10^3$	$2.74 \cdot 10^3$	0.80
$2b1j$	$1.48 \cdot 10^4$	$1.30 \cdot 10^4$	0.88
$2b2j$	$1.61 \cdot 10^4$	$1.43 \cdot 10^4$	0.88
$2b3j$	$9.42 \cdot 10^3$	$8.47 \cdot 10^3$	0.89
$2b4j$	$3.69 \cdot 10^3$	$3.42 \cdot 10^3$	0.92
$2b5j$	$1.16 \cdot 10^3$	$1.09 \cdot 10^3$	0.93
$2b6j$	280	271	0.96
$2b7j$	66.4	75	1.17
$2b8j$	16.3	18	1.13
$2b9j$	1.11	4	
$2b10j$	$8.06 \cdot 10^{-2}$	1	
$3b$	666	440	0.65
$3b1j$	$1.19 \cdot 10^3$	$1.07 \cdot 10^3$	0.89
$3b2j$	$1.02 \cdot 10^3$	956	0.93
$3b3j$	503	548	1.11
$3b5j$	57.0	61	1.11
$3b4j$	210	208	0.99
$3b6j$	11.3	13	1.25
$3b7j$	4.16	5	1.29
$3b8j$	0.461	0	
$3b9j$	0.115	0	
$4b$	125	45	0.33
$4b1j$	130	93	0.70
$4b2j$	69.4	52	0.72
$4b3j$	33.2	18	0.44
$4b4j$	10.2	9	0.85
$4b5j$	1.48	5	10.0
$4b6j$	0.687	1	
$5b$	17.7	4	
$5b1j$	10.3	5	0.44
$5b2j$	5.09	2	
$5b3j$	0.820	0	
$5b4j$	2.54	0	
$5b7j$	0.127	0	
$6b$	0.510	0	
$6b1j$	1.06	0	
$6b2j$	$2.11 \cdot 10^{-2}$	1	
$6b3j$	0.114	0	
$7b$	0.141	0	
$8b1j$	$6.29 \cdot 10^{-5}$	1	

Table D.2: Normalisation factors (N.F.) applied to the $\gamma+\text{jets}$ MC normalisation in event classes having 1γ and additional j and/or b objects (left), and to the $2\gamma(+\text{jets})$ MC normalisation in event classes having 2γ and (possibly) additional j and/or b objects (right). The blank entries correspond to event classes for which no rescaling has been applied, as those event classes have $C_{\text{obs}} \leq 4$. Note that C_{SM} includes the $\gamma+\text{jets}$ / $2\gamma(+\text{jets})$ and other possible background contributions.

Event class	C_{SM}	C_{obs}	N.F.
$1\gamma 1j$	$3.73 \cdot 10^{5}$	$4.38 \cdot 10^{5}$	1.20
$1\gamma 2j$	$1.23 \cdot 10^{5}$	$1.46 \cdot 10^{5}$	1.22
$1\gamma 3j$	$2.39 \cdot 10^{4}$	$3.07 \cdot 10^{4}$	1.33
$1\gamma 4j$	$4.14 \cdot 10^{3}$	$5.65 \cdot 10^{3}$	1.38
$1\gamma 5j$	764	959	1.27
$1\gamma 6j$	129	181	1.41
$1\gamma 7j$	21.6	23	1.07
$1\gamma 8j$	3.69	8	2.27
$1\gamma 9j$	0.946	0	
$1\gamma 10j$	$3.55 \cdot 10^{-2}$	2	
$1\gamma 1b$	$2.15 \cdot 10^{4}$	$2.70 \cdot 10^{4}$	1.30
$1\gamma 1b1j$	$1.13 \cdot 10^{4}$	$1.70 \cdot 10^{4}$	1.51
$1\gamma 1b2j$	$3.49 \cdot 10^{3}$	$5.50 \cdot 10^{3}$	1.60
$1\gamma 1b3j$	948	$1.47 \cdot 10^{3}$	1.59
$1\gamma 1b4j$	215	310	1.50
$1\gamma 1b5j$	48.0	70	1.54
$1\gamma 1b6j$	8.66	14	1.74
$1\gamma 1b7j$	1.97	4	
$1\gamma 1b8j$	0.182	0	
$1\gamma 2b$	756	$1.34 \cdot 10^{3}$	1.80
$1\gamma 2b1j$	451	757	1.74
$1\gamma 2b2j$	182	308	1.84
$1\gamma 2b3j$	55.9	81	1.68
$1\gamma 2b4j$	16.5	21	1.47
$1\gamma 2b5j$	7.78	3	
$1\gamma 2b6j$	0.893	0	
$1\gamma 2b7j$	0.156	0	
$1\gamma 3b$	17.2	34	2.11
$1\gamma 3b1j$	18.1	19	1.07
$1\gamma 3b2j$	8.56	6	0.54
$1\gamma 3b3j$	1.98	4	
$1\gamma 3b4j$	0.801	0	
$1\gamma 3b5j$	0.115	0	
$1\gamma 4b$	0.375	1	
$1\gamma 4b1j$	0.382	1	
$1\gamma 4b2j$	0.248	1	

Event class	C_{SM}	C_{obs}	N.F.
2γ	$9.34 \cdot 10^{3}$	$1.34 \cdot 10^{4}$	1.47
$2\gamma 1j$	$1.78 \cdot 10^{3}$	$2.54 \cdot 10^{3}$	1.46
$2\gamma 2j$	445	737	1.77
$2\gamma 3j$	73.8	147	2.03
$2\gamma 4j$	15.8	29	2.01
$2\gamma 5j$	2.74	6	2.40
$2\gamma 6j$	0.814	2	
$2\gamma 7j$	0.205	1	
$2\gamma 1b$	89.1	160	1.89
$2\gamma 1b1j$	49.6	77	1.67
$2\gamma 1b2j$	14.0	20	1.49
$2\gamma 1b3j$	4.35	6	1.50
$2\gamma 1b4j$	1.38	3	
$2\gamma 1b5j$	0.236	0	
$2\gamma 1b6j$	0.104	0	
$2\gamma 2b$	3.28	8	2.69
$2\gamma 2b1j$	2.31	2	
$2\gamma 2b2j$	1.01	4	
$2\gamma 2b3j$	0.361	0	
$2\gamma 3b2j$	0.106	0	

E All event classes and yields in the 2015 dataset

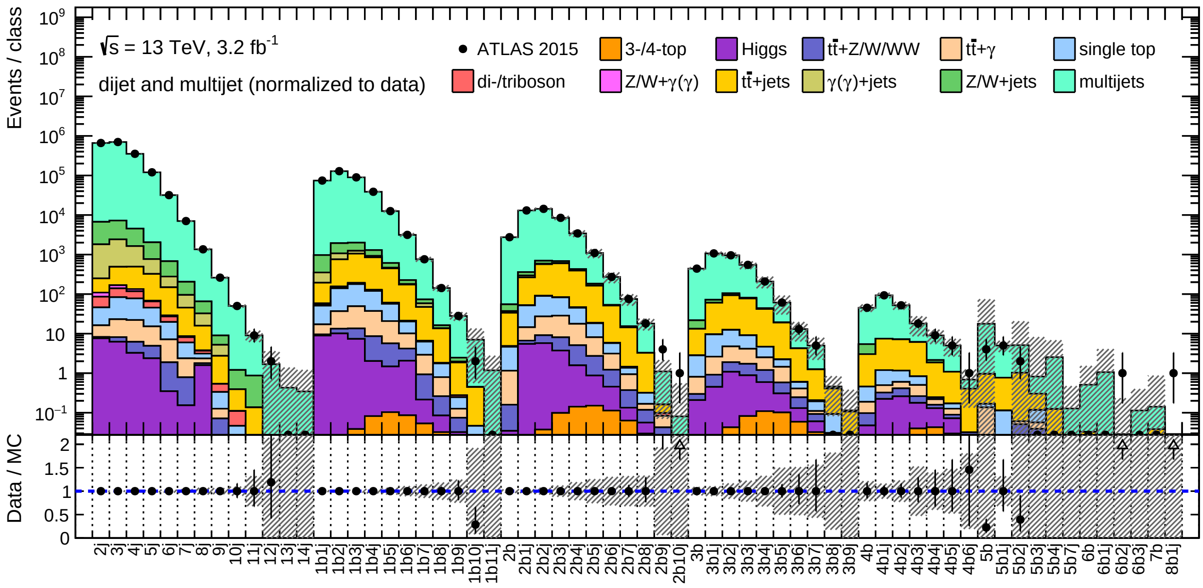

Figure E.1: Expected and observed number of events in all classes with (b-)jets (no $E_{\mathrm{T}}^{\mathrm{miss}}$, leptons or photons). The class labels list the type and multiplicity of reconstructed objects in the events. In event classes with more than four data events, the multijet MC samples are scaled to data. The total uncertainty on the SM prediction is indicated by hatched bands.

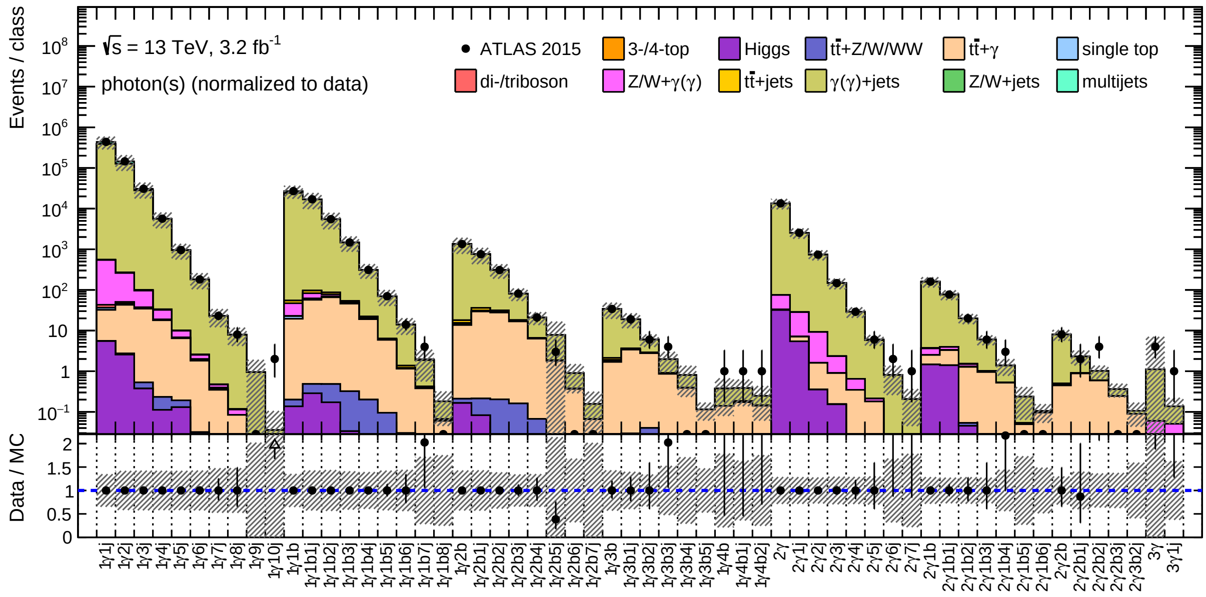

Figure E.2: Expected and observed number of events in all classes with at least one photon and (b-)jets (no leptons or $E_{\mathrm{T}}^{\mathrm{miss}}$). The class labels list the type and multiplicity of reconstructed objects in the events. In event classes with more than four data events, the $\gamma+$jets and $\gamma\gamma+$jets MC samples are scaled to data in the single-photon and diphoton event classes respectively. The total uncertainty on the SM prediction is indicated by hatched bands.

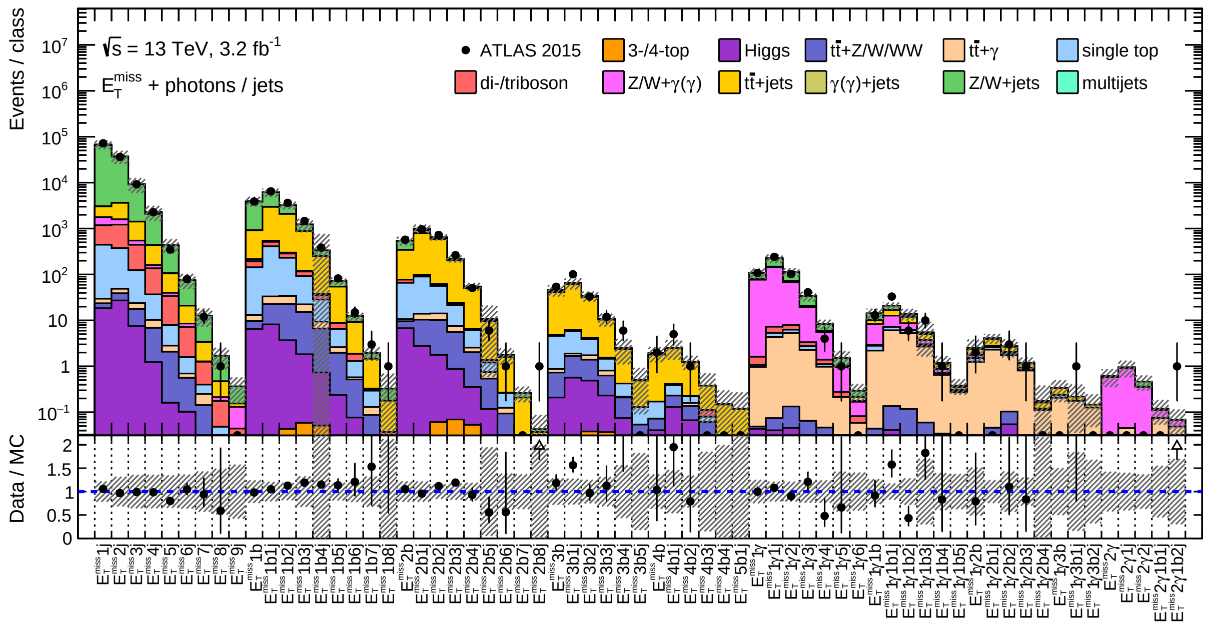

Figure E.3: Expected and observed number of events in all classes with large $E_{\mathrm{T}}^{\mathrm{miss}}$, ($b$-)jets and/or photons (no leptons). The class labels list the type and multiplicity of reconstructed objects in the events. The total uncertainty on the SM prediction is indicated by hatched bands.

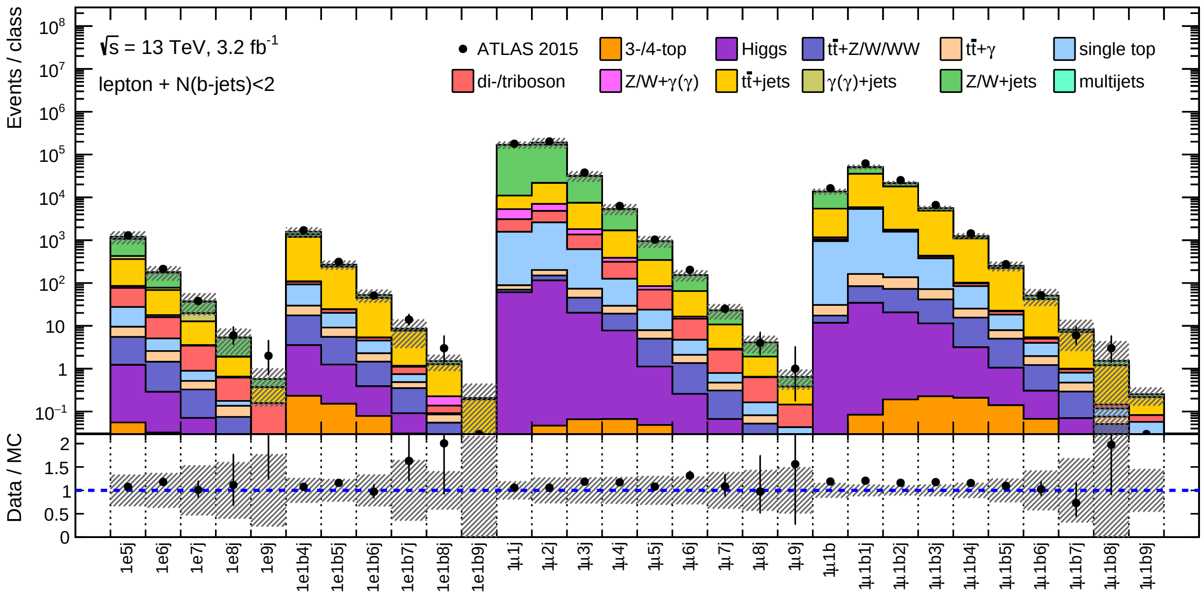

Figure E.4: Expected and observed number of events in all classes with one lepton (electron or muon) and at most one b-jet (no $E_{\mathrm{T}}^{\mathrm{miss}}$ or photons). The class labels list the type and multiplicity of reconstructed objects in the events. The total uncertainty on the SM prediction is indicated by hatched bands.

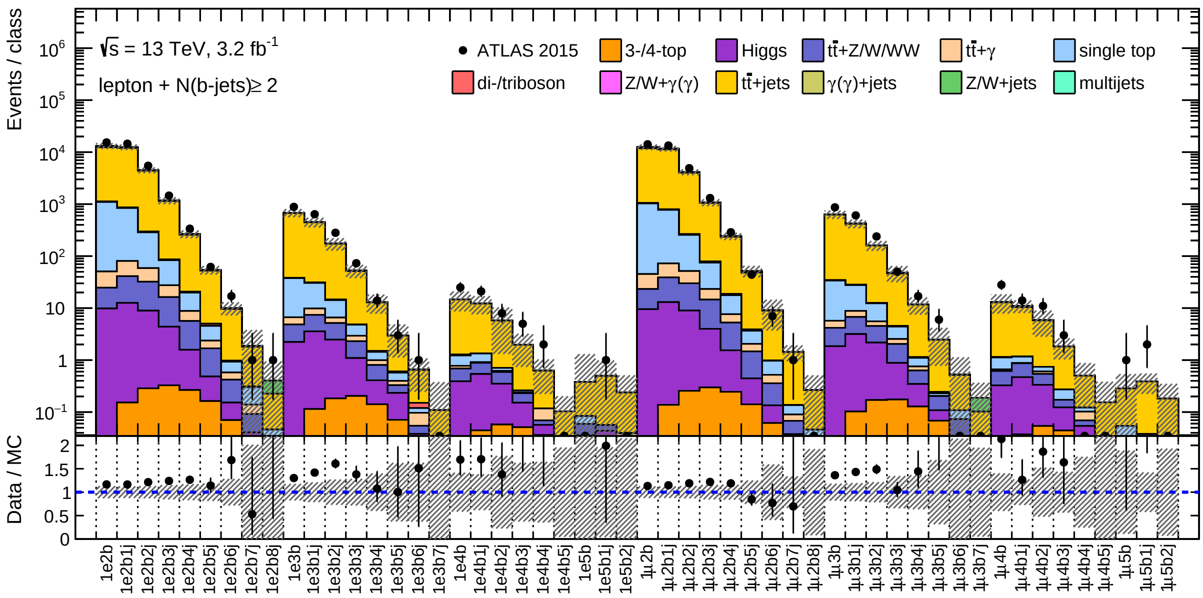

Figure E.5: Expected and observed number of events in all classes with one lepton (electron or muon) and at least two b-jets (no $E_{\mathrm{T}}^{\mathrm{miss}}$ or photons). The class labels list the type and multiplicity of reconstructed objects in the events. The total uncertainty on the SM prediction is indicated by hatched bands.

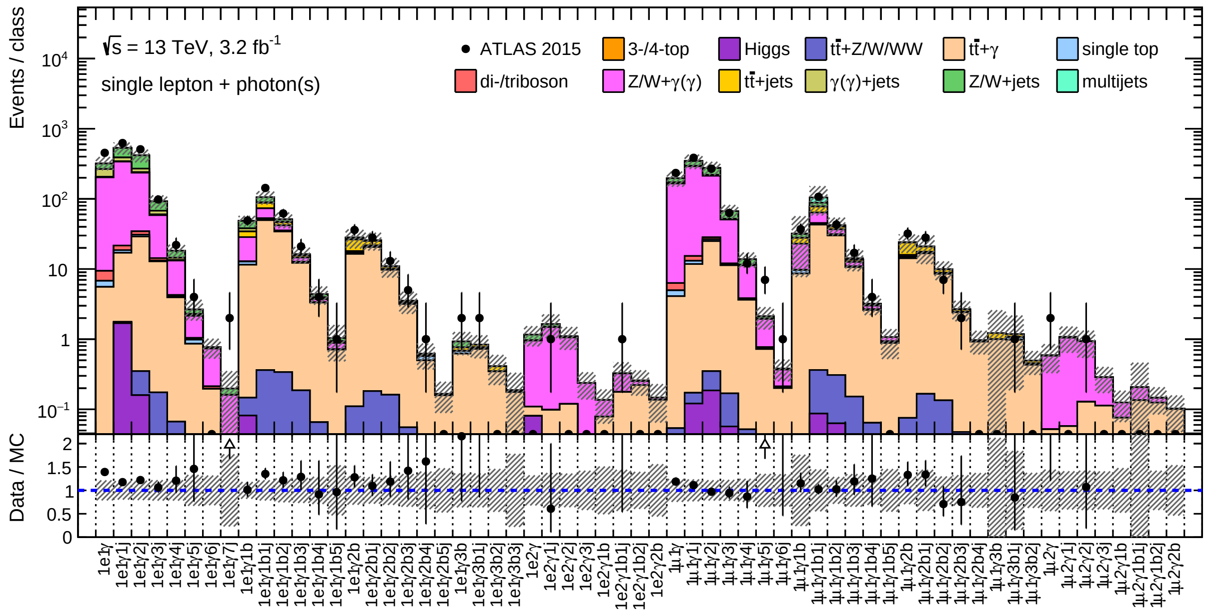

Figure E.6: Expected and observed number of events in all classes with one lepton (electron or muon) and at least one photon (no E_T^{miss}). The class labels list the type and multiplicity of reconstructed objects in the events. The total uncertainty on the SM prediction is indicated by hatched bands.

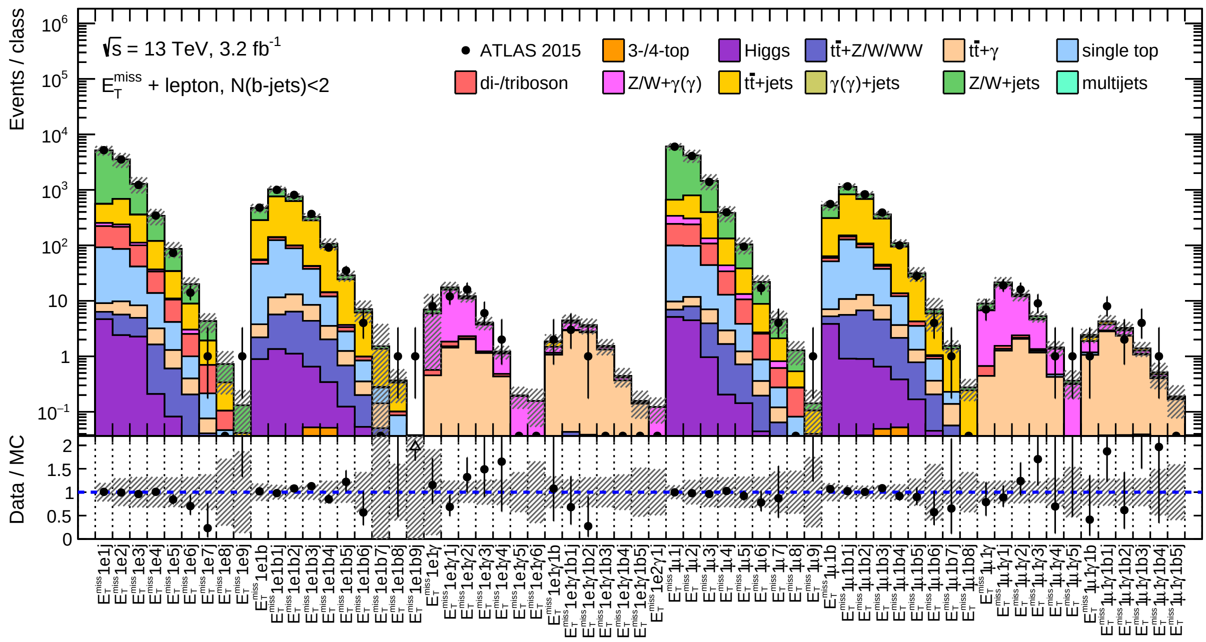

Figure E.7: Expected and observed number of events in all classes with large E_T^{miss}, one lepton (electron or muon) and at most one b-jet (including additional photons). The class labels list the type and multiplicity of reconstructed objects in the events. The total uncertainty on the SM prediction is indicated by hatched bands.

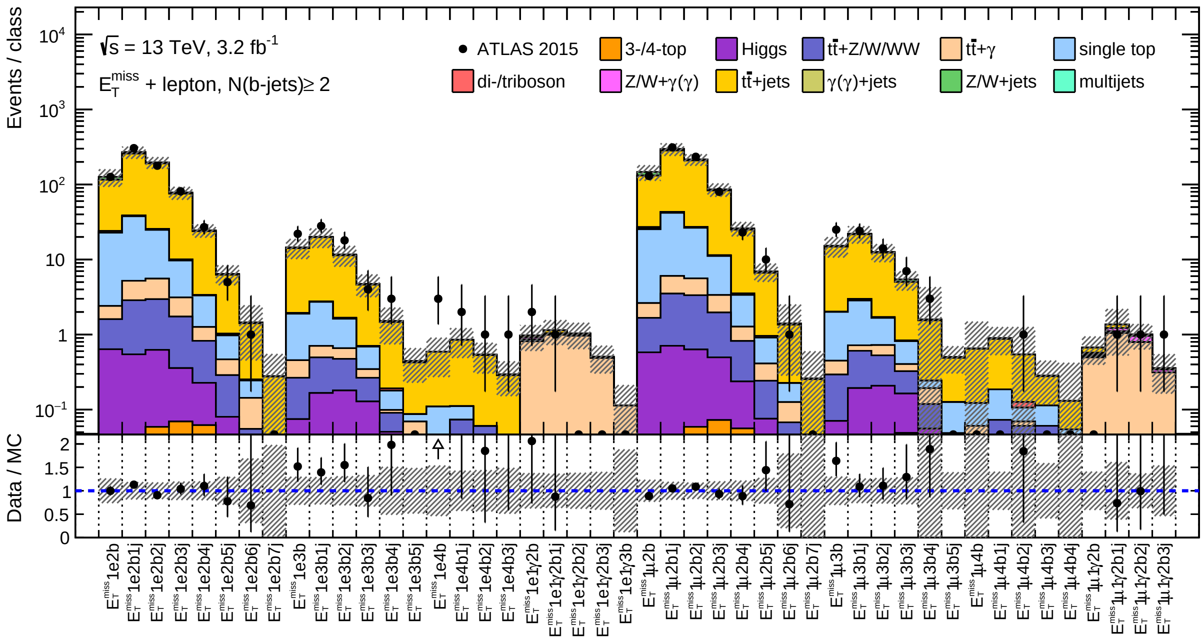

Figure E.8: Expected and observed number of events in all classes with large $E_{\mathrm{T}}^{\mathrm{miss}}$, one lepton (electron or muon) and at least two b-jets (including additional photons). The class labels list the type and multiplicity of reconstructed objects in the events. The total uncertainty on the SM prediction is indicated by hatched bands.

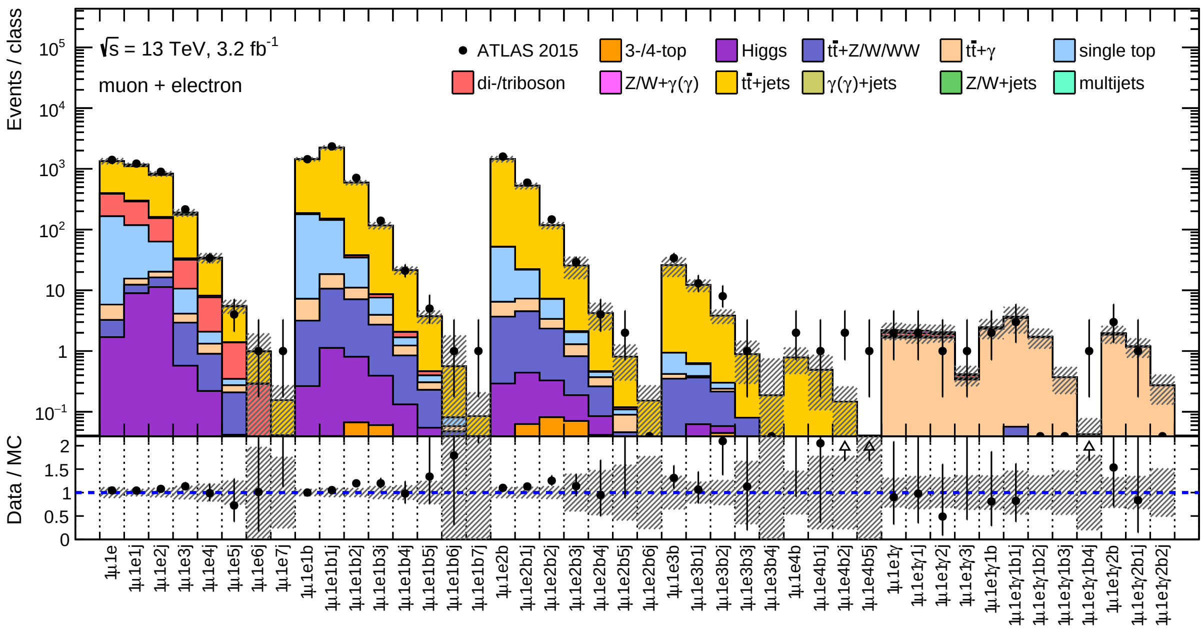

Figure E.9: Expected and observed number of events in all classes with one muon and one electron (including additional jets and photons, no $E_{\mathrm{T}}^{\mathrm{miss}}$). The class labels list the type and multiplicity of reconstructed objects in the events. The total uncertainty on the SM prediction is indicated by hatched bands.

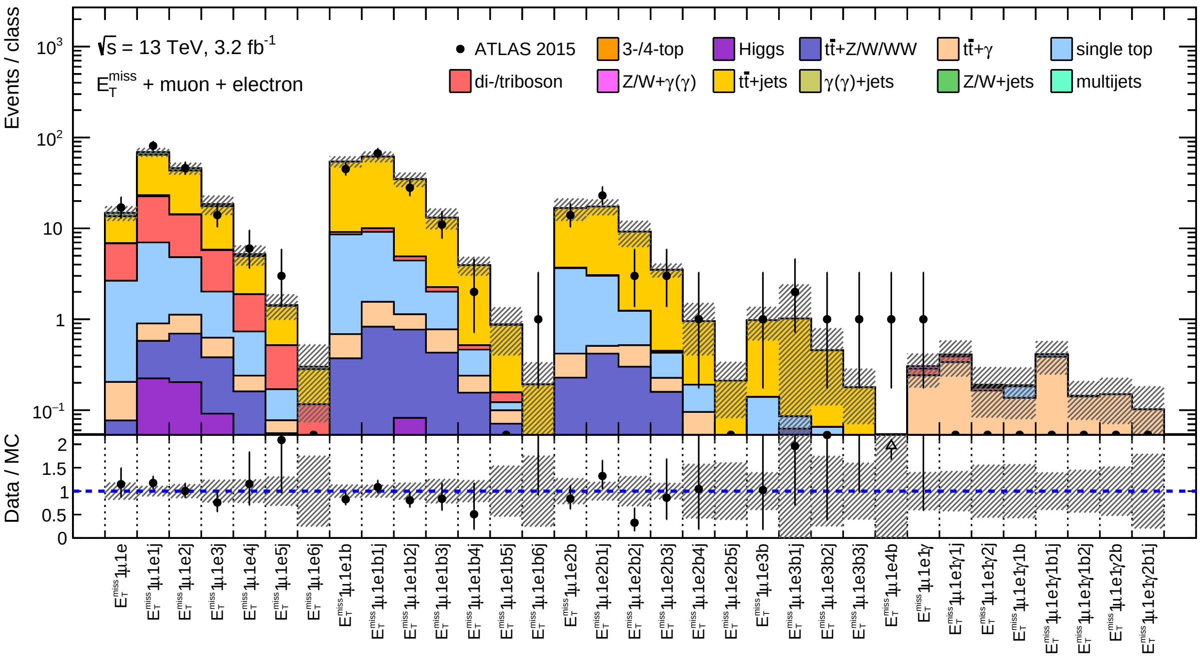

Figure E.10: Expected and observed number of events in all classes with large $E_{\mathrm{T}}^{\mathrm{miss}}$, one muon and one electron (including additional jets and photons). The class labels list the type and multiplicity of reconstructed objects in the events. The total uncertainty on the SM prediction is indicated by hatched bands.

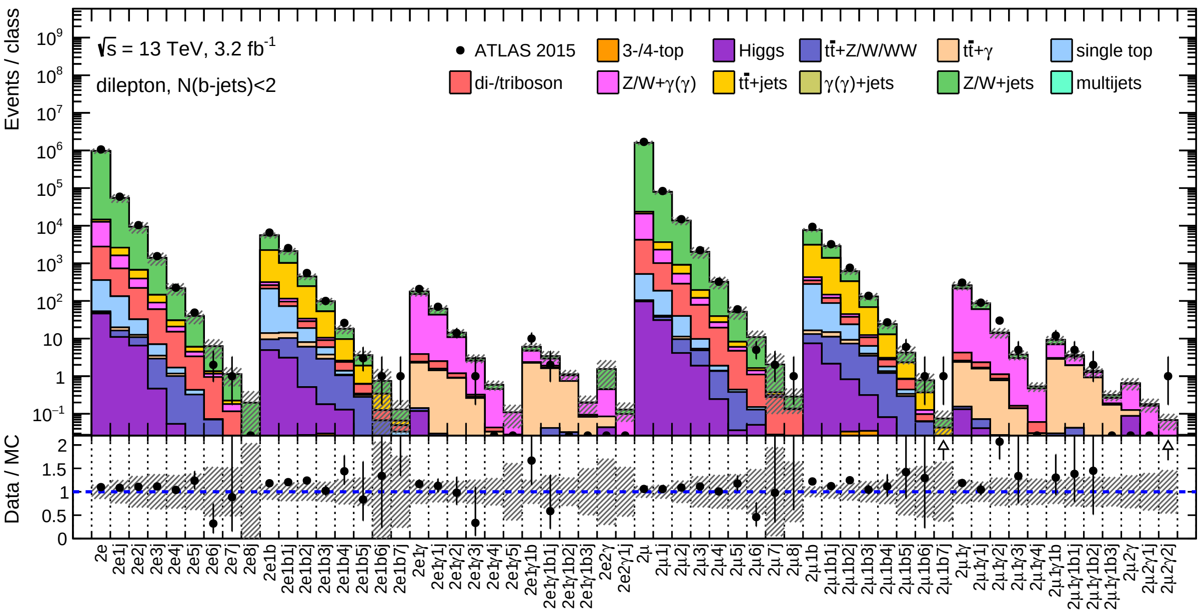

Figure E.11: Expected and observed number of events in all classes with two same-flavour leptons and at most one b-jet (including additional photons, no $E_{\mathrm{T}}^{\mathrm{miss}}$). The class labels list the type and multiplicity of reconstructed objects in the events. The total uncertainty on the SM prediction is indicated by hatched bands.

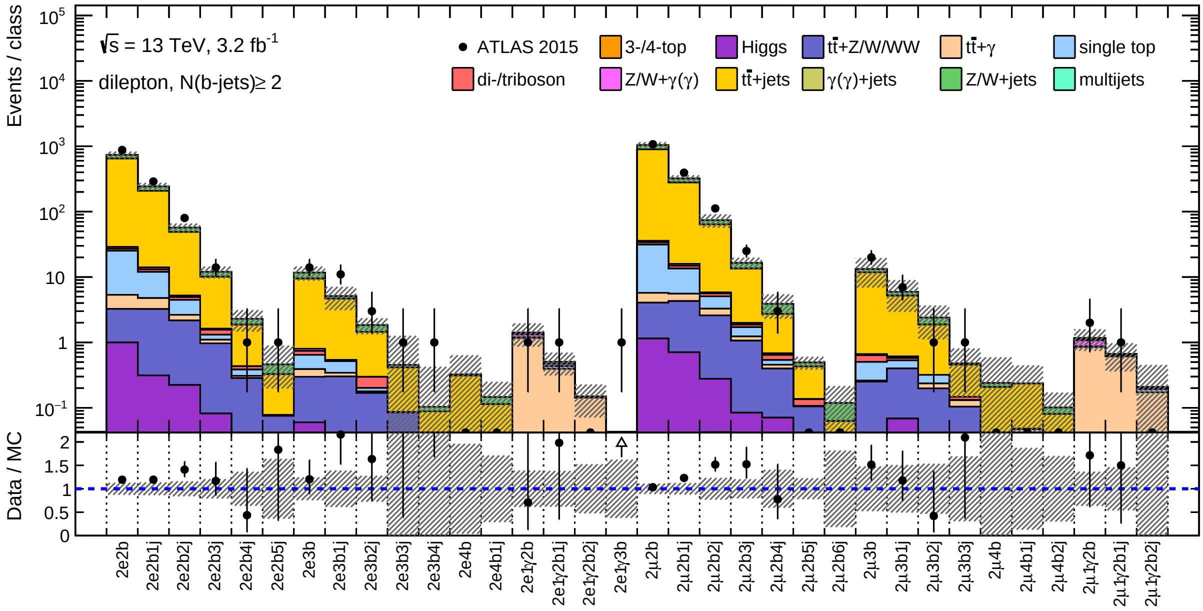

Figure E.12: Expected and observed number of events in all classes with two same-flavour leptons and at least two b-jets (including additional photons, no $E_{\mathrm{T}}^{\mathrm{miss}}$). The class labels list the type and multiplicity of reconstructed objects in the events. The total uncertainty on the SM prediction is indicated by hatched bands.

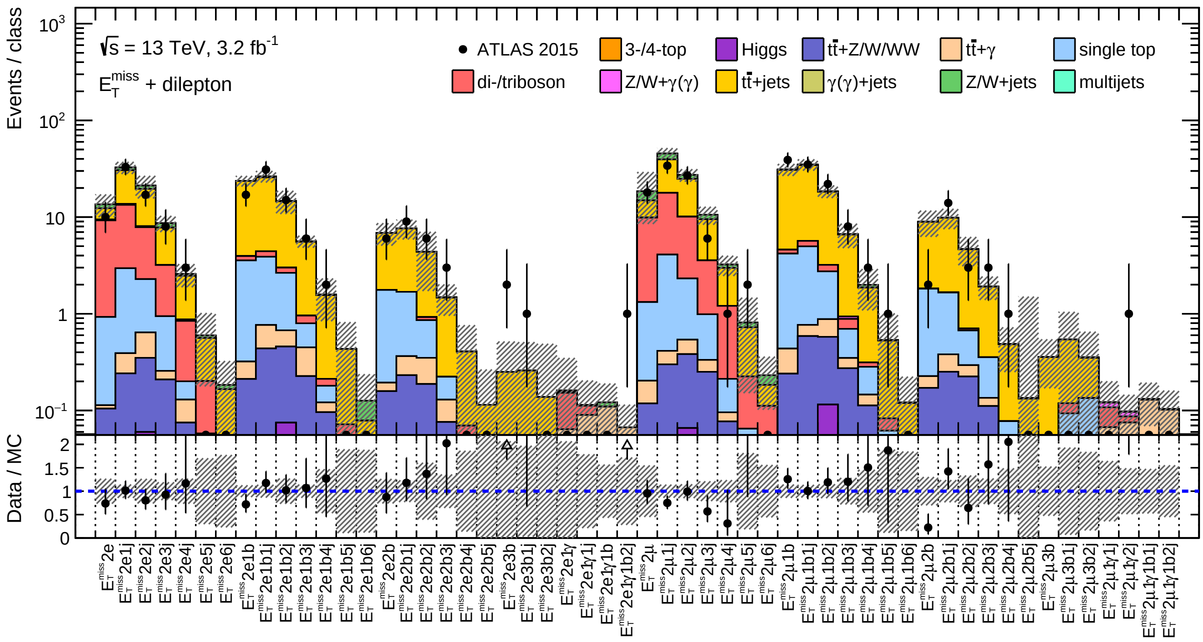

Figure E.13: Expected and observed number of events in all classes with large $E_{\mathrm{T}}^{\mathrm{miss}}$ and two same-flavour leptons (including additional jets and photons). The class labels list the type and multiplicity of reconstructed objects in the events. The total uncertainty on the SM prediction is indicated by hatched bands.

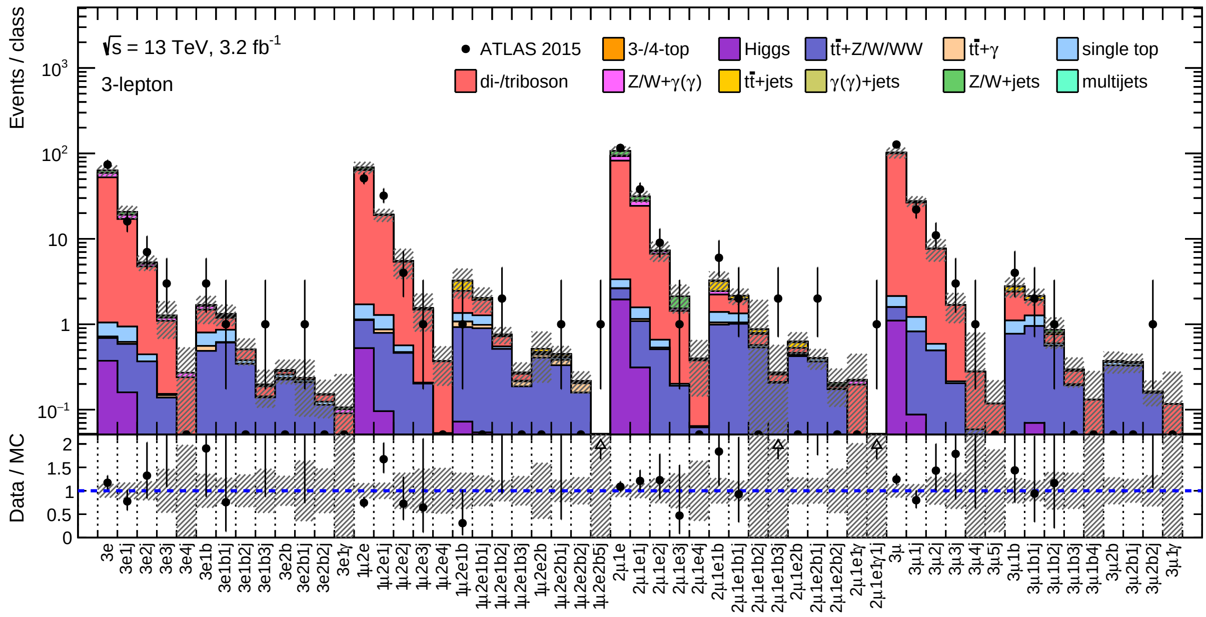

Figure E.14: Expected and observed number of events in all classes with three leptons (including additional jets and photons, no $E_{\mathrm{T}}^{\mathrm{miss}}$). The class labels list the type and multiplicity of reconstructed objects in the events. The total uncertainty on the SM prediction is indicated by hatched bands.

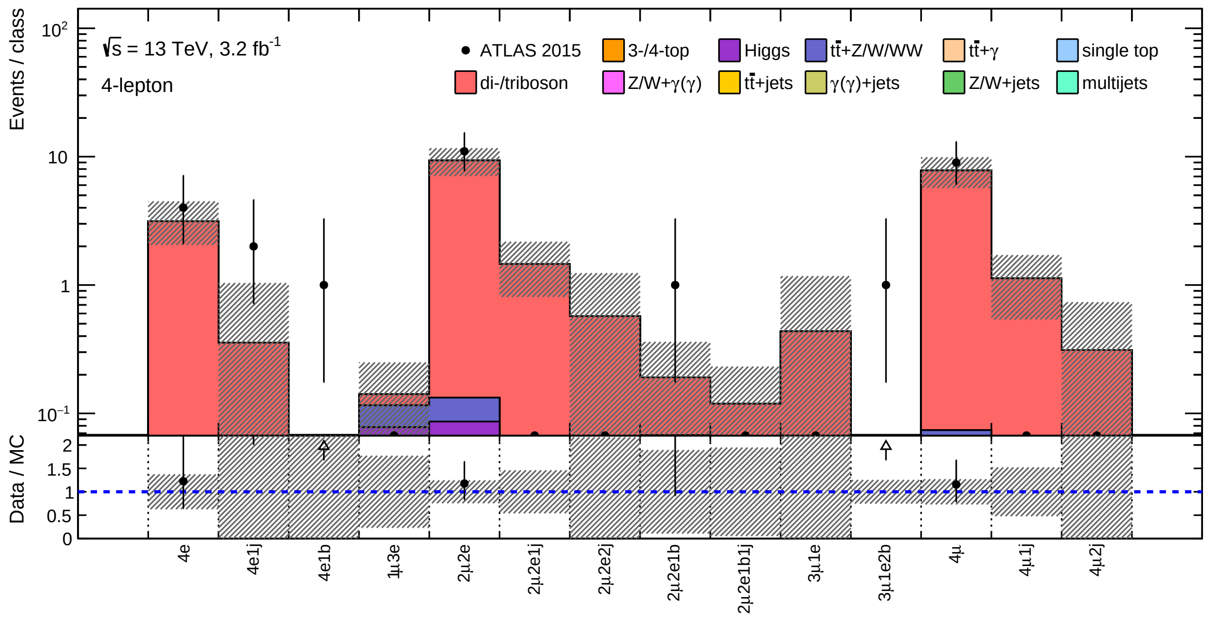

Figure E.15: Expected and observed number of events in all classes with four leptons (including additional jets and photons, no $E_{\mathrm{T}}^{\mathrm{miss}}$). The class labels list the type and multiplicity of reconstructed objects in the events. The total uncertainty on the SM prediction is indicated by hatched bands.

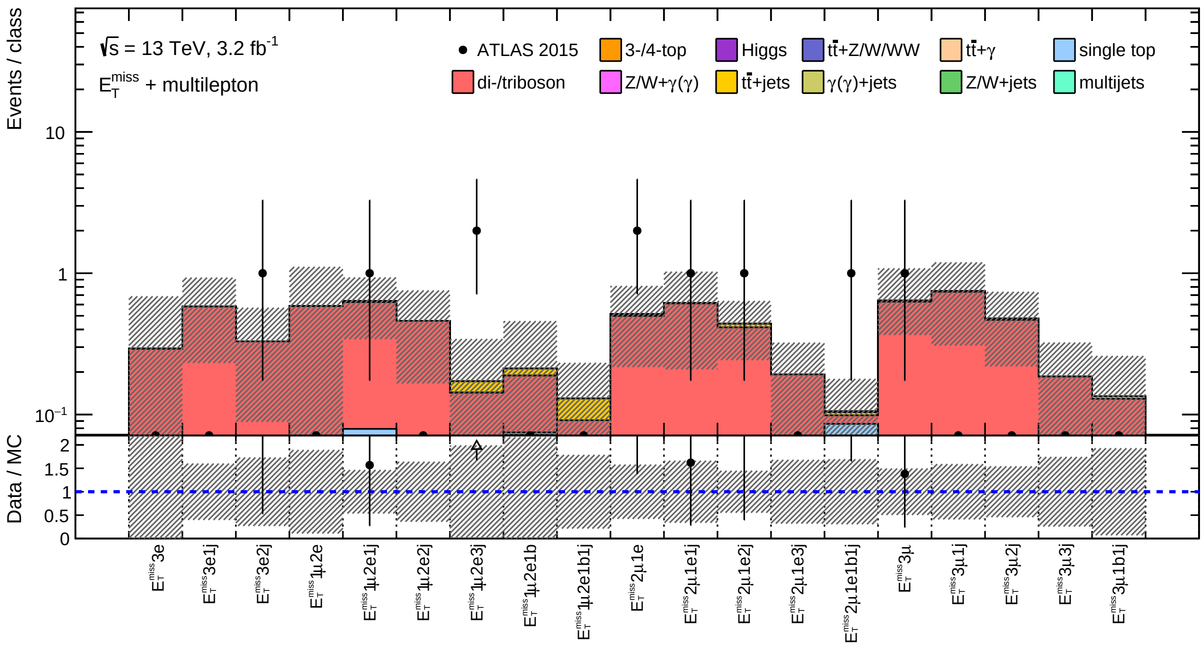

Figure E.16: Expected and observed number of events in all classes with large $E_{\mathrm{T}}^{\mathrm{miss}}$ and at least three leptons (including additional jets and photons). The class labels list the type and multiplicity of reconstructed objects in the events. The total uncertainty on the SM prediction is indicated by hatched bands.

F Classes excluded from scan

The presence of a signal can add to the event classes that are not considered for the search algorithm and statistical analysis, i.e. event classes with $C_{\text{obs}} \geq 1$ and $C_{\text{SM}} < 0.1$. Table F.1 lists the number of event classes having a signal-plus-SM expectation (C_{BSM}) value over a given threshold and $C_{\text{SM}} < 0.1$ using the supersymmetric gluino signals and Z' signals described in Section 5.2.1. Similarly, Table F.2 lists these values by comparing to an incomplete SM background model. An SM process is removed from the background model and the modified expectation value is denoted $C_{\text{SM,incomplete}}$. The table lists the number of event classes having an C_{SM} value over a given threshold and $C_{\text{SM,incomplete}} < 0.1$.

Table F.1: Number of event classes having a signal-plus-SM expectation value (C_{BSM}) over a given threshold and a SM expectation value (C_{SM}) less than 0.1 using the supersymmetric gluino signals and Z' signals described in Section 5.2.1.

Injected signal	Number of event classes with $C_{\text{SM}} < 0.1$ &				
	$C_{\text{BSM}} > 0.1$	$C_{\text{BSM}} > 0.5$	$C_{\text{BSM}} > 1.0$	$C_{\text{BSM}} > 2.0$	$C_{\text{BSM}} > 3.0$
$\tilde{g}$ (1.0 TeV) $\rightarrow t\bar{t}\tilde{\chi}_1^0$	88	15	5	1	-
$\tilde{g}$ (1.2 TeV) $\rightarrow t\bar{t}\tilde{\chi}_1^0$	39	3	1	-	-
$\tilde{g}$ (1.4 TeV) $\rightarrow t\bar{t}\tilde{\chi}_1^0$	14	-	-	-	-
$\tilde{g}$ (1.6 TeV) $\rightarrow t\bar{t}\tilde{\chi}_1^0$	7	-	-	-	-
Z' (2.0 TeV) $\rightarrow f\bar{f}$	1	-	-	-	-
Z' (2.5 TeV) $\rightarrow f\bar{f}$	2	-	-	-	-
Z' (3.0 TeV) $\rightarrow f\bar{f}$	2	-	-	-	-
Z' (3.5 TeV) $\rightarrow f\bar{f}$	1	-	-	-	-

Table F.2: Number of event classes having an SM expectation value (C_{SM}) over a given threshold and a modified SM expectation value ($C_{\text{SM,incomplete}}$), from which a given SM process has been removed, less than 0.1.

Removed SM process	Number of event classes with $C_{\text{SM,incomplete}} < 0.1$ &				
	$C_{\text{SM}} > 0.1$	$C_{\text{SM}} > 0.5$	$C_{\text{SM}} > 1.0$	$C_{\text{SM}} > 2.0$	$C_{\text{SM}} > 3.0$
$t\bar{t} + \gamma$	49	6	3	-	-
$t\bar{t} + W/Z/WW$	21	-	-	-	-
WZ	18	4	-	-	-
ZZ	11	2	1	-	-
3-/4-top	4	-	-	-	-
Higgs	1	-	-	-	-

G Effect of correlation model and uncertainty size on DDSR thresholds

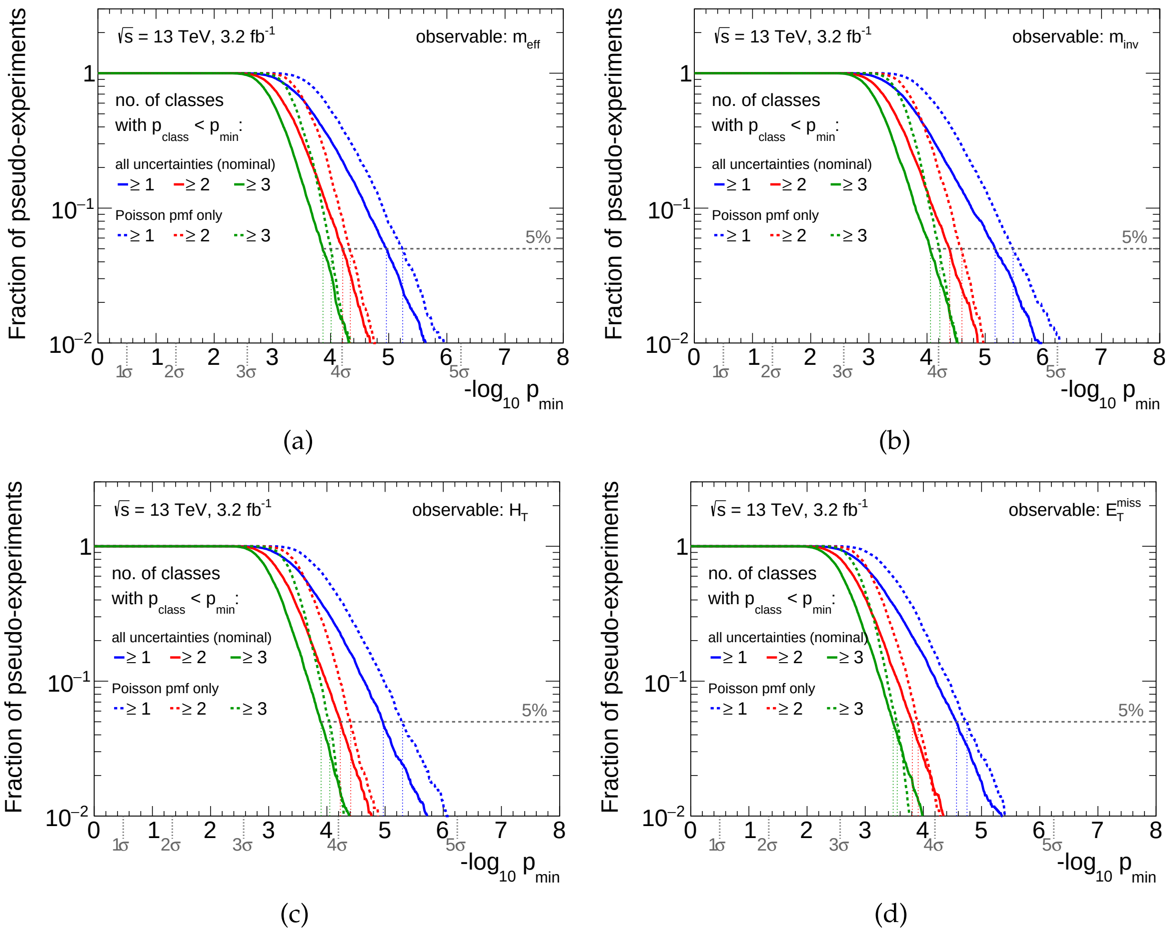

Figure G.1: Comparison of the fractions of pseudo-experiments which have at least one, two and three p_{class}-values below a given p_{min} in the scan of the m_{eff} (a), m_{inv} (b), H_{T} (c) and $E_{\text{T}}^{\text{miss}}$ (d) observable. A background model without *any* experimental or theoretical uncertainties (dashed curves) is compared to the nominal background model (solid curves). For both background models the resulting thresholds for which $P_{\text{exp},i} < 5\%$ are marked by vertical dotted lines.

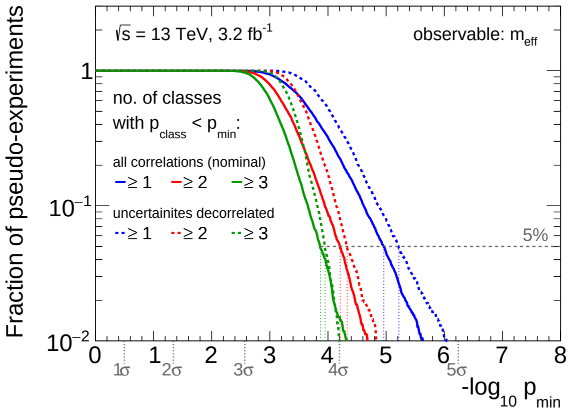

(a)

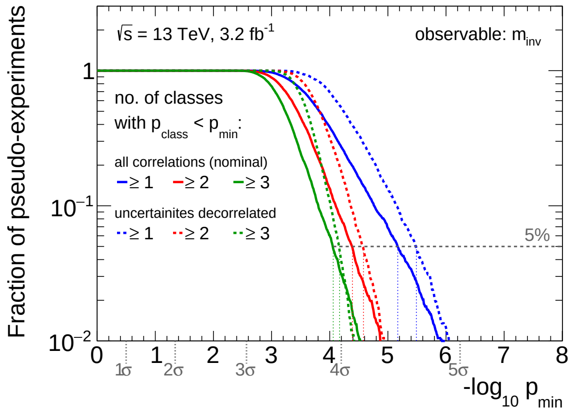

(b)

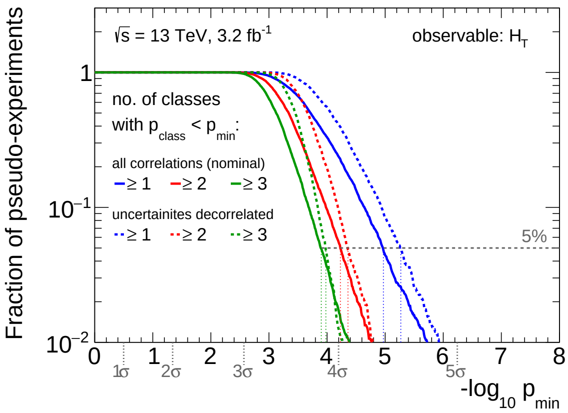

(c)

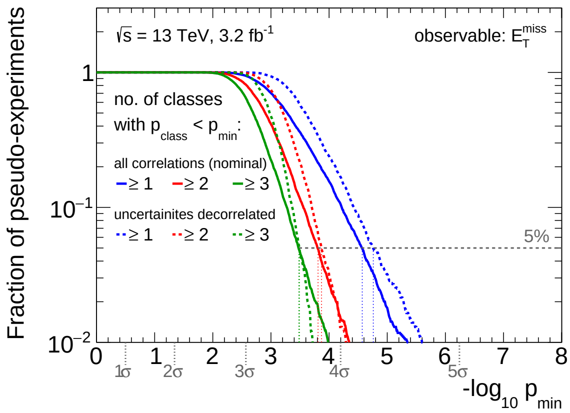

(d)

Figure G.2: Comparison of the fractions of pseudo-experiments which have at least one, two and three p_{class}-values below a given $p_{\min}$ in the scan of the m_{eff} (a), m_{inv} (b), H_{T} (c) and $E_{\text{T}}^{\text{miss}}$ (d) observable. A background model in which all bin-by-bin correlations in the uncertainties are decorrelated (dashed curves) is compared to the nominal background model (solid curves). For both background models the resulting thresholds for which $P_{\text{exp},i} < 5\%$ are marked by vertical dotted lines.

H Validation distributions using 2015+2016 dataset

H.1 $W(\to \ell\nu) +$ jets

H.1.1 Electron channel

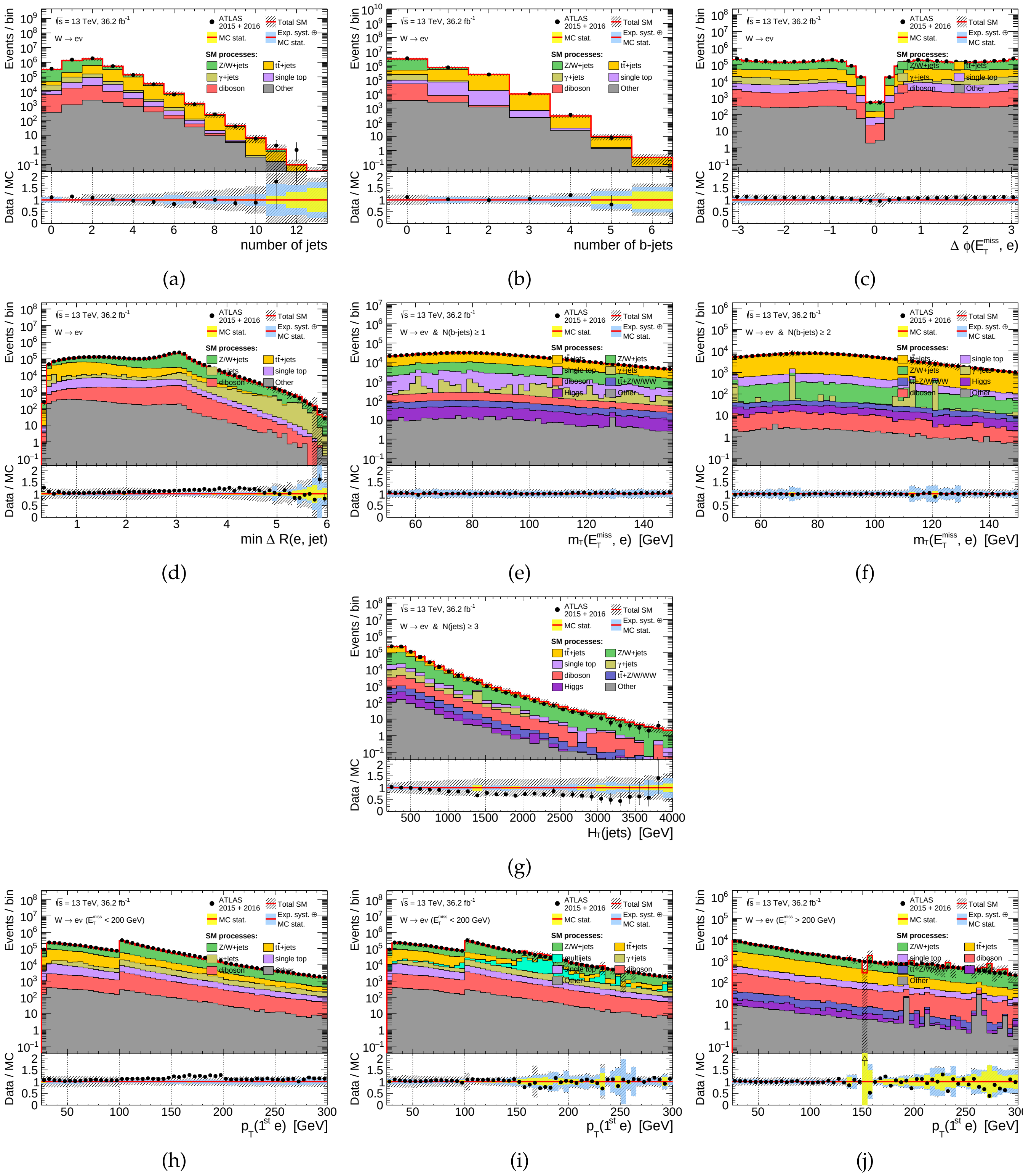

Figure H.1: Validation distributions for the $W(\to e\nu) +$ jets selection (see Table 5.4). The bottom three plots have an additional cut on $E_{\mathrm{T}}^{\mathrm{miss}}$. The bottom-left plot reveals a discrepancy between data and expectation. The bottom-middle plot includes the multijet MC sample in the background model and shows no discrepancy, indicating a large fake contribution. For a selection with large $E_{\mathrm{T}}^{\mathrm{miss}}$ (bottom-right plot) no such discrepancy is observed.

H.1.2 Muon channel

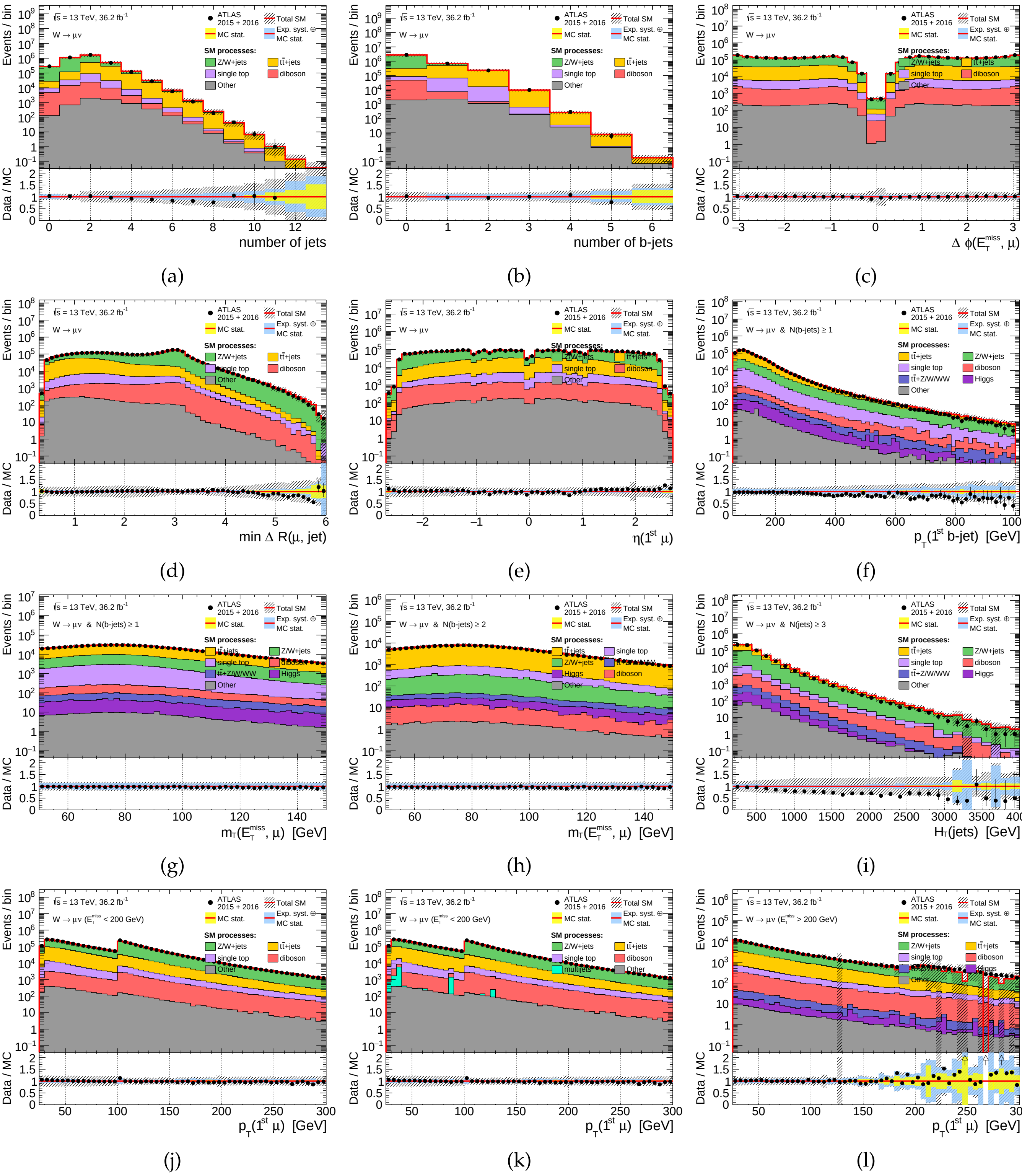

Figure H.2: Validation distributions for the $W(\to \mu\nu) +$ jets selection (see Table 5.4). The bottom three plots have an additional cut on $E_{\mathrm{T}}^{\mathrm{miss}}$. The bottom-left plot uses the nominal background model without the contribution of multijet samples. The bottom-middle plot includes the multijet MC sample in the background model.

H.2 $W + \gamma(\gamma)$

H.2.1 Electron channel

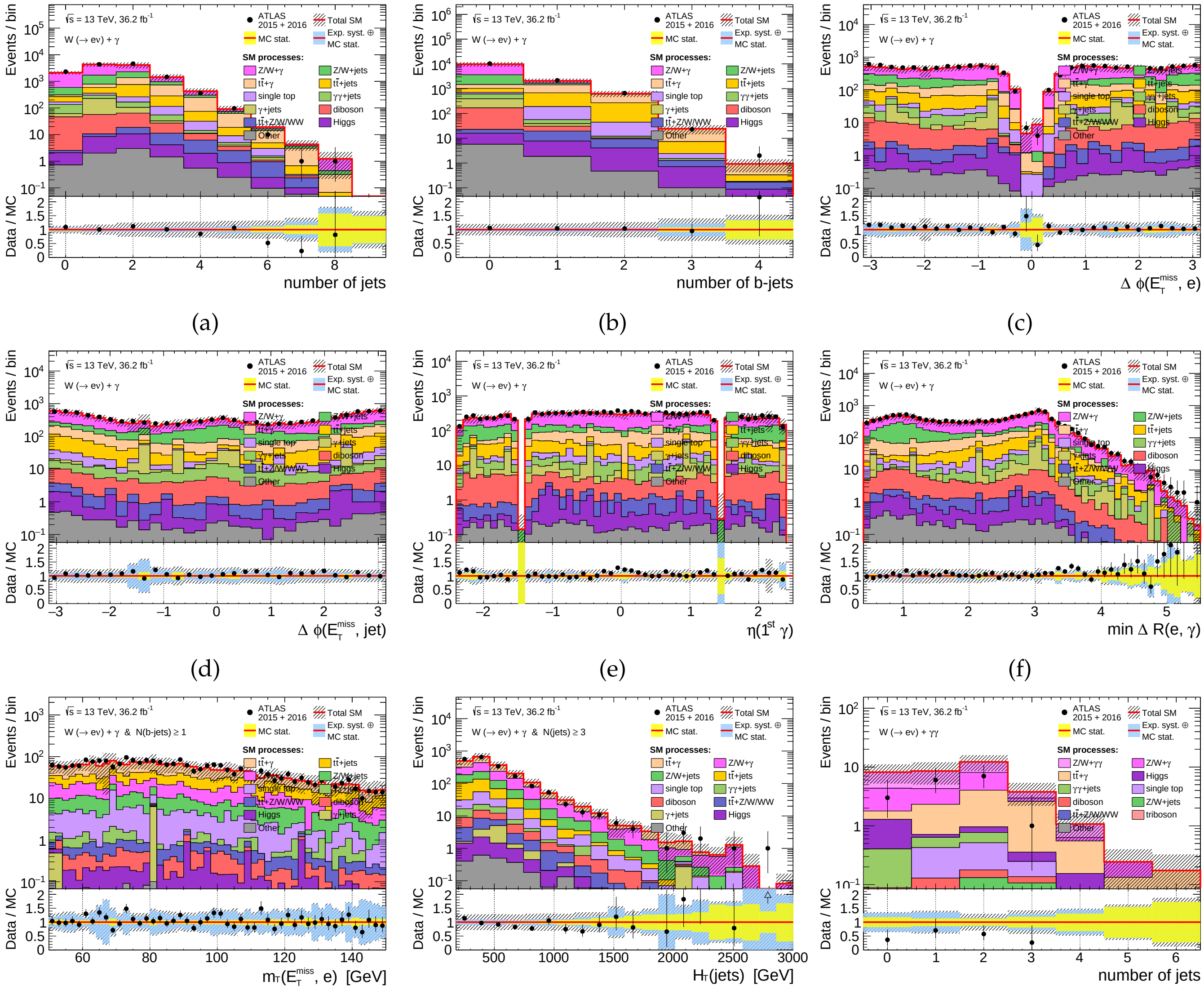

(a) (b) (c)

(d) (e) (f)

(g) (h) (i)

Figure H.3: Validation distributions for the $W(\to e\nu) + \gamma(\gamma)$ selection (see Table 5.4).

H.2.2 Muon channel

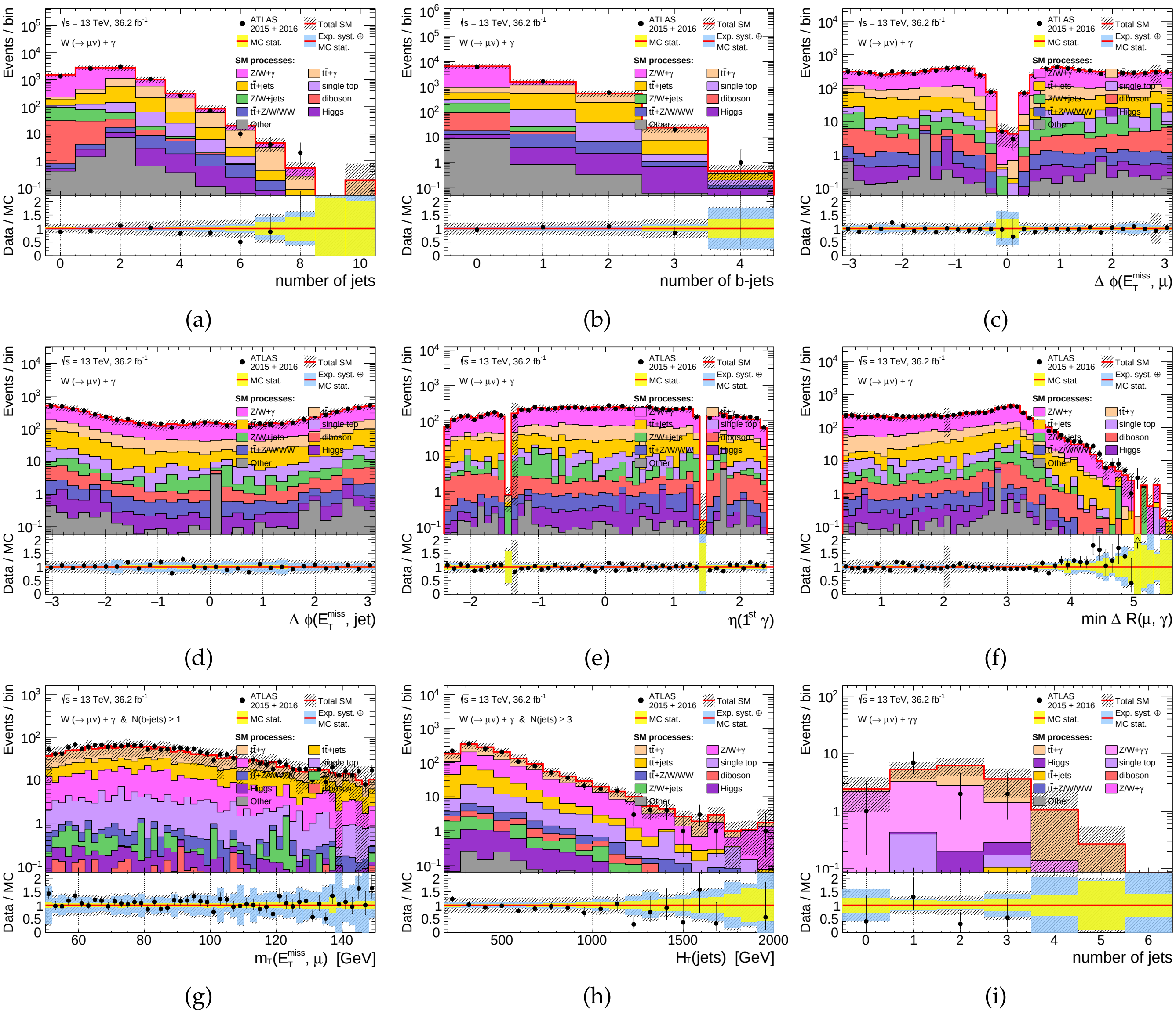

(a) (b) (c)

(d) (e) (f)

(g) (h) (i)

Figure H.4: Validation distributions for the $W(\rightarrow \mu\nu)+\gamma(\gamma)$ selection (see Table 5.4).

H.3 $Z(\to \ell\ell) +$ jets

H.3.1 Electron channel

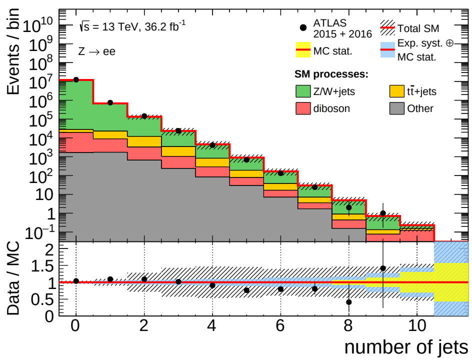

(a)

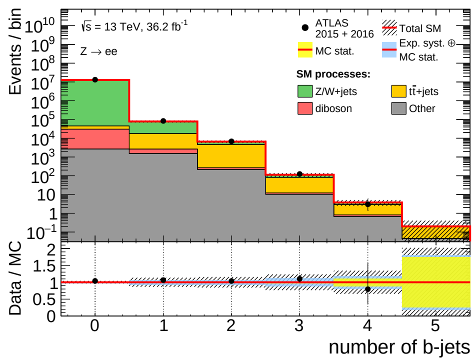

(b)

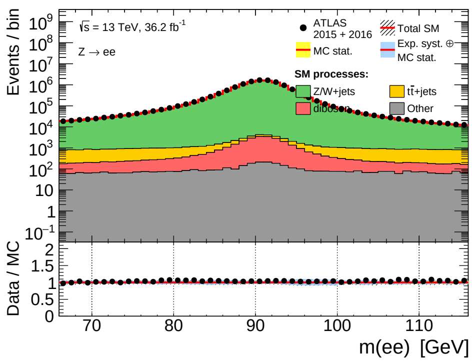

(c)

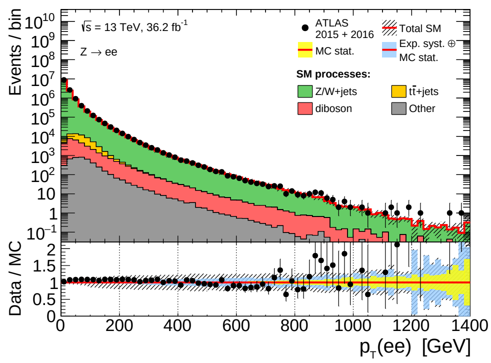

(d)

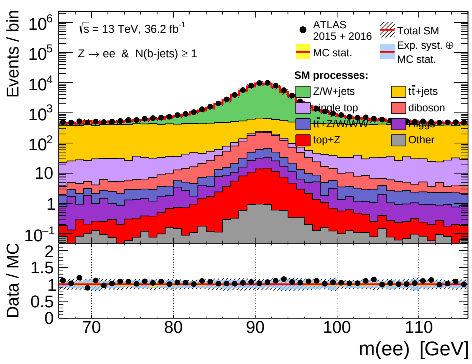

(e)

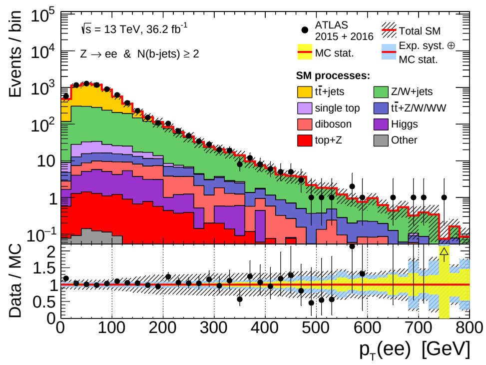

(f)

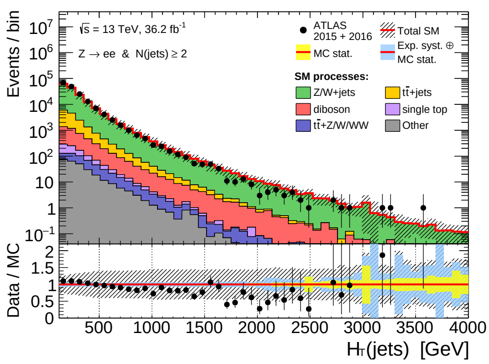

(g)

Figure H.5: Validation distributions for the $Z(\to ee)$ selection (see Table 5.4).

H.3.2 Muon channel

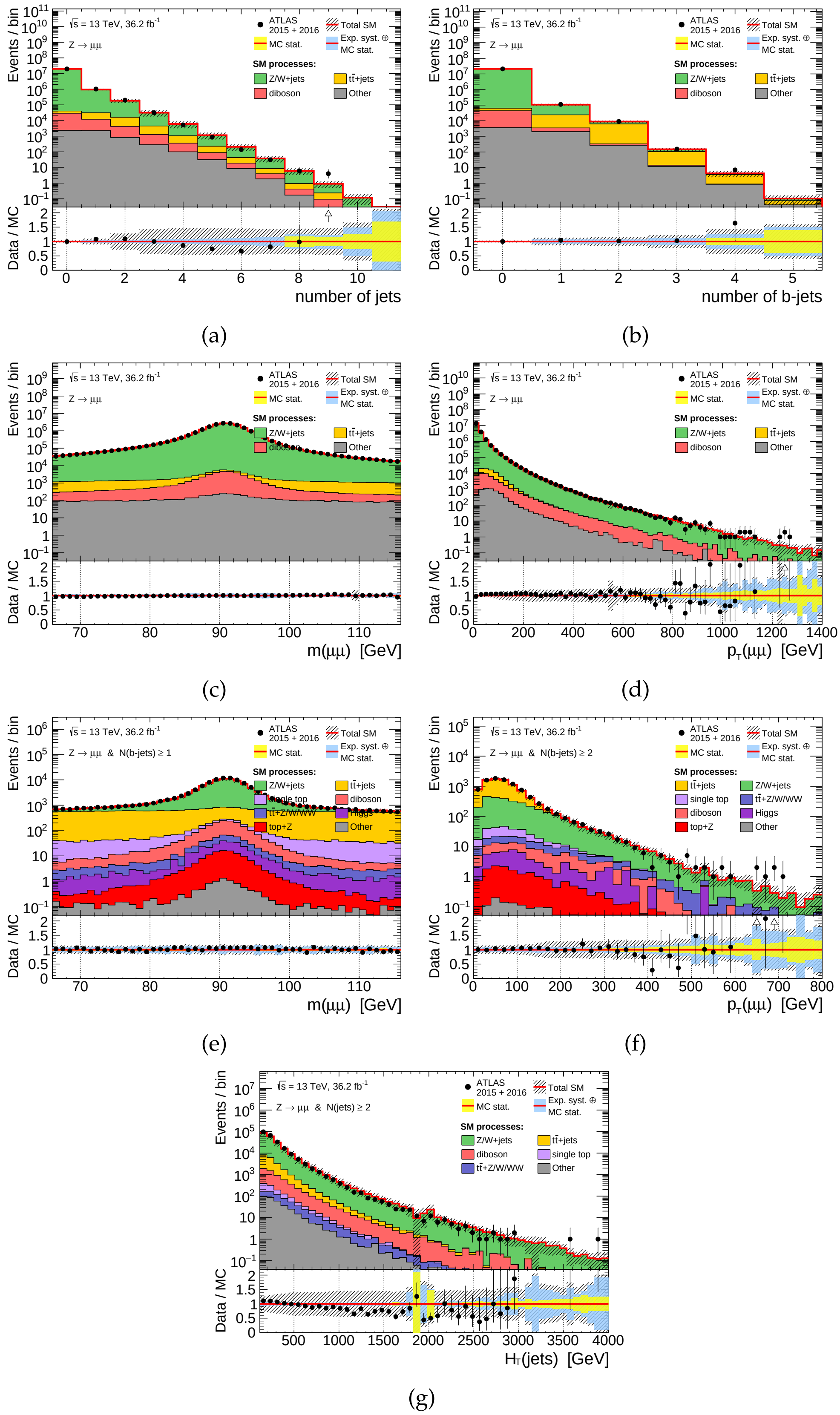

Figure H.6: Validation distributions for the $Z(\to \mu\mu)$ selection (see Table 5.4).

H.4 $Z + \gamma(\gamma)$

H.4.1 Electron channel

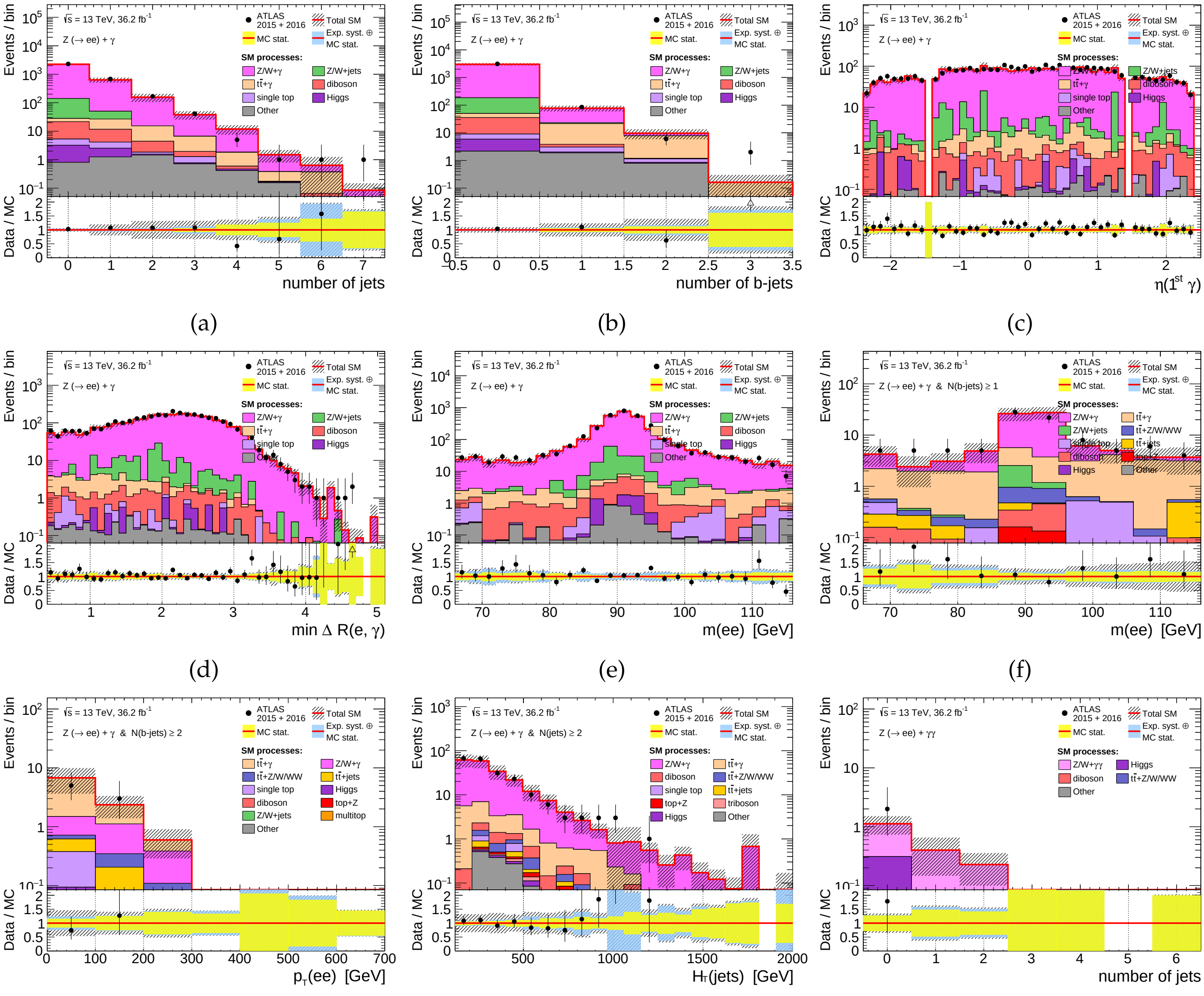

(a) (b) (c)

(d) (e) (f)

(g) (h) (i)

Figure H.7: Validation distributions for the $Z(\rightarrow ee) + \gamma(\gamma)$ selection (see Table 5.4).

H.4.2 Muon channel

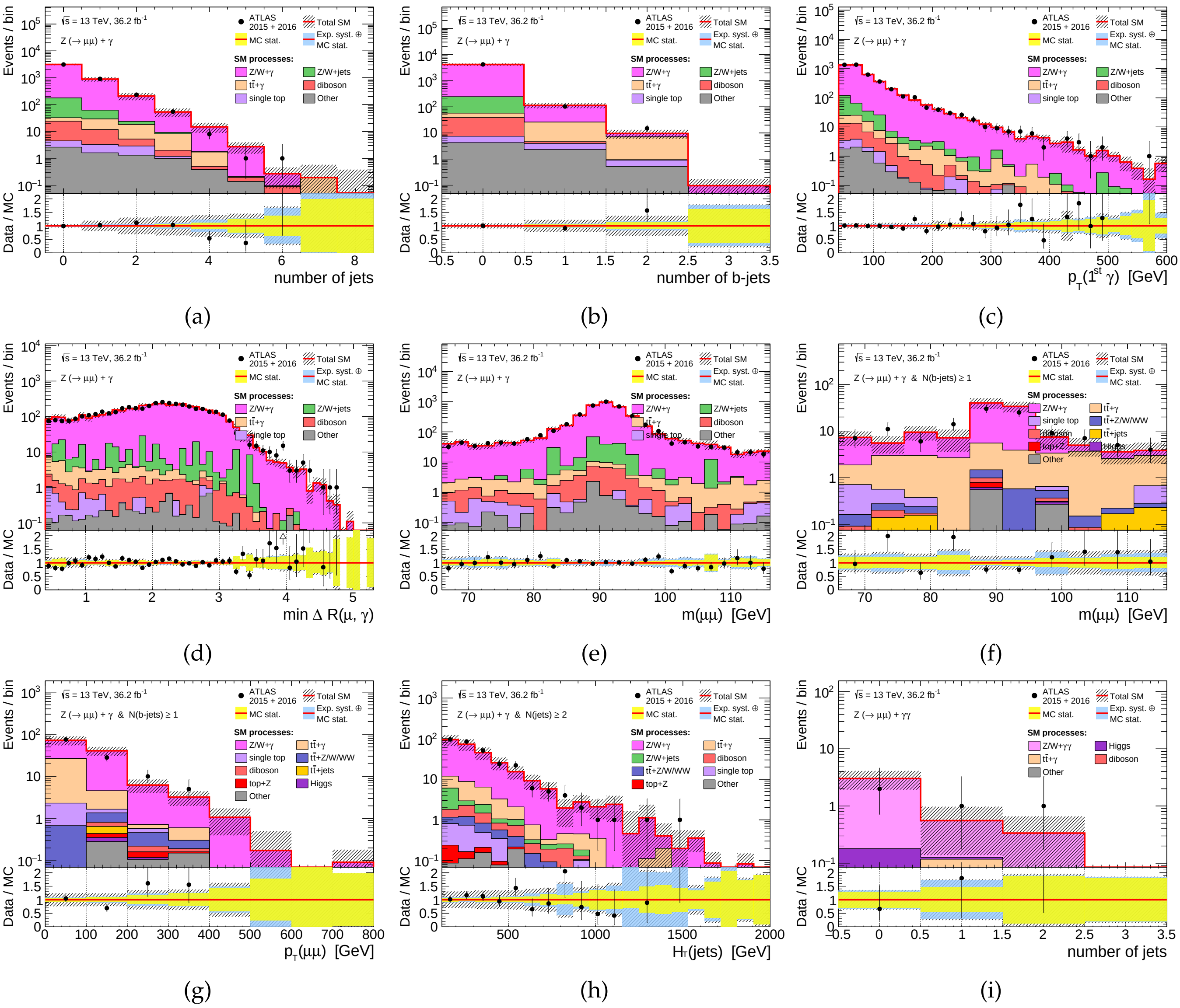

Figure H.8: Validation distributions for the $Z(\rightarrow \mu\mu) + \gamma(\gamma)$ selection (see Table 5.4).

H.5 $\gamma +$ jets

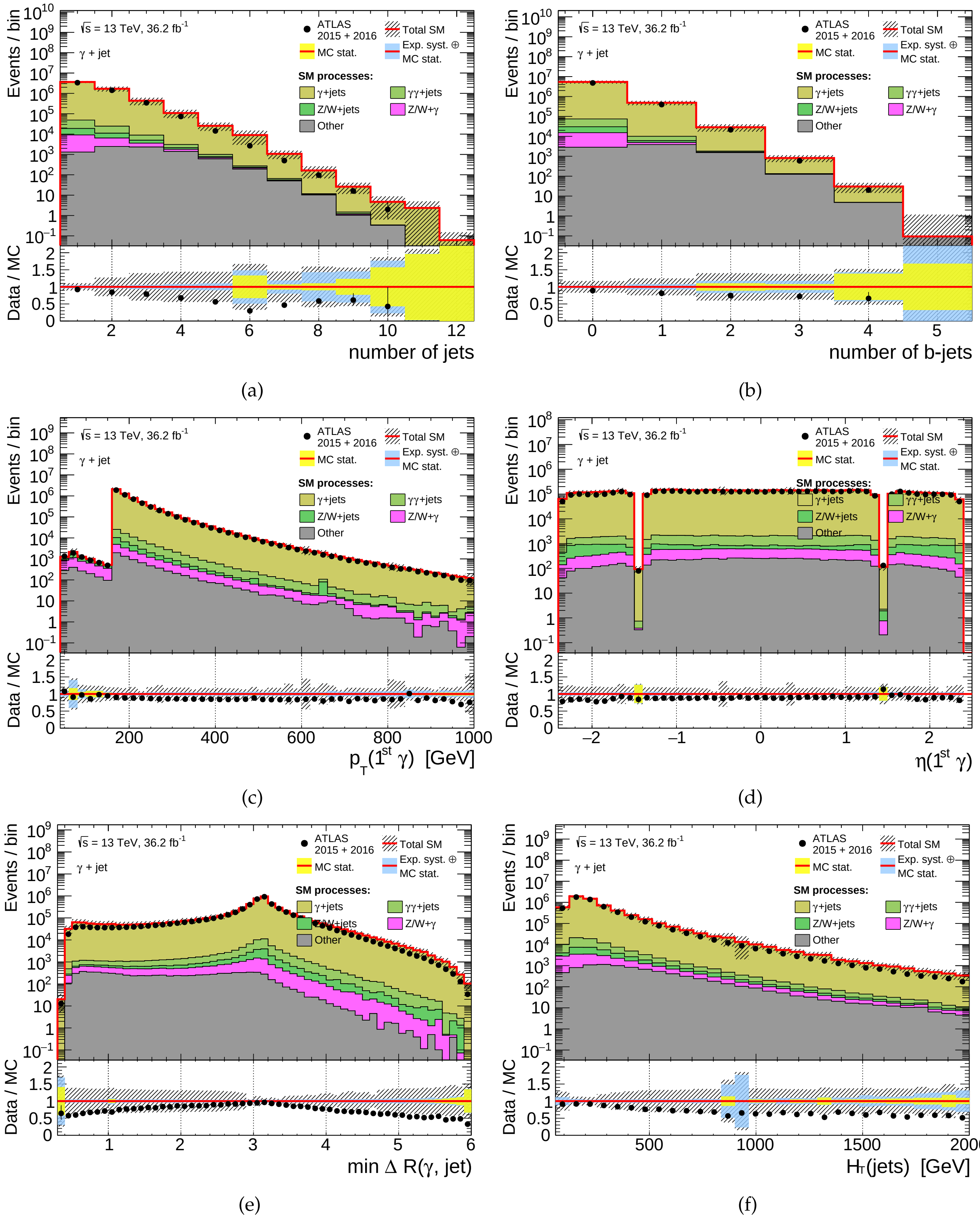

Figure H.9: Validation distributions for the $\gamma +$ jets selection (see Table 5.4).

H.6 Diphoton

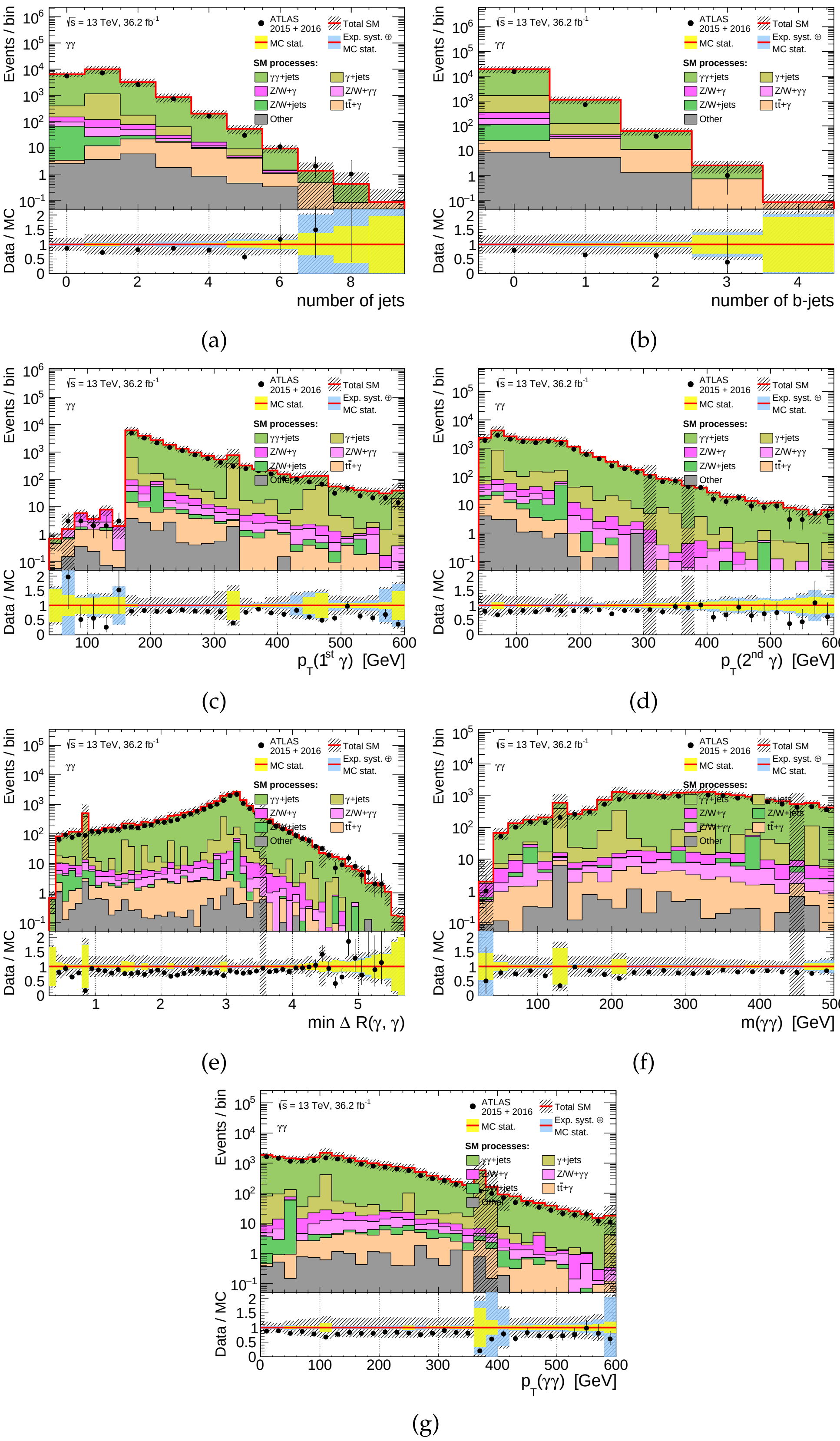

Figure H.10: Validation distributions for the diphoton selection (see Table 5.4).

H.7 $t\bar{t}$ semi-leptonic decay

H.7.1 Electron channel

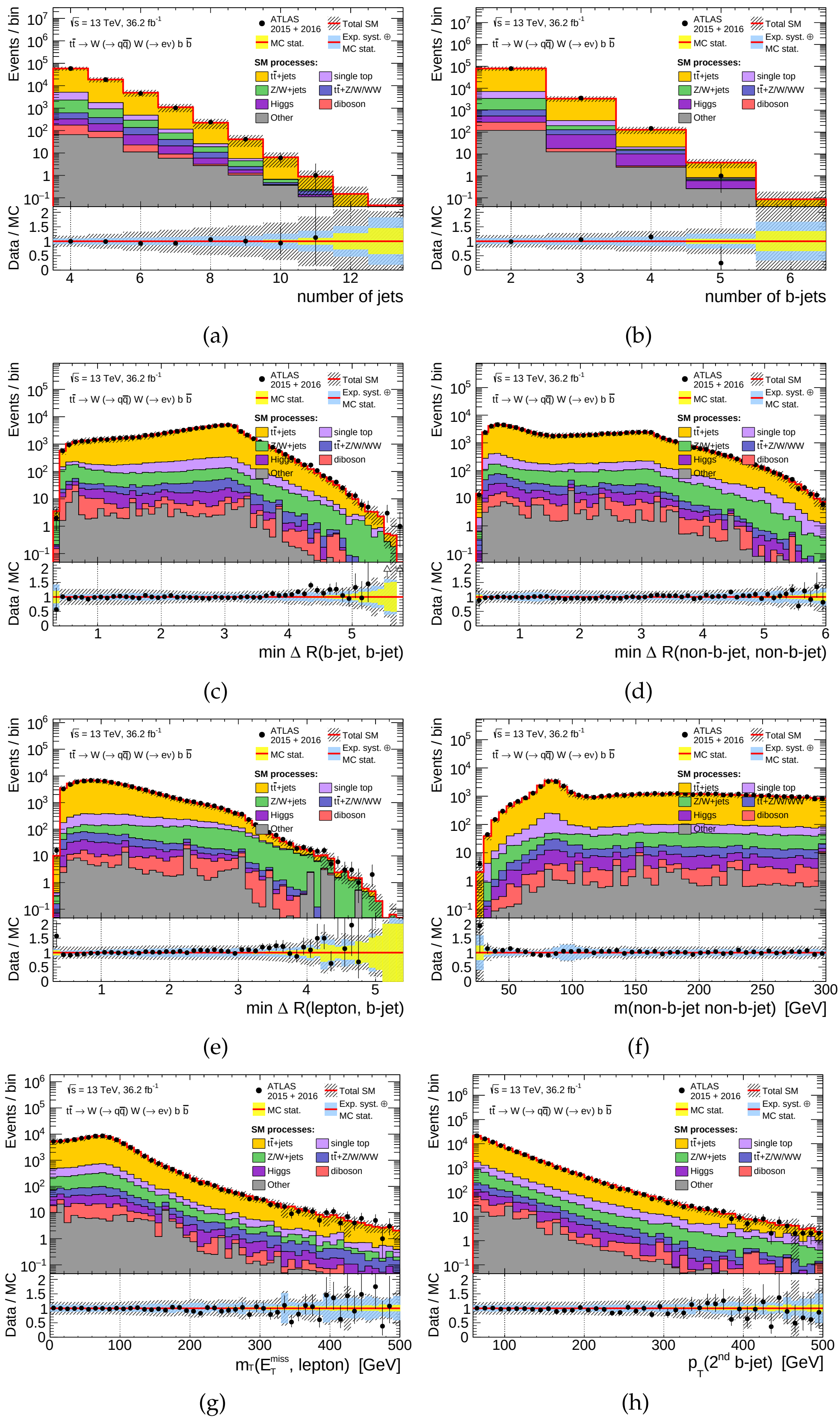

Figure H.11: Validation distributions for the semi-leptonic e-channel $t\bar{t}$ selection (see Table 5.4).

H.7.2 Muon channel

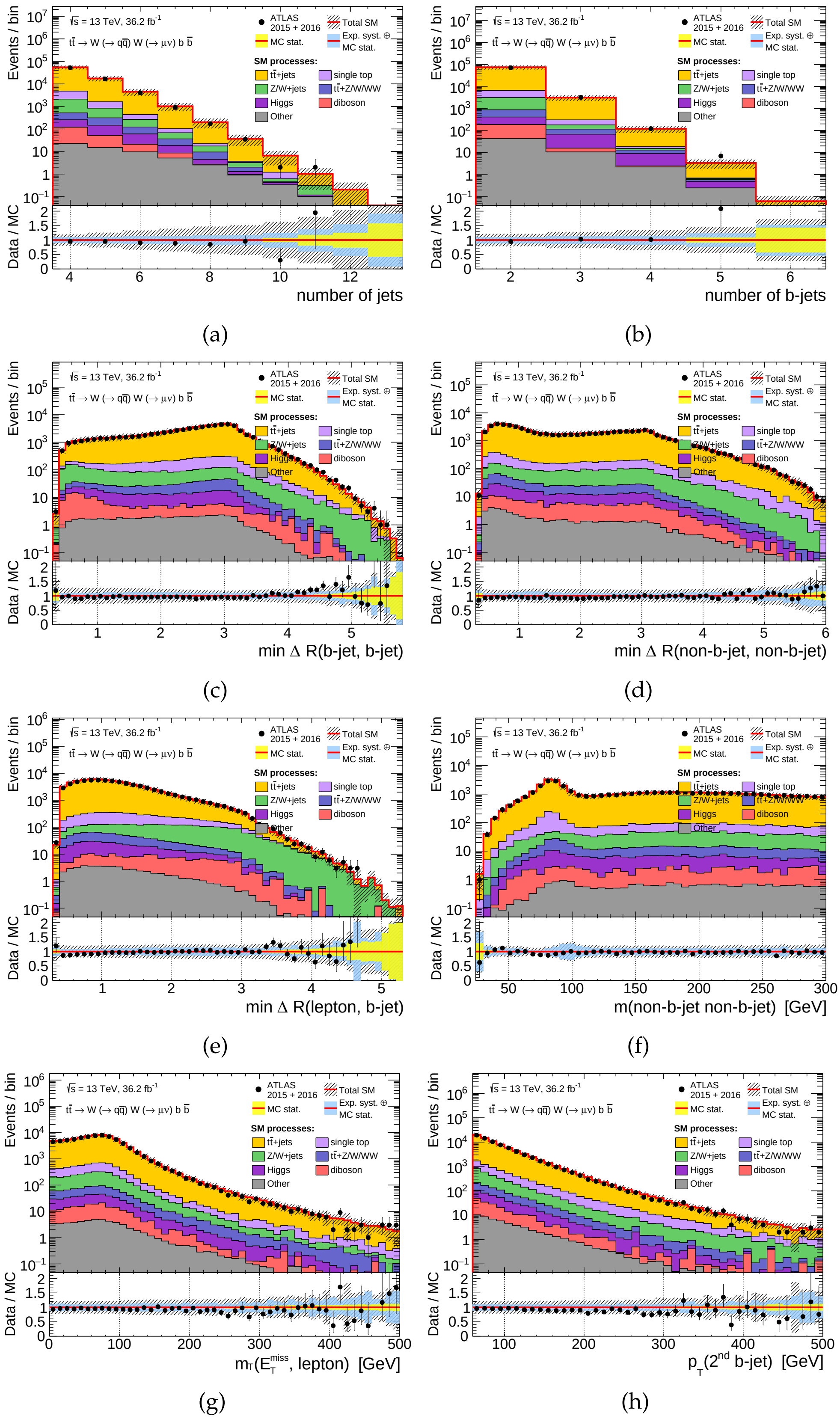

Figure H.12: Validation distributions for the semi-leptonic μ-channel $t\bar{t}$ selection (see Table 5.4).

H.8 $t\bar{t}$ leptonic decay

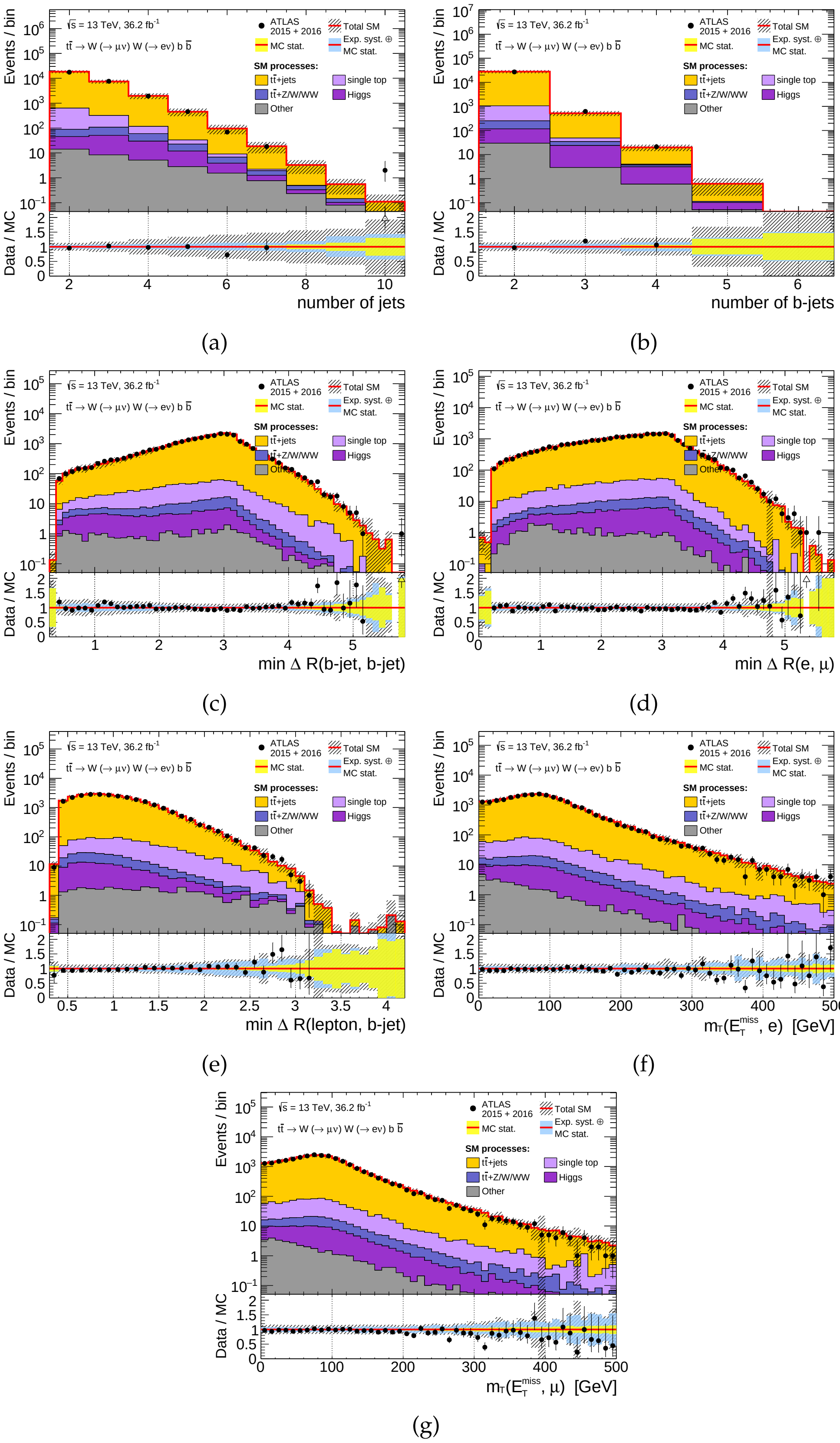

Figure H.13: Validation distributions for the leptonic $t\bar{t}$ selection (see Table 5.4).

H.9 Diboson

H.9.1 $W(\to e\nu)W(\to \mu\nu)$

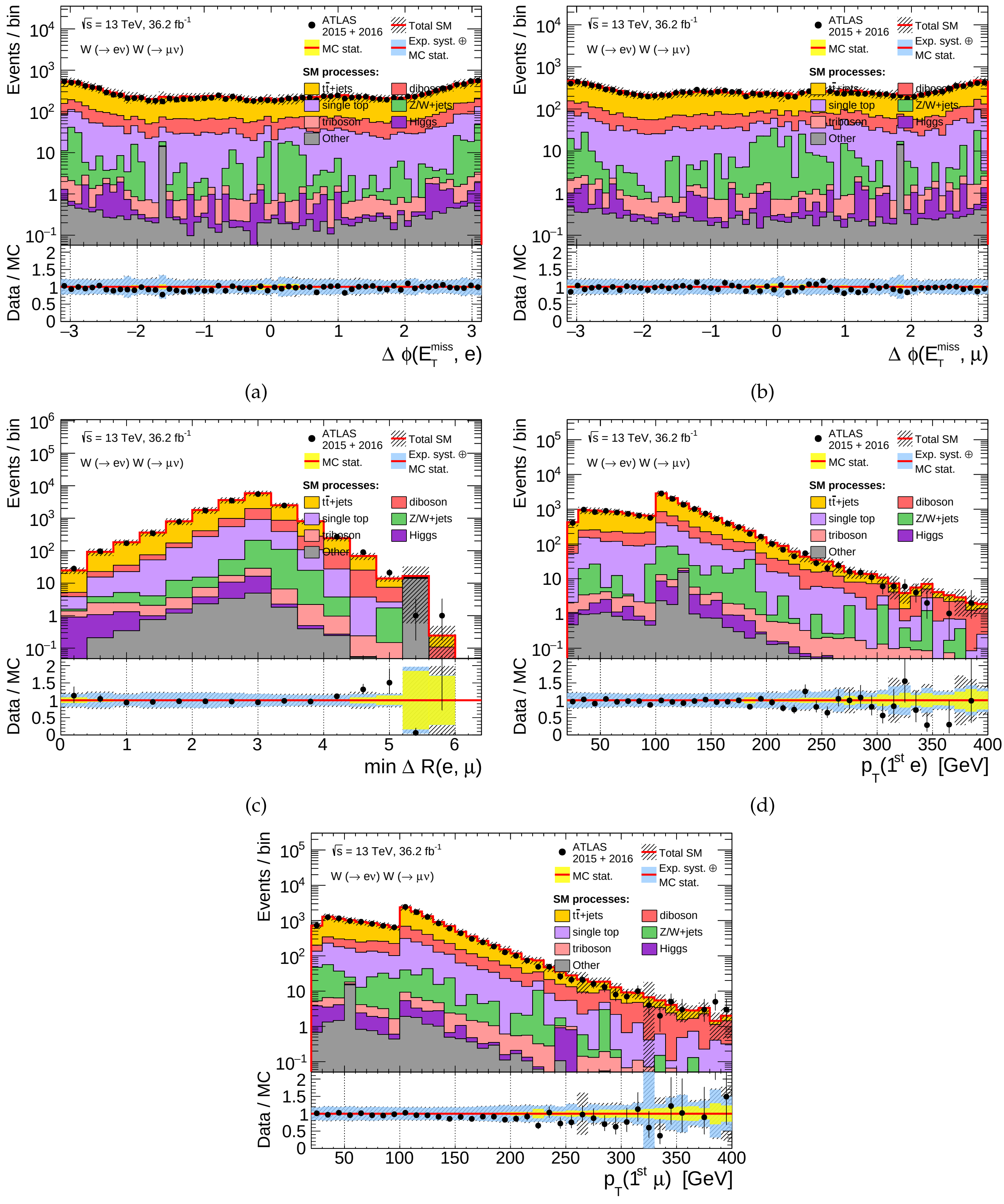

(a) (b) (c) (d) (e)

Figure H.14: Validation distributions for the diboson WW selection (see Table 5.4).

H.9.2 $W(\to e\nu)Z(\to \mu\mu)$

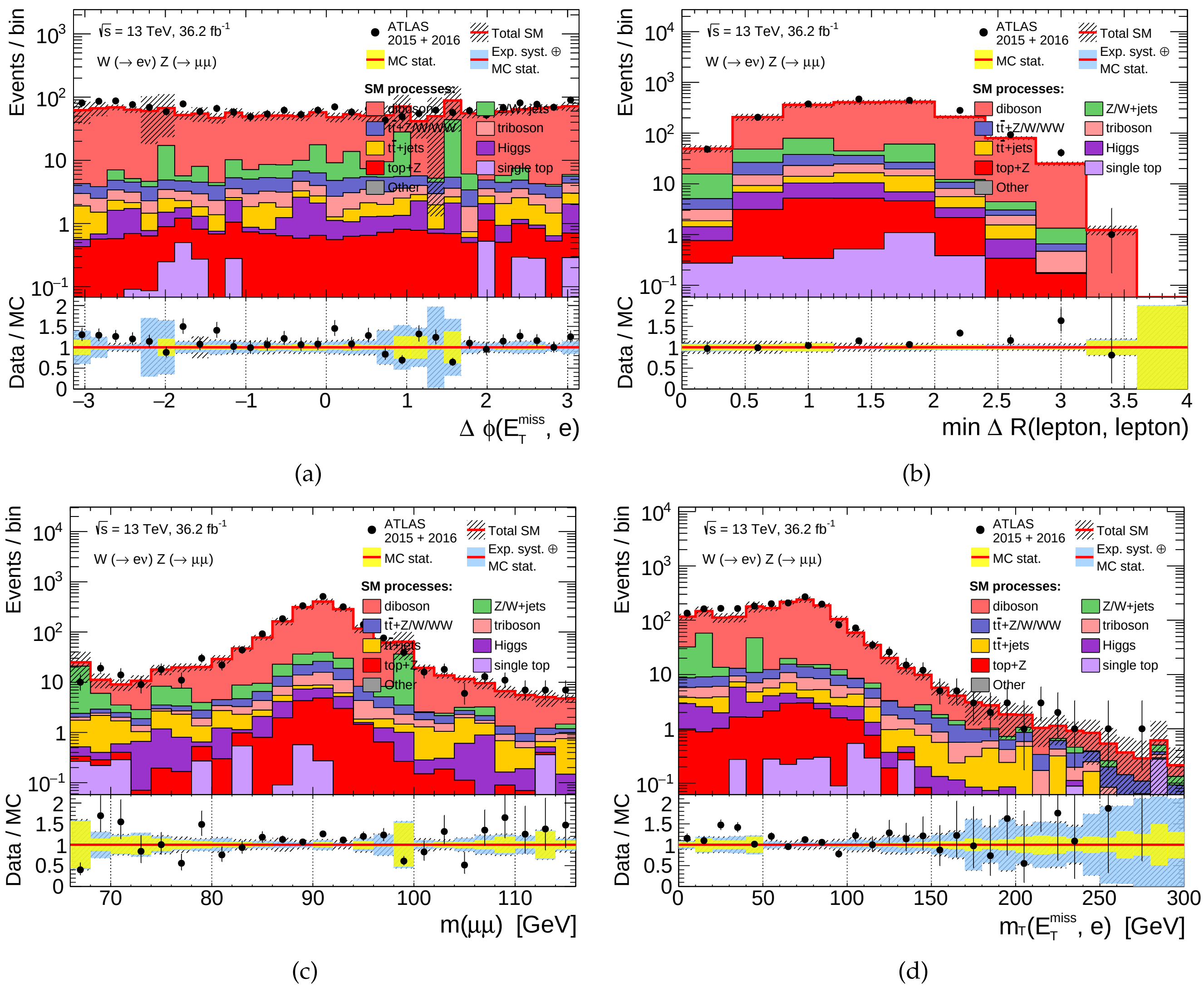

Figure H.15: Validation distributions for the diboson $W(\to e\nu)Z(\to \mu\mu)$ selection (see Table 5.4).

H.9.3 $W(\to \mu\nu)Z(\to ee)$

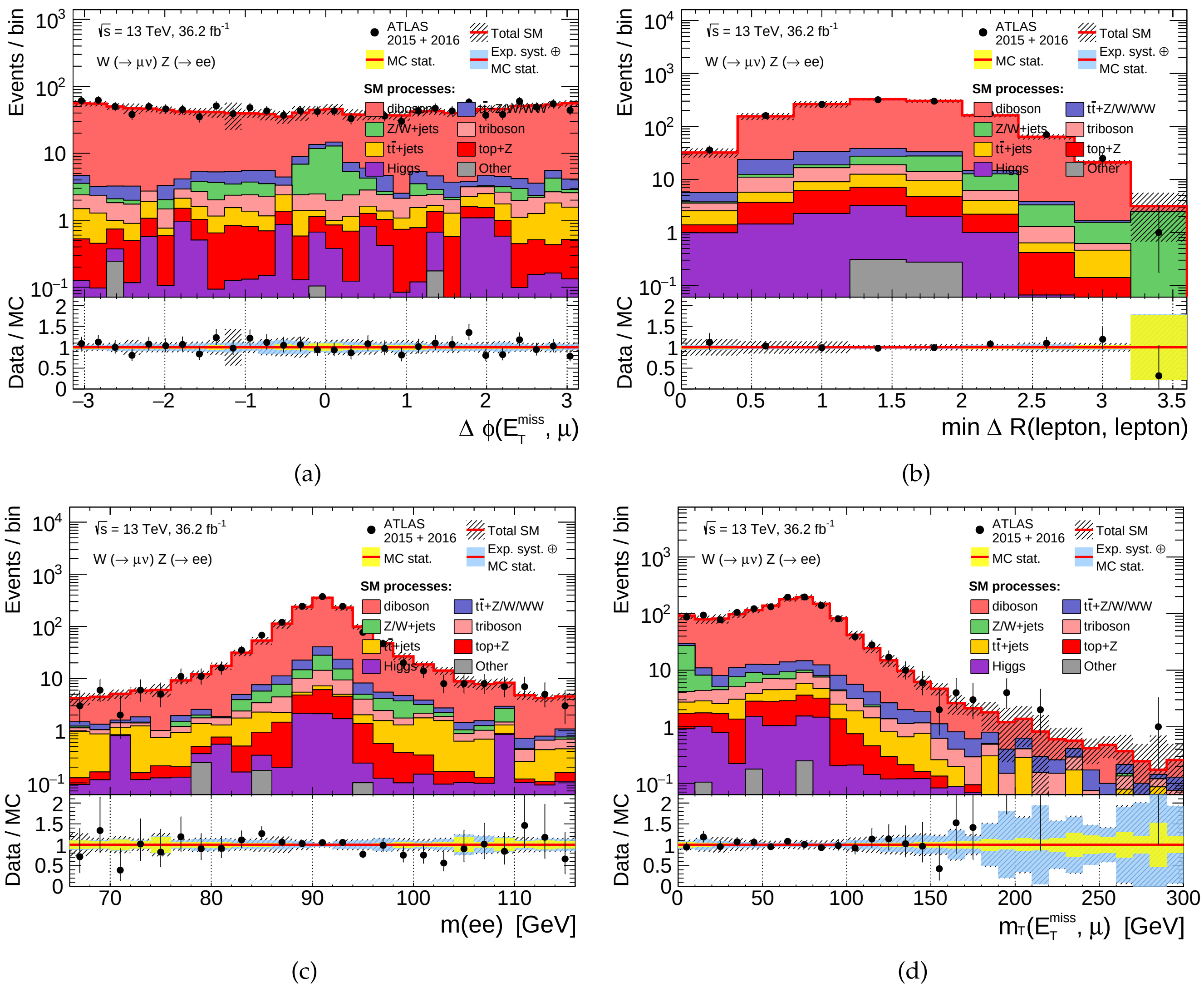

Figure H.16: Validation distributions for the diboson $W(\to \mu\nu)Z(\to ee)$ selection (see Table 5.4).

H.9.4 $Z(\to \ell\ell)Z(\to \ell\ell)$

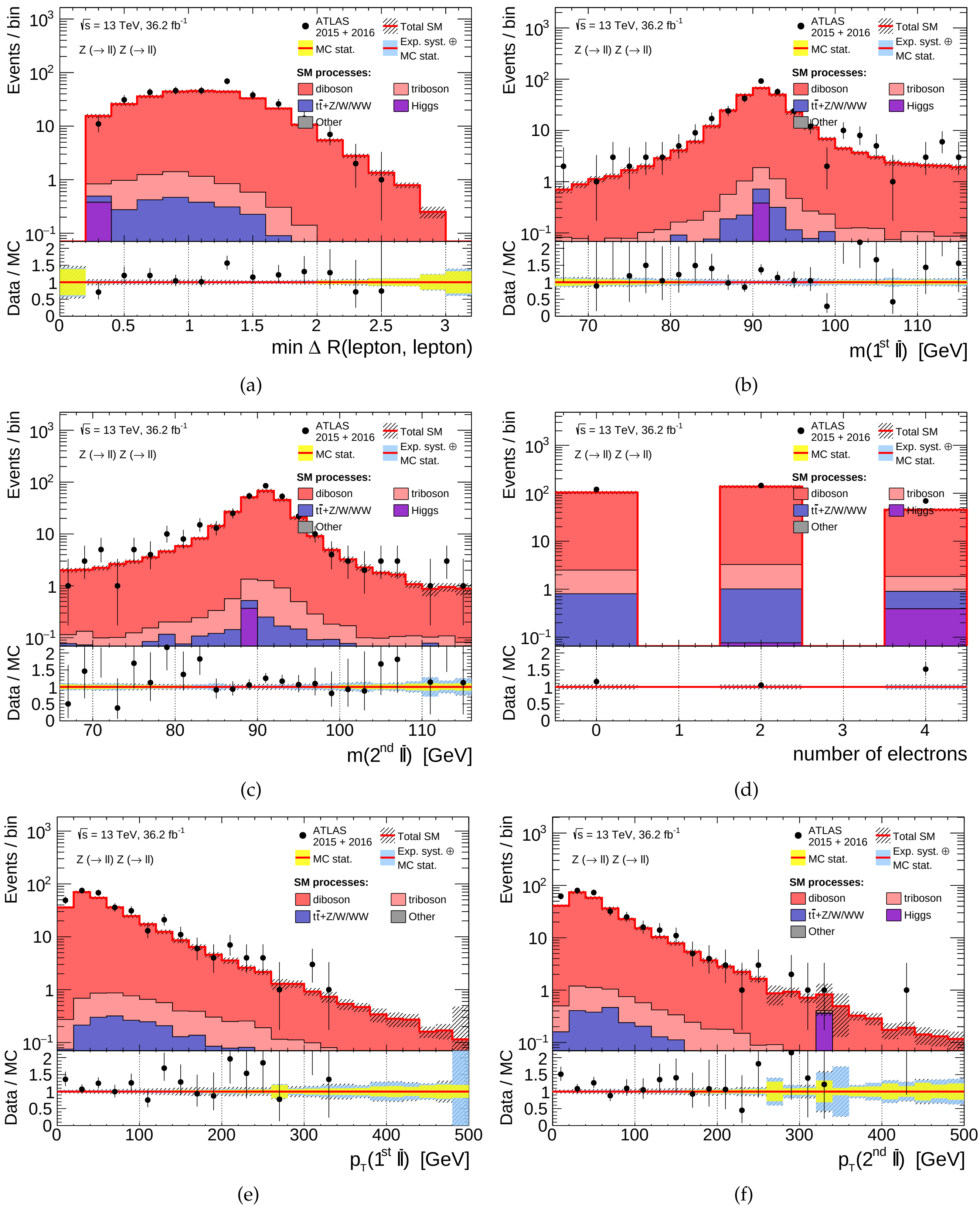

Figure H.17: Validation distributions for the diboson $Z(\to \ell\ell)Z(\to \ell\ell)$ selection (see Table 5.4).

H.10 Jets and $E_{\mathrm{T}}^{\mathrm{miss}}$

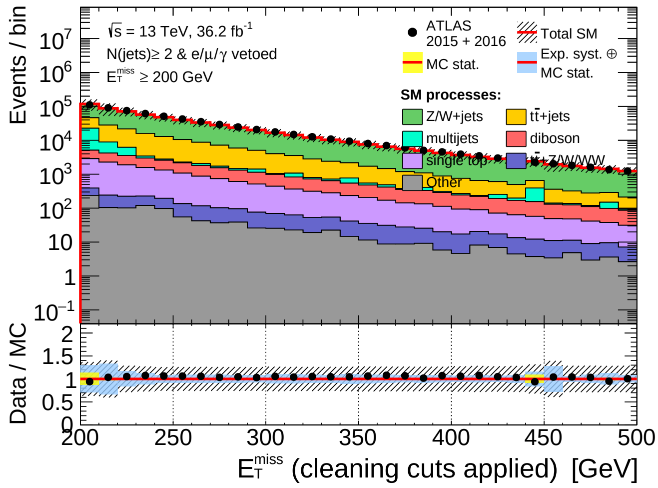

(a)

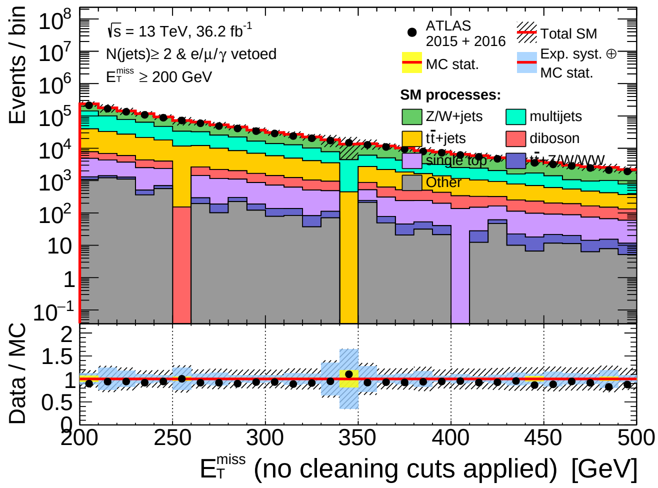

(b)

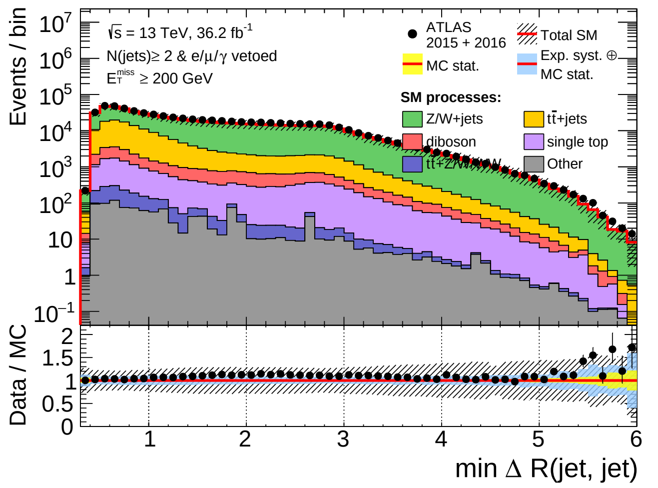

(c)

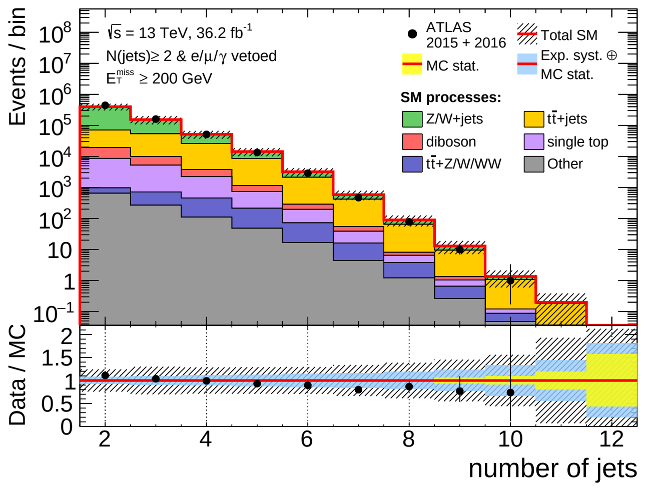

(d)

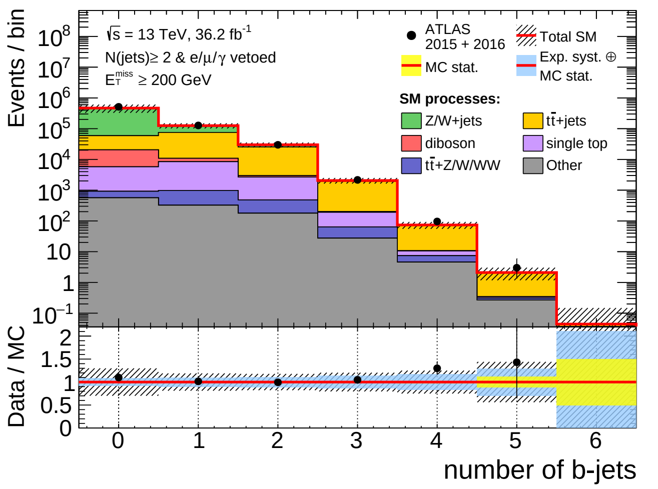

(e)

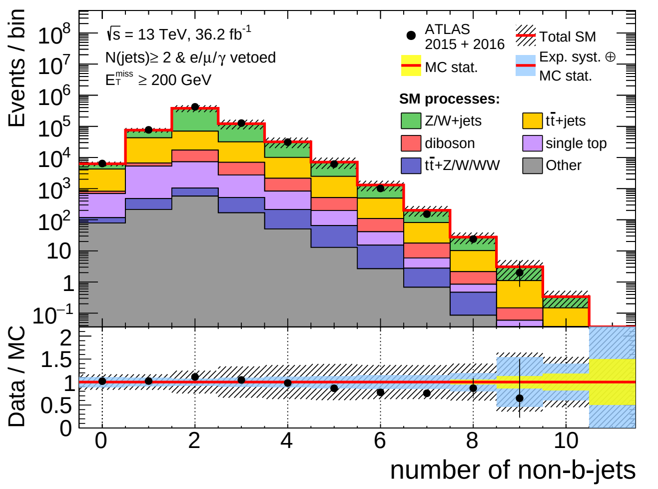

(f)

Figure H.18: Validation distributions for the jets + $E_{\mathrm{T}}^{\mathrm{miss}}$ selection.

I All event classes and yields in the 2015+2016 dataset

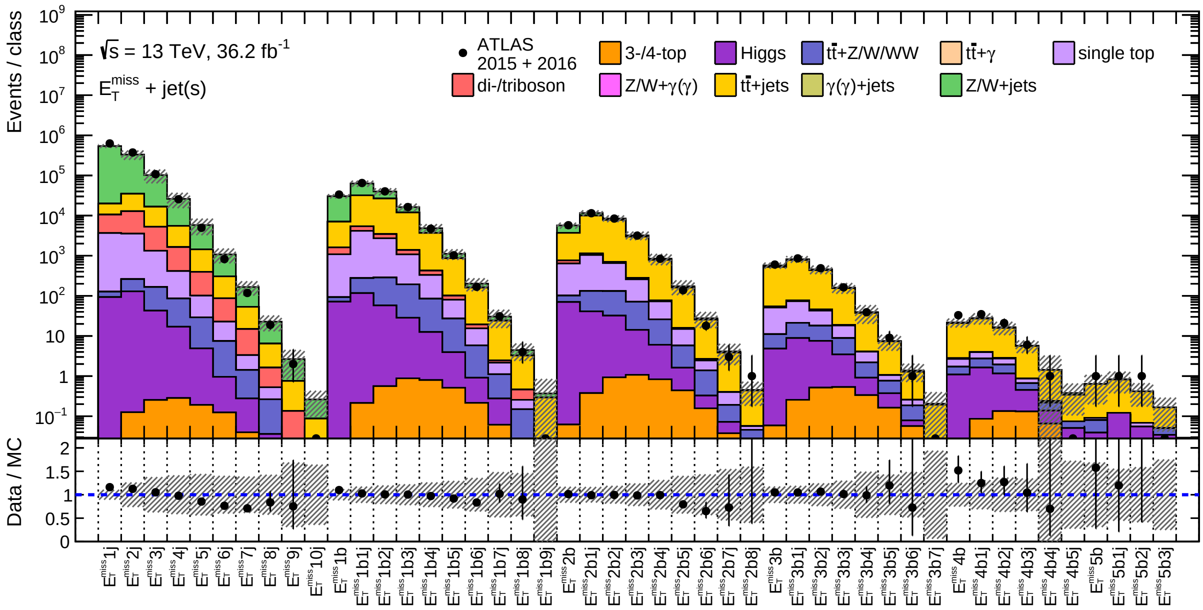

Figure I.1: Expected and observed number of events in all classes with large $E_{\mathrm{T}}^{\mathrm{miss}}$ and (b-)jets (no leptons or photons). The class labels list the type and multiplicity of reconstructed objects in the events. The total uncertainty on the SM prediction is indicated by hatched bands.

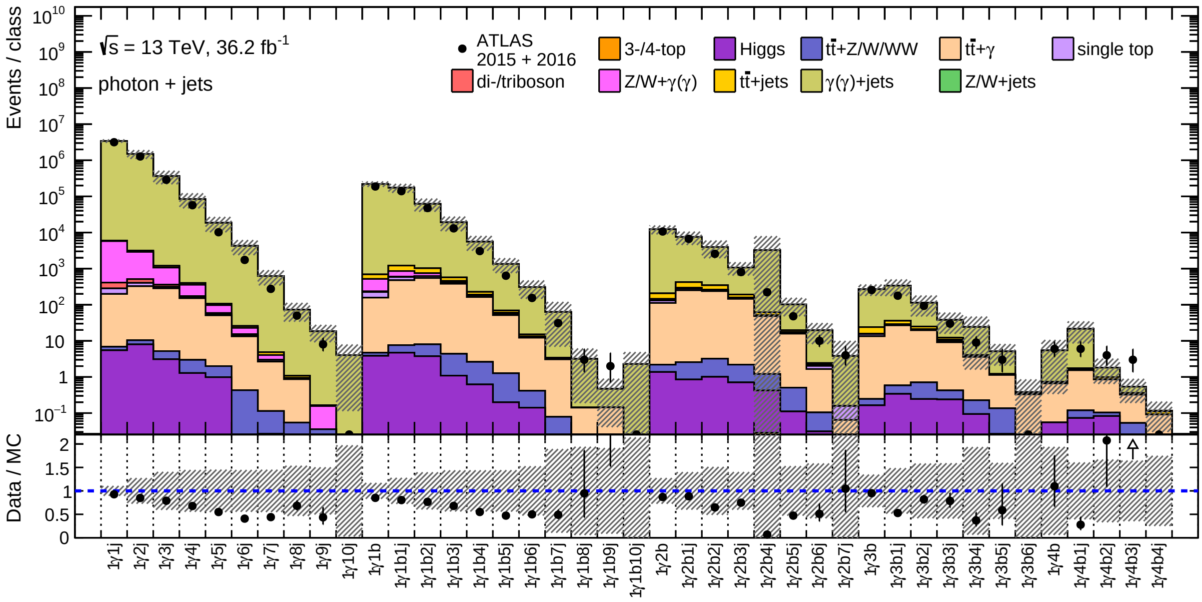

Figure I.2: Expected and observed number of events in all classes with one photon and (*b*-)jets (no leptons or $E_{\mathrm{T}}^{\mathrm{miss}}$). The class labels list the type and multiplicity of reconstructed objects in the events. The total uncertainty on the SM prediction is indicated by hatched bands.

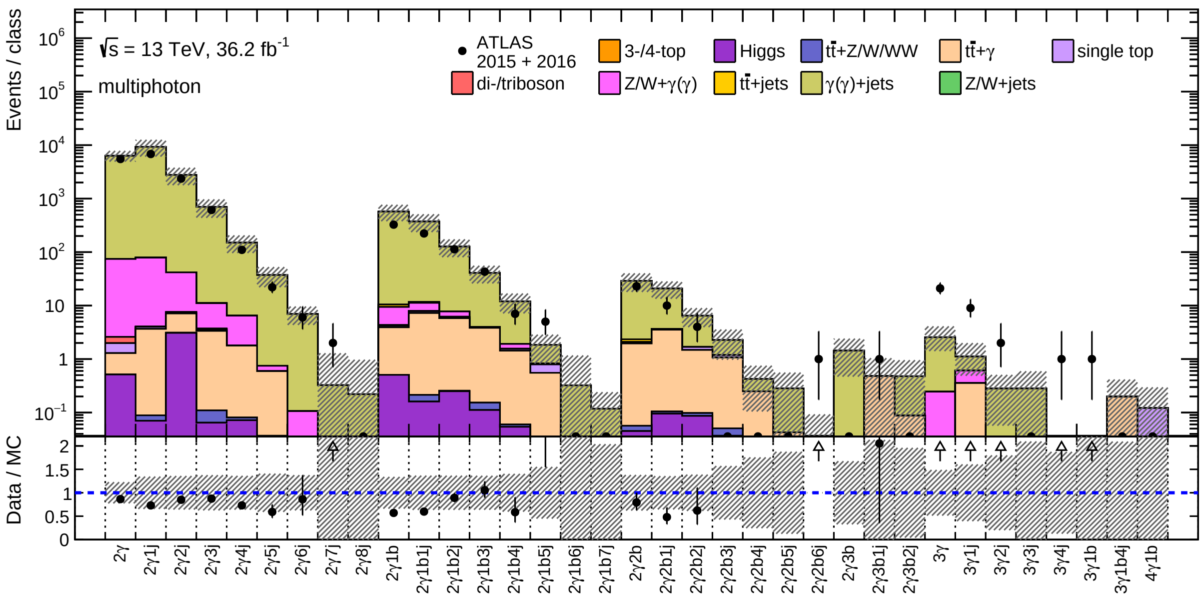

Figure I.3: Expected and observed number of events in all classes with at least two photons (no leptons or $E_{\mathrm{T}}^{\mathrm{miss}}$). The class labels list the type and multiplicity of reconstructed objects in the events. The total uncertainty on the SM prediction is indicated by hatched bands. Large excesses are observed in the three photon event classes which lack a MC estimation of the event yield from SM triple-photon-event production processes.

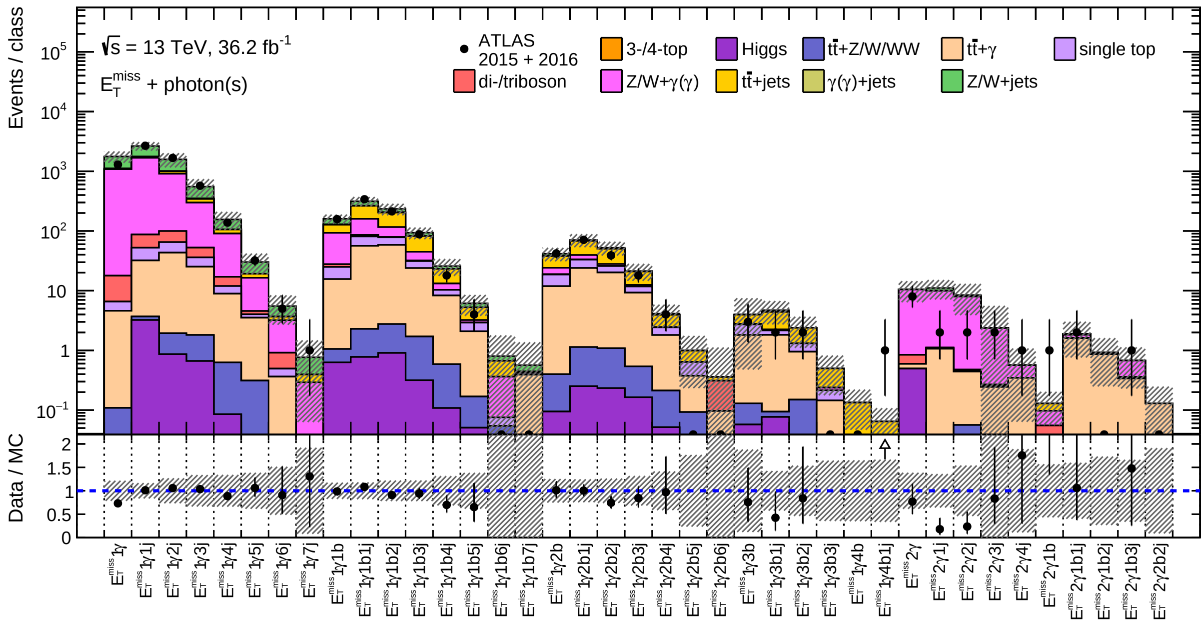

Figure I.4: Expected and observed number of events in all classes with large $E_{\mathrm{T}}^{\mathrm{miss}}$ and at least one photon (no leptons). The class labels list the type and multiplicity of reconstructed objects in the events. The total uncertainty on the SM prediction is indicated by hatched bands.

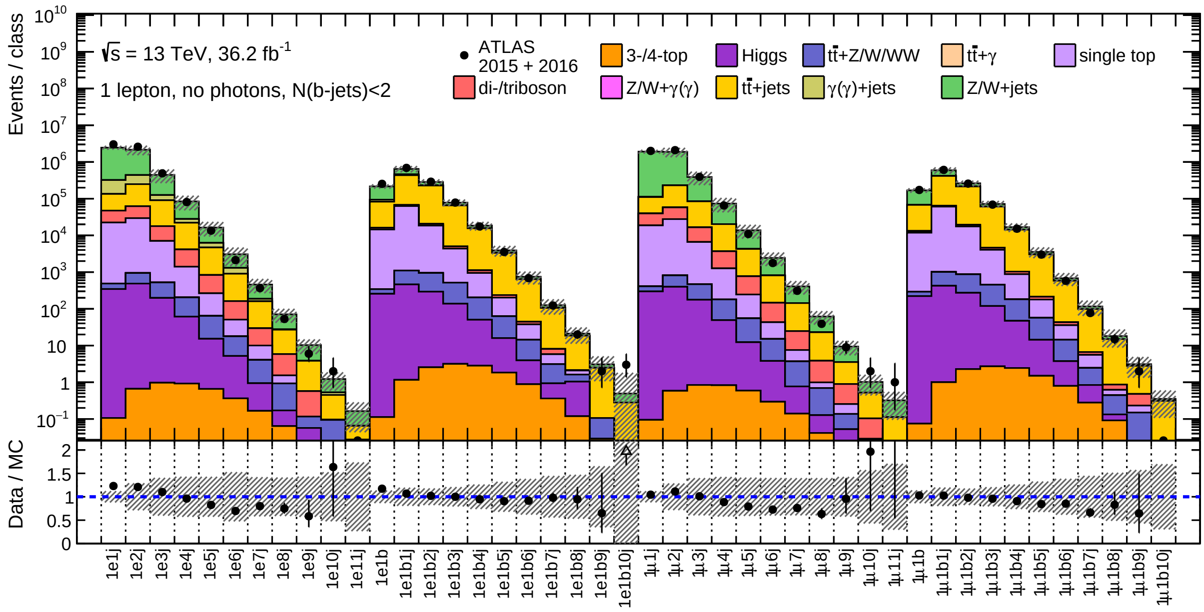

Figure I.5: Expected and observed number of events in all classes with one lepton (electron or muon) and at most one b-jet (no $E_{\mathrm{T}}^{\mathrm{miss}}$ or photons). The class labels list the type and multiplicity of reconstructed objects in the events. The total uncertainty on the SM prediction is indicated by hatched bands.

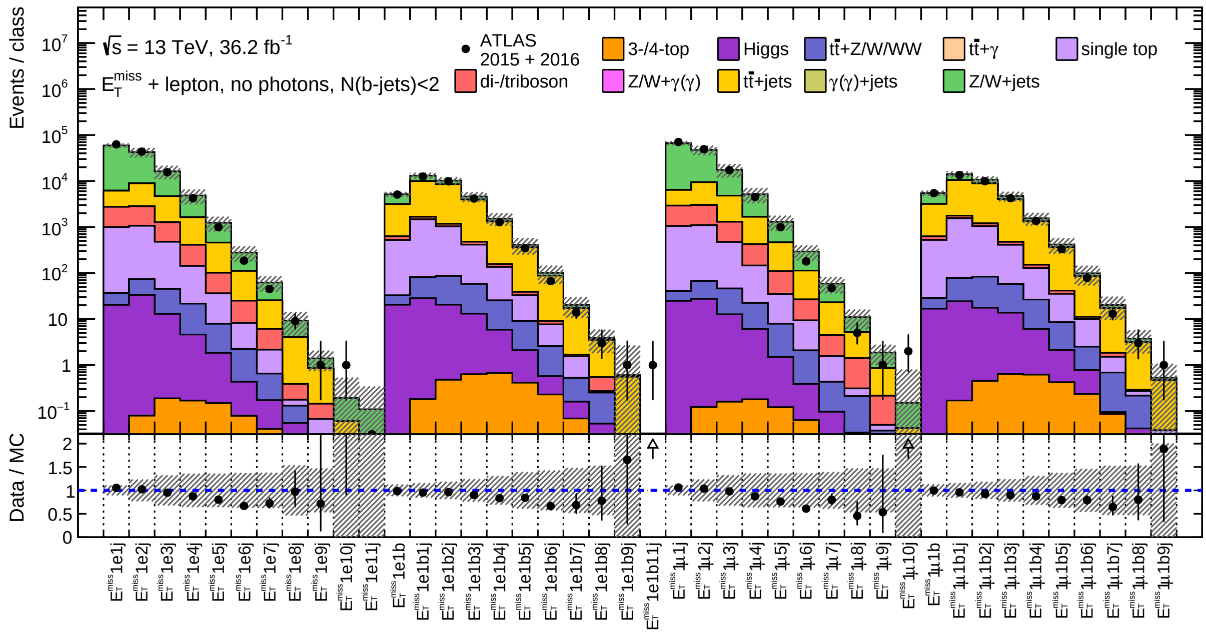

Figure I.6: Expected and observed number of events in all classes with large $E_{\mathrm{T}}^{\mathrm{miss}}$, one lepton (electron or muon) and at most one b-jet (no photons). The class labels list the type and multiplicity of reconstructed objects in the events. The total uncertainty on the SM prediction is indicated by hatched bands.

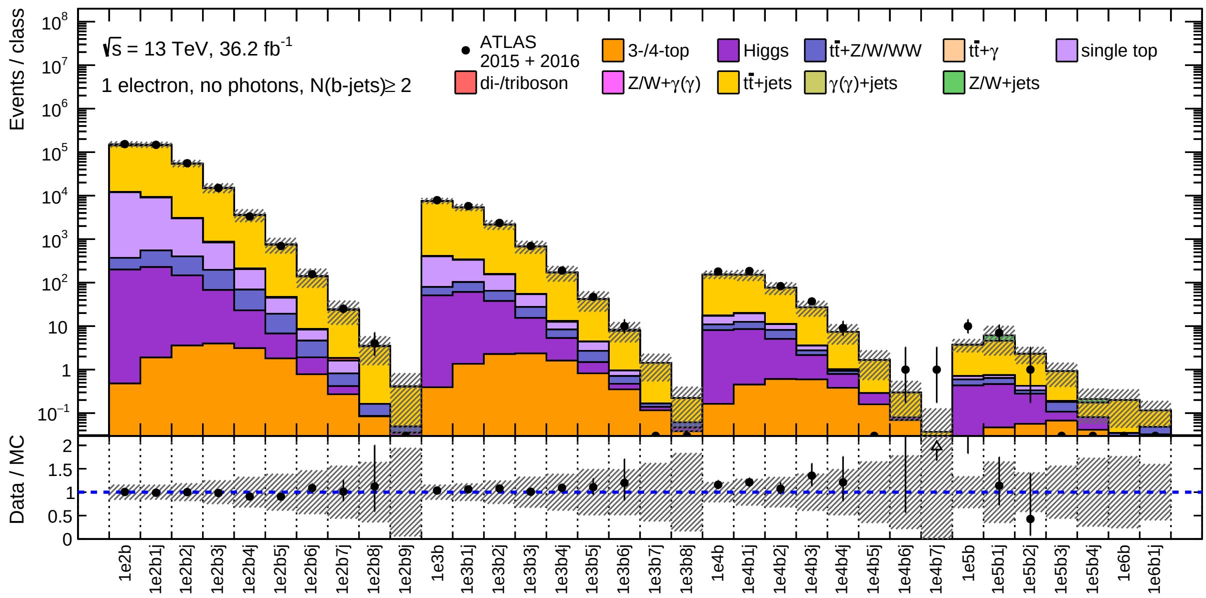

Figure I.7: Expected and observed number of events in all classes with one electron and at least two b-jets (no $E_{\mathrm{T}}^{\mathrm{miss}}$ or photons). The class labels list the type and multiplicity of reconstructed objects in the events. The total uncertainty on the SM prediction is indicated by hatched bands.

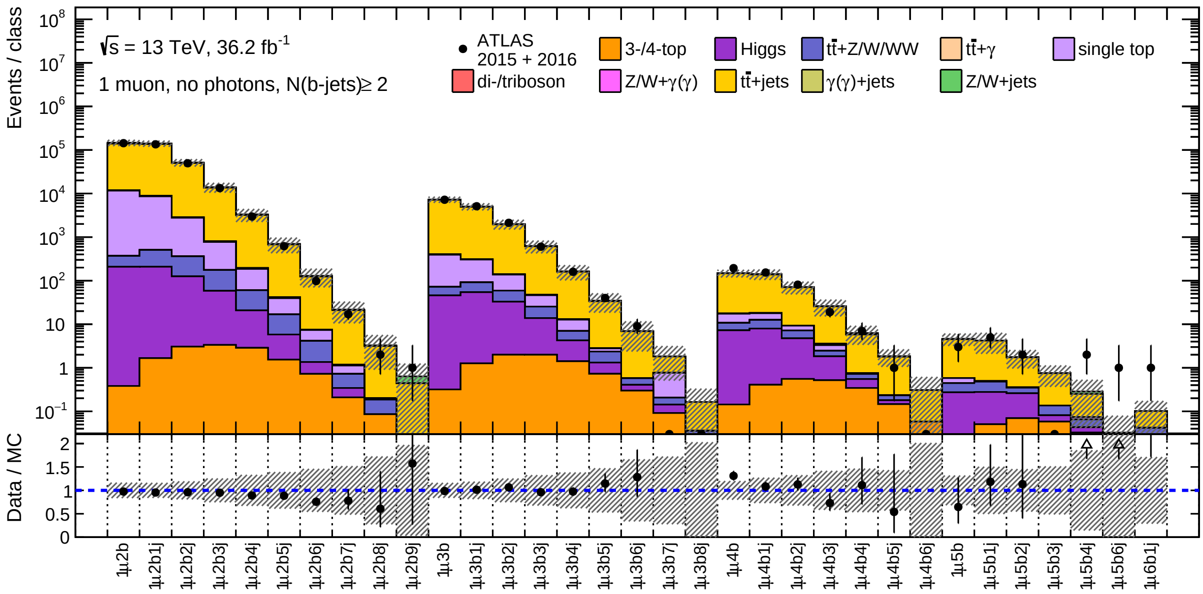

Figure I.8: Expected and observed number of events in all classes with one muon and at least two b-jets (no $E_{\mathrm{T}}^{\mathrm{miss}}$ or photons). The class labels list the type and multiplicity of reconstructed objects in the events. The total uncertainty on the SM prediction is indicated by hatched bands.

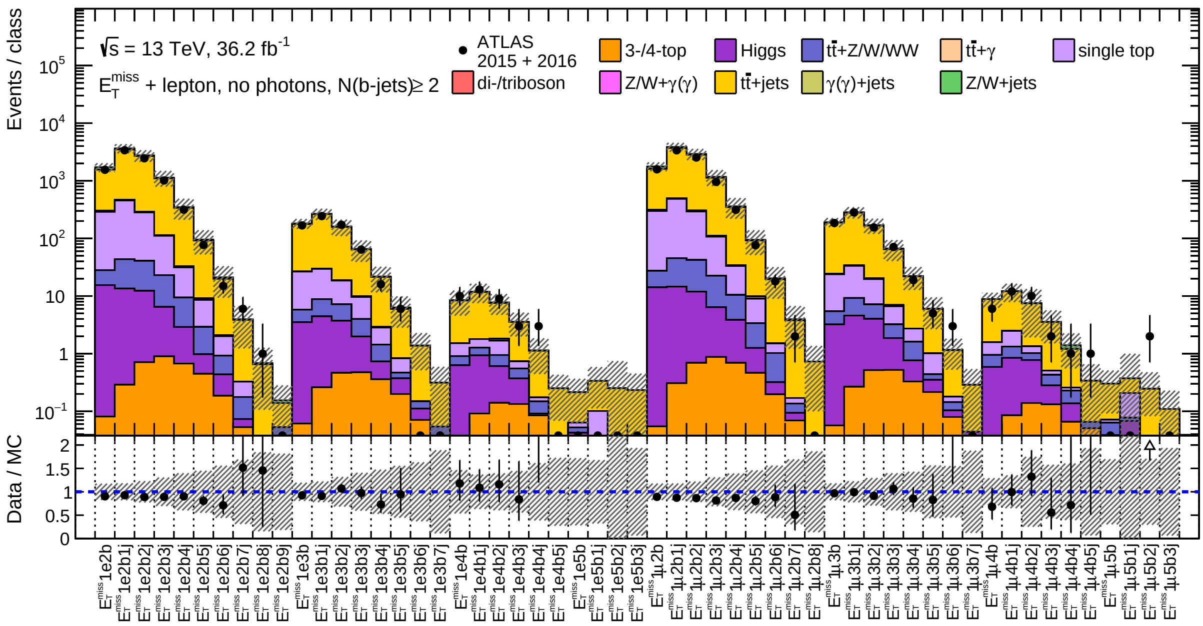

Figure I.9: Expected and observed number of events in all classes with large $E_{\mathrm{T}}^{\mathrm{miss}}$, one lepton (electron or muon) and at least two b-jets (no photons). The class labels list the type and multiplicity of reconstructed objects in the events. The total uncertainty on the SM prediction is indicated by hatched bands.

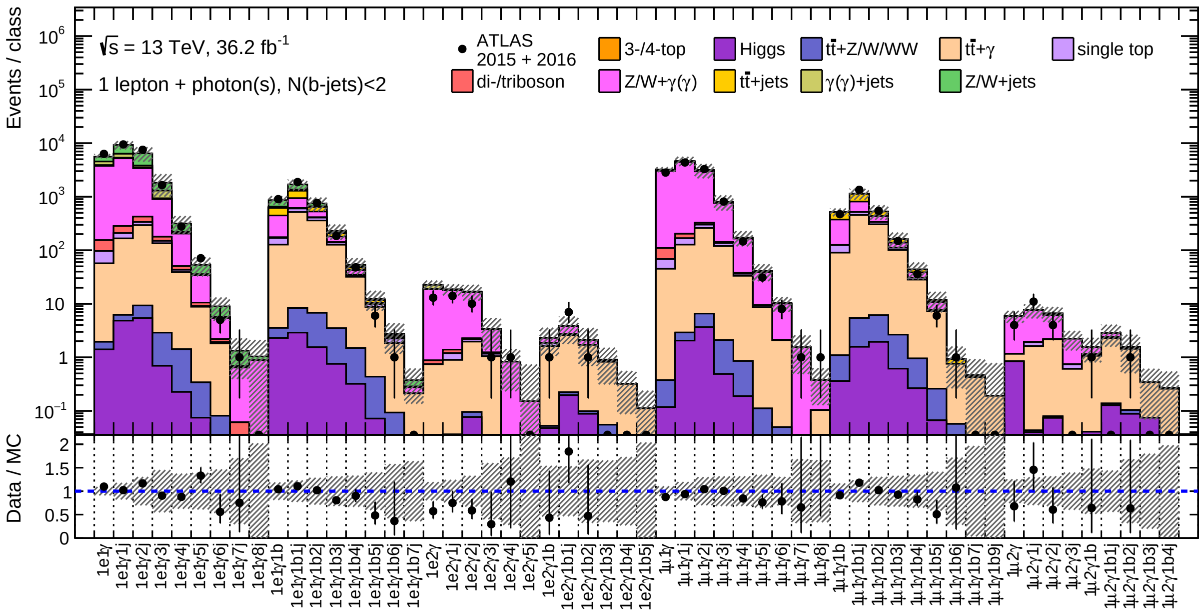

Figure I.10: Expected and observed number of events in all classes with one lepton (electron or muon), at least one photon and at most one b-jet (no E_T^{miss}). The class labels list the type and multiplicity of reconstructed objects in the events. The total uncertainty on the SM prediction is indicated by hatched bands.

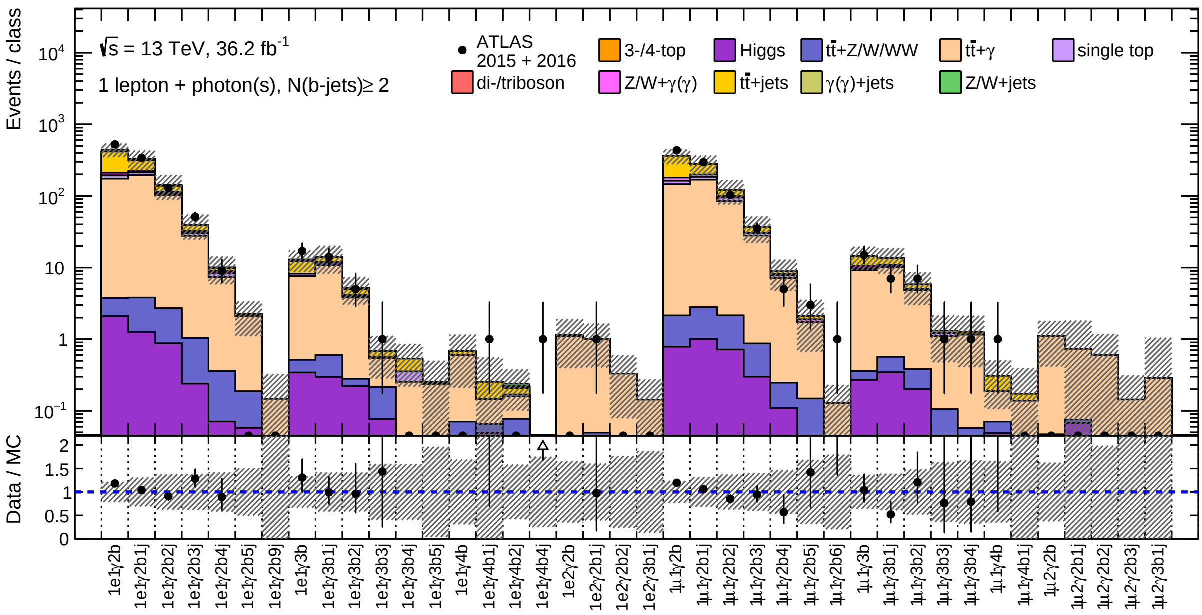

Figure I.11: Expected and observed number of events in all classes with one lepton (electron or muon), at least one photon and at least two b-jet (no E_T^{miss}). The class labels list the type and multiplicity of reconstructed objects in the events. The total uncertainty on the SM prediction is indicated by hatched bands.

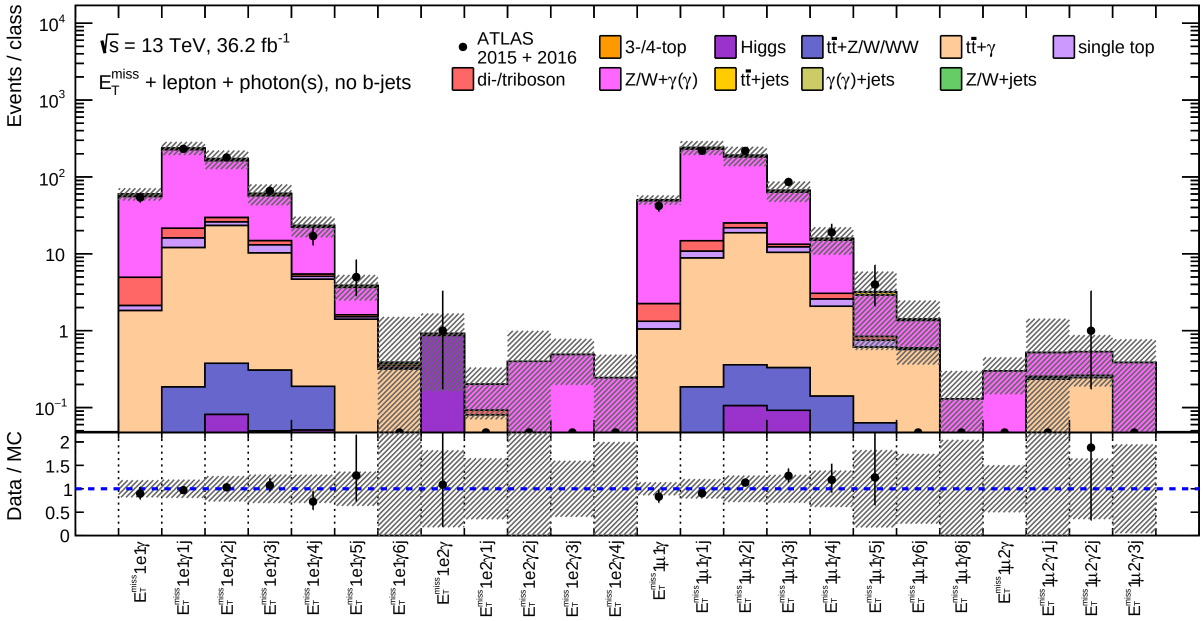

Figure I.12: Expected and observed number of events in all classes with large $E_{\mathrm{T}}^{\mathrm{miss}}$, one lepton (electron or muon), at least one photon and no b-jets. The class labels list the type and multiplicity of reconstructed objects in the events. The total uncertainty on the SM prediction is indicated by hatched bands.

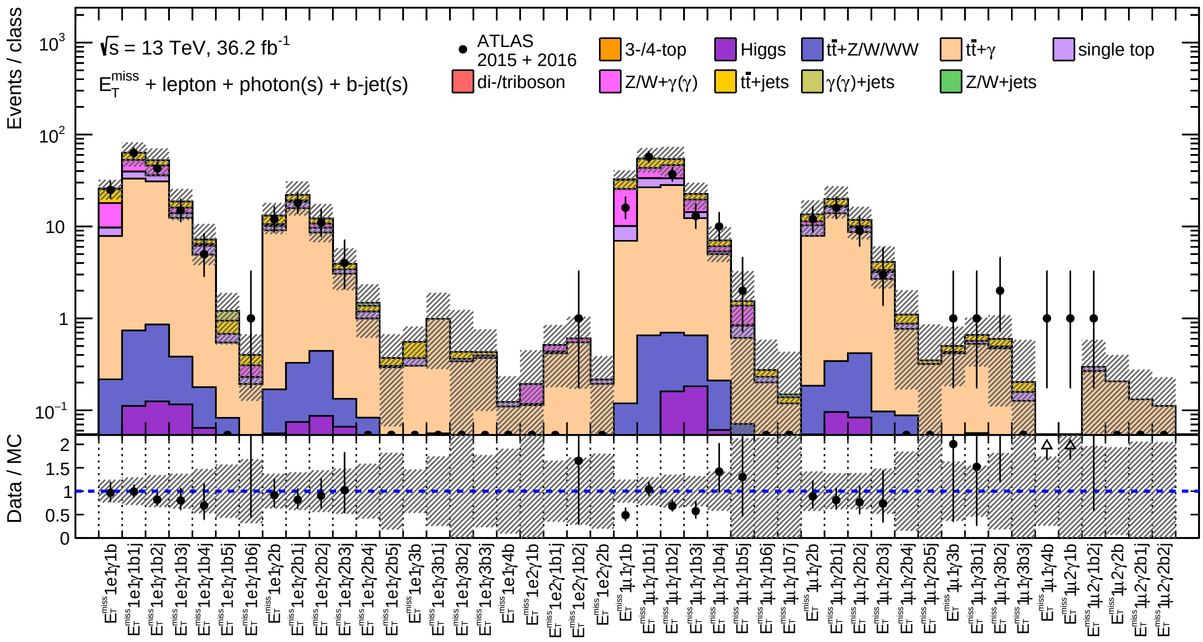

Figure I.13: Expected and observed number of events in all classes with large $E_{\mathrm{T}}^{\mathrm{miss}}$, one lepton (electron or muon), at least one photon and no b-jets. The class labels list the type and multiplicity of reconstructed objects in the events. The total uncertainty on the SM prediction is indicated by hatched bands.

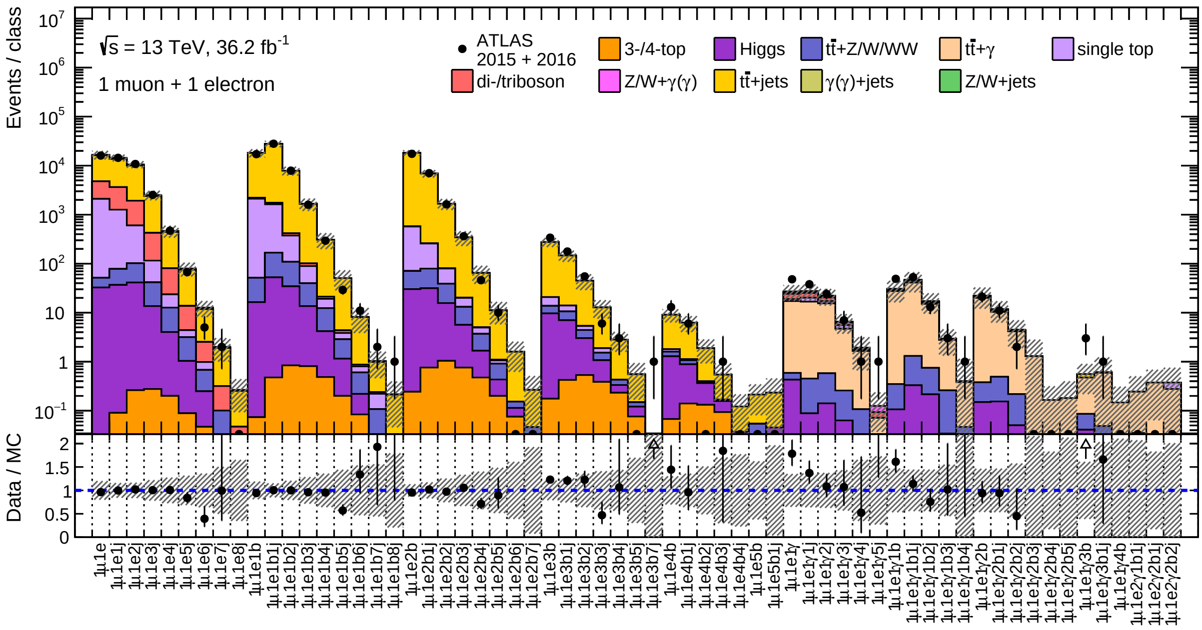

Figure I.14: Expected and observed number of events in all classes with one muon and one electron (no $E_{\mathrm{T}}^{\mathrm{miss}}$). The class labels list the type and multiplicity of reconstructed objects in the events. The total uncertainty on the SM prediction is indicated by hatched bands.

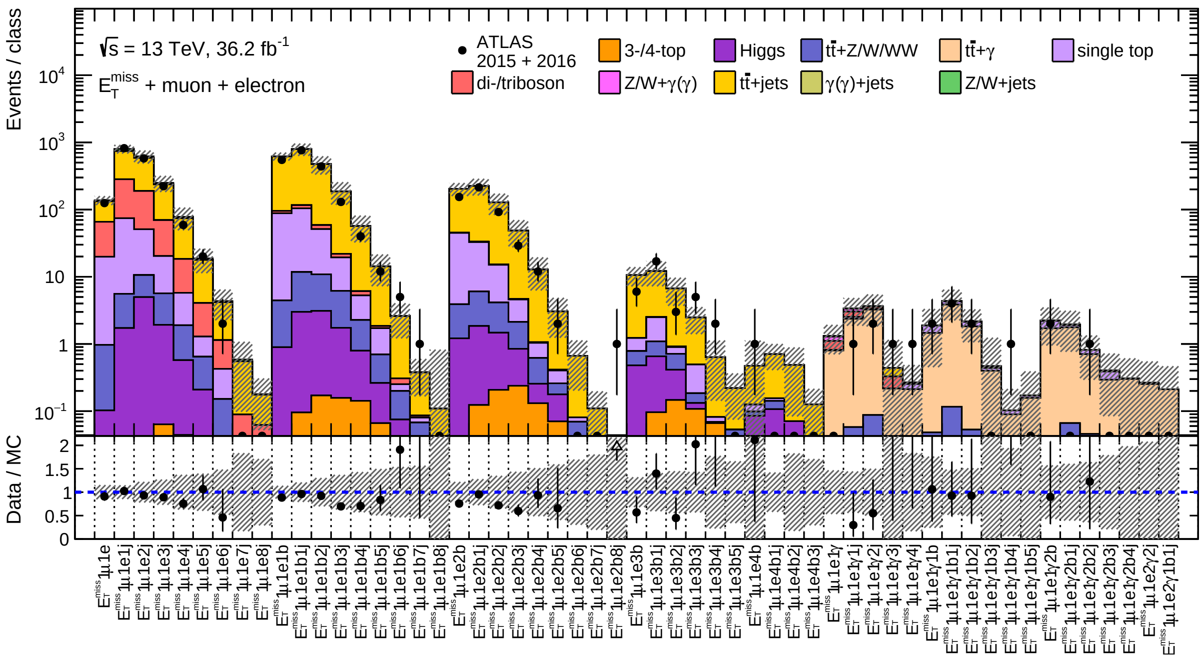

Figure I.15: Expected and observed number of events in all classes with large $E_{\mathrm{T}}^{\mathrm{miss}}$, one muon and one electron. The class labels list the type and multiplicity of reconstructed objects in the events. The total uncertainty on the SM prediction is indicated by hatched bands.

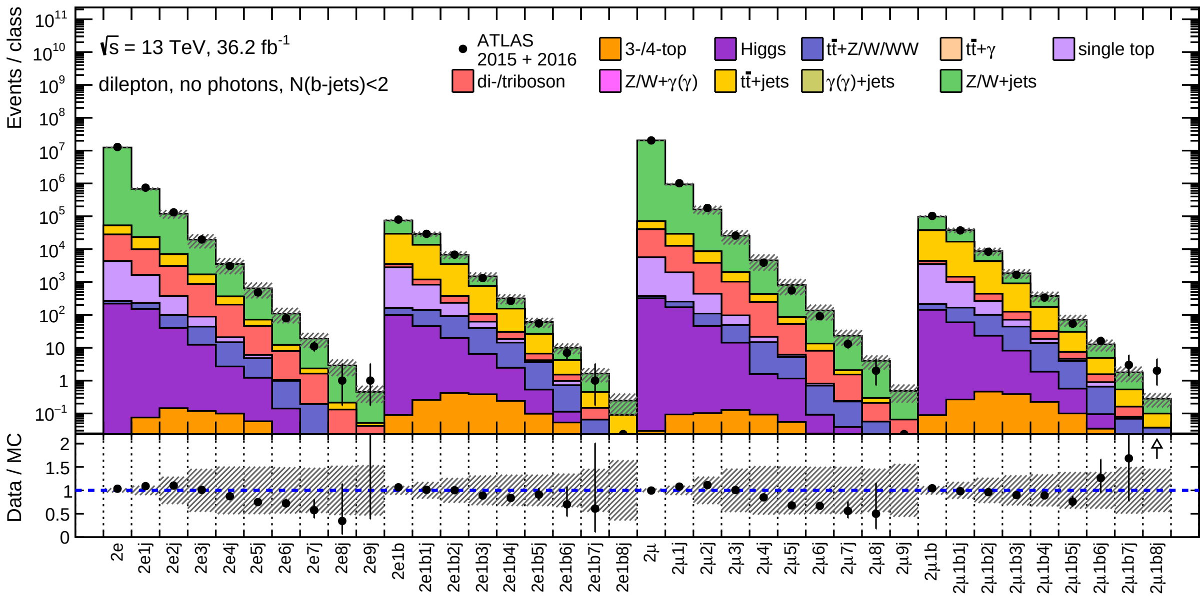

Figure I.16: Expected and observed number of events in all classes with two same-flavour leptons (electrons or muons) and at most one b-jet (no $E_{\mathrm{T}}^{\mathrm{miss}}$ or photons). The class labels list the type and multiplicity of reconstructed objects in the events. The total uncertainty on the SM prediction is indicated by hatched bands.

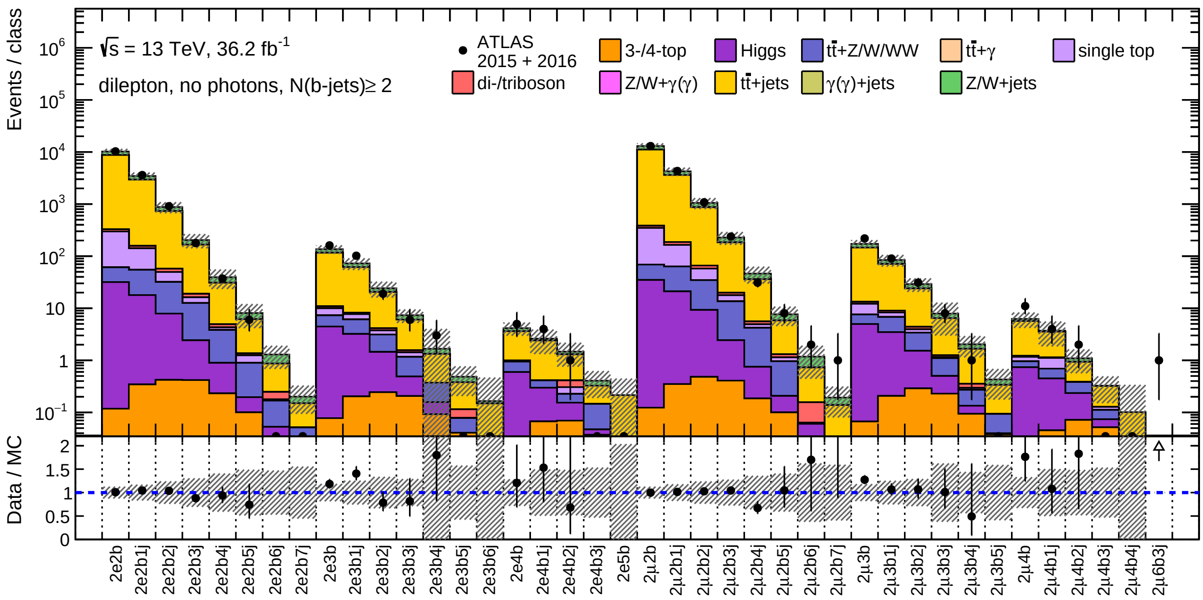

Figure I.17: Expected and observed number of events in all classes with two same-flavour leptons (electrons or muons) and at least two b-jet (no $E_{\mathrm{T}}^{\mathrm{miss}}$ or photons). The class labels list the type and multiplicity of reconstructed objects in the events. The total uncertainty on the SM prediction is indicated by hatched bands.

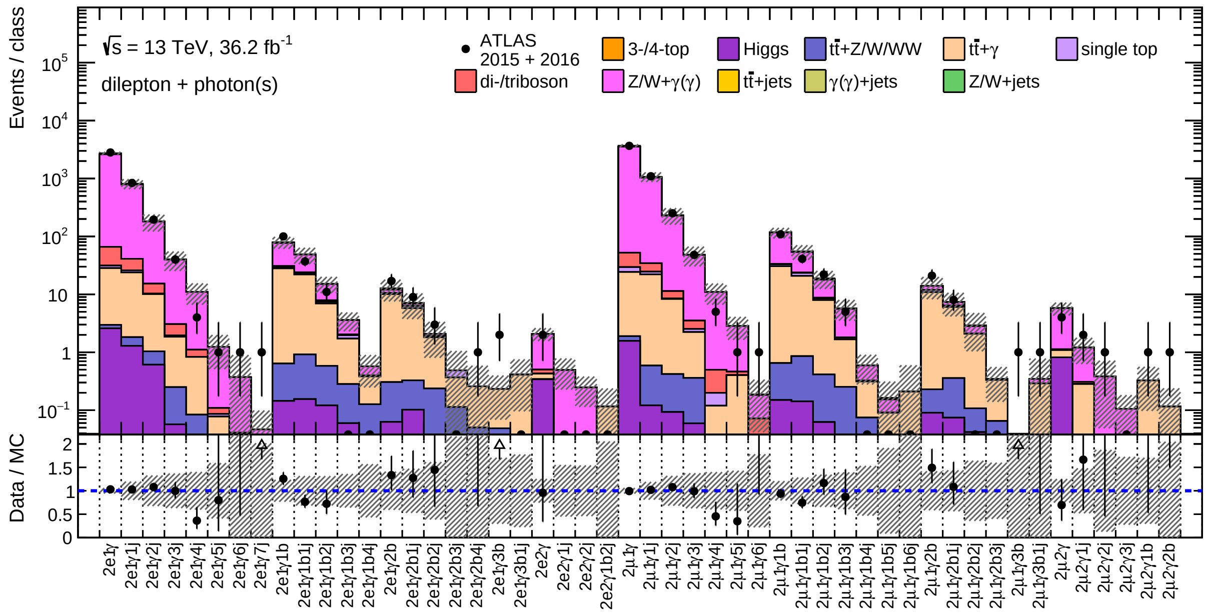

Figure I.18: Expected and observed number of events in all classes with two same-flavour leptons (electrons or muons) and at least one photon (no $E_{\mathrm{T}}^{\mathrm{miss}}$). The class labels list the type and multiplicity of reconstructed objects in the events. The total uncertainty on the SM prediction is indicated by hatched bands.

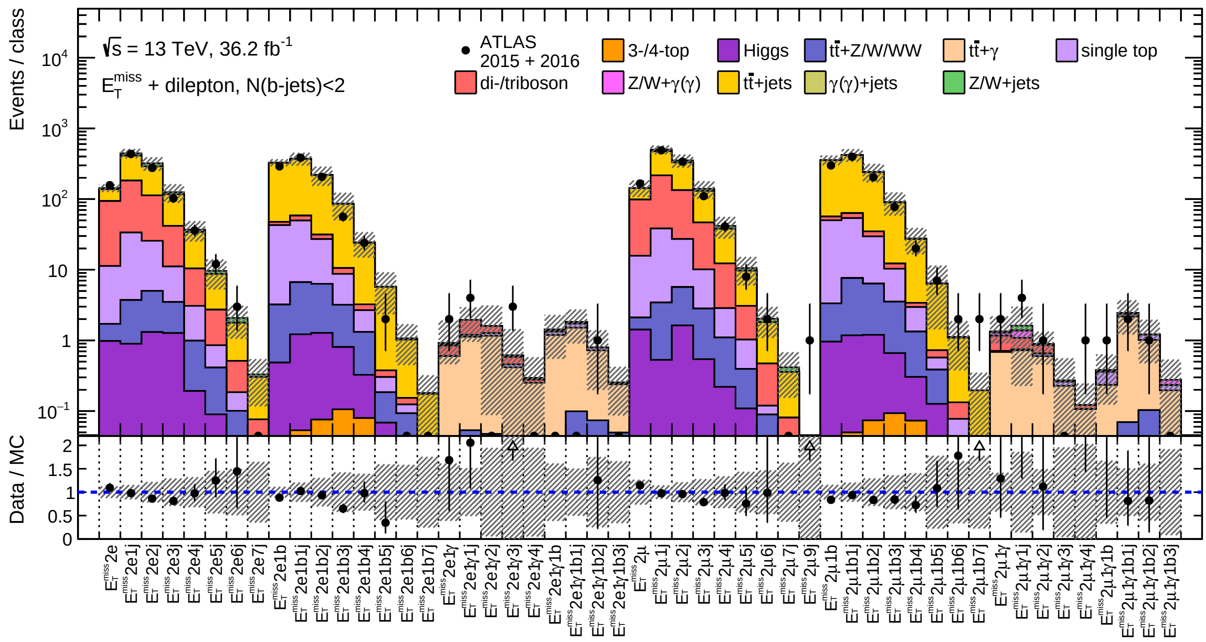

Figure I.19: Expected and observed number of events in all classes with large $E_{\mathrm{T}}^{\mathrm{miss}}$, two same-flavour leptons (electrons or muons) and at most one b-jet. The class labels list the type and multiplicity of reconstructed objects in the events. The total uncertainty on the SM prediction is indicated by hatched bands.

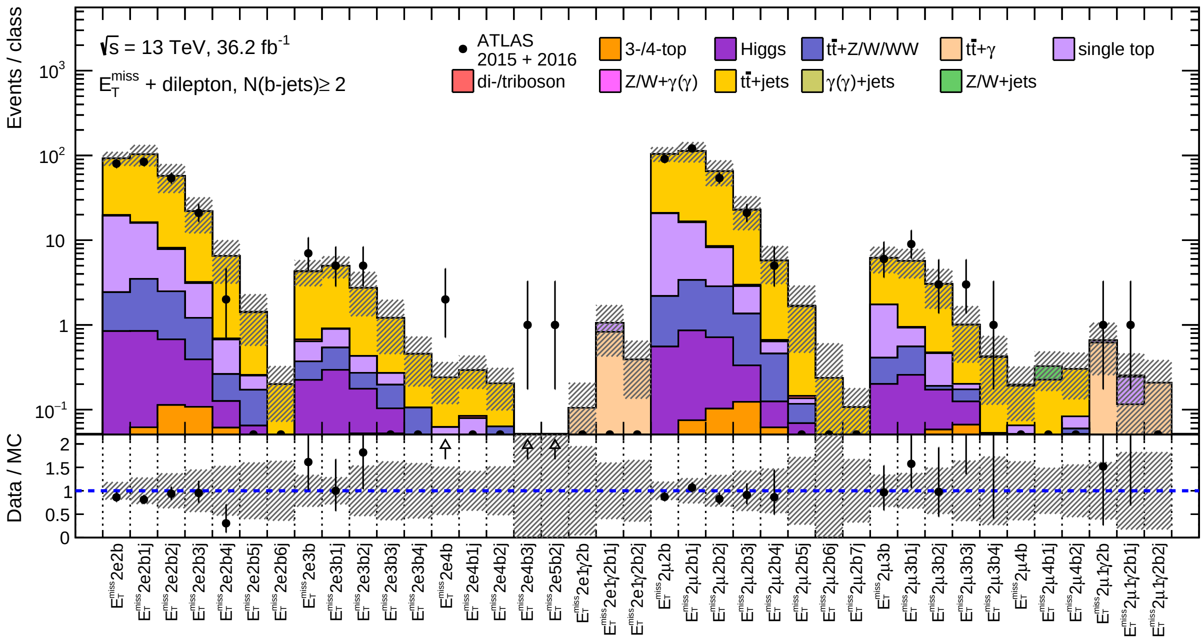

Figure I.20: Expected and observed number of events in all classes with large E_T^{miss}, two same-flavour leptons (electrons or muons) and at least two b-jets. The class labels list the type and multiplicity of reconstructed objects in the events. The total uncertainty on the SM prediction is indicated by hatched bands.

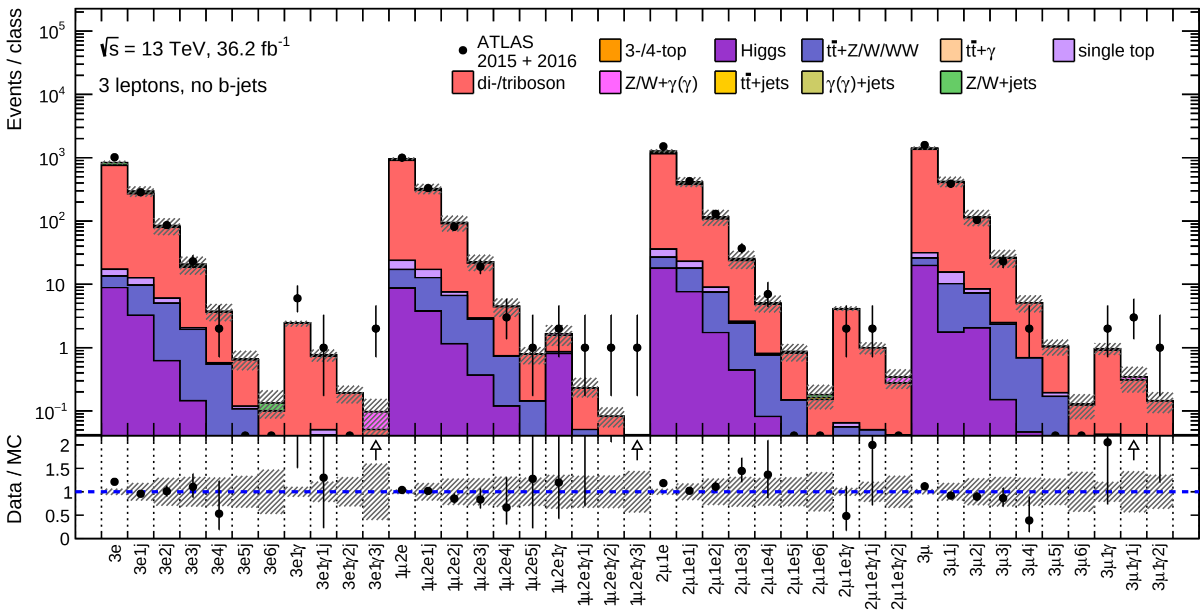

Figure I.21: Expected and observed number of events in all classes with three leptons and no b-jets (no E_T^{miss}). The class labels list the type and multiplicity of reconstructed objects in the events. The total uncertainty on the SM prediction is indicated by hatched bands.

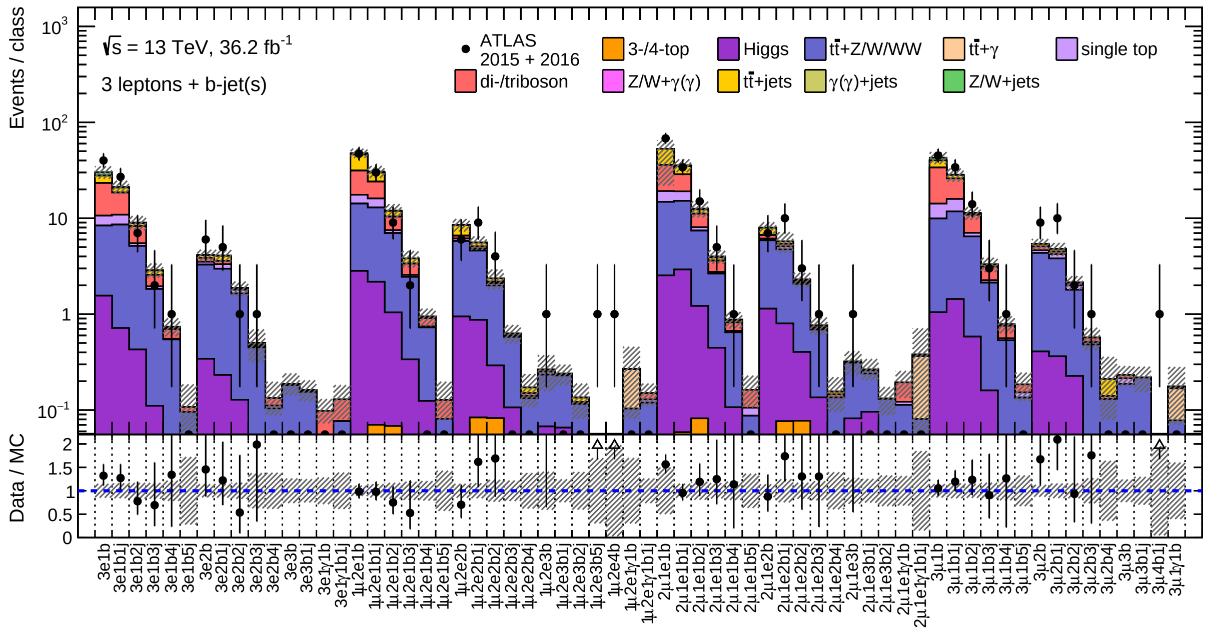

Figure I.22: Expected and observed number of events in all classes with three leptons and at least one b-jet (no E_T^{miss}). The class labels list the type and multiplicity of reconstructed objects in the events. The total uncertainty on the SM prediction is indicated by hatched bands.

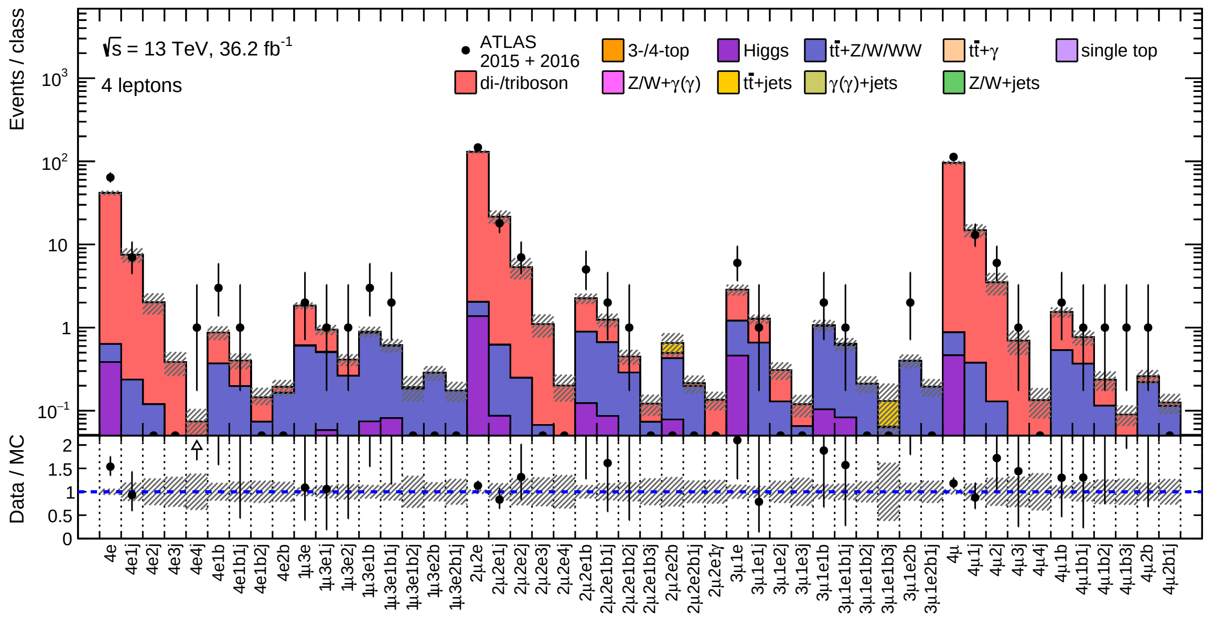

Figure I.23: Expected and observed number of events in all classes with four leptons (no E_T^{miss}). The class labels list the type and multiplicity of reconstructed objects in the events. The total uncertainty on the SM prediction is indicated by hatched bands.

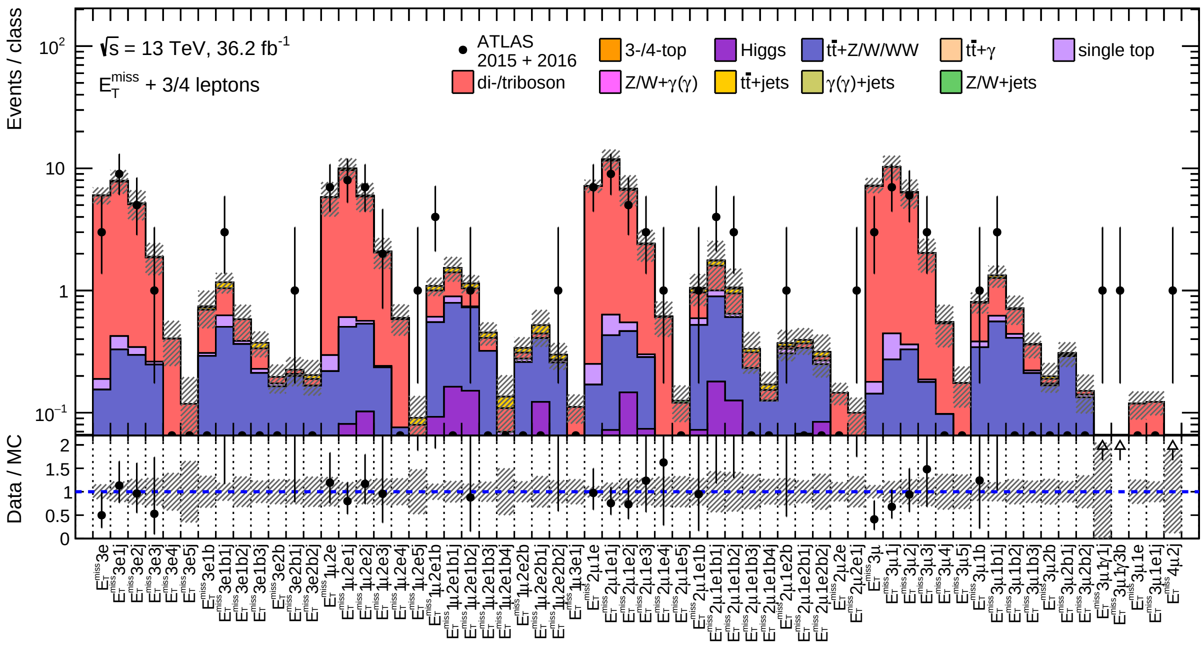

Figure I.24: Expected and observed number of events in all classes with large E_T^{miss} and at least three leptons. The class labels list the type and multiplicity of reconstructed objects in the events. The total uncertainty on the SM prediction is indicated by hatched bands.

Acronyms

L1Muon Level-1 Muon trigger 25, 26

L1Topo Level-1 Topological trigger 26

LAr liquid-argon 23, 47

LEE look-elsewhere effect 49, 52, 57, 64, 67, 68, 101, 122

LHC Large Hadron Collider . . . . . . vii, viii, 9, 10, 13, 14, 16, 19, 20, 25, 102, 123

LO leading order 16, 76–80, 106, 121

MC Monte Carlo . . . . . . viii, 16–18, 26, 30, 32, 36, 42, 44, 50, 55, 56, 59, 62, 63, 67, 68, 71, 74, 75, 78–80, 82, 84–87, 96, 102, 104, 105, 107–110, 112, 114, 120, 121, 123, 128, 131, 137–140, 154, 155, 174

MDT Monitored Drift Tube 24, 25, 36

ME matrix element 16, 17, 75–77, 79, 105

MS Muon Spectrometer 24, 25, 27, 35–37

NLL next-to-leading logarithmic 78

NLO next-to-leading order 16, 76–79, 104, 106, 120

NNLL next-to-next-to-leading logarithmic 76, 79

NNLO next-to-next-to-leading order 76, 77, 79

PDF parton density function 15–17, 74–80, 102, 104–106

pdf probability density function 51, 59, 88, 125, 126

pmf probability mass function 59, 64, 89

PS parton shower 17, 18, 75–79, 102, 104, 105

QCD quantum chromodynamics 1, 2, 4, 9, 11, 14, 16, 20, 77, 79, 104, 107, 114, 121, 124

QED quantum electrodynamics 1–3, 9

QFT quantum field theory 1, 8, 9

RoI Region-of-Interest 25, 33, 36, 37, 45, 85–87, 95, 97, 107, 110, 112, 114, 116–119

RPC Resistive-Plate Chamber 24, 25, 36

SCT Semiconductor Tracker 21, 22, 26, 29, 30

SM Standard Model vii, viii, 1–5, 8–14, 16, 19, 20, 49–51, 59, 63–68, 74, 75, 77–95, 102, 104–112, 116–121, 123, 124, 131, 132, 139–147, 149, 173–185

SUSY supersymmetry 12–14

TDAQ Trigger and Data Acquisition system 20, 25, 26

TGC Thin-Gap Chamber 24–26, 36

TRT Transition Radiation Tracker 21, 22, 29, 30, 32, 38

UL upper limit 84, 109, 110

Bibliography

[1] D0 Collaboration, *Search for new physics in $e\mu X$ data at DØ using SLEUTH: A quasi-model-independent search strategy for new physics*, Phys. Rev. D **62** (2000) 092004, arXiv: hep-ex/0006011.

[2] D0 Collaboration, *Quasi-model-independent search for new physics at large transverse momentum*, Phys. Rev. D **64** (2001) 012004, arXiv: hep-ex/0011067.

[3] D0 Collaboration, *Quasi-Model-Independent Search for New High p_T Physics at DØ*, Phys. Rev. Lett. **86** (2001) 3712, arXiv: hep-ex/0011071.

[4] D0 Collaboration, *Model independent search for new phenomena in $p\bar{p}$ collisions at $\sqrt{s} = 1.96$ TeV*, Phys. Rev. D **85** (2012) 092015, arXiv: 1108.5362 [hep-ex].

[5] H1 Collaboration, *A general search for new phenomena in ep scattering at HERA*, Phys. Lett. B **602** (2004) 14, arXiv: hep-ex/0408044.

[6] H1 Collaboration, *A general search for new phenomena at HERA*, Phys. Lett. B **674** (2009) 257, arXiv: 0901.0507 [hep-ex].

[7] CDF Collaboration, *Model-independent and quasi-model-independent search for new physics at CDF*, Phys. Rev. D **78** (2008) 012002, arXiv: 0712.1311 [hep-ex].

[8] CDF Collaboration, *Global search for new physics with 2.0 fb^{-1} at CDF*, Phys. Rev. D **79** (2009) 011101, arXiv: 0809.3781 [hep-ex].

[9] ATLAS Collaboration, *A general search for new phenomena with the ATLAS detector in pp collisions at $\sqrt{s} = 7$ TeV*, ATLAS-CONF-2012-107, 2012, URL: https://cds.cern.ch/record/1472686.

[10] ATLAS Collaboration, *A general search for new phenomena with the ATLAS detector in pp collisions at $\sqrt{s} = 8$ TeV*, ATLAS-CONF-2014-006, 2014, URL: https://cds.cern.ch/record/1666536.

[11] ATLAS Collaboration, *A strategy for a general search for new phenomena using data-derived signal regions and its application within the ATLAS experiment*, Eur. Phys. J. C **79** (2019) 120, arXiv: 1807.07447 [hep-ex].

[12] CMS Collaboration, *Model Unspecific Search for New Physics in pp Collisions at $\sqrt{s} = 7$ TeV*, CMS-PAS-EXO-10-021, 2011, URL: https://cds.cern.ch/record/1360173.

[13] CMS Collaboration, *MUSiC, a Model Unspecific Search for New Physics, in pp Collisions at $\sqrt{s} = 8$ TeV*, CMS-PAS-EXO-14-016, 2017, URL: http://cds.cern.ch/record/2256653.

[14] J. Schouwenberg, *Kalman Filter Trained Look-Up Tables for the ATLAS Level-1 Topological Missing Transverse Energy Trigger*, Master's thesis (2014), URL: https://www.ru.nl/publish/pages/913395/master_thesis_schouwenberg.pdf.

[15] ATLAS Collaboration, *Dark matter interpretations of ATLAS searches for the electroweak production of supersymmetric particles in $\sqrt{s} = 8$ TeV proton–proton collisions*, JHEP **09** (2016) 175, arXiv: 1608.00872 [hep-ex].

[16] S. L. Glashow, *Partial Symmetries of Weak Interactions*, Nucl. Phys. **22** (1961) 579.

[17] S. Weinberg, *A Model of Leptons*, Phys. Rev. Lett. **19** (1967) 1264.

[18] A. Salam, *Weak and Electromagnetic Interactions*, Conf. Proc. **C680519** (1968) 367.

[19] S. Tomonaga, *On a relativistically invariant formulation of the quantum theory of wave fields*, Prog. Theor. Phys. **1** (1946) 27.

[20] J. S. Schwinger, *Quantum electrodynamics. I A covariant formulation*, Phys. Rev. **74** (1948) 1439.

[21] R. P. Feynman, *Mathematical formulation of the quantum theory of electromagnetic interaction*, Phys. Rev. **80** (1950) 440.

[22] H. Fritzsch, M. Gell-Mann and H. Leutwyler, *Advantages of the Color Octet Gluon Picture*, Phys. Lett. **47B** (1973) 365.

[23] D. J. Gross and F. Wilczek, *Ultraviolet Behavior of Non-Abelian Gauge Theories*, Phys. Rev. Lett. **30** (1973) 1343.

[24] H. D. Politzer, *Reliable Perturbative Results for Strong Interactions?*, Phys. Rev. Lett. **30** (1973) 1346.

[25] S. L. Glashow, J. Iliopoulos and L. Maiani, *Weak Interactions with Lepton-Hadron Symmetry*, Phys. Rev. **D2** (1970) 1285.

[26] M. Kobayashi and T. Maskawa, *CP-Violation in the Renormalizable Theory of Weak Interaction*, Prog. Theor. Phys. **49** (1973) 652.

[27] G. S. Guralnik, C. R. Hagen and T. W. B. Kibble, *Global Conservation Laws and Massless Particles*, Phys. Rev. Lett. **13** (1964) 585.

[28] P. W. Higgs, *Broken Symmetries and the Masses of Gauge Bosons*, Phys. Rev. Lett. **13** (1964) 508.

[29] F. Englert and R. Brout, *Broken Symmetry and the Mass of Gauge Vector Mesons*, Phys. Rev. Lett. **13** (1964) 321.

[30] P. W. Anderson, *Plasmons, Gauge Invariance, and Mass*, Phys. Rev. **130** (1963) 439.

[31] G. Zweig, *An SU(3) model for strong interaction symmetry and its breaking*, CERN-TH-401, 1964, URL: http://cds.cern.ch/record/352337.

[32] M. Gell-Mann, *A Schematic Model of Baryons and Mesons*, Phys. Lett. **8** (1964) 214.

[33] G. 't Hooft and M. J. G. Veltman, *Regularization and Renormalization of Gauge Fields*, Nucl. Phys. **B44** (1972) 189.

[34] C. N. Yang and R. L. Mills, *Conservation of Isotopic Spin and Isotopic Gauge Invariance*, Phys. Rev. **96** (1954) 191.

[35] G. Altarelli and G. Parisi, *Asymptotic Freedom in Parton Language*, Nucl. Phys. **B126** (1977) 298.

[36] Gargamelle Neutrino Collaboration, *Observation of Neutrino Like Interactions Without Muon Or Electron in the Gargamelle Neutrino Experiment*, Phys. Lett. **46B** (1973) 138.

[37] UA1 Collaboration, *Experimental observation of isolated large transverse energy electrons with associated missing energy at* $\sqrt{s} = 540$ *GeV*, Phys. Lett. **122B** (1983) 103.

[38] UA2 Collaboration, *Observation of single isolated electrons of high transverse momentum in events with missing transverse energy at the CERN* $\bar{p}p$ *collider*, Phys. Lett. **122B** (1983) 476.

[39] UA1 Collaboration, *Experimental observation of lepton pairs of invariant mass around 95 GeV/*c^2 *at the CERN SPS collider*, Phys. Lett. **126B** (1983) 398.

[40] UA2 Collaboration, *Evidence for* $Z^0 \rightarrow e^+e^-$ *at the CERN* $\bar{p}p$ *collider*, Phys. Lett. **129B** (1983) 130.

[41] Y. Nambu and G. Jona-Lasinio, *Dynamical Model of Elementary Particles Based on an Analogy with Superconductivity. I*, Phys. Rev. **122** (1961) 345.

[42] Y. Nambu and G. Jona-Lasinio, *Dynamical Model of Elementary Particles Based on an Analogy with Superconductivity. II*, Phys. Rev. **124** (1961) 246.

[43] J. Goldstone, *Field Theories with Superconductor Solutions*, Nuovo Cim. **19** (1961) 154.

[44] E. Fermi, *Versuch einer Theorie der β-Strahlen. I*, Z. Phys. **88** (1934) 161.

[45] Y.-S. Tsai, *Decay Correlations of Heavy Leptons in* $e^+e^- \rightarrow \ell^+\ell^-$, Phys. Rev. **D4** (1971) 2821, [Erratum: Phys. Rev.D13,771(1976)].

[46] J. E. Augustin et al., *Discovery of a Narrow Resonance in* e^+e^- *Annihilation*, Phys. Rev. Lett. **33** (1974) 1406.

[47] J. J. Aubert et al., *Experimental Observation of a Heavy Particle* J, Phys. Rev. Lett. **33** (1974) 1404.

[48] S. W. Herb et al., *Observation of a Dimuon Resonance at 9.5 GeV in 400 GeV Proton-Nucleus Collisions*, Phys. Rev. Lett. **39** (1977) 252.

[49] M. L. Perl et al., *Evidence for Anomalous Lepton Production in* e^+ - e^- *Annihilation*, Phys. Rev. Lett. **35** (1975) 1489.

[50] K. Kodama et al., *Observation of tau neutrino interactions*, Phys. Lett. **B504** (2001) 218, arXiv: `hep-ex/0012035 [hep-ex]`.

[51] ATLAS Collaboration, *Observation of a new particle in the search for the Standard Model Higgs boson with the ATLAS detector at the LHC*, Phys. Lett. B **716** (2012) 1, arXiv: `1207.7214 [hep-ex]`.

[52] CMS Collaboration, *Observation of a new boson at a mass of 125 GeV with the CMS experiment at the LHC*, Phys. Lett. B **716** (2012) 30, arXiv: `1207.7235 [hep-ex]`.

[53] M. Tanabashi and others (Particle Data Group), *Review of Particle Physics*, Phys. Rev. **D98** (2018) 030001.

[54] D. Griffiths, *Introduction to elementary particles*, 2008, ISBN: 9783527406012.

[55] M. E. Peskin and D. V. Schroeder, *An Introduction to quantum field theory*, Addison-Wesley, 1995, ISBN: 9780201503975.

[56] M. Robinson, *Symmetry and the standard model: Mathematics and particle physics*, Springer, 2011, ISBN: 9781441982667.

[57] N. Cabibbo, *Unitary Symmetry and Leptonic Decays*, Phys. Rev. Lett. **10** (1963) 531.

[58] K. G. Wilson, *Confinement of Quarks*, Phys. Rev. **D10** (1974) 2445.

[59] B. Pontecorvo, *Inverse beta processes and nonconservation of lepton charge*, Sov. Phys. JETP **7** (1958) 172, [Zh. Eksp. Teor. Fiz.34,247(1957)].

[60] Z. Maki, M. Nakagawa and S. Sakata, *Remarks on the unified model of elementary particles*, Prog. Theor. Phys. **28** (1962) 870, [,34(1962)].

[61] J. Silk et al., *Particle Dark Matter: Observations, Models and Searches*, ed. by G. Bertone, Cambridge Univ. Press, 2010, ISBN: 9781107653924.

[62] S. Weinberg, *The Cosmological Constant Problem*, Rev. Mod. Phys. **61** (1989) 1.

[63] Super-Kamiokande Collaboration, *Evidence for oscillation of atmospheric neutrinos*, Phys. Rev. Lett. **81** (1998) 1562, arXiv: `hep-ex/9807003 [hep-ex]`.

[64] J. Schechter and J. W. F. Valle, *Neutrino Masses in SU(2) $\otimes$ U(1) Theories*, Phys. Rev. **D22** (1980) 2227.

[65] Planck Collaboration, *Planck 2015 results. XIII. Cosmological parameters*, Astron. Astrophys. **594** (2016) A13, arXiv: `1502.01589 [astro-ph.CO]`.

[66] L. Canetti, M. Drewes and M. Shaposhnikov, *Matter and Antimatter in the Universe*, New J. Phys. **14** (2012) 095012, arXiv: `1204.4186 [hep-ph]`.

[67] R. Foot, H. Lew and R. R. Volkas, *Electric charge quantization*, J. Phys. **G19** (1993) 361, [Erratum: J. Phys.G19,1067(1993)], arXiv: `hep-ph/9209259 [hep-ph]`.

[68] M. Nowakowski and A. Pilaftsis, *A Note on charge quantization through anomaly cancellation*, Phys. Rev. **D48** (1993) 259, arXiv: `hep-ph/9304312 [hep-ph]`.

[69] J. Baumann, J. Kalus, R. Gahler and W. Mampe, *Experimental Limit for the Charge of the Free Neutron*, Phys. Rev. **D37** (1988) 3107.

[70] G. Bressi et al., *Testing the neutrality of matter by acoustic means in a spherical resonator*, Phys. Rev. **A83** (2011) 052101, arXiv: `1102.2766 [physics.atom-ph]`.

[71] J. M. Pendlebury et al., *Revised experimental upper limit on the electric dipole moment of the neutron*, Phys. Rev. **D92** (2015) 092003, arXiv: `1509.04411 [hep-ex]`.

[72] R. D. Peccei and H. R. Quinn, *CP Conservation in the Presence of Instantons*, Phys. Rev. Lett. **38** (1977) 1440, [,328(1977)].

[73] S. Weinberg, *A New Light Boson?*, Phys. Rev. Lett. **40** (1978) 223.

[74] F. Wilczek, *Problem of Strong P and T Invariance in the Presence of Instantons*, Phys. Rev. Lett. **40** (1978) 279.

[75] W. Gohn, 'The Muon g-2 Experiment at Fermilab', *Proceedings, 18th Lomonosov Conference on Elementary Particle Physics: Moscow, Russia, August 24-30, 2017*, 2019 232, arXiv: 1801.00084 [hep-ex], URL: http://lss.fnal.gov/archive/2017/conf/fermilab-conf-17-602-ppd.pdf.

[76] H. Georgi and S. L. Glashow, *Unity of All Elementary Particle Forces*, Phys. Rev. Lett. **32** (1974) 438.

[77] H. Georgi, *The State of the Art–Gauge Theories*, AIP Conf. Proc. **23** (1975) 575.

[78] S. Dimopoulos, S. Raby and F. Wilczek, *Supersymmetry and the Scale of Unification*, Phys. Rev. D **24** (1981) 1681.

[79] J. C. Pati and A. Salam, *Lepton Number as the Fourth "Color"*, Phys. Rev. **D10** (1974) 275, [Erratum: Phys. Rev.D11,703(1975)].

[80] Super-Kamiokande Collaboration, *Search for proton decay via $p \to e^+\pi^0$ and $p \to \mu^+\pi^0$ in 0.31 megaton·years exposure of the Super-Kamiokande water Cherenkov detector*, Phys. Rev. **D95** (2017) 012004, arXiv: 1610.03597 [hep-ex].

[81] S. P. Martin, *A Supersymmetry primer*, Adv. Ser. Direct. High Energy Phys. **18** (1998) 1, arXiv: hep-ph/9709356.

[82] D. Stockinger, *The Muon Magnetic Moment and Supersymmetry*, J. Phys. **G34** (2007) R45, arXiv: hep-ph/0609168 [hep-ph].

[83] M. Ibe, T. T. Yanagida and N. Yokozaki, *Muon g-2 and 125 GeV Higgs in Split-Family Supersymmetry*, JHEP **08** (2013) 067, arXiv: 1303.6995 [hep-ph].

[84] S. R. Coleman and J. Mandula, *All Possible Symmetries of the S Matrix*, Phys. Rev. **159** (1967) 1251.

[85] R. Haag, J. T. Lopuszanski and M. Sohnius, *All Possible Generators of Supersymmetries of the s Matrix*, Nucl. Phys. **B88** (1975) 257, [,257(1974)].

[86] M. Shifman, *Large Extra Dimensions: Becoming acquainted with an alternative paradigm*, Int. J. Mod. Phys. **A25** (2010) 199, arXiv: 0907.3074 [hep-ph].

[87] T. Kaluza, *Zum Unitätsproblem der Physik*, Sitzungsber. Preuss. Akad. Wiss. Berlin (Math. Phys.) **1921** (1921) 966, arXiv: 1803.08616 [physics.hist-ph].

[88] O. Klein, *Quantum Theory and Five-Dimensional Theory of Relativity*, Z. Phys. **37** (1926) 895.

[89] O. Klein, *The Atomicity of Electricity as a Quantum Theory Law*, Nature **118** (1926) 516.

[90] H. Mandel, *Zur Herleitung der Feldgleichungen in der allgemeinen Relativitätstheorie*, Zeitschrift für Physik **39** (1926) 136.

[91] N. Arkani-Hamed, S. Dimopoulos and G. R. Dvali, *The Hierarchy problem and new dimensions at a millimeter*, Phys. Lett. **B429** (1998) 263, arXiv: hep-ph/9803315 [hep-ph].

[92] I. Antoniadis, N. Arkani-Hamed, S. Dimopoulos and G. R. Dvali, *New dimensions at a millimeter to a Fermi and superstrings at a TeV*, Phys. Lett. **B436** (1998) 257, arXiv: hep-ph/9804398 [hep-ph].

[93] L. Randall and R. Sundrum, *A Large mass hierarchy from a small extra dimension*, Phys. Rev. Lett. **83** (1999) 3370, arXiv: hep-ph/9905221 [hep-ph].

[94] L. Randall and R. Sundrum, *An Alternative to compactification*, Phys. Rev. Lett. **83** (1999) 4690, arXiv: hep-th/9906064 [hep-th].

[95] G. R. Dvali, G. Gabadadze and M. Porrati, *4-D gravity on a brane in 5-D Minkowski space*, Phys. Lett. **B485** (2000) 208, arXiv: hep-th/0005016 [hep-th].

[96] T. Appelquist, H.-C. Cheng and B. A. Dobrescu, *Bounds on universal extra dimensions*, Phys. Rev. **D64** (2001) 035002, arXiv: hep-ph/0012100 [hep-ph].

[97] D. London and J. L. Rosner, *Extra gauge bosons in E_6*, Phys. Rev. D **34** (1986) 1530.

[98] G. Altarelli, B. Mele and M. Ruiz-Altaba, *Searching for New Heavy Vector Bosons in $p\bar{p}$ Colliders*, Z. Phys. **C45** (1989) 109, [Erratum: Z. Phys.C47,676(1990)].

[99] P. Langacker, *The physics of heavy Z' gauge bosons*, Rev. Mod. Phys. **81** (2009) 1199, arXiv: 0801.1345 [hep-ph].

[100] E. Salvioni, G. Villadoro and F. Zwirner, *Minimal Z-prime models: Present bounds and early LHC reach*, JHEP **11** (2009) 068, arXiv: 0909.1320 [hep-ph].

[101] Y. L. Dokshitzer, *Calculation of the structure functions for deep-inelastic scattering and e^+e^- annihilation by perturbation theory in quantum chromodynamics.*, Sov. Phys. JETP **46** (1977) 641, [Zh. Eksp. Teor. Fiz. 73, 1216 (1977)].

[102] V. N. Gribov and L. N. Lipatov, *Deep inelastic ep scattering in perturbation theory*, Sov. J. Nucl. Phys. **15** (1972) 438, [Yad. Fiz. 15, 781 (1972)].

[103] T. Gleisberg et al., *Event generation with SHERPA 1.1*, JHEP **02** (2009) 007, arXiv: 0811.4622 [hep-ph].

[104] E. Bothmann et al., *Event Generation with Sherpa 2.2*, SciPost Phys. **7** (2019) 034, arXiv: 1905.09127 [hep-ph].

[105] T. Sjöstrand, S. Mrenna and P. Skands, *PYTHIA 6.4 physics and manual*, JHEP **05** (2006) 026, arXiv: hep-ph/0603175.

[106] T. Sjöstrand, S. Mrenna and P. Z. Skands, *A brief introduction to PYTHIA 8.1*, Comput. Phys. Commun. **178** (2008) 852, arXiv: 0710.3820 [hep-ph].

[107] T. Sjöstrand et al., *An Introduction to PYTHIA 8.2*, Comput. Phys. Commun. **191** (2015) 159, arXiv: 1410.3012 [hep-ph].

[108] G. Corcella et al., *HERWIG 6: an event generator for hadron emission reactions with interfering gluons (including supersymmetric processes)*, JHEP **01** (2001) 010, arXiv: hep-ph/0011363.

[109] M. Bahr et al., *Herwig++ Physics and Manual*, Eur. Phys. J. C **58** (2008) 639, arXiv: 0803.0883 [hep-ph].

[110] J. Bellm et al., *Herwig 7.0/Herwig++ 3.0 release note*, Eur. Phys. J. **C76** (2016) 196, arXiv: 1512.01178 [hep-ph].

[111] A. Buckley et al., *General-purpose event generators for LHC physics*, Phys. Rept. **504** (2011) 145, arXiv: 1101.2599 [hep-ph].

[112] F. Bloch and A. Nordsieck, *Note on the Radiation Field of the electron*, Phys. Rev. **52** (1937) 54.

[113] T. Kinoshita, *Mass singularities of Feynman amplitudes*, J. Math. Phys. **3** (1962) 650.

[114] T. D. Lee and M. Nauenberg, *Degenerate Systems and Mass Singularities*, Phys. Rev. **133** (1964) B1549, [,25(1964)].

[115] R. K. Ellis, W. J. Stirling and B. R. Webber, *QCD and collider physics*, Camb. Monogr. Part. Phys. Nucl. Phys. Cosmol. **8** (1996) 1.

[116] B. Andersson, G. Gustafson, G. Ingelman and T. Sjöstrand, *Parton Fragmentation and String Dynamics*, Phys. Rept. **97** (1983) 31.

[117] D. Amati and G. Veneziano, *Preconfinement as a Property of Perturbative QCD*, Phys. Lett. **83B** (1979) 87.

[118] L. Evans and P. Bryant, *LHC Machine*, JINST **3** (2008) S08001.

[119] ATLAS Collaboration, *Improved luminosity determination in pp collisions at $\sqrt{s} = 7$ TeV using the ATLAS detector at the LHC*, Eur. Phys. J. C **73** (2013) 2518, arXiv: `1302.4393 [hep-ex]`.

[120] ATLAS Collaboration, *Luminosity determination in pp collisions at $\sqrt{s} = 8$ TeV using the ATLAS detector at the LHC*, Eur. Phys. J. C **76** (2016) 653, arXiv: `1608.03953 [hep-ex]`.

[121] ATLAS Collaboration, *LuminosityPublicResultsRun2*, 2018, URL: `https://twiki.cern.ch/twiki/bin/view/AtlasPublic/LuminosityPublicResultsRun2` (visited on 24/08/2018).

[122] ATLAS Collaboration, *The ATLAS Experiment at the CERN Large Hadron Collider*, JINST **3** (2008) S08003.

[123] CMS Collaboration, *The CMS experiment at the CERN LHC*, JINST **3** (2008) S08004.

[124] ATLAS Collaboration, *Expected performance of the ATLAS experiment: detector, trigger and physics*, (2009), arXiv: `0901.0512 [hep-ex]`.

[125] CMS Collaboration, *CMS Physics Technical Design Report, Volume II: Physics Performance*, J. Phys G **34** (2007) 995.

[126] ATLAS Collaboration, *ATLAS Insertable B-Layer Technical Design Report*, ATLAS-TDR-19 (2010), URL: `https://cds.cern.ch/record/1291633`, *ATLAS Insertable B-Layer Technical Design Report Addendum*, ATLAS-TDR-19-ADD-1 (2012), URL: `https://cds.cern.ch/record/1451888`.

[127] J. Jimenez Peña, *Novel time-dependent alignment of the ATLAS Inner Detector in the LHC Run 2*, JINST **11** (2016) C11036.

[128] ATLAS Collaboration, *Performance of the ATLAS trigger system in 2015*, Eur. Phys. J. C **77** (2017) 317, arXiv: `1611.09661 [hep-ex]`.

[129] ATLAS Collaboration, *The ATLAS Simulation Infrastructure*, Eur. Phys. J. C **70** (2010) 823, arXiv: `1005.4568 [physics.ins-det]`.

[130] G. Duckeck et al., *ATLAS computing: Technical design report*, (2005).

[131] M. Dobbs and J. B. Hansen, *The HepMC C++ Monte Carlo event record for High Energy Physics*, Comput. Phys. Commun. **134** (2001) 41.

[132] S. Agostinelli et al., GEANT4 *a simulation toolkit*, Nucl. Instrum. Meth. A **506** (2003) 250.

[133] A. Sidoti, *Minimum Bias Trigger Scintillators in ATLAS Run II*, JINST **9** (2014) C10020.

[134] G. Barrand et al., *GAUDI - A software architecture and framework for building HEP data processing applications*, Comput. Phys. Commun. **140** (2001) 45.

[135] ATLAS Collaboration, *Performance of the ATLAS track reconstruction algorithms in dense environments in LHC Run 2*, Eur. Phys. J. C **77** (2017) 673, arXiv: 1704.07983 [hep-ex].

[136] R. Fruhwirth, *Application of Kalman filtering to track and vertex fitting*, Nucl. Instrum. Meth. **A262** (1987) 444.

[137] ATLAS Collaboration, *A neural network clustering algorithm for the ATLAS silicon pixel detector*, JINST **9** (2014) P09009, arXiv: 1406.7690 [hep-ex].

[138] ATLAS Collaboration, *The Optimization of ATLAS Track Reconstruction in Dense Environments*, ATL-PHYS-PUB-2015-006, 2015, URL: https://cds.cern.ch/record/2002609.

[139] ATLAS Collaboration, *Training and validation of the ATLAS pixel clustering neural networks*, ATL-PHYS-PUB-2018-002, 2018, URL: https://cds.cern.ch/record/2309474.

[140] ATLAS Collaboration, *Performance of the reconstruction of large impact parameter tracks in the inner detector of ATLAS*, ATL-PHYS-PUB-2017-014, 2017, URL: https://cds.cern.ch/record/2275635.

[141] ATLAS Collaboration, *Early Inner Detector Tracking Performance in the 2015 Data at $\sqrt{s} = 13$ TeV*, ATL-PHYS-PUB-2015-051, 2015, URL: https://cds.cern.ch/record/2110140.

[142] ATLAS Collaboration, *Reconstruction of primary vertices at the ATLAS experiment in Run 1 proton–proton collisions at the LHC*, Eur. Phys. J. C **77** (2017) 332, arXiv: 1611.10235 [hep-ex].

[143] ATLAS Collaboration, *Vertex Reconstruction Performance of the ATLAS Detector at $\sqrt{s} = 13$ TeV*, ATL-PHYS-PUB-2015-026, 2015, URL: https://cds.cern.ch/record/2037717.

[144] ATLAS Collaboration, *Electron efficiency measurements with the ATLAS detector using the 2015 LHC proton–proton collision data*, ATLAS-CONF-2016-024, 2016, URL: https://cds.cern.ch/record/2157687.

[145] ATLAS Collaboration, *Muon reconstruction performance of the ATLAS detector in proton–proton collision data at $\sqrt{s} = 13$ TeV*, Eur. Phys. J. C **76** (2016) 292, arXiv: 1603.05598 [hep-ex].

[146] ATLAS Collaboration, *Photon identification in 2015 ATLAS data*, ATL-PHYS-PUB-2016-014, 2016, URL: https://cds.cern.ch/record/2203125.

[147] ATLAS Collaboration, *Measurement of the photon identification efficiencies with the ATLAS detector using LHC Run 2 data collected in 2015 and 2016*, Eur. Phys. J. C **79** (2019) 205, arXiv: 1810.05087 [hep-ex].

[148] ATLAS Collaboration,
Topological cell clustering in the ATLAS calorimeters and its performance in LHC Run 1,
Eur. Phys. J. C **77** (2017) 490, arXiv: 1603.02934 [hep-ex].

[149] M. Cacciari, G. P. Salam and G. Soyez, *The anti-k_t jet clustering algorithm*,
JHEP **04** (2008) 063, arXiv: 0802.1189 [hep-ph].

[150] M. Cacciari, G. P. Salam and G. Soyez, *FastJet user manual*,
Eur. Phys. J. C **72** (2012) 1896, arXiv: 1111.6097 [hep-ph].

[151] ATLAS Collaboration, *Jet energy scale measurements and their systematic uncertainties in proton–proton collisions at $\sqrt{s} = 13$ TeV with the ATLAS detector*,
Phys. Rev. D **96** (2017) 072002, arXiv: 1703.09665 [hep-ex].

[152] ATLAS Collaboration, *Monte Carlo Calibration and Combination of In-situ Measurements of Jet Energy Scale, Jet Energy Resolution and Jet Mass in ATLAS*, ATLAS-CONF-2015-037, 2015, URL: https://cds.cern.ch/record/2044941.

[153] ATLAS Collaboration, *Performance of pile-up mitigation techniques for jets in pp collisions at $\sqrt{s} = 8$ TeV using the ATLAS detector*, Eur. Phys. J. C **76** (2016) 581,
arXiv: 1510.03823 [hep-ex].

[154] ATLAS Collaboration, *Performance of b-jet identification in the ATLAS experiment*,
JINST **11** (2016) P04008, arXiv: 1512.01094 [hep-ex].

[155] ATLAS Collaboration, *Expected performance of the ATLAS b-tagging algorithms in Run-2*,
ATL-PHYS-PUB-2015-022, 2015, URL: https://cds.cern.ch/record/2037697.

[156] ATLAS Collaboration, *Performance of missing transverse momentum reconstruction with the ATLAS detector using proton–proton collisions at $\sqrt{s} = 13$ TeV*,
Eur. Phys. J. C **78** (2018) 903, arXiv: 1802.08168 [hep-ex].

[157] ATLAS Collaboration,
Selection of jets produced in 13 TeV proton–proton collisions with the ATLAS detector,
ATLAS-CONF-2015-029, 2015, URL: https://cds.cern.ch/record/2037702.

[158] A. Martin, W. Stirling, R. Thorne and G. Watt, *Parton distributions for the LHC*,
Eur. Phys. J. C **63** (2009) 189, arXiv: 0901.0002 [hep-ph].

[159] ATLAS Collaboration, *Summary of ATLAS Pythia 8 tunes*, ATL-PHYS-PUB-2012-003,
2012, URL: https://cds.cern.ch/record/1474107.

[160] D. J. Lange, *The EvtGen particle decay simulation package*,
Nucl. Instrum. Meth. A **462** (2001) 152.

[161] ATLAS Collaboration, *ATLAS Pythia 8 tunes to 7 TeV data*, ATL-PHYS-PUB-2014-021,
2014, URL: https://cds.cern.ch/record/1966419.

[162] R. D. Ball et al., *Parton distributions with LHC data*, Nucl. Phys. B **867** (2013) 244,
arXiv: 1207.1303 [hep-ph].

[163] M. H. Seymour and A. Siodmok,
Constraining MPI models using σ_{eff} and recent Tevatron and LHC Underlying Event data,
JHEP **10** (2013) 113, arXiv: 1307.5015 [hep-ph].

[164] J. Pumplin et al.,
New Generation of Parton Distributions with Uncertainties from Global QCD Analysis,
JHEP **07** (2002) 012, arXiv: hep-ph/0201195.

[165] H.-L. Lai et al., *New parton distributions for collider physics*, Phys. Rev. D **82** (2010) 074024, arXiv: 1007.2241 [hep-ph].

[166] S. Schumann and F. Krauss, *A parton shower algorithm based on Catani-Seymour dipole factorisation*, JHEP **03** (2008) 038, arXiv: 0709.1027 [hep-ph].

[167] ATLAS Collaboration, *Monte Carlo Generators for the Production of a W or Z/γ^* Boson in Association with Jets at ATLAS in Run 2*, ATL-PHYS-PUB-2016-003, 2016, URL: https://cds.cern.ch/record/2120133.

[168] T. Gleisberg and S. Höche, *Comix, a new matrix element generator*, JHEP **12** (2008) 039, arXiv: 0808.3674 [hep-ph].

[169] F. Cascioli, P. Maierhöfer and S. Pozzorini, *Scattering Amplitudes with Open Loops*, Phys. Rev. Lett. **108** (2012) 111601, arXiv: 1111.5206 [hep-ph].

[170] S. Höche, F. Krauss, M. Schönherr and F. Siegert, *QCD matrix elements + parton showers. The NLO case*, JHEP **04** (2013) 027, arXiv: 1207.5030 [hep-ph].

[171] R. Gavin, Y. Li, F. Petriello and S. Quackenbush, *FEWZ 2.0: A code for hadronic Z production at next-to-next-to-leading order*, Comput. Phys. Commun. **182** (2011) 2388, arXiv: 1011.3540 [hep-ph].

[172] R. Gavin, Y. Li, F. Petriello and S. Quackenbush, *W physics at the LHC with FEWZ 2.1*, Comput. Phys. Commun. **184** (2013) 208, arXiv: 1201.5896 [hep-ph].

[173] J. M. Campbell and R. K. Ellis, *Update on vector boson pair production at hadron colliders*, Phys. Rev. D **60** (1999) 113006, arXiv: hep-ph/9905386.

[174] J. M. Campbell, R. K. Ellis and C. Williams, *Vector boson pair production at the LHC*, JHEP **07** (2011) 018, arXiv: 1105.0020 [hep-ph].

[175] J. Alwall et al., *The automated computation of tree-level and next-to-leading order differential cross sections, and their matching to parton shower simulations*, JHEP **07** (2014) 079, arXiv: 1405.0301 [hep-ph].

[176] S. Alioli, P. Nason, C. Oleari and E. Re, *A general framework for implementing NLO calculations in shower Monte Carlo programs: the POWHEG BOX*, JHEP **10** (2010) 043, arXiv: 1002.2581 [hep-ph].

[177] ATLAS Collaboration, *Simulation of top-quark production for the ATLAS experiment at $\sqrt{s} = 13$ TeV*, ATL-PHYS-PUB-2016-004, 2016, URL: https://cds.cern.ch/record/2120417.

[178] P. Artoisenet, R. Frederix, O. Mattelaer and R. Rietkerk, *Automatic spin-entangled decays of heavy resonances in Monte Carlo simulations*, JHEP **03** (2013) 015, arXiv: 1212.3460 [hep-ph].

[179] P. Z. Skands, *Tuning Monte Carlo generators: The Perugia tunes*, Phys. Rev. D **82** (2010) 074018, arXiv: 1005.3457 [hep-ph].

[180] N. Kidonakis, *Two-loop soft anomalous dimensions for single top quark associated production with a W^- or H^-*, Phys. Rev. D **82** (2010) 054018, arXiv: 1005.4451 [hep-ph].

[181] N. Kidonakis, *Next-to-next-to-leading logarithm resummation for s-channel single top quark production*, Phys. Rev. D **81** (2010) 054028, arXiv: 1001.5034 [hep-ph].

[182] N. Kidonakis, *Next-to-next-to-leading-order collinear and soft gluon corrections for t-channel single top quark production*, Phys. Rev. D **83** (2011) 091503, arXiv: 1103.2792 [hep-ph].

[183] M. Czakon and A. Mitov, *Top++: A program for the calculation of the top-pair cross-section at hadron colliders*, Comput. Phys. Commun. **185** (2014) 2930, arXiv: 1112.5675 [hep-ph].

[184] M. Czakon, D. Heymes and A. Mitov, *High-Precision Differential Predictions for Top-Quark Pairs at the LHC*, Phys. Rev. Lett. **116** (2016) 082003, arXiv: 1511.00549 [hep-ph].

[185] M. Czakon, D. Heymes and A. Mitov, *Dynamical scales for multi-TeV top-pair production at the LHC*, JHEP **04** (2017) 071, arXiv: 1606.03350 [hep-ph].

[186] F. Cascioli, P. Maierhöfer, N. Moretti, S. Pozzorini and F. Siegert, *NLO matching for $t\bar{t}b\bar{b}$ production with massive b-quarks*, Phys. Lett. **B734** (2014) 210, arXiv: 1309.5912 [hep-ph].

[187] ATLAS Collaboration, *Multi-boson simulation for 13 TeV ATLAS analyses*, ATL-PHYS-PUB-2016-002, 2016, URL: https://cds.cern.ch/record/2119986.

[188] ATLAS Collaboration, *Modelling of the $t\bar{t}H$ and $t\bar{t}V(V = W, Z)$ processes for $\sqrt{s} = 13$ TeV ATLAS analyses*, ATL-PHYS-PUB-2016-005, 2016, URL: https://cds.cern.ch/record/2120826.

[189] ATLAS Collaboration, *Measurement of the Z/γ^* boson transverse momentum distribution in pp collisions at $\sqrt{s} = 7$ TeV with the ATLAS detector*, JHEP **09** (2014) 145, arXiv: 1406.3660 [hep-ex].

[190] LHC Higgs Cross Section Working Group, *Handbook of LHC Higgs Cross Sections: 2. Differential Distributions*, CERN-2012-002, arXiv: 1201.3084 [hep-ph].

[191] Yu. A. Golfand and E. P. Likhtman, *Extension of the Algebra of Poincare Group Generators and Violation of p Invariance*, JETP Lett. **13** (1971) 323, [Pisma Zh. Eksp. Teor. Fiz. **13** (1971) 452].

[192] D. V. Volkov and V. P. Akulov, *Is the Neutrino a Goldstone Particle?*, Phys. Lett. B **46** (1973) 109.

[193] J. Wess and B. Zumino, *Supergauge Transformations in Four-Dimensions*, Nucl. Phys. B **70** (1974) 39.

[194] J. Wess and B. Zumino, *Supergauge Invariant Extension of Quantum Electrodynamics*, Nucl. Phys. B **78** (1974) 1.

[195] S. Ferrara and B. Zumino, *Supergauge Invariant Yang-Mills Theories*, Nucl. Phys. B **79** (1974) 413.

[196] A. Salam and J. Strathdee, *Super-symmetry and non-Abelian gauges*, Phys. Lett. B **51** (1974) 353.

[197] L. Lonnblad and S. Prestel, *Matching tree-level matrix elements with interleaved showers*, JHEP **03** (2012) 019, arXiv: 1109.4829 [hep-ph].

[198] W. Beenakker, M. Kramer, T. Plehn, M. Spira and P. M. Zerwas, *Stop production at hadron colliders*, Nucl. Phys. B **515** (1998) 3, arXiv: hep-ph/9710451.

[199] W. Beenakker et al., *Supersymmetric top and bottom squark production at hadron colliders*, JHEP **08** (2010) 098, arXiv: 1006.4771 [hep-ph].

[200] W. Beenakker et al., *Squark and gluino hadroproduction*, Int. J. Mod. Phys. A **26** (2011) 2637, arXiv: 1105.1110 [hep-ph].

[201] ATLAS Collaboration, *Electron and photon energy calibration with the ATLAS detector using data collected in 2015 at $\sqrt{s} = 13$ TeV*, ATL-PHYS-PUB-2016-015, 2016, URL: https://cds.cern.ch/record/2203514.

[202] ATLAS Collaboration, *Luminosity determination in pp collisions at $\sqrt{s} = 13$ TeV using the ATLAS detector at the LHC*, ATLAS-CONF-2019-021, 2019, URL: https://cds.cern.ch/record/2677054.

[203] S. Frixione, E. Laenen, P. Motylinski, B. R. Webber and C. D. White, *Single-top hadroproduction in association with a W boson*, JHEP **07** (2008) 029, arXiv: 0805.3067 [hep-ph].

[204] ATLAS Collaboration, *Measurements of $W\gamma$ and $Z\gamma$ production in pp collisions at $\sqrt{s} = 7$ TeV with the ATLAS detector at the LHC*, Phys. Rev. D **87** (2013) 112003, arXiv: 1302.1283 [hep-ex], Erratum: Phys. Rev. D **91** (2015) 119901.

[205] ATLAS Collaboration, *Search for supersymmetry at $\sqrt{s} = 13$ TeV in final states with jets and two same-sign leptons or three leptons with the ATLAS detector*, Eur. Phys. J. C **76** (2016) 259, arXiv: 1602.09058 [hep-ex].

[206] ATLAS Collaboration, *Search for resonances in diphoton events at $\sqrt{s} = 13$ TeV with the ATLAS detector*, JHEP **09** (2016) 001, arXiv: 1606.03833 [hep-ex].

[207] ATLAS Collaboration, *Search for new phenomena in high-mass diphoton final states using 37 fb^{-1} of proton–proton collisions collected at $\sqrt{s} = 13$ TeV with the ATLAS detector*, Phys. Lett. B **775** (2017) 105, arXiv: 1707.04147 [hep-ex].

[208] ATLAS Collaboration, *Electron reconstruction and identification in the ATLAS experiment using the 2015 and 2016 LHC proton–proton collision data at $\sqrt{s} = 13$ TeV*, Eur. Phys. J. C **79** (2019) 639, arXiv: 1902.04655 [hep-ex].

[209] ATLAS Collaboration, *Optimisation of the ATLAS b-tagging performance for the 2016 LHC Run*, ATL-PHYS-PUB-2016-012, 2016, URL: https://cds.cern.ch/record/2160731.

[210] ATLAS Collaboration, *The Pythia 8 A3 tune description of ATLAS minimum bias and inelastic measurements incorporating the Donnachie–Landshoff diffractive model*, ATL-PHYS-PUB-2016-017, 2016, URL: https://cds.cern.ch/record/2206965.

[211] R. D. Ball et al., *Parton distributions for the LHC Run II*, JHEP **04** (2015) 040, arXiv: 1410.8849 [hep-ph].

[212] ATLAS Collaboration, *ATLAS simulation of boson plus jets processes in Run 2*, ATL-PHYS-PUB-2017-006, 2017, URL: https://cds.cern.ch/record/2261937.

[213] ATLAS Collaboration, *Multi-Boson Simulation for 13 TeV ATLAS Analyses*, ATL-PHYS-PUB-2017-005, 2017, URL: https://cds.cern.ch/record/2261933.

[214] ATLAS Collaboration, *Improvements in $t\bar{t}$ modelling using NLO+PS Monte Carlo generators for Run 2*, ATL-PHYS-PUB-2018-009, 2018, URL: https://cds.cern.ch/record/2630327.

[215] S. Dulat et al.,
New parton distribution functions from a global analysis of quantum chromodynamics,
Phys. Rev. **D93** (2016) 033006, arXiv: 1506.07443 [hep-ph].

[216] L. A. Harland-Lang, A. D. Martin, P. Motylinski and R. S. Thorne,
Parton distributions in the LHC era: MMHT 2014 PDFs, Eur. Phys. J. **C75** (2015) 204,
arXiv: 1412.3989 [hep-ph].

[217] ATLAS Collaboration, *Search for heavy ZZ resonances in the $\ell^+\ell^-\ell^+\ell^-$ and $\ell^+\ell^-\nu\bar{\nu}$ final states using proton–proton collisions at $\sqrt{s} = 13$ TeV with the ATLAS detector*,
Eur. Phys. J. C **78** (2018) 293, arXiv: 1712.06386 [hep-ex].

[218] ATLAS Collaboration, *Measurement of the production cross section of three isolated photons in pp collisions at $\sqrt{s} = 8$ TeV using the ATLAS detector*, Phys. Lett. B **781** (2018) 55,
arXiv: 1712.07291 [hep-ex].

[219] J. M. Campbell and C. Williams, *Triphoton production at hadron colliders*,
Phys. Rev. **D89** (2014) 113001, arXiv: 1403.2641 [hep-ph].

[220] ATLAS Collaboration, *Study of $WW\gamma$ and $WZ\gamma$ production in pp collisions at $\sqrt{s} = 8$ TeV and search for anomalous quartic gauge couplings with the ATLAS experiment*,
Eur. Phys. J. C **77** (2017) 646, arXiv: 1707.05597 [hep-ex].

[221] CMS Collaboration, *A search for $WW\gamma$ and $WZ\gamma$ production and constraints on anomalous quartic gauge couplings in pp collisions at $\sqrt{s} = 8$ TeV*, Phys. Rev. D **90** (2014) 032008,
arXiv: 1404.4619 [hep-ex].

Summary

The high-energy collision data gathered by the LHC experiments allow many hypothetical models of beyond the Standard Model physics to be tested. Signals of beyond the Standard Model physics might, however, remain hidden from direct searches motivated by theoretical models. This thesis describes a strategy employed by the ATLAS Collaboration to systematically search for deviations of the collider data from the Standard Model prediction.

The strategy used is one of sequential hypothesis testing on two independent datasets. Initially, many background-only tests are performed in orthogonal data selections using Monte Carlo simulated background estimates. A significant deviation, in a given data selection, between the event counts observed in the experiment and expected from the simulated background declares that data selection a *data-derived signal region*. A data-derived signal region is then analysed in a dedicated analysis for which the background model can be optimised further, e.g. by using data-driven techniques.

This strategy is first applied to 3.2 fb^{-1} of proton–proton collision data at a centre-of-mass energy of 13 TeV collected with the ATLAS detector at the LHC in 2015. Collision events are classified according to their final state into 750 mutually exclusive event classes. For each event class, an automated search algorithm tests whether the data are compatible with the Monte Carlo simulated expectation in several distributions sensitive to the effects of new physics. The significance of a deviation is quantified using pseudo-experiments. Nearly 10^6 regions have been analysed, however, no significant deviations have been found, and consequently, no data-derived signal regions for a follow-up analysis are defined.

Following this, the strategy is applied to a larger dataset of 36.2 fb^{-1} collected in 2015 and 2016. Several distributions of more than 1,000 mutually exclusive event classes are tested in a preliminary version of the analysis. Additionally, the data are tested using fewer but more inclusive event classes enhancing the sensitivity to possible signals that might otherwise be distributed over many classes. This is supplemented with the reconstruction of Z and Higgs bosons in typical decay channels. Due to the incomplete background model used for this preliminary analysis, regions can only be eliminated from data-derived-signal-region candidacy. The majority of regions are ruled out for candidacy, however, several regions cannot be ruled out. These regions will need to be re-examined with a complete background model for those regions to either rule them out from candidacy or confirm the region as a data-derived signal region.

Samenvatting

De data afkomstig van deeltjesbotsingen bij hoge energie die verzameld worden door de LHC-experimenten maken het mogelijk om vele hypothetische uitbreidingen van het standaardmodel te toetsen. Het is echter mogelijk dat tekenen van nieuwe fysica (fysica die niet wordt beschreven door het standaardmodel) verborgen blijven voor zoektochten die zijn gebaseerd op theoretische modellen en zich beperken tot de voorspelde signalen. Dit proefschrift beschrijft een strategie die wordt gebruikt door de ATLAS Collaboratie om systematisch te zoeken naar afwijkingen in de botsingsdata ten opzichte van de standaardmodelverwachting.

De strategie die wordt toegepast toetst een hypothese in serie op twee onafhankelijke datasets. Aanvankelijk wordt het standaardmodel getoetst aan de data in een groot aantal orthogonale dataselecties met behulp van Monte Carlo gesimuleerde standaardmodelverwachtingen. Een significante afwijking, in een gegeven dataselectie, tussen het aantal waarnemingen in het experiment en de verwachting op basis van de simulaties benoemt de betreffende selectie tot een *van-data-afgeleid signaalgebied*. Zulke signaalgebieden worden vervolgens geanalyseerd en getoetst met een analyse die specifiek is toegewijd aan een signaalgebied waardoor het achtergrondmodel verder kan worden geoptimaliseerd, bijvoorbeeld door het toepassen van gebruikelijke data-gedreven technieken.

Deze strategie is eerst toegepast op 3.2 fb^{-1} aan proton–proton-botsingsdata met een zwaartepuntsenergie van 13 TeV vastgelegd met de ATLAS-detector aan de LHC in 2015. Botsingswaarnemingen worden ingedeeld in 750 elkaar uitsluitende klassen aan de hand van de waargenomen deeltjes, objecten en eigenschappen na een botsingsgebeurtenis. Voor elke klasse toetst een geautomatiseerd zoekalgoritme of de Monte Carlo gesimuleerde verwachtingswaarden compatibel zijn met de data in verschillende distributies die gevoelig zijn voor de effecten van nieuwe fysica. De significantie van een afwijking wordt gekwantificeerd met behulp van pseudo-experimenten. Bijna 10^6 regio's zijn geanalyseerd, waarbij geen significante afwijkingen zijn gevonden. Bijgevolg zijn er geen van-data-afgeleide signaalgebieden gedefinieerd voor een vervolg analyse.

Vervolgens is de strategie toegepast op een grotere dataset van 36.2 fb^{-1} vastgelegd in 2015 en 2016. Verschillende distributies van meer dan 1.000 elkaar uitsluitende klassen zijn getoetst met een voorlopige versie van de analyse. Daarnaast worden de data ook getoetst gebruikmakend van minder maar inclusievere klassen wat de gevoeligheid verbetert voor signalen die anders mogelijk verdund worden over een groot aantal klassen. Dit wordt aangevuld met de reconstructie van Z- en Higgsbosonen in typische vervalkanalen. Vanwege het onvolledige achtergrondmodel dat wordt gebruikt voor deze voorlopige analyse, kunnen regio's alleen worden uitgesloten als mogelijke van-data-afgeleide signaalgebieden. De meeste regio's kunnen worden uitgesloten als signaalgebieden en slechts enkele regio's kunnen niet worden uitgesloten. Deze regio's zullen opnieuw moeten worden onderzocht met een compleet achtergrondmodel, zodra dit beschikbaar is voor die regio's, om ze uit te sluiten of om de regio aan te merken als een van-data-afgeleid signaalgebied.

Curriculum vitae

Jeroen Schouwenberg was born in Boxmeer on the 2nd of August 1987. He received bilingual education at College Den Hulster in Venlo where he graduated in 2007. In 2009, he enrolled in the Applied Physics bachelor programme of Eindhoven University of Technology where he received a BSc degree in March 2013. In March 2015, he received his MSc degree *cum laude* from Radboud University Nijmegen after completing the Physics and Astronomy master programme. His master's thesis on the topic of the ATLAS trigger system, titled *Kalman Filter Trained Look-Up Tables for the ATLAS Level-1 Topological Missing Transverse Energy Trigger*, was conducted under the supervision of Dr. Sascha Caron.

In 2014, the author was selected for the CERN Summer Student Programme and spend three months at CERN where he worked on test setups for prototypes of silicon pixel detectors for the ALICE experiment under the supervision of Dr. Hartmut Hillemanns.

In February 2015, the author started as a graduate student in the department of Experimental High Energy Physics at the Radboud University Nijmegen under the supervision of Prof. Nicolo de Groot and Dr. Sascha Caron. This thesis is a result of the work performed during the graduate programme. One year of the graduate programme was spend at CERN. As a graduate student, he also took on responsibilities in teaching bachelor courses and advanced particle physics courses at the Radboud University Nijmegen.

Acknowledgements

This thesis came about through the contributions, help and input of many others whom I would like to acknowledge in this section.

First of all, I would like to thank Dr. Sascha Caron for introducing me to the topic of BSM-model-independent searches, for giving me the opportunity to be a PhD student under his guidance and for the many fruitful discussions over the years. I would also like to thank my thesis supervisor, Prof. Nicolo de Groot as well as the members of the manuscript committee: Prof. Gabriel Lord, Prof. Thomas Hebbeker, Prof. Robert Fleischer, Prof. Paul de Jong and Dr. Ivo van Vulpen, for agreeing to be on the committee and for taking the time to carefully read the thesis.

Although the final stages of this work and the writing of the thesis were pretty much a solo job, the journey started out an proceeded with a small team that has made this result possible. I want to thank all the members of the analysis team for the pleasant and fruitful collaboration over the years. In particular, I would like to mention Simone Amoroso, Marina Rotaru, Adam Jinaru and Alexandra Tudorache and thank them for teaching me the ropes when I got started, for their input and contributions without which this work would not have been possible, and of course for their company and hospitality on the rare occasions we actually met in person.

This work, in many ways, is also shaped by all the feedback received from the many members within the ATLAS Collaboration during the preparation of the 'General Search' publication. Thanks to all who have taken an interest and shared their feedback, thoughts and opinion along the way. In this light, a special thanks to the members of the editorial board, the Exotics (sub)group conveners and the physics coordinators.

Embarking on a PhD adventure does not only shape your life during working hours (as far as those are defined) but just as much outside those. A big and warm *thank you* to my fellow PhD students, friends, colleagues and family with whom I have had the pleasure to share so many wonderful moments during this time. Whether the holidays together, the activities in Geneva, the Vierdaagse, the Italian dinners, or simply the times we spent in each other's company, you have given me many fond memories of my time as a PhD student which I will cherish.